Control of robotic mobile manipulators : application to civil engineering

Kamal Mohy El Dine

Université Clermont Auvergne

École doctorale Sciences Pour l'Ingénieur
Spécialité "Électronique et systèmes"

Ph.D. Thesis

Control of Robotic Mobile Manipulators: Application to Civil Engineering

Presented by
M. Kamal MOHY EL DINE

Defended on May 23rd, 2019 in front of the committee composed of:

M. Ahmed RAHMANI	Professeur des universités, CRIStAL	Rapporteur
M. Omar TAHRI	Maître de conférences HDR, PRISME	Rapporteur
Mme. Véronique PERDEREAU	Professeur des universités, ISIR	Examinateur
M. Giovanni LEGNANI	Professeur des universités, UNIBS	Examinateur
M. Burkhard CORVES	Prof.-Univ. Dr.-Ing. Dr. h. c., RWTH Aachen	Examinateur
M. Jean-Christophe FAUROUX	Maître de conférences HDR, Institut Pascal	Directeur de thèse
M. Juan-Antonio CORRALES-RAMON	Maître de conférences, Institut Pascal	Encadrant
M. Youcef MEZOUAR	Professeur des universités, Institut Pascal	Encadrant

Université Clermont Auvergne - SIGMA Clermont
Institut Pascal, UMR 6602 CNRS/UCA/SIGMA Clermont, F-63171 Aubière, France

Acknowledgments

The Robots to Re-Construction project (Bots2ReC https://www.bots2rec.eu), has received funding from the European Union's Horizon 2020 Innovation Action programme under grant agreement No. 687593.

This dissertation is the summary of my research from March 2016 to March 2019 as a member of "Institut Pascal" the joint laboratory of SIGMA-Clermont. It has never been completed without the time and the help of many people.

First of all, I would like to express my sincere gratitude to my supervisors: Dr. Jean-Christophe FAUROUX, Dr. Juan-Antonio CORRALES-RAMON and Prof. Youcef MEZOUAR in SIGMA-Clermont for the continuous support during this research period. Without their precious support, it would not be possible to conduct this research and reach this point; their guidance, useful comments and remarks helped me in all the time of research and writing of this thesis.

Besides my supervisors, I would like to thank the rest of my thesis committee: Prof. Ahmed RAHMANI, Dr. Omar TAHRI, Prof. Véronique PERDEREAU, Prof. Giovanni LEGNANI and Prof. Burkhard CORVES from whom I will be happy to receive insightful comments which will help me widening my research from various perspectives.

I would like also to sincerely thank Prof. Toshiyuki MURAKAMI. He was my master's thesis supervisor in japan, he inspired me and was a source of my motivation.

In his memory, a very special thanks goes to my previous professor Wisama KHALIL who passed away more than a year ago. Beside his research that has influenced a large robotics community, his trust, help, insight and encouragements were never missing. He has taught me a lot and ignited the spirit of ambition within me.

My sincere thanks also go to the complete consortium and specifically to the partners in the project and their teams: RWTH Aachen University, Robotnik Automation SLL, Telerobot Labs Srl, Indurad, Fundacio Eurecat and Bouygues Construction. Their help, discussions, feedback and technical support helped me very much in achieving this work.

I gratefully acknowledge my colleagues in "Institut Pascal" laboratory for their discussions, assistance and comments.

Last but not the least, I would like to thank my loved ones and my family who have spiritually supported me throughout the entire process and my life in general, both by keeping me harmonious and helping me putting pieces together. I will be grateful forever for your love.

April, 2019

Kamal MOHY EL DINE

Contents

Table of contents **v**

List of figures **vi**

List of tables **vii**

1 Introduction **1**
- 1.1 Background of This Dissertation . . . 1
- 1.2 Asbestos: Its Usage, Implications and Regulations . . . 1
- 1.3 The Bots2ReC Project . . . 5
- 1.4 Objective of This Dissertation . . . 8
- 1.5 Approach . . . 10
- 1.6 Chapters Organization . . . 12

2 Observers **13**
- 2.1 Dynamics Based DC Motor Control . . . 14
- 2.2 Disturbance Observer . . . 15
- 2.3 Zero Moment Point Disturbance Observer . . . 20
  - 2.3.1 Results . . . 23
- 2.4 Recurrent Neural Network Force-Torque Sensor Disturbance Observer . . . 26
  - 2.4.1 Technical approach . . . 27
  - 2.4.2 Data collection and testing . . . 28
  - 2.4.3 Results . . . 29
- 2.5 Conclusion . . . 36

3 Wall Grinding Based on Active Force Control **37**
- 3.1 Interaction With the Environment . . . 38
  - 3.1.1 Impedance control and its alternatives . . . 38
  - 3.1.2 Hybrid position-force control . . . 39
- 3.2 Polishing and grinding controllers review . . . 40
  - 3.2.1 Polishing . . . 41
  - 3.2.2 Grinding . . . 42
- 3.3 Smooth Position-Force Controller with Compliant Wrist for Wall Grinding . . . 43
  - 3.3.1 Hybrid position-force control in operational space . . . 44
  - 3.3.2 Force and position control Loops: . . . 45
  - 3.3.3 Smooth transition control . . . 46
  - 3.3.4 Impedance/Admittance based orientation control . . . 46
  - 3.3.5 Radar based orientation . . . 48

3.3.6 Disturbance grinding torque for simulation . . . 48
3.3.7 Adams-Matlab/Simulink co-simulation . . . 48
3.3.8 Experiments . . . 56
3.3.9 Conclusion . . . 61
3.4 Model Based Adaptive Hybrid Velocity-Position-Force Controller for Wall Grinding . . . 62
3.4.1 Hybrid velocity-force control in the compliant frame . . . 62
3.4.2 Modeling of the feeding grinding force . . . 64
3.4.3 Non-contact forces elimination from the force-torque sensor readings . . . 69
3.4.4 Force and motion control Loops . . . 72
3.4.5 Experimental evaluation . . . 74
3.4.6 Discussions . . . 91
3.4.7 Conclusions . . . 91
3.5 Summary . . . 92

4 Mobile Manipulator Control for On-line Tip-over Avoidance **93**
4.1 Control Framework . . . 94
4.1.1 Operational space dynamics . . . 94
4.1.2 Operational space position control of the end-effector . . . 96
4.1.3 Stability controller . . . 96
4.1.4 Maximum manipulability in the null space . . . 98
4.2 Adams-Matlab/Simulink Dynamic Simulation . . . 99
4.3 Summary . . . 105

General conclusion and perspectives **107**

List of publications **109**

Bibliography **110**

List of Figures

1.1 Apparent asbestos consumption in Europe in the last century (the apparent consumption is calculated in the basis of the national production of asbestos and imports and exports) (Bouygues Construction [2015]) 2
1.2 World production of asbestos (metric tons) from 1900 to the present (Future Timeline [2018]) 3
1.3 Asbestos removal tasks 5
1.4 Conceptual sketch of the automated removal of asbestos contamination . 8
1.5 Bots2ReC work packages and their relation to each other 9
1.6 Bots2ReC robots 10
1.7 Conceptual block diagram for designing a dynamic controller that considers interaction between mobile manipulator and environment while grinding 11
1.8 Bots2ReC system architecture given by **Fundacio Eurecat** 11
1.9 Chapters organization 12

2.1 Simple feedback system with disturbance and observer that compensates it 14
2.2 Simple feedback system with sensor disturbance and observer that compensates it 14
2.3 Nominal dynamic model of rotational DC motor 15
2.4 Disturbance calculation based on velocity response and first order low pass filter 16
2.5 Equivalent block diagram of low pass filter 16
2.6 Block diagram of the disturbance observer (DOB) 17
2.7 Disturbance compensation via current feedback 17
2.8 Disturbance compensation via torque feedback 18
2.9 Visualization of the effect of DOB 18
2.10 Block diagram equivalent to Figure 2.9 19
2.11 Detailed analysis of DOB with pseudo differentiation 19
2.12 Block diagram equivalent to Figure 2.11 20
2.13 DOB block diagram with position feedback 20
2.14 COM position errors illustrated on a m-link manipulator 21
2.15 Zero moment point observer (ZMPOB) 22
2.16 Two link manipulator modeled for Adams/Matlab-Simulink co-simulation 23
2.17 End-point x and z positions 24
2.18 2-R robot joints angular accelerations 24
2.19 End-point accelerations along x and z directions 24
2.20 Zero moment point observer vs. original ZMP form evaluation under uncertainties ($\boldsymbol{\Delta l} = [\Delta l_1, \Delta l_2]$) added to the center of masses positions ($\boldsymbol{l} = [l_1, l_2]$) of the links 25
2.21 Experimental setup and the proposed force observer 27
2.22 Collision test setup 29

2.23 RMS errors for the RNN models based on different training inputs 30
2.24 Non-contact forces estimated by the RNNOB for an unseen automatic trajectory with no load attached to the force-torque sensor. 32
2.25 Non-contact wrench estimation of the proposed RNNOB compared with an analytical-based approach and as measured by the force-torque sensor for an unseen manual trajectory with an external load. 33
2.26 Contact force estimation of the proposed approach compared to the reference force measurement 34
2.27 Non-contact wrench estimation of RNNOB compared with an analytical-based approach and as measured by the force-torque sensor 35

3.1 Conceptual block diagram of hybrid controller 39
3.2 End-effector illustrating passive compliant accommodation to the surface using springs 41
3.3 Kinematic structure of the robotic system equipped with a grinding tool, several 1D-distance radar sensors around it for attitude measurement, and a force/torque sensor to perform asbestos removal on the wall 44
3.4 Hybrid controller block diagram: force control loop (green), position control loop (blue), admittance control loop (red) 45
3.5 Joint based admittance controller block diagram 47
3.6 Tool absolute orientation 48
3.7 Adams-Matlab co-simulation 49
3.8 Position desired and response values in Adams-Matlab co-simulation . . 49
3.9 Position errors in Adams-Matlab co-simulation 50
3.10 Velocity desired and response values in Adams-Matlab co-simulation . . 50
3.11 Velocity errors in Adams-Matlab co-simulation 51
3.12 The desired and response values of normal force on the wall in Adams-Matlab co-simulation 51
3.13 Normal force desired-response errors in Adams-Matlab co-simulation . . 52
3.14 Smooth switching from position to force control in Adams-Matlab co-simulation 53
3.15 The reaction torques on 5^{th} and 6^{th} joints from Adams-Matlab co-simulation 53
3.16 Zero-moment-point on the end-effector in Adams-Matlab co-simulation . 54
3.17 Suppressing the disc noise and random impacts by impedance control in Adams-Matlab co-simulation 55
3.18 Position compensation by admittance control in Adams-Matlab co-simulation 55
3.19 The robotic system equipped with a grinding tool, camera for distance measurement, and a force/torque sensor to perform grinding on a piece of wall 56
3.20 Hybrid controller block diagram in Figure 3.4 adapted for KUKA LWR tests: force control loop (green), position control loop (blue), KUKA impedance control loop (red) 57
3.21 Position desired versus response values 59
3.22 Velocity desired versus response values 59
3.23 Position desired-response errors 59
3.24 Raw reaction forces on the tool while grinding 60
3.25 The desired and response value of normal force on the wall 60
3.26 Normal force error 60
3.27 Smooth switching from position to force control. $(1,1)$ is the index to the first element of the selection matrix 60

3.28 Zero-moment-point on the end-effector in Adams-Matlab co-simulation . 61
3.29 Grinding quality obtained from the position-force controller with compliant wrist . . . 61
3.30 The robotic system equipped with grinding tool and force/torque sensor to perform grinding on a piece of wall. The grid is to evaluate the wall before and after grinding . . . 63
3.31 The choice of the frames for simultaneous force and motion control . . . 63
3.32 The manual grinding setup used to determine the normal grinding force f^{reac} and the translational velocity of the disc on the wall v_{norm}. The system equipped with grinding tool, force/torque sensor and a handle to perform grinding on the wall . . . 65
3.33 Normal grinding forces collected from 3 manual tests . . . 66
3.34 Translational velocities of the disc on the wall collected from 3 manual tests 66
3.35 Grinding parameters . . . 66
3.36 Surface roughness measurement setup . . . 68
3.37 Feeding force estimation ($\mu_e = 3.469 \times 10^8$ and $\mu_f = 0.00126$) . . . 68
3.38 Recurrent neural network observer to estimate non-contact forces. $\{o\}$ is the robot operational frame and $\{s\}$ is the force-torque sensor frame . . . 70
3.39 Non-contact forces estimated by the RNNOB against the ones measured by the force torque sensor . . . 71
3.40 Non-contact torques estimated by the RNNOB against the ones measured by the force torque sensor . . . 71
3.41 Orientation adaptive function . . . 74
3.42 Different wall geometries to grind. On the left side of the figure, the walls are placed on coordinate-measuring machine (CMM) to evaluate their surface before grinding. On the left side is the mesh obtained for each wall, it is measured in the machine frame $\{M\}$ shown in the figure a.1. The color map corresponds to the depth along ${}^{M}\vec{z}$ . . . 75
3.43 Switching from velocity to force control using interactive slider . . . 76
3.44 Force control performance in tracking the desired force value . . . 77
3.45 Velocity control performance in tracking the desired velocity value . . . 78
3.46 Orientation control performance in tracking the desired angle value . . . 78
3.47 Feeding force variation . . . 79
3.48 Flat wall top view before and after grinding straightly between p_0 and p_1 79
3.50 Grinding path depth evaluated under the lines L_1 and L_2 shown in Figure 3.49b . . . 80
3.51 Force control performance in tracking the desired force value . . . 81
3.52 Velocity control performance in tracking the desired velocity value . . . 82
3.53 Orientation control performance in tracking the desired angle value . . . 82
3.54 Feeding force variation . . . 83
3.55 Convex wall top view before and after grinding straightly between the way-points p_0 to p_{11} . . . 83
3.57 Depth map describing the shortest distance (depth of the cut) between the meshes before and after grinding shown in Figure 3.56a . . . 85
3.58 Grinding path depth evaluated under the curves C_1 to C_7 shown in Figure 3.56b . . . 85
3.59 Force control performance in tracking the desired force value . . . 86
3.60 Velocity control performance in tracking the desired velocity value . . . 87
3.61 Orientation control performance in tracking the desired angle value . . . 87

3.62 Feeding force variation . . . 88
3.63 Concave wall top view before and after grinding straightly between the way-points p_0 to p_{10} . . . 88
3.65 Depth map describing the shortest distance (depth of the cut) between the meshes before and after grinding shown in Figure 3.64a . . . 90
3.66 Grinding path depth evaluated under the curves C_2 to C_5 shown in Figure 3.64b . . . 90

4.1 A top heavy mobile manipulator following a spatial trajectory $\boldsymbol{r}(t)$ is critically unstable and might tip over. The kinematics of the robot are depicted in the figure above . . . 95
4.2 Mobile base modeling . . . 97
4.3 7-dof robotic arm kinematics for maximum manipulability. . . . 98
4.4 Position desired vs. response values . . . 100
4.5 Velocity desired vs. response values . . . 101
4.6 End-effector position errors . . . 101
4.7 End-effector velocity errors . . . 102
4.8 Desired accelerations. . . . 102
4.9 Zero moment point control on a desired point during the trajectory execution . . . 103
4.10 Orientation control of the ZMP deviation from the axis x_m (Figure 4.2) . . . 103
4.11 Velocity control behavior of the mobile base . . . 104
4.12 ZMP projection in the base support plane. . . . 104

List of Tables

1.1 Asbestos consumption (in t) in the European community in 1973 (Asbestos Trade Association, France) 6
1.2 Bots2ReC robot technical requirements 9

2.1 Root mean square errors on the zero-moment-point estimation using the ZMPOB and the original method 23
2.2 The root mean square errors on the automatic and manual test datasets with no external load 31
2.3 The root mean square errors on the dataset with an external load for the RNNOB and the analytical method based on identification 31

3.1 Controller gains used in the experiments 58
3.2 Parameters of the grinding model 67
3.3 The RNNOB root mean square errors on the rotational test dataset with the grinder attached. 70
3.4 Controller gains used in the experiments 76

4.1 Mobile base parameters. 96

Chapter 1

Introduction

Chapter 1 presents the background and the objective of this dissertation. It also presents the asbestos problem in the field of construction industry, and how it formed the motivation behind the project that funds this Ph.D.

1.1 Background of This Dissertation

Despite the advances in industrial automation, robotic solutions are not yet commonly used in civil engineering, construction, de-construction and re-construction sectors. However, over the past few decades, various automation concepts for construction have been developed as a response to the strongly growing civil engineering domain. The number of robots implemented in construction and demolition industries is in continuous growth as the International Federation of Robotics (IFR) states that the number of robots and automatic systems supplied in 2015 was 568 unit and expected to reach 2,800 units in 2019 (IFR [2018]). However, construction tasks remain a challenge for robots, as they require varied techniques, specific tools, highly skilled operators and they take place in varied and complex environments that require advanced perception capacities. At this time, the majority of the tasks is still performed by human operators using conventional electrical and hydraulic tools. However, with the decrease in the relative cost of machinery with respect to human labor and with the strict health regulations on some risky jobs, robots are progressively becoming credible alternatives to replace humans. For example, the refurbishment of the buildings that contain asbestos is still made by human workers, which subjects them to serious health hazards resulting from asbestos dust that can infiltrate into their respiratory system, even with the use of protections. Additionally, the productivity is currently limited by the human performance while the surface area of contaminated flats is considerable. Thus, the Robots to Re-Construction (Bots2ReC) project has started as an H2020 Innovation Action to efficiently automate the asbestos removal in real rehabilitation sites without endangering the human workers' health (Bots2ReC [2015]).

1.2 Asbestos: Its Usage, Implications and Regulations

Asbestos is a natural mineral that has been mined and used for centuries because it is a very good heat, electricity and sound insulator and it has long durability (Alleman and Mossman [1997]). It has been used in thousands of products, mainly, construction

materials. Over time, however, asbestos was related to the sickness that seemed to follow workers who worked with it.

Asbestos has been known to be hazardous since the beginning of the 20th century, where Romans have observed that sickness will follow the slaves who worked with asbestos. Hence, they recommended never to buy asbestos quarry slaves as they often die young (UNRV [2019]). Recently, since at least the 1920s, researchers realized that when asbestos materials are disturbed or damaged, asbestos fibers can be released into the air and cause dangerous exposure. When people accidentally inhale or ingest the microscopic fibers, the mineral can eventually lead to serious health problems like mesothelioma, cancer and other asbestos-related diseases (Straif et al. [2009], World Health Organization et al. [2017] and Mesothelioma and Asbestos Awareness Center [2019]). Despite the early awareness of the health problems that can be caused by asbestos, the production and the usage of this mineral didn't slow down.

As it can be seen in Figures 1.1 and 1.2, asbestos use skyrocketed throughout Europe and the world from the late 1940s through the late 1970s, putting millions of people at risk of exposure. Throughout this same time period, the connection between asbestos exposure and cancer risk became more clear, as more reports of mesothelioma and other asbestos diseases flooded in. Any amount of asbestos exposure, even limited, is considered dangerous and can later lead to a mesothelioma diagnosis. When inhaled or ingested, the microscopic asbestos fibers work their way into the lining of the lungs, abdomen or heart. Over a period of 10 to upwards of 50 years, the fibers can cause inflammation and scarring, which can eventually develop into mesothelioma tumors or other related conditions (Mesothelioma and Asbestos Awareness Center [2019]).

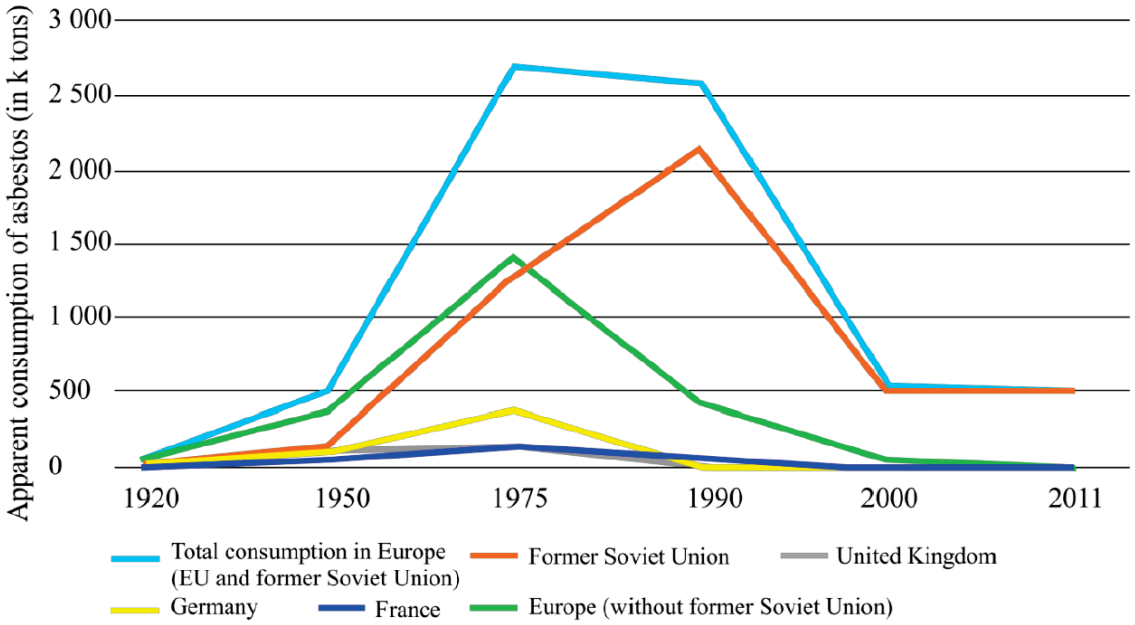

Figure 1.1: Apparent asbestos consumption in Europe in the last century (the apparent consumption is calculated in the basis of the national production of asbestos and imports and exports) (Bouygues Construction [2015])

As the connection between asbestos exposure and cancer risk became clear, it was subsequently banned in more than 55 countries around the world, including Japan, Australia and all countries in the European Union. Iceland was the first to ban asbestos imports due to health concerns in 1983, followed soon after by Sweden. A complete

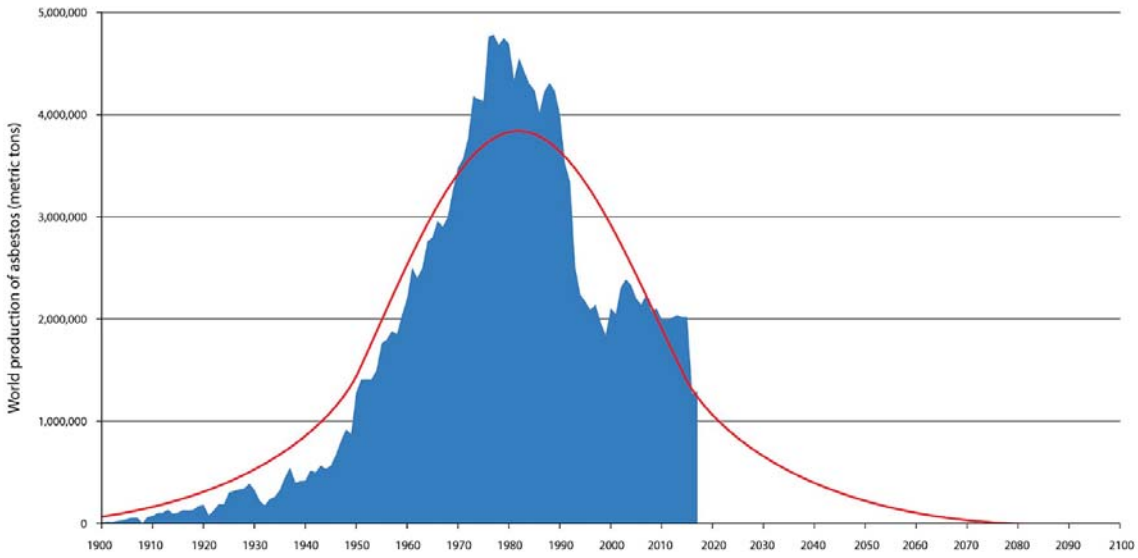

Figure 1.2: World production of asbestos (metric tons) from 1900 to the present (Future Timeline [2018])

ban on asbestos was adopted in France in 1997 (French government [1996]), Germany banned asbestos in 1992 and UK did so in 1999. However, it continues to be used around the world, especially in Asia and Russia, and in small amounts in the US (King [2017]). Additionally, in the countries that banned asbestos usage, regulations apply to the buildings constructed before the ban. In France for example, governmental regulations are intended to protect the general population from the risks of exposure to asbestos. They provide for detection and monitoring of materials containing asbestos and for information to occupants of buildings containing asbestos. Flocked asbestos surfaces, insulation and suspended ceilings containing asbestos must be identified and monitored on a regular basis. An initial assessment of the state of repair of these materials must be carried out by a technical inspector using an evaluation chart that covers the apparent wear of the materials, their physical protection, exposure to shocks and vibrations, and air circulation. On the basis of the results of this assessment (score 1, 2 or 3), the owner of the building must:

- either conduct a periodic control on the state of repair within three years if the result is 1;
- monitor the level of dust accumulation if the result is 2;
- carry out suitable maintenance within 12 months if the result is 3.

An identification programme for other materials containing asbestos such as floor tiles, coatings, and asbestos-cement products, has also been in place since 2001. Furthermore, regardless of the type of materials in place, the level of dust accumulation measured inside the buildings must not exceed the regulatory threshold of 5 fibres per litre (f/l). Additionally, for all buildings that were granted a building permit before 1 July 1997, i.e. the date on which asbestos use was banned in France, the results of this identification must be reported in an asbestos technical file (DTA). This file is the responsibility of the owner and must be updated at each intervention (removal, monitoring, maintenance, etc.) on asbestos-containing materials located in the building (French Agency for

Food, Environmental and Occupational Health and Safety [2019] and French Ministry of Health [2016]).

Concerning the workers who have the risk of being exposed to asbestos, specific regulatory provisions apply to their protection in addition to the general prevention measures in the work environment. In order to limit risks for workers, French regulations require that employers implement: 1 - common prevention measures for all activities with a risk of exposure to asbestos; 2 - specific prevention measures for removal and encapsulation of asbestos or items containing asbestos, and for operations on materials, equipment, or articles that may cause release of asbestos fibers. Common prevention measures applicable to all activities involving contact with asbestos include:

- initial risk assessment;
- information and training of staff;
- control of dust accumulation levels for asbestos fibers by analytical transmission electron microscopy (TEM) in order to guarantee compliance with limit values;
- worker protection measures focused specifically on containment, operating techniques and methods that limit release as much as possible, implementation of collective protection measures and personal protection equipment suitable for each operation.

Depending on the dust accumulation levels and the processes implemented, Ministerial Orders adopted by the Ministry of Labor stipulate the technical rules to be followed by companies, collective protection measures and personal protection equipment, measures for the protection of work site environments, and applicable provisions on completion of works. Encapsulation activities and removal operations for asbestos and asbestos-containing materials are carried out by certified companies. Generally, young workers and temporary staff are prohibited from carrying out activities that may result in release of asbestos fibers. The mean concentration of asbestos fibres, over eight hours of work, must not exceed 10 fibres per litre (French Ministry of Labor [2012]). Therefore, when performing refurbishment in the buildings contaminated with asbestos, intense safety measures should be taken to reduce the health risks for employees as Figure 1.3 shows. As can be seen in the figure, the workers are using heavy equipments and they are wearing special tight suits and masks to avoid exposing to the asbestos.

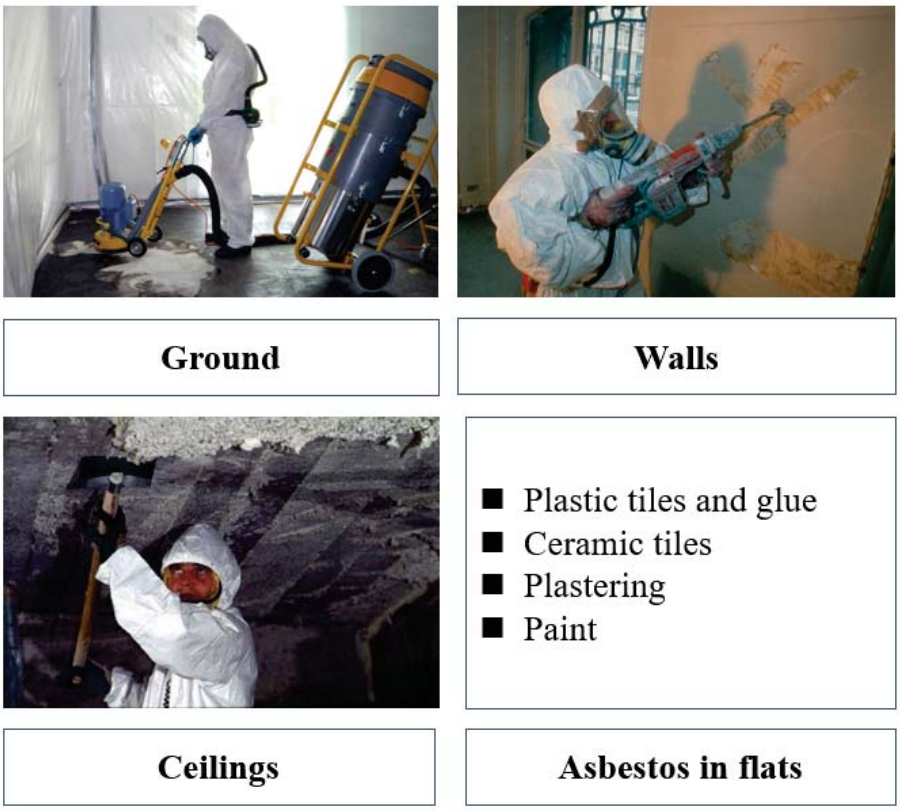

Figure 1.3: Asbestos removal tasks

1.3 The Bots2ReC Project

Due to the very inefficient or even prohibited manual performance of asbestos removal, and the very tiring working conditions, automated solutions have emerged and started to be seen as a realistic alternative. Furthermore, in order to judge the impact of automating the asbestos removal tasks, a study regarding the situation of asbestos contamination in Europe was assigned. However, it is still quite difficult to evaluate the quantity of asbestos present in European buildings as there is no proper documentation for that. The situation is documented well for France and there are few legal dispositions or studies focused for certain other countries.

In France, according to the publication of the Social Union for Habitat (L'Union sociale pour l'habitat [2014]), more than 40% of the housing stock is contaminated by asbestos (around 15 million flats). An important study of the 'Centre Scientifique et Technique du Bâtiment' confirms these numbers and shows that 2 million out of 3,6 million non-residential buildings are contaminated (Chaventré and Cochet [2005]). In Great Britain, the estimations are quite approximated, but 4,4 million buildings are said to need asbestos removal (Bouygues Construction and Audencia Junior Conseil [2015]). In Hungary, an isolated study of the NIOH detected presence of asbestos in 500 buildings of Budapest. Moreover, more than 4 million tons and 3 million tons of asbestos were imported in France and Great Britain respectively during the 20th century (Association Nationale de Défense des Victimes de l'Amiante [2011] and Bouygues Construction and Audencia Junior Conseil [2015]). For Spain, the imports are around 2.6 million tons, and the German situation can be estimated to be similar to the Spanish one. In Italy, some studies announce very high amounts between 30 and 40 million tons of asbestos. For Belgium it was estimated that 800 thousand tons of asbestos were present in 2001. These

numbers from various European countries prove that asbestos contamination is present in millions of flats all over Europe, even if exact figures are limited. The asbestos exists in different forms: Chrysotile, Amosite, Crocidolite and Anthophyllite. Its consumption in the European Community in 1973 (when major amounts of asbestos were used) indicates that in Western Europe, the main countries probably present similar quantities of asbestos as France (see Table 1.1), where the figures are well known. A peculiar case is

Table 1.1: Asbestos consumption (in t) in the European community in 1973 (Asbestos Trade Association, France)

	Chrysotile	Amosite	Crocidolite	Anthophyllite	TOTAL
Ireland	6,400	600			7,000
France	150,000	2,800	3,100	100	15,600
Denmark	28,000	4,800			33,000
Netherlands	37,400		600		38,000
Belgium+Luxembourg	76,000	5,000	5,000		86,000
Italy	130,600	2,200	6,200		139,000
United Kingdom	147,700	24,000		300	172,000
Germany	194,100	1,900	3,300	1,700	201,000
TOTAL	770,400	41,300	18,200	2,100	832,000

Russia and the ex-Soviet union countries, where the asbestos market is still existing and the public institutions deny the danger linked to asbestos. There is potentially a very big quantity of asbestos in these countries, but no market for asbestos removal for the moment (Bouygues Construction and Audencia Junior Conseil [2015]).

Few studies allow estimating the global costs of necessary refurbishment and clearance procedure for the European market. The publications concerning the French market indicate a total amount of 80 billion Euros (L'Union sociale pour l'habitat [2014]) to 200 billion Euros (Guérin and Jouan [2014]) for private housing. For France, the most moderated sources announce 15 billion Euros needed to clean the polluted social housings only (Guérin and Jouan [2014]). Taking into account the private housings and the non-residential sector, the total amount would exceed 100 billion Euros. In Great Britain the estimated costs are much lower: 15 billion Euros are estimated for the all buildings. It must be considered that in Great Britain, asbestos treatment is to keep the pollution in place, and cover it with some protection. This is far less expensive, and partly already done, which can explain the difference in the estimation compared to France (Bouygues Construction and Audencia Junior Conseil [2015]). Based on the data presented above, it can be estimated that the 5 to 6 biggest countries in Western Europe are in situation similar to France. Even if the cost of asbestos removal can be reduced in future, it can be estimated that the total market of asbestos removal reaches several 100 billion Euros for these countries only.

Hence, the contamination clearance from European flats is expensive (11500 Euros per flat on average, according to *Pertuy Construction*'s investigations) as the European asbestos removal market is very large. Moreover, the regulations mentioned in Section 1.2 should be respected, which means that the workers need to wear personal protective equipment complying with the highest technological standards and exchange it regularly. Thus, the automation of such kind of processes would allow the demolition and refurbishment industries in Europe to operate more efficiently (Detert et al. [2017]). In addition to that, automation will decrease the refurbishment costs and, at the same time, prevent the employees from being exposed to the asbestos microscopic fibers.

Motivated by the mentioned reasons, the "Robots to Re-Construction" Bots2ReC project was launched in February 2016. The project objectives include:

> "Introducing, testing and validating an operational process for the automated removal of asbestos contamination at a real world rehabilitation site using a robotic system."

The project introduces a new robotized system dedicated to asbestos removal as Figure 1.4 shows. The Bots2ReC consortium consists of seven partners. There are two universities (RWTH and SIGMA Clermont), three Small and Medium Enterprises (Robotnik, TLabs and Indurad), a robotic integrator (Eurecat) and a final customer (Bouygues):

1. **RWTH Aachen University** is a research institution that augments the state of the art technology in the areas of control, task planning and sensor data processing.
2. **SIGMA-Clermont** brings research expertise in mechatronic design, modeling, perception and collaborative control for simulating and piloting the robotic system in its environment.
3. **Robotnik Automation SLL** develops and manufactures mobile platforms and manipulators for service robotics applications and unmanned ground vehicles. It develops the mobile base of the Bots2ReC robot.
4. **Telerobot Labs Srl** offers high level competences in design, development and production of robotic and mechatronic devices. It develops the robotic arm and tools for the Bots2ReC robot.
5. **Indurad** is a producer and integrator of optical and radar sensor technology with a unique data processing and visualization software framework. It develops sensors for single dimensional distance measurement and for localization of the Bots2ReC robot.
6. **Fundacio Eurecat** is an experienced system integrator, that will integrate the robotic system including the developed operational process for the use case.
7. **Bouygues Construction** participates as the end-user and industrial partner. It is responsible for the clearance and refurbishment of a site and the system operation.

The Bots2ReC is driven by Bouygues Construction as the main customer. As the final product should be produced by a separate society, and the asbestos cleaning, as a service, should also be offered by other societies, Bouygues Construction aims to subcontract those two types of societies to provide asbestos clearance services which meet the end user needs. Additionally, Bouygues Construction supported the project by building a realistic testing site equipped with the facilities to test the robot during the development stages. SIGMA-Clermont and RWTH Aachen are two universities respectively in charge of the modeling and supervision of the robots (Bots2ReC [2015]).

The H2020 project is decomposed into work packages (WPs) and managed by RWTH Aachen as shown in Figure 1.5. Sigma Clermont is the leader of WP2 (Overall System Layout and Analysis) that consists in:

1. Developing a simulation environment and simplified model of the robotic unit.
2. Developing a simulation environment and model of the representative asbestos removal use-case with achievable precision.

3. Developing algorithms for precise, dynamic and centralized control strategies.

As can be seen in Figure 1.5, the work-package WP2 is directly connected to WP4, WP5 and WP6 where Sigma was involved in some engineering and development activities for the project as:

- Proposing stabilizers for the mobile manipulators.
- Proposing several arm architectures and analyzing them.
- Analyzing the stability of the mobile manipulator.
- Calculating the torques needed for the grinding application in order to choose the arm actuators.
- Involvement in the discussions to decide the control architecture of the system.
- Involvement in the discussions about sensors placements.
- . . .

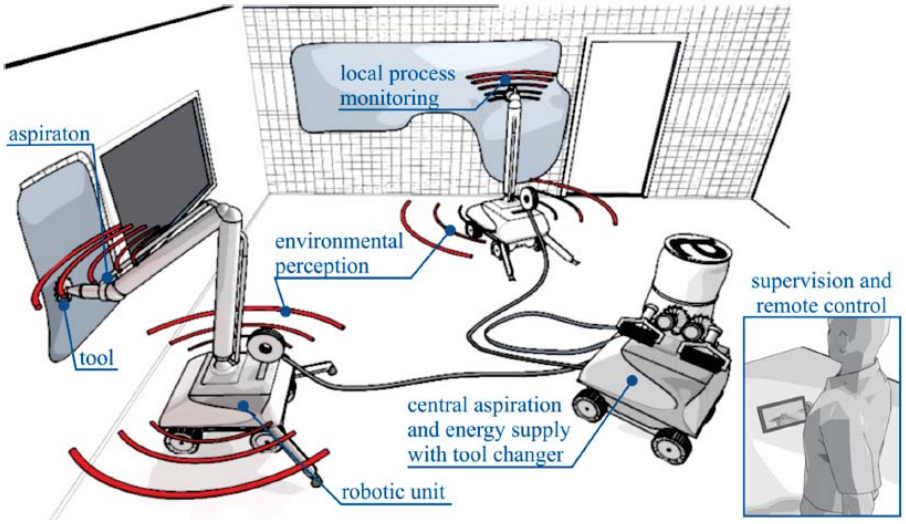

Figure 1.4: Conceptual sketch of the automated removal of asbestos contamination. The sketch shows the rehabilitation site with two robotic units

In addition to that, within the scope of the H2020 Bots2ReC project, SIGMA-Clermont is directing two Ph.D. theses with two different themes:

1. Modeling and control of a collaborative mechatronic system for robotized asbestos removal.
2. Control of robotic mobile manipulators for asbestos removal.

This Ph.D. covers the second theme and its objectives are more detailed in the next section.

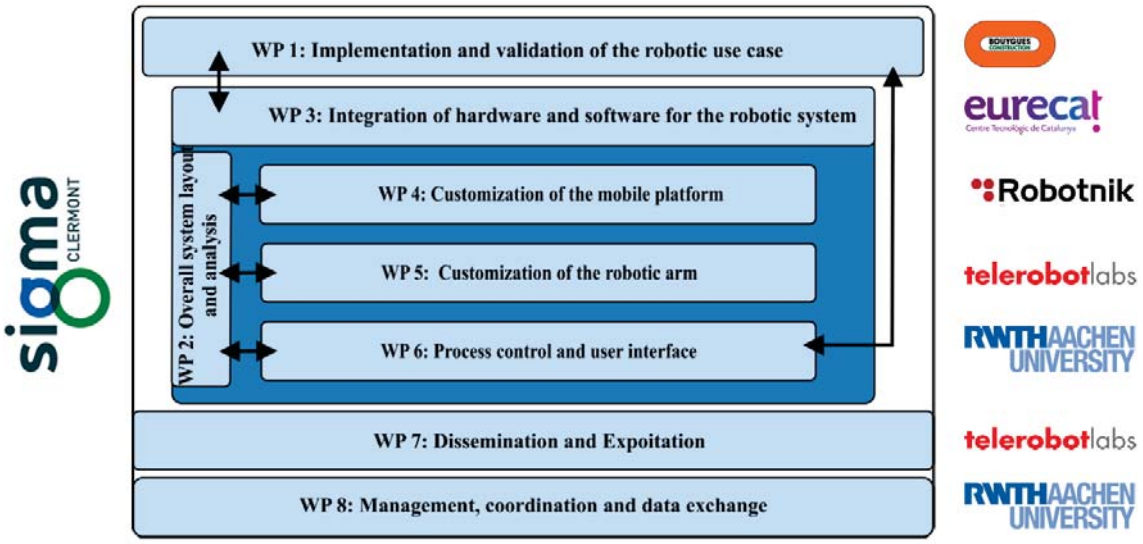

Figure 1.5: Bots2ReC work packages and their relation to each other

1.4 Objective of This Dissertation

The objective of this dissertation is to develop a multi-modal control for mobile manipulators based on the association between visual information or radars and force data to achieve a clean, safe, efficient and productive asbestos cleaning process. For that, one should understand how the grinding operation is manually performed in the construction industry, and how humans use their natural motor control to achieve the task. Hence, the aimed controller should be able to grind the surface (of a wall, a ground or a ceiling) and to handle the environmental uncertainties in texture, change in materials, and disturbances of the grinding process. In addition to that, the development of the Bots2ReC robot must comply with some technical requirements in order to ensure the performance and reliability of the system. A summary of the requirements can be seen in Table 1.2.

Table 1.2: Bots2ReC robot technical requirements

Requirement description	**Type**
The end-effector must reach floor, wall, ceiling (3m high), skirting, etc and still be capable to work	Asbestos removal task
The mobile manipulator must pass through doors of dimensions (80 x 200 cm) and fit in an elevator 200 cm high	Geometry
The mobile manipulator should be capable to clean corridors as narrow as 70 cm	Geometry
The overall mass/area ratio of the system shall be <300 Kg/m2	Mass
The robot should be able to grind walls with a leaning angle of 0/90 degrees	Geometry
The robot should be able to grind walls with a radius between 1.5 m and 2.0 m, e.g., spiral stair case walls	Geometry
The robotic unit must be able to turn coming from a corridor of 70 cm width perpendicular to corridor of 70 cm width in manual mode	Geometry
The robotic unit must be able to move on a slope <5% measured from horizontal	Motion capability
The robotic unit must be able to move with a speed of 1m/s	Motion capability
The robotic unit shall provide the necessary operatioal forces for each asbestos removal task: -Normal operational force: 50 N - 80 N -Lateral operational force around 15 N	Force capability

Thus, complying with the mentioned requirements, results a critically stable top-heavy robot with a small support polygon compared to its size as can be seen in Figure 1.6. In addition to the critical stability resulting from the mass and length of the arm and the small support area of the base, instability may occur because of the interaction forces between the robot and the environment, and the fast dynamic motions. Hence, in order to ensure the stability of the system throughout the cleaning operation, the aimed controller should be designed to take care about the online-stability of the robot while operating to avoid tipping over.

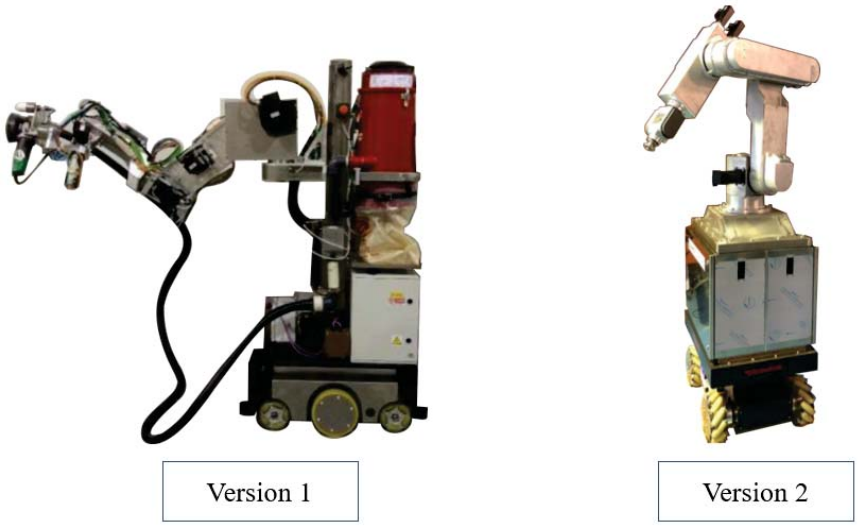

Figure 1.6: Bots2ReC robots

1.5 Approach

This dissertation proposes a novel surface grinding control approach for automating the grinding process. Additionally, a new approach for controlling the stability of mobile manipulators in real time is proposed. The base is controlled using task redundancy in the null configuration space of the robot to keep the zero moment point on a desired stable point without affecting the end-effector performance. Moreover, the modeling and sensors uncertainties are taken into account. In accordance with the above-mentioned strategies, this study proposes a unified grinding control for mobile manipulators by dividing the problem into four parts as follows:

- Active hybrid motion-force control of the arm: responsible of a homogeneous grinding with a constant force on the surface while respecting the grinding constraints.
- Adaptive wrist control: responsible for orienting and adapting the tool to the wall based on grinding forces.
- Tip-over stability control: communicates with the arm controller and the mobile base controller to keep the system stable, i.e., ensuring at any time the stability of the robot while grinding.
- Methods to compensate the modeling and sensors uncertainties.

Figure 1.7 is a conceptual block diagram that shows the plan of the work that lies ahead of this dissertation. It shows the interaction between the different controllers discussed above. The proposed block diagram can be integrated easily in the system architecture given by Fundacio Eurecat and shown in Figure 1.8.

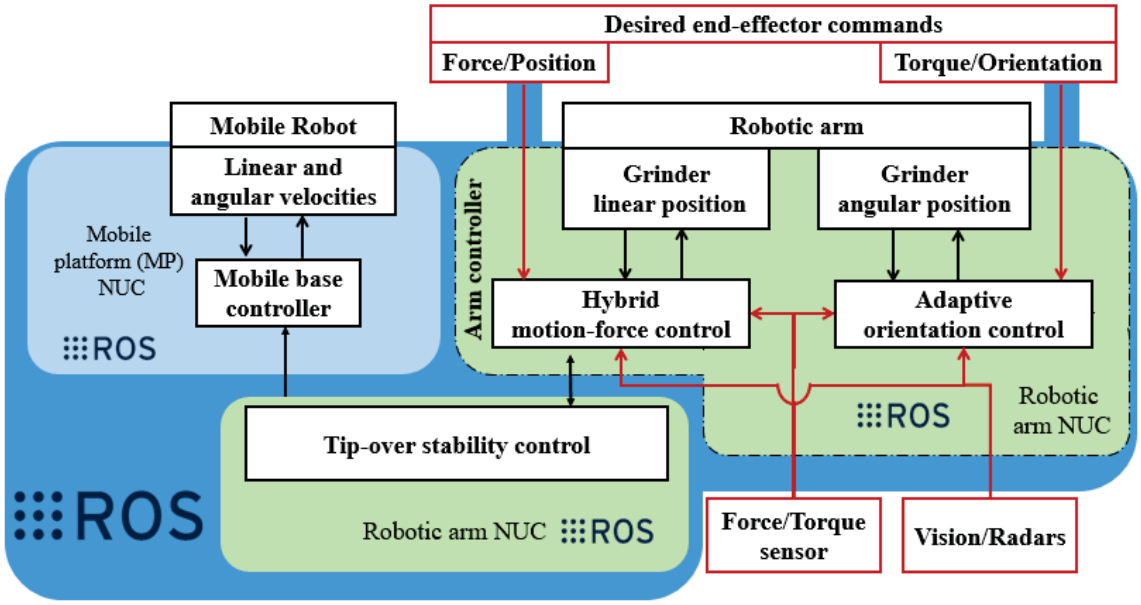

Figure 1.7: Conceptual block diagram for designing a dynamic controller that considers interaction between mobile manipulator and environment while grinding

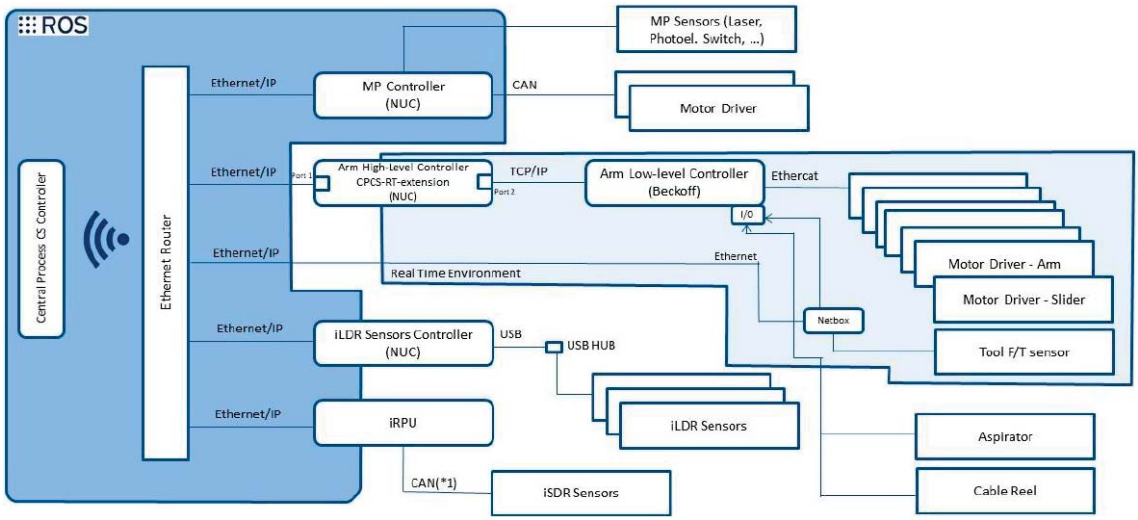

Figure 1.8: Bots2ReC system architecture given by **Fundacio Eurecat**

.

1.6 Chapters Organization

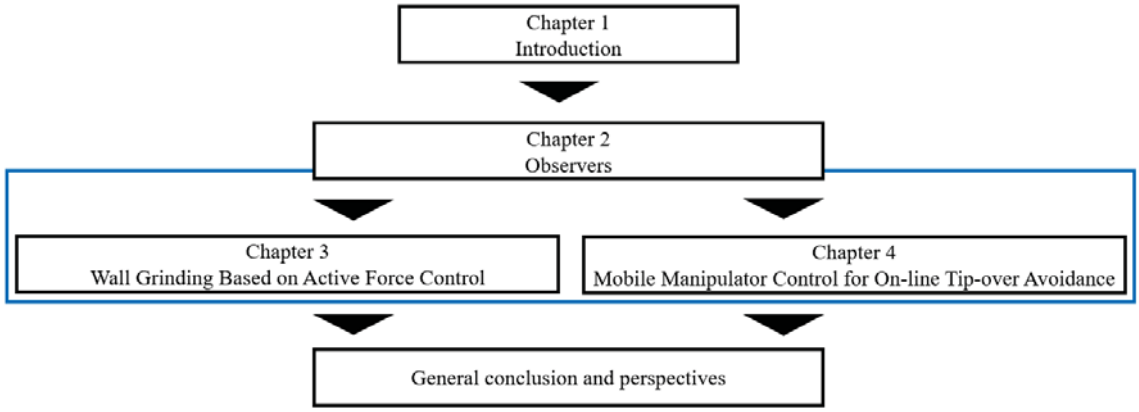

Figure 1.9: Chapters organization

Figure 1.9 shows the chapters organization. Chapter 2 describes fundamental technologies of disturbance compensation in motor control. The compensation concept is extended to other applications and a zero-moment-point observer is derived directly to compensate errors in zero moment point estimation. Moreover, a novel observer that estimates the non-contact forces acting on a force-torque sensor is presented. Chapter 3 reviews the research field of robot-environment interaction. It also presents the recent technical advances in metallic polishing and grinding operations. Additionally, chapter 3 presents two surface grinding controllers with their analytical development. This chapter also shows the experimental results of the two controllers, and their performance is evaluated. Chapter 4 reviews several tip-over stability methods presented in the literature, and it presents a new approach for controlling tip-over stability of mobile manipulators in real time based on the zero-moment-point observer presented in chapter 3. The proposed approach is verified by dynamic simulations using differential mobile base with 7-degrees-of-freedom arm fixed on its top. Finally, the last section summarizes and concludes this dissertation. It also discusses the future perspectives.

Chapter 2

Observers

Observers are digital algorithms that combine sensor outputs with knowledge of the system to provide results superior to traditional structures, which rely wholly on sensors. For example, the state of an omni-directional robot (Robotino) was estimated using an observer in Hadji and Rahmani [2010]. In Murakami et al. [1993], sensor-less force control for a robotic manipulator was achieved using a reaction torque observer without the need of using a force sensor. In Simoni et al. [2017], the joint temperature was used in the joint friction model. The latter is eliminated from the joint torque sensor value and the accuracy of estimating the contact force between the robot and the environment was improved.

Observers have been used in control systems for years (Ellis [2002]). In order to improve the performance of our controllers, observers will be introduced, developed and discussed in this chapter before discussing the latter topics as they will be utilized later in the dissertation. Actuators (motors) and sensors are essential parts of most robotic systems. Increasing robustness and accuracy of motor control, reliability of sensor's output and estimation of high level information from sensor data are direct result of the deployment of observers in robotic or mechatronic systems (e.g. Tahri et al. [2017]).

For a controllable system, like a DC motor, disturbances and external forces will always affect the stability of the system and directly its position, velocity or force tracking performance. Hence, it is necessary to design dedicated disturbance observers that can compensate disturbances in the controller and achieve high performance in such systems. Figure 2.1 shows a general feedback system with disturbance and observer.

Furthermore, robots executing force controlled tasks require accurate perception of the applied force in order to guarantee precision. However, dynamic motions generate non-contact forces due to the inertial effect of the load on the force-torque sensor. These non-contact forces can be regarded as disturbances to be removed such that only the forces generated by contacts with the environment remain. Figure 2.2 shows a general feedback system with a disturbance affecting the sensor and an observer that compensates it.

In the following sections, the theory of disturbance observers for DC motors is introduced. In addition to that, two main contributions are presented in this chapter:

- A zero moment point (ZMP) observer, that estimates the disturbances on ZMP and corrects its position, is developed based on the theory of disturbance observers.
- An observer that estimates the non-contact forces measured by a force-torque sensor is developed based on recurrent neural networks

The two contributions are discussed more in details in Sections 2.3 and 2.4.

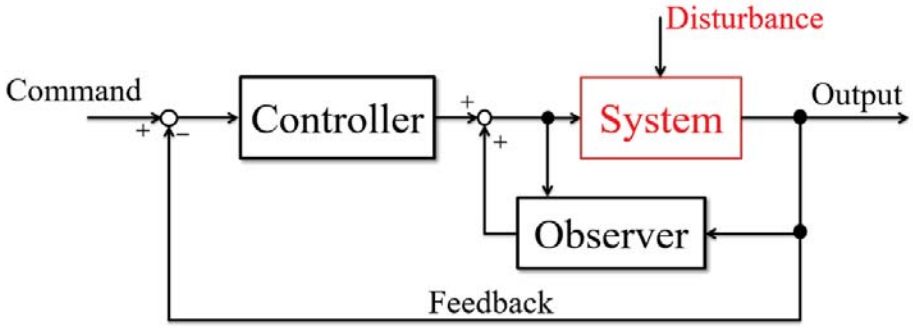

Figure 2.1: Simple feedback system with disturbance and observer that compensates it

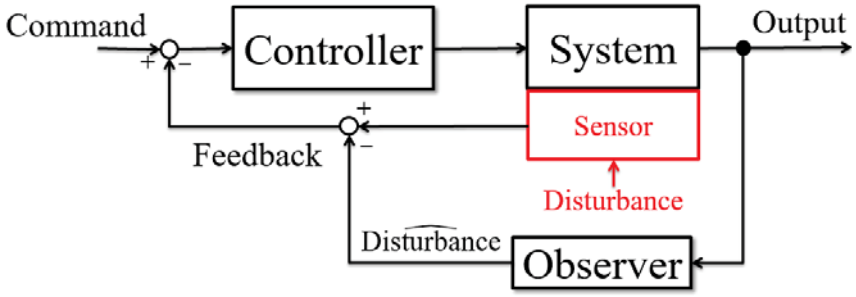

Figure 2.2: Simple feedback system with sensor disturbance and observer that compensates it

2.1 Dynamics Based DC Motor Control

In robotic applications, the harmonic actuators are one main disturbance reason because of the electromagnetic effect caused from the coil and magnet inside. This kind of disturbance is complicated to model because of its uncertainties. Hence it harms the robustness of the system. The motion equation of the rotational actuator is obtained as

$$\tau^{motor} = J_m \ddot{\theta}^{res} + \tau^{l} \tag{2.1}$$

where J_m, $\ddot{\theta}^{res}$, τ^{l}, and τ^{motor} denote the motor shaft inertia, the angular acceleration response of the motor axis, the load torque, and the torque generated by an actuator, respectively. The load torque τ^{l} is expressed as

$$\tau^{l} = \tau^{int} + \tau^{ext} + \tau^{fri} \tag{2.2}$$

it includes the motor internal interfering torque τ^{int}, the external reaction torque τ^{ext} and the friction forces τ^{fri}. The generated motor torque is obtained by multiplication of the armature current i_a and the torque constant K_t. Here it is assumed that the armature current is exactly the same as the current reference i^{ref},

$$\tau^{motor} = K_t i_a = K_t i^{ref} \tag{2.3}$$

and the motion equation is restated as

$$J_m \ddot{\theta}^{res} = K_t i^{ref} - (\tau^{int} + \tau^{ext} + \tau^{fri}) \tag{2.4}$$

In real applications, the torque constant K_t consists of complicated terms with some perturbations that vary according to the state of the robot and the distribution of the

magnetic flux, and the motor inertia constant J_m contains some uncertain ripples. These differences between the nominal values and the real values are expressed by ΔJ_m and ΔK_t as

$$J_m = J_{mn} + \Delta J_m \tag{2.5}$$
$$K_t = K_{tn} + \Delta K_t \tag{2.6}$$

where J_{mn} is the nominal inertia constant, K_{tn} is the nominal torque constant, they can be obtained from the data-sheet of motor specifications. ΔJ_m and ΔK_t are inertia perturbation and torque perturbation respectively. Assuming the motor axis is placed along the gravity, the gravity effect on the motor can be neglected. Taking into account the uncertainties in inertia and the torque perturbation, the disturbance torque can be defined as:

$$\tau^{dis} = \tau^{int} + \tau^{ext} + \tau^{fri} + \Delta J_m \ddot{\theta}^{res} - \Delta K_t i^{ref} \tag{2.7}$$

Based on the eqs. (2.1 to 2.7), the disturbance torque can be written as,

$$\tau^{dis} = K_{tn} i^{ref} - J_{mn} \ddot{\theta}^{res} \tag{2.8}$$

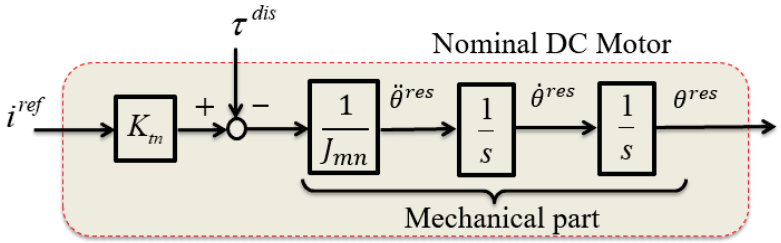

Figure 2.3: Nominal dynamic model of rotational DC motor

Figure 2.3 shows the block diagram of the nominal dynamic model of DC motor. In feedback control system, both angular velocity $\dot{\theta}^{res}$ and position θ^{res} can be used as feedback terms. Usually, there is no direct measurement for the angular acceleration of the motor, however its angular position is measured by the encoder and then the velocity and acceleration are derived by differentiation. In order to achieve precise motor control, the disturbance torque τ^{dis} needs to be well compensated. Generally, DC motors can be controlled by generating the appropriate current reference i^{ref} that corresponds to the desired position, velocity, acceleration, or torque. However, as the motor is subject to disturbance, the ideal i^{ref} cannot be easily decided without any disturbance compensation. In the next section an observer that compensates this disturbance torque is explained in details.

2.2 Disturbance Observer

Disturbance observer (DOB) is widely used in motor control to achieve high performance robust systems. It was proposed in Ohnishi [1993a], Ohnishi [1993b] and Ohnishi et al. [1996], where the author explained the functionality and the efficiency of the DOB. In DOB, the disturbance torque τ^{dis} is calculated using the current reference i^{ref} and the angular acceleration response $\ddot{\theta}^{res}$. However, the acceleration is calculated by twice differentiating the position response θ^{res} measured by the encoder. Since the derivation enhances the noise effect on $\ddot{\theta}^{res}$ especially in the high frequency domain, a first order

low pass filter (LPF) is employed to maintain the robustness of the system. Figure 2.4 describes eq. (2.8) and shows the disturbance estimation with first-order LPF. The disturbance is estimated in the Laplacian domain as,

$$\hat{\tau}^{dis} = \frac{g}{s+g}\tau^{dis} \tag{2.9}$$

with g standing for the cutoff frequency of the low pass filter and s for the Laplace complex variable.

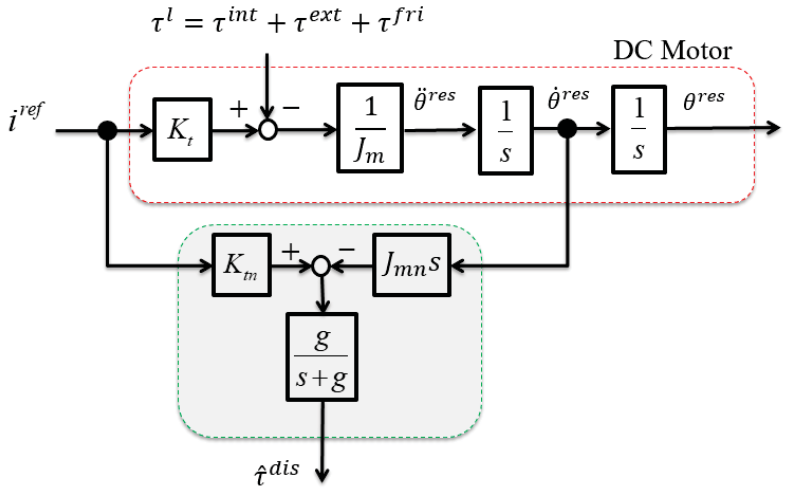

Figure 2.4: Disturbance calculation based on velocity response and first order low pass filter

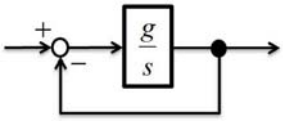

Figure 2.5: Equivalent block diagram of low pass filter

Figure 2.5 shows the equivalent block diagram of the low pass filter. According to Figures 2.4 and 2.5, the disturbance torque τ^{dis} can be obtained by a simple integration. Hence, this method can be easily applied in digital systems applications. Manipulating $J_{mn}s$ gives:

$$J_{mn}s = \frac{J_{mn}s}{s}(s+g-g) = gJ_{mn}\frac{(s+g)}{g} - gJ_{mn} \tag{2.10}$$

Substituting eq. (2.10) and eq. (2.8) in eq. (2.9) gives:

$$\begin{aligned}\frac{g}{s+g}(K_{tn}i^{ref} - J_{mn}\ddot{\theta}^{res}) &= \frac{g}{s+g}[K_{tn}i^{ref} - (gJ_{mn}\frac{(s+g)}{g} - gJ_{mn})\dot{\theta}^{res}] \\ &= \frac{g}{s+g}K_{tn}i^{ref} + \frac{g}{s+g}gJ_{mn}\dot{\theta}^{res} - gJ_{mn}\dot{\theta}^{res}\end{aligned} \tag{2.11}$$

Figure 2.6 is the block diagram describing eq. (2.11), it is equivalent to Figure 2.4 with an integrator utilized instead of the differentiator. Inside the gray area is the DOB structure.

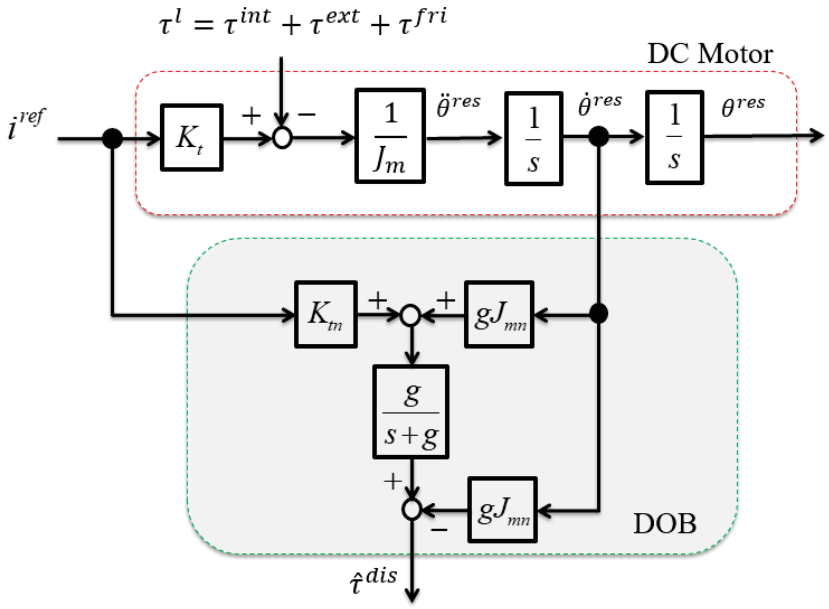

Figure 2.6: Block diagram of the disturbance observer (DOB)

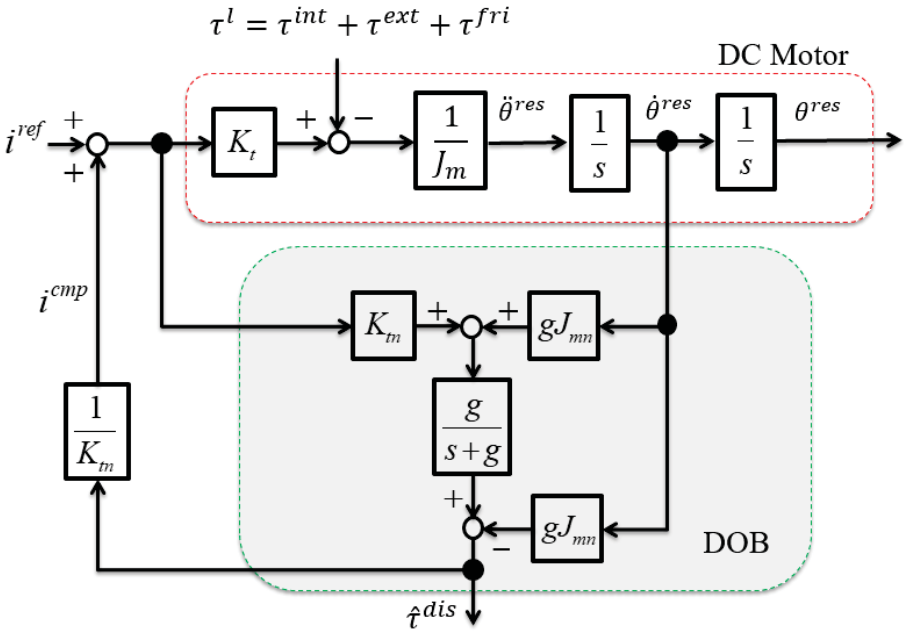

Figure 2.7: Disturbance compensation via current feedback

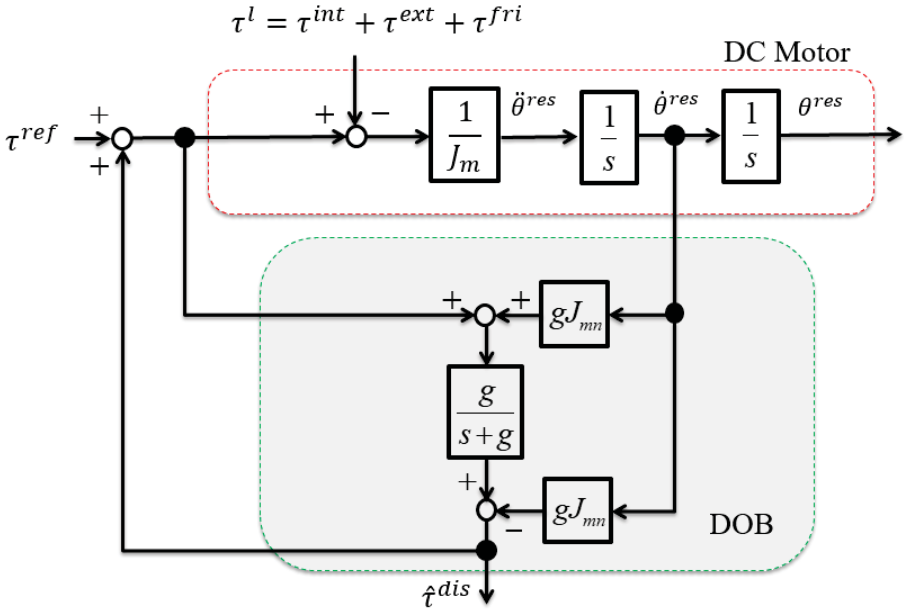

Figure 2.8: Disturbance compensation via torque feedback

After estimating the disturbance torque $\hat{\tau}^{dis}$, the compensation current for disturbance suppression is derived as

$$i^{cmp} = \frac{\hat{\tau}^{dis}}{K_{tn}} \tag{2.12}$$

When the compensation current is fed back into the system, the disturbance is canceled as shown in Figure 2.7 where the final block diagram of DOB control is depicted. If one needs to use torque control instead of current, K_t and K_{tn} will be eliminated and τ^{ref} will be the reference torque to the motor as Figure 2.8 shows.

Figure 2.9 shows the equivalent block diagram of Figure 2.7, it describes visually the effect of DOB where the disturbance is suppressed by the low pass filter forward term. If the system bandwidth is infinite ($g = \infty$), a robust control system is achieved, Figure 2.10 depicts the DOB effect with $g = \infty$.

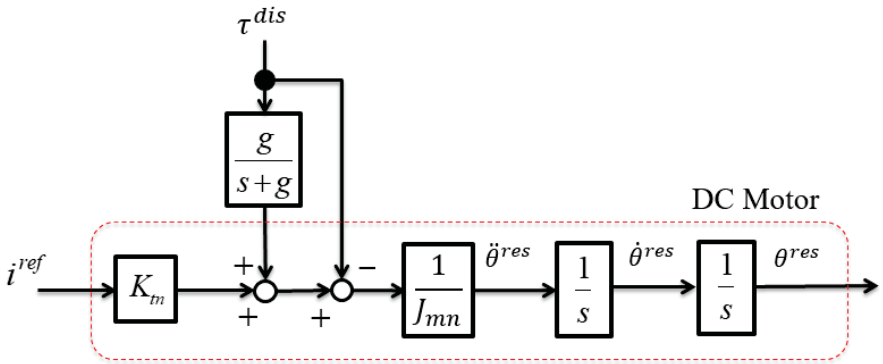

Figure 2.9: Visualization of the effect of DOB

As discussed before, a first order low pass filter is used to reduce the high frequency noise in the DOB. However, the filter introduces time delay that can affect the stability of the feedback control system.

In the DOB application, acceleration response is needed to estimate the disturbance torque τ^{dis}. Hence, the term $J_{mn}s$ is used to derive the angular acceleration from angular

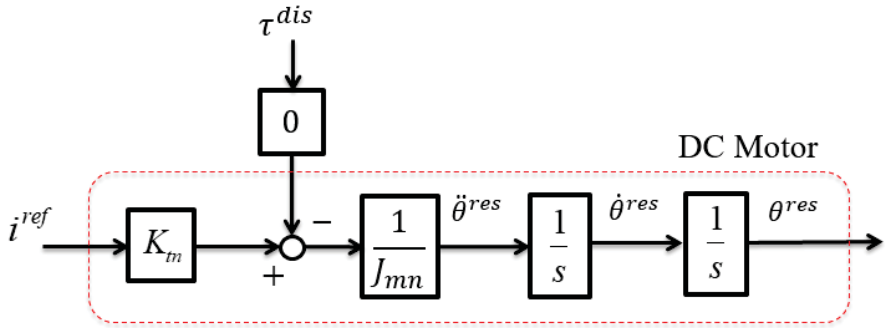

Figure 2.10: Block diagram equivalent to Figure 2.9

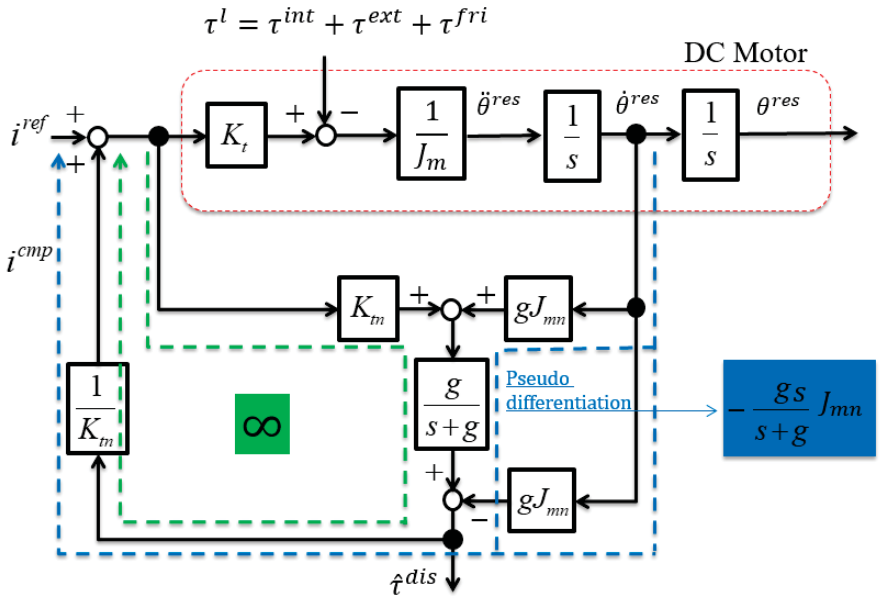

Figure 2.11: Detailed analysis of DOB with pseudo differentiation

velocity as Figure 2.4 shows. In order to decrease the gain in high frequency, the pseudo differentiation $\frac{gs}{s+g}$ is used in the DOB. Figure 2.11 depicts the the pseudo differentiation and the two feedback loops of the DOB. The green loop is when $g \to \infty$, and the low pass filter is in full bandwidth as

$$\lim_{g\to\infty} \frac{g}{s+g} \approx 1 \tag{2.13}$$

In the blue feedback loop the pseudo differentiation is represented as,

$$\frac{g}{s+g} gJ_{mn}\dot{\theta}^{res} - gJ_{mn}\dot{\theta}^{res} = -\frac{gs}{s+g} J_{mn}\dot{\theta}^{res} \approx -sJ_{mn}\dot{\theta}^{res} \tag{2.14}$$

Figure 2.12 shows the equivalent block diagram of Figure 2.11. The green loop is equivalent to an infinite gain and the blue loop is equivalent to an acceleration feedback. This means that DOB can completely compensate the disturbance torque as shown in Figure 2.10 where the disturbance torque gain goes to zero.

However, in the mentioned discussions, the DOB calculations are based on velocity feedback. In real applications, velocity can not be measured directly by encoders as they can only give the angle position. As the low pass filter has the time delay problem, it is not enough to calculate the velocity from position response by only applying the

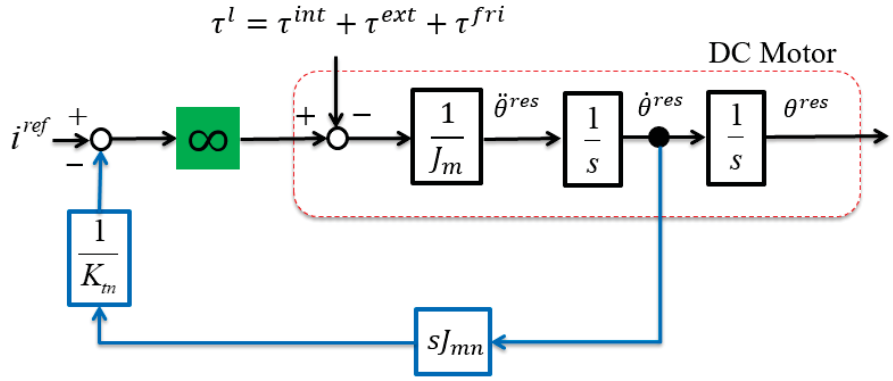

Figure 2.12: Block diagram equivalent to Figure 2.11

pseudo differentiation. In order to keep the same time delay for both input torque and the output one, a low pass filter should be added in the input torque loop. By applying this, the effect of differentiation and the low pass filter in DOB can be reduced. Figure 2.13 shows the new DOB block diagram based on position feedback.

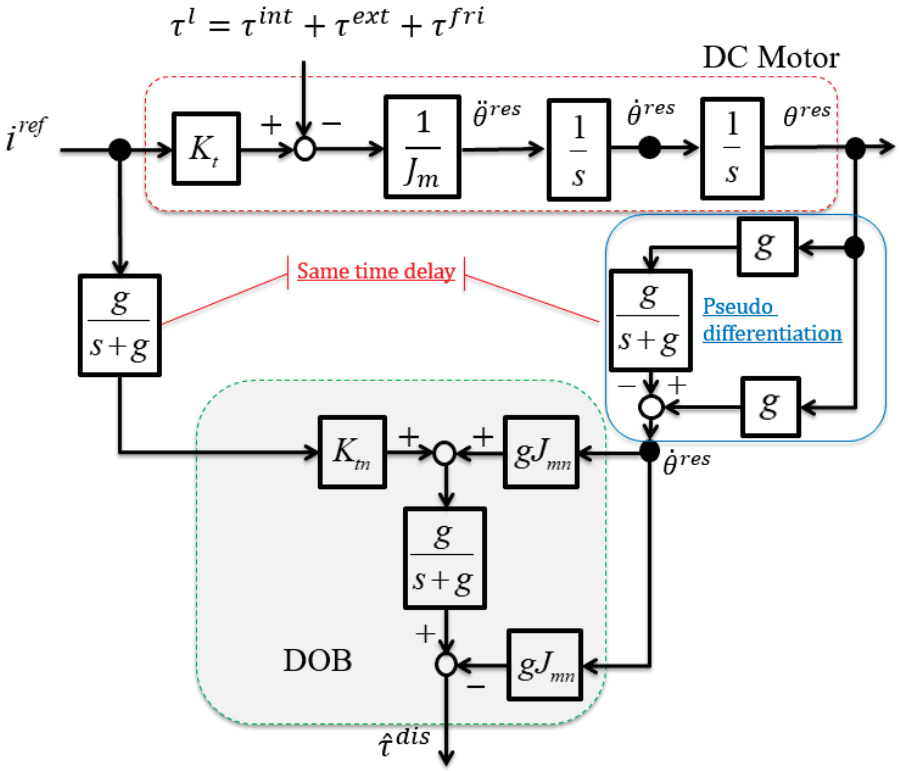

Figure 2.13: DOB block diagram with position feedback

2.3 Zero Moment Point Disturbance Observer

The Zero Moment Point (ZMP) is a point on the ground where the total moment generated due to gravity and inertia equals to zero. For mobile manipulators, the ZMP must fall inside the convex hull of the robot base support area to ensure stability and avoid tipping over while moving. Hence, it is an important concept of dynamic stability. In

the literature, it is used in its original form presented by Sugano et al. [1993]:

$$ZMP_x = \frac{\Sigma_i m_i x_i(\ddot{z}_i + g_{rav}) - \Sigma_i m_i \ddot{x}_i z_i - \Sigma_i I_{iy}\ddot{\theta}_{iy}}{\Sigma_i m_i(\ddot{z}_i + g_{rav})} \tag{2.15}$$

$$ZMP_y = \frac{\Sigma_i m_i y_i(\ddot{z}_i + g_{rav}) - \Sigma_i m_i \ddot{y}_i z_i + \Sigma_i I_{ix}\ddot{\theta}_{ix}}{\Sigma_i m_i(\ddot{z}_i + g_{rav})} \tag{2.16}$$

Where m_i is the mass of ith body and g_{rav} is the gravity value; x_i, y_i and z_i are the positions of centers of mass of each body segment; I_{ix} And I_{iy} are the inertia around x and y respectively; $\ddot{\theta}_{ix}$ and $\ddot{\theta}_{iy}$ are the angular accelerations of each link around x and y respectively. In (2.15) and (2.16) the inertias are assumed to be nominal, and the center of mass (COM) position of each link assumed to be known. Nevertheless, in practice it is not the case. This point can be illustrated with the m-link manipulator in Figure 2.14. The Errors in the center of mass positions $\Delta \boldsymbol{l} = [\Delta l_1, \Delta l_2, \cdots, \Delta l_m]$ have a significant effect on ZMP_x (refer to eq.(2.15)). Inertial errors will also have notable effects on stability, especially when the mobile base is relatively small and the robot is top heavy. The dynamics of m links robotic manipulator can be expressed as:

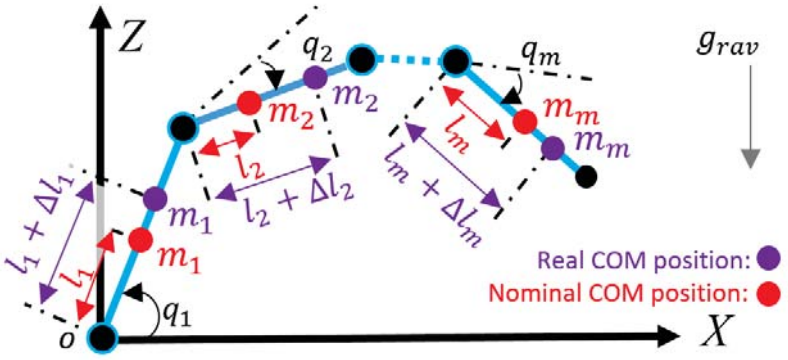

Figure 2.14: COM position errors illustrated on a m-link manipulator

$$\boldsymbol{\tau}^{manip} = \boldsymbol{H}_n(\boldsymbol{q})\ddot{\boldsymbol{q}} + \boldsymbol{\tau}^{dis} \tag{2.17}$$

$\boldsymbol{q} = [q_1, q_2, \cdots, q_m]$ is the joints position vector, $\boldsymbol{\tau}^{manip} = [\tau_1^{manip}, \tau_2^{manip}, \cdots, \tau_m^{manip}]$ is the joints torque value, $\boldsymbol{H}(\boldsymbol{q})$ is the inertia matrix and $\boldsymbol{H}_n(\boldsymbol{q})$ is the nominal one. Reformulating eq.(2.7) as presented in Ohnishi [1993b] and Murakami et al. [1993], and ignoring the uncertain motor dynamics as their effect can be considered small enough, $\boldsymbol{\tau}_{dis}$ is estimated using disturbance observer (DOB) presented in the previous section as:

$$\hat{\boldsymbol{\tau}}^{dis} = \boldsymbol{\tau}^{int} + \boldsymbol{\tau}^{ext} + \boldsymbol{\tau}^{fri} + (\boldsymbol{H} - \boldsymbol{H}_n)\ddot{\boldsymbol{q}} \tag{2.18}$$

$\boldsymbol{\tau}^{ext} = 0$ when there is no contact with the environment. $\boldsymbol{\tau}^{int}$ is equivalent to gravity and Coriolis torques in joint space $\boldsymbol{H}(\boldsymbol{q}, \ddot{\boldsymbol{q}})$. The errors $\Delta \boldsymbol{l}$ will result internal torque disturbances. Eq.(2.18) can be rewritten as:

$$\hat{\boldsymbol{\tau}}^{dis} = \boldsymbol{G}_n + \boldsymbol{\tau}^{(G-G_n)} + \boldsymbol{\tau}^{fri} + (\boldsymbol{H} - \boldsymbol{H}_n)\ddot{\boldsymbol{q}} \tag{2.19}$$

$\boldsymbol{\tau}^{(G-G_n)}$ is the disturbance torque corresponding to the COMs position errors. $\boldsymbol{G}_n$ is the nominal gravity and Coriolis torques in joint space, it can be easily calculated using the nominal distances and dynamic parameters. $\boldsymbol{\tau}^{fri}$ is obtained by friction identification

tests. Hence, the resultant disturbance from COM position errors and inertial errors will be:

$$\hat{\boldsymbol{\tau}}^{dis} = \boldsymbol{\tau}^{(G-G_n)} + (\boldsymbol{H} - \boldsymbol{H}_n)\ddot{\boldsymbol{q}} \tag{2.20}$$

This disturbance torque can be projected to the workspace forces using the Jacobian of the m-link manipulator $\boldsymbol{J}_{manip}$:

$$\widehat{\boldsymbol{W}}^{dis} = (\boldsymbol{J}^T_{manip})^{-1}\hat{\boldsymbol{\tau}}^{dis} \tag{2.21}$$

For a general task of dimension $n \in R^6$, $\widehat{\boldsymbol{W}}^{dis} = [\hat{\boldsymbol{f}}^{dis}, \hat{\boldsymbol{m}}^{dis}]^T$, where $\hat{\boldsymbol{f}}^{dis} = [\hat{f}^x_{dis}, \hat{f}^y_{dis}, \hat{f}^z_{dis}]$ and $\hat{\boldsymbol{m}}^{dis} = [\hat{m}^x_{dis}, \hat{m}^y_{dis}, \hat{m}^z_{dis}]$ are the estimated disturbance forces and moments respectively. $\widehat{\boldsymbol{W}}^{dis}$ can be integrated in (2.15) and (2.16) using the general ZMP formula presented in Sugano et al. [1993]:

$$\widehat{ZMP_x} = \frac{\Sigma_i m_i x_i(\ddot{z}_i + g_{rav}) - \Sigma_i m_i \ddot{x}_i z_i - \Sigma_i I_{iy}\ddot{\theta}_{iy} - p^x \hat{f}^z_{dis} + {}^o\hat{m}^y_{dis}}{\Sigma_i m_i(\ddot{z}_i + g_{rav}) - \hat{f}^z_{dis}} \tag{2.22}$$

$$\widehat{ZMP_y} = \frac{\Sigma_i m_i y_i(\ddot{z}_i + g_{rav}) - \Sigma_i m_i \ddot{y}_i z_i + \Sigma_i I_{ix}\ddot{\theta}_{ix} - p^y \hat{f}^z_{dis} - {}^o\hat{m}^x_{dis}}{\Sigma_i m_i(\ddot{z}_i + g_{rav}) - \hat{f}^z_{dis}} \tag{2.23}$$

$\boldsymbol{p} = [p^x, p^y, p^z]$ is the end-effector position. g_{rav} is the gravity value. ${}^o\hat{m}^y_{dis}$ and ${}^o\hat{m}^x_{dis}$ are the projection of $\hat{m}^y_{dis}$ and $\hat{m}^x_{dis}$ to origin frame respectively. Figure 2.15 shows the block diagram of ZMP disturbance observer (ZMPOB).

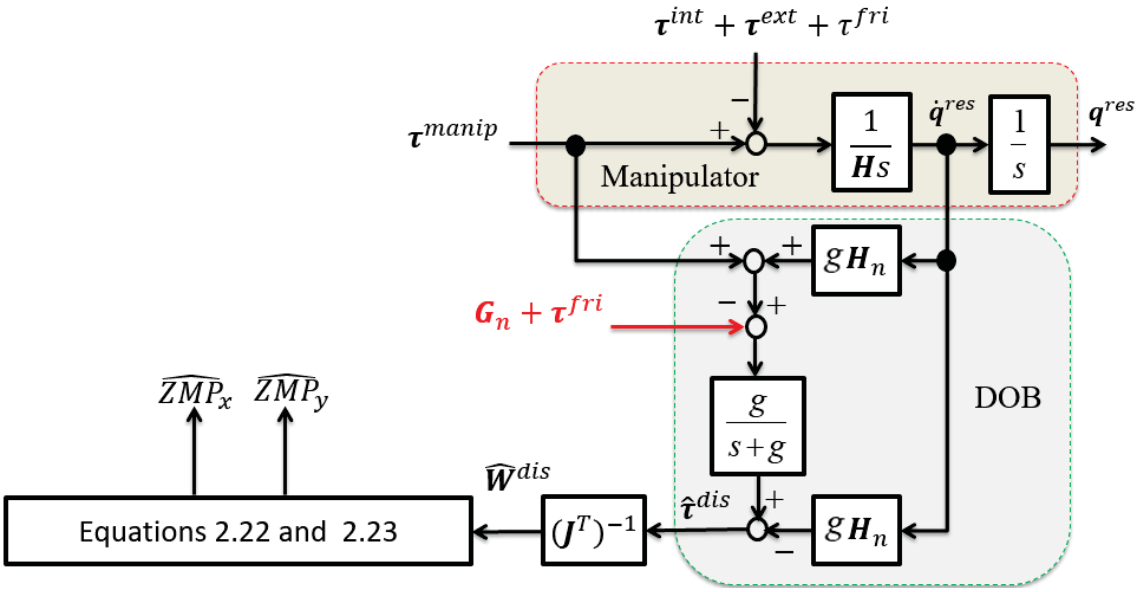

Figure 2.15: Zero moment point observer (ZMPOB)

2.3.1 Results

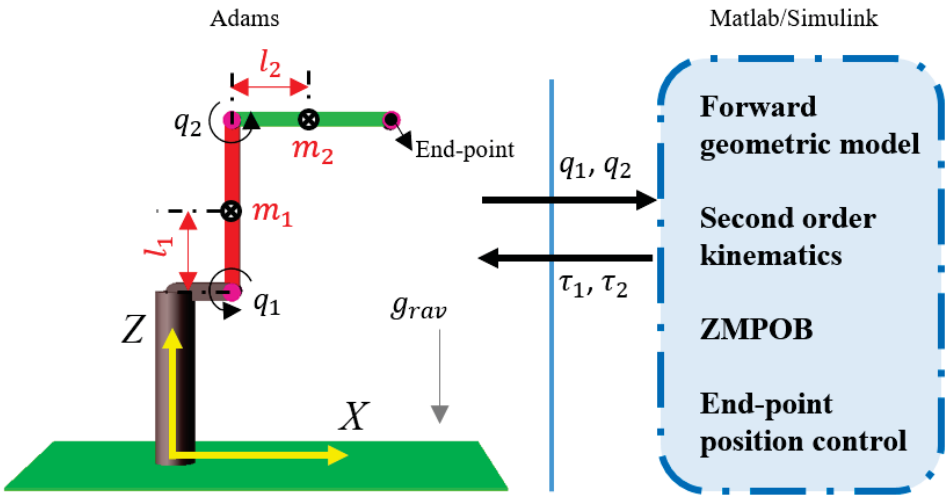

Figure 2.16: Two link manipulator modeled for Adams/Matlab-Simulink co-simulation

In order to evaluate the performance of the zero-moment-point observer presented in the section above, it is implemented for a 2-R robot using Adams-Matlab co-simulation as Figure 2.16 shows. The robot is commanded to move its end-point between three points. Additionally, errors Δl, are added to the center of mass positions shown in Figures 2.16 and 2.14. Then, the zero moment point obtained using the ZMPOB is compared against the one obtained using the ZMP original form described in equation 2.15.

The end-point position in x and z directions is shown in Figure 2.17. Consequently, the joint angular accelerations ($\ddot{q}_1$ and $\ddot{q}_2$) and the end-point linear accelerations ($\ddot{x}$ and $\ddot{z}$) along the trajectory are shown in the Figures 2.18 and 2.19 respectively.

Figure 2.20 shows the proposed ZMPOB compared with the original zero-moment-point form. Both methods are compared against the zero-moment point with 0 errors obtained from Adams which is used as reference. Errors of 10%, 20%, 30%, 40% and 90% are added to the center of mass positions (l_1 and l_2) used in the kinematic modeling which in turn is used for the zero-moment-point calculation (equation 2.15). It can be clearly seen in the figure that the ZMPOB outperforms the original zero-moment-point form. The root mean square errors of the zero-moment-point estimated from the ZMPOB are much less than the ones obtained using the ZMP original form, they can be seen in Table 2.1. This observer is going to be used for controlling the tip-over stability of the mobile manipulator in Chapter 4. The next section presents a newly proposed observer to compensate the effect of non-contact forces on the force-torque sensor's readings.

Table 2.1: Root mean square errors on the zero-moment-point estimation using the ZMPOB and the original method

		$\Delta_l(m)$				
		$l \times 10\%$	$l \times 20\%$	$l \times 30\%$	$l \times 40\%$	$l \times 90\%$
Error (m)	**ZMPOB**	0.0048	0.0073	0.0105	0.0141	0.0366
	ZMP original	0.0149	0.0299	0.0448	0.0598	0.1345

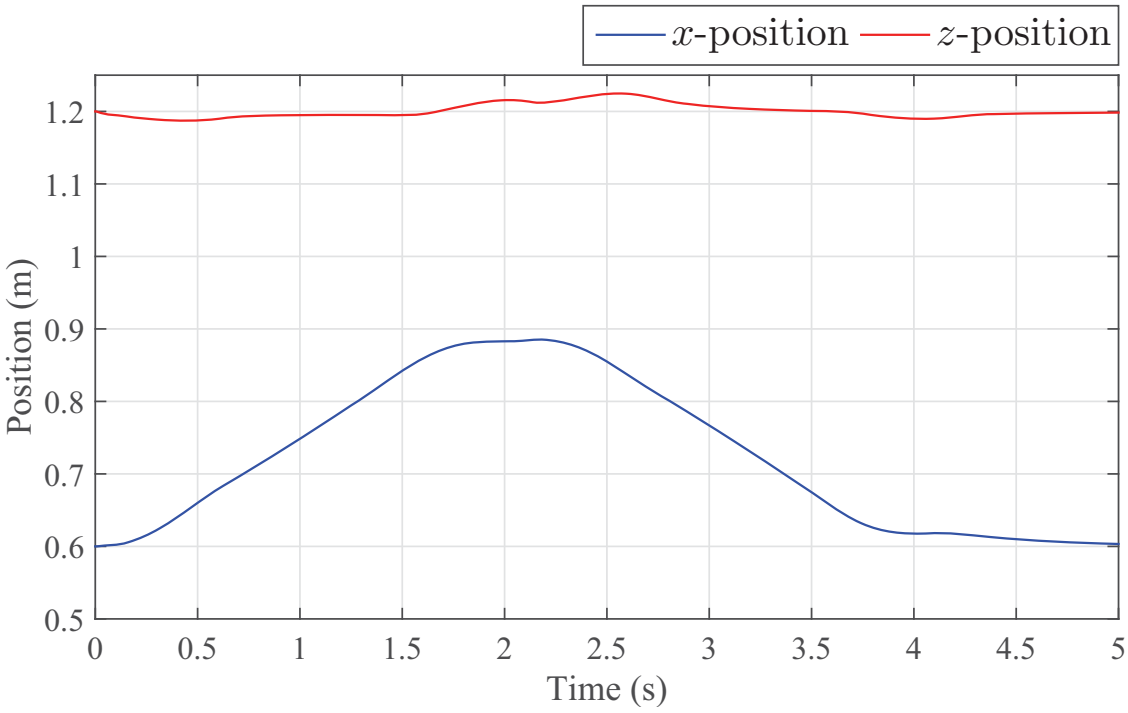

Figure 2.17: End-point x and z positions

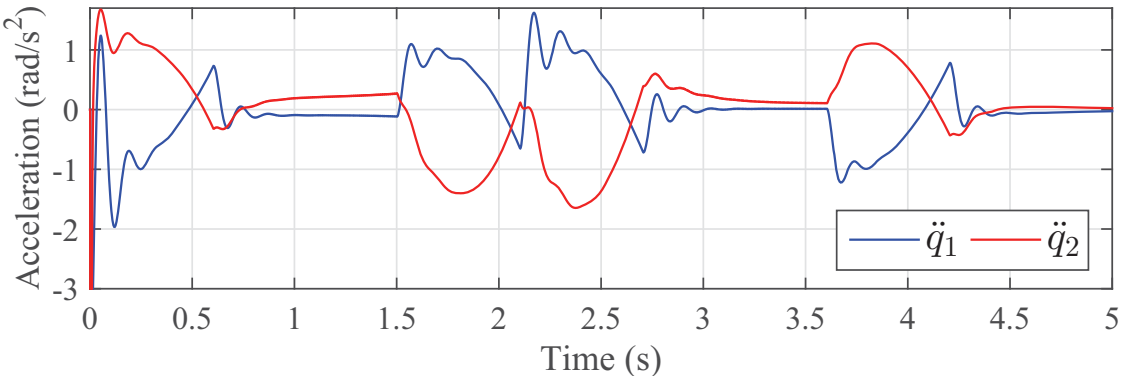

Figure 2.18: 2-R robot joints angular accelerations

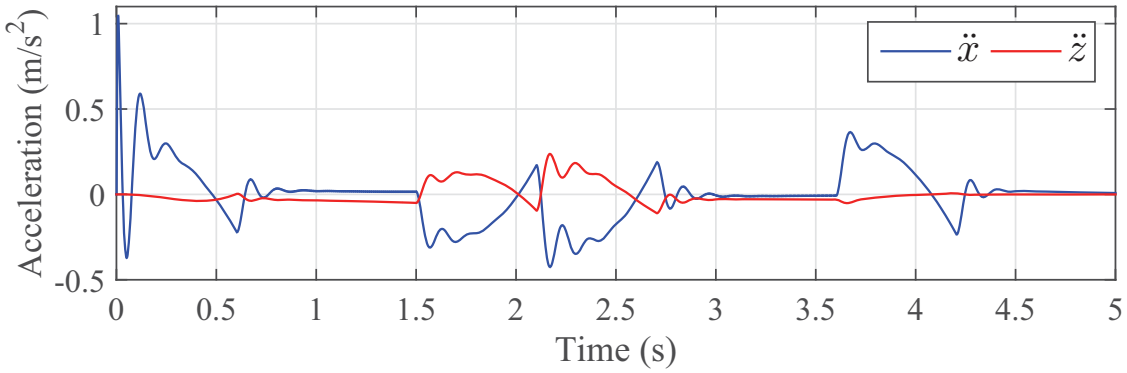

Figure 2.19: End-point accelerations along x and z directions

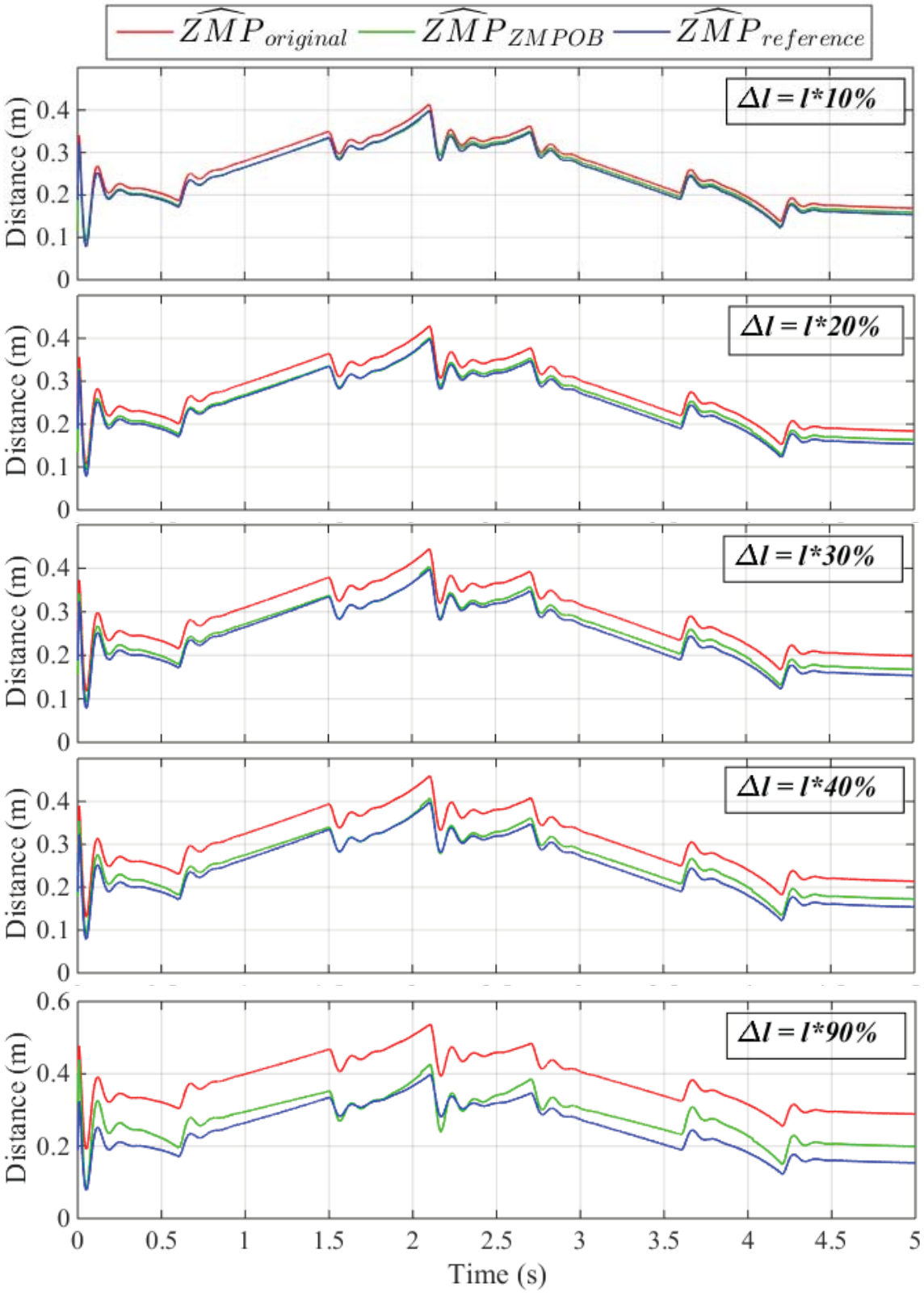

Figure 2.20: Zero moment point observer vs. original ZMP form evaluation under uncertainties ($\boldsymbol{\Delta l} = [\Delta l_1, \Delta l_2]$) added to the center of masses positions ($\boldsymbol{l} = [l_1, l_2]$) of the links

2.4 Recurrent Neural Network Force-Torque Sensor Disturbance Observer

Robots used to realize physical human-robot collaboration, haptic control (e.g. bilateral teleoperation), locomotion or any other task that involves physical interactions with an unknown and dynamic environment, must accurately and timely perceive the contacts with such environment. Thus, for a successful robotic task where contacts are present, external contact forces need to be perceived correctly. Usually, the interaction forces between the robot and its environment are measured by force-torque sensors attached typically to the robot's end-effector. However, such sensors measure both external and internal forces, namely the ones caused by gravitational, inertial, Coriolis and centrifugal forces. Such forces are regarded as *non-contact* forces. Thus, in order monitor or control the pure *contact* environmental reaction force at desired value, it is necessary to first estimate the *non-contact* forces and then subtract them from the force-torque sensor output in order to obtain the pure *contact* forces. Figure 2.21a shows the experimental setup with the force-torque sensor and the IMU mounted on the KUKA robot. Figure 2.21b shows the block diagram of the developed recurrent neural network observer (RNNOB) to estimate the *contact* forces.

Several works have focused on estimating the effect of *non-contact* forces on the force-torque sensor by incorporating acceleration signals. For example, in García et al. [2005], the author developed an observer based on a state-space system that included the dynamics of the robot to estimate the *non-contact* forces. Similarly, in Kröger et al. [2006], a known load was attached to the force-torque sensor and then equations based on inertia matrix were used to estimate the *non-contact* forces. Consecutively, the inertial parameters of the attached load were estimated by identification, then the corresponding internal forces were calculated using the Newton-Euler formulation in Kubus and Wahl [2009].

More recently, many researchers were attracted by the success of applying machine learning in robotics and sensor domains. Thus, instead of modeling and requiring accurate estimation of the load inertial parameters namely, inertia matrix, mass and the center of mass position, machine learning methods were directly applied to estimate forces. Smith et al. [2006] presents one of the earliest works of applying neural networks to estimate forces, where a feed-forward neural network approximates two-dimensional forces based on the robot's joint positions, velocities and accelerations. Recently, in Kollmitz et al. [2018], six-dimensional contact force was estimated on a robot platform using a time-delay neural network, where the network delayed the inputs namely, the wrench and acceleration measurements in order to include temporal information. Another neural network architectures that make use of sequential data are recurrent neural networks (RNNs). This type of networks has been successfully applied to estimate forces in robotic tasks. For instance, in Erickson et al. [2017], a force distribution map on a person's limb generated by contacts with a hospital gown was estimated. Karlsson et al. [2018] presented a detection strategy for contact transients during a snap-fit assembly task. In Loza et al. [2018], an accurate BioTactile sensor model is developed using RNNs, it estimates the 3D force magnitude from 21 tactile signals. Hence, based on the recent success of RNNs in estimating forces in robotic tasks, a recurrent neural network is deployed here to estimate directly the non-contact forces. The network is trained using the robot's proprioceptive information and a low-cost accelerometer.

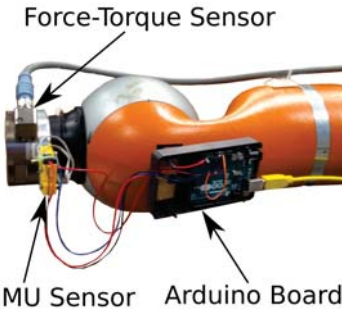

(a) Experimental setup showing the force-torque sensor and the IMU mounted on a KUKA robot

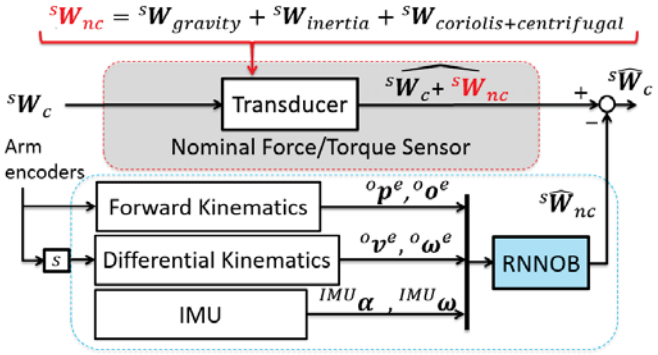

(b) Recurrent neural network observer to estimate the non-contact forces (o: robot frame, e: end-effector frame, s: force-torque sensor frame, IMU: IMU frame)

Figure 2.21: Experimental setup and the proposed force observer

2.4.1 Technical approach

The wrench output of the force-torque sensor can be expressed as

$$\boldsymbol{W} = \boldsymbol{W}_{nc} + \boldsymbol{W}_{c} = \begin{bmatrix} \boldsymbol{F}_{msr} \\ \boldsymbol{\Gamma}_{msr} \end{bmatrix} \tag{2.24}$$

where

$$\boldsymbol{W}_{nc} = \boldsymbol{W}_{gravity} + \boldsymbol{W}_{inertia} + \boldsymbol{W}_{coriolis+centrifugal} \tag{2.25}$$

is the disturbance wrench affecting the sensor due to the non-contact forces and torques f_{nc} and $\boldsymbol{\tau}_{nc}$ respectively. $\boldsymbol{W}_c$ is the pure contact wrench due to contact forces and torques f_c and $\boldsymbol{\tau}_c$ respectively. $\boldsymbol{F}_{msr}$ and $\boldsymbol{\Gamma}_{msr}$ are the force and torque values measured in the sensor frame s respectively as,

$$\boldsymbol{F}_{msr} = f_{nc} + f_c \tag{2.26}$$

$$\boldsymbol{\Gamma}_{msr} = \boldsymbol{\tau}_{nc} + \boldsymbol{\tau}_c \tag{2.27}$$

Using the Newton-Euler approach, f_{nc} and $\boldsymbol{\tau}_{nc}$ can be expanded and equations (2.26) and (2.27) can be rewritten as:

$$\boldsymbol{F}_{msr} = m\boldsymbol{\alpha} - m\boldsymbol{g}_{rav} + \dot{\boldsymbol{\omega}} \times m\boldsymbol{c} + \boldsymbol{\omega} \times (\boldsymbol{\omega} \times m\boldsymbol{c}) + f_c \tag{2.28}$$

$$\boldsymbol{\Gamma}_{msr} = \boldsymbol{I}\dot{\boldsymbol{\omega}} + \boldsymbol{\omega} \times (\boldsymbol{I}\boldsymbol{\omega}) + m\boldsymbol{c} \times \boldsymbol{\alpha} - m\boldsymbol{c} \times \boldsymbol{g}_{rav} + \boldsymbol{\tau}_c \tag{2.29}$$

where $\boldsymbol{\omega}$ is the angular velocity vector of the sensor with respect to its frame, $\boldsymbol{\alpha}$ and $\dot{\boldsymbol{\omega}}$ are the linear and angular acceleration vectors respectively, $\boldsymbol{g}_{rav}$ is the vector corresponding for gravity, m is the mass of the load, $\boldsymbol{c}$ is its center of mass coordinates vector and $\boldsymbol{I}$ is a 3×3 symmetric matrix representing the inertia matrix in the sensor frame.

In standard control approaches, when accuracy is not critical, the sensor measurements in equations (2.26) and (2.27) are used in their default form taking both contact and non-contact forces as the feedback signal to the controller. However, when accurate force control is required, non-contact forces need to be removed as they can lead to wrong reference force values fed back to the controller. In order to estimate these forces precisely, the ten inertial parameters of the load should be known, namely: m, $\boldsymbol{c}$ and the values of $\boldsymbol{I}$. In the literature, researchers usually use identification methods to obtain these values and then apply equations (2.28) and (2.29) to calculate the non-contact

forces and torques. However, the accuracy of estimating non-contact forces and torques based on identification is dependent on the accuracy of the center of mass position of the load $\boldsymbol{c}$ and the calculation of the kinematic vectors $\boldsymbol{\alpha}$, $\boldsymbol{\omega}$ and $\dot{\boldsymbol{\omega}}$ in the same frame.

To overcome these inaccuracies, the RNNOB is developed to estimate directly the non-contact forces independently of the twist and acceleration transformations. Since the involved signals are sequential, an RNN architecture using Long Short-term Memory (LSTM) units, as described in Graves et al. [2013], is ideal to correlate the sensor's kinematics to its wrench output. Figure 2.21 shows the sensors mounted on the arm along with the block diagram of the RNNOB showing how the non-contact forces are estimated and then canceled from the force-torque sensor measurements.

2.4.2 Data collection and testing

As equations (2.28) and (2.29) show, non-contact forces are directly related to angular velocities and accelerations, linear accelerations and the sensor orientation (due to gravity effects). Thus, in order to train the observer it is necessary to generate a broad spectrum of states for these variables. To this end, two datasets were collected using the joint encoders of a KUKA LWR-4 arm with the ATI Gamma[1] force-torque sensor and an Adafruit (L3GD20H + LSM303)[2] inertial measurement unit (IMU) mounted on its wrist. The first dataset was collected without an external load attached to the sensor as Figure 2.21a shows, while the second had the Shadow Dexterous Hand[3] attached as an external load as shown in Figure 2.22. The measurement and average rates for the sensors used, as depicted in Figure 2.21, are described below:

1. **ATI Gamma:** measures a six-dimensional wrench expressed in the sensor's frame s at 1,000 Hz.

2. **Adafruit (L3GD20H + LSM303):** measures the linear accelerations and angular velocities expressed in the IMU frame at 300 Hz.

3. **Joint encoders:** provide, through forward and differential kinematics, the end-effector orientation (in quaternion representation) plus linear and angular velocities expressed in the robot frame Σ_O at 500 Hz.

Since the sensors operate at different rates, the data were recorded at 500 Hz to have a uniform sampling rate. Thus, the force-torque sensor is effectively down sampled and the last output of the IMU is kept until a new sample is published.

2.4.2.1 Data collection without load

For this dataset, the data collected were generated by *manual* and *automatic* trajectories. The manual data was collected by setting the robot controller to gravity compensation mode and then moving the wrist manually to various poses in the workspace with random velocities and accelerations. The automatic data (e.g. without human intervention) were generated by moving the robot between random points in its workspace using various trapezoidal velocity profiles. The manual data were collected in six trials, each about four minutes long and the automatic data were collected in ten trials with an average time of two minutes each. These datasets were then combined into one training

[1] http://www.ati-ia.com/products/ft/ft_models.aspx?id=Gamma
[2] https://www.adafruit.com/product/1714
[3] https://www.shadowrobot.com/products/dexterous-hand/

dataset, where one trial of each of the manual and automatic data were separated to create a test dataset. The validation of the RNN during training used 20% of the training dataset.

2.4.2.2 Data collection with external load

Besides the manual and automatic trajectories, described in subsection 2.4.2.1, an additional *sinusoidal* trajectory on the xy-plane of the robot (see Figure 2.22) frame was generated for this dataset. During this sinusoidal trajectory the end-effector was rotated around each axis sequentially (i.e. roll, pitch and then yaw).

The manual data were collected in five trials, each about five minutes long; the automatic data were collected in ten trials with an average time of two minutes each, and the sinusoidal data were collected in one trial about three minutes long. These datasets were then combined into one training dataset, where one trial of each of the manual and automatic data were separated to create a test dataset. The sinusoidal data was used entirely for training. The validation of the RNN during training used 20% of the training dataset. Additionally to the testing set described above, a pure *rotational* motion test was used to validate the proposed observer against gravitational forces. This rotational test can be seen in Figure 2.27, where the angular rotations are shown at the bottom of the figure.

2.4.2.3 Collision test

To show the accuracy of the RNNOB in estimating pure contact forces, an ATI Mini45[4] force-torque sensor was used as reference. The arm was set to gravity compensation mode to move the external load and collide it ten times with the reference force-torque sensor fixed on the table as shown in Figure 2.22.

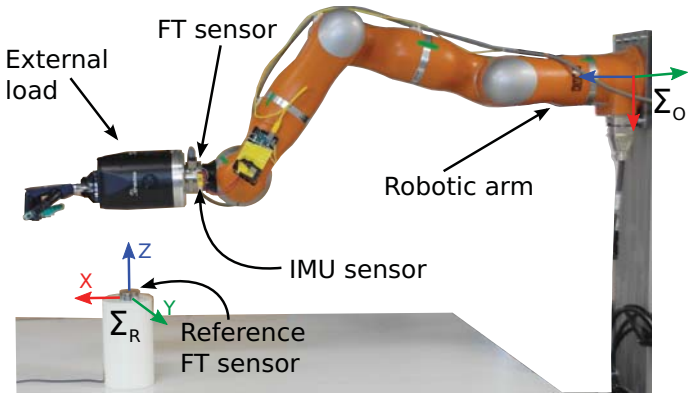

Figure 2.22: Collision test setup

2.4.3 Results

2.4.3.1 RNN model

For the RNNOB validation, TFLearn deep learning library[5] was deployed to train different models using the position (p), orientation (o) and the twist (v, ω) derived from

[4] https://www.ati-ia.com/products/ft/ft_models.aspx?id=Mini45
[5] http://tflearn.org/

the joint encoders[6]; and the linear acceleration obtained from the IMU (${}^{IMU}\alpha$). Besides different input features, models with different hyper-parameters such as the number of epochs, sequence length and learning rate, were also tested. However, the difference in performance between these networks was not statistically noticeable. Thus, the three different models based on the *pose* (p, o), *orientation and twist* (o, v, ω), and *linear acceleration, orientation and twist* $({}^{IMU}a, o, v, \omega)$ were evaluated. All these models were trained for 20 epochs using an architecture with two hidden layers, with 15 and 10 LSTM units respectively, and a sequence length for the input layer of 20 time steps (0.2 seconds). In the output layer, Stochastic Gradient Descent was applied with a learning rate of 0.01 to minimize the mean square error of the regression problem. A hyperbolic tangent sigmoid function was used as the activation function between the hidden layers and for the output layer a linear activation function was used.

Figure 2.23 shows the performance of the models based on different input features on the dataset with an external load as described in Section 2.4.2.2. It can be clearly seen that the model incorporating the measurements from the IMU $({}^{IMU}a, o, v, \omega)$ achieves the best overall performance. However, for the rotation test, as the accelerations are small and only the orientation changes, this model is slightly outperformed by the one using only pose information (p, o).

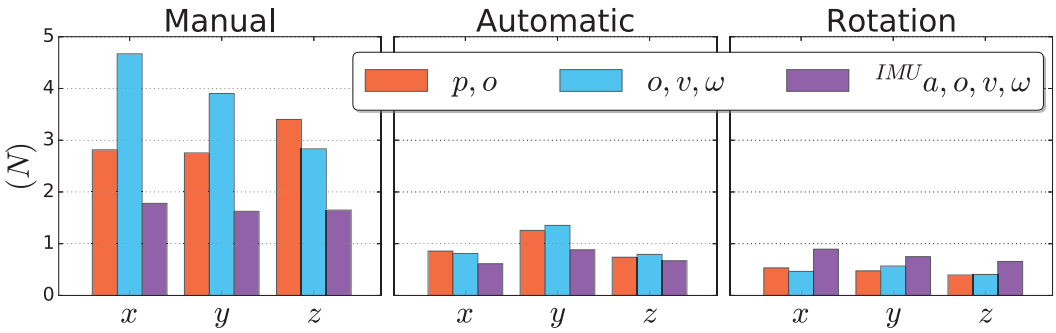

(a) Linear errors for the three types of test motions

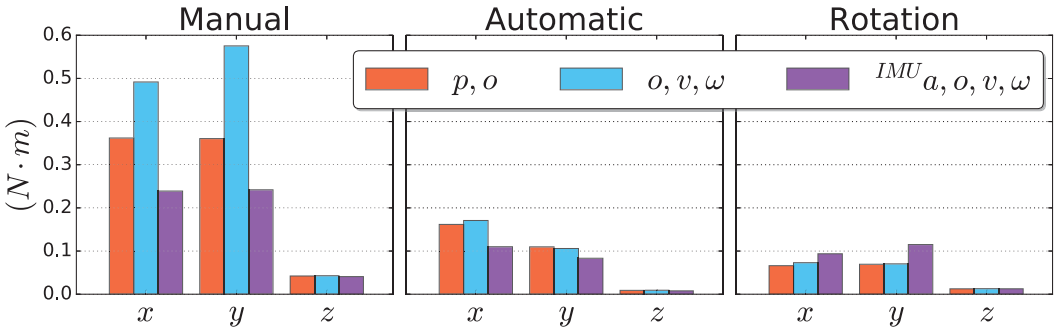

(b) Angular errors for the three types of test motions

Figure 2.23: RMS errors for the RNN models based on: 1) pose (p, o), 2) orientation and twist (o, v, ω) and 3) linear acceleration, orientation and twist $({}^{IMU}a, o, v, \omega)$

[6]Note that for simplicity, when the subscripts are not indicated the quantities are assumed to be of the end-effector expressed on the robot frame.

2.4.3.2 Force estimation without external load

The root mean square (RMS) errors on the test datasets of the automatic and manual motions without load, as described in Section 2.4.2.1, are summarized in Table 2.2. This table shows the force estimation of the RNN observer for previously unseen automatic and manual trajectories compared to the measurement of the force-torque sensor. Since no load was attached to the sensor, except for the top plate which has a negligible mass, the generated wrenches remained very low. The force values were under ± 1.2 N while the torques did not exceed ± 0.6 N·m as Figure 2.24 shows.

Table 2.2: The root mean square errors on the automatic and manual test datasets with no external load

Automatic

	N	N·m
X	0.0432	0.0010
Y	0.0380	0.0007
Z	0.0268	0.0009

Manual

	N	N·m
X	0.1943	0.0022
Y	0.1814	0.0022
Z	0.1100	0.0012

2.4.3.3 Force estimation with external load

To compare the performance of RNNOB to classical methods, the *analytical* observer using the method described in Kubus and Wahl [2009] is implemented. As this method requires knowledge of the inertial parameters, they were estimated using least squares optimization on a trial of the manual dataset described in Section 2.4.2.2. Both methods were compared against the wrenches measured by the force-torque sensor and their corresponding RMS errors are shown in Table 2.3. These results were obtained for the three motion tests described in Section 2.4.2.2, namely, manual, automatic and rotational. An example of the force estimation from both RNN and analytical, observers against the measured forced for a previously unseen manual trajectory can be seen in Figure 2.25.

Table 2.3: The root mean square errors on the dataset with an external load for the RNNOB and the analytical method based on identification

		Manual		**Automatic**		**Rotational**	
		RNNOB	**Analytical**	**RNNOB**	**Analytical**	**RNNOB**	**Analytical**
Error (N)	f_x	1.6578	2.8934	0.8075	2.4436	0.8405	2.6900
	f_y	1.7235	2.6943	1.1334	2.8558	0.7189	1.2193
	f_z	1.5420	2.2989	0.7829	1.5147	0.7082	1.2204
Error (N·m)	τ_x	0.2538	0.3358	0.1384	0.2835	0.0911	0.1408
	τ_y	0.2332	0.3420	0.0995	0.2020	0.1053	0.1601
	τ_z	0.0403	0.0513	0.0089	0.0132	0.0118	0.0301

Additionally, the efficiency of these methods in estimating gravitational forces was evaluated by the rotational test as it can be seen in Figure 2.27. Table 2.3 clearly shows that the RNNOB outperforms the analytical observer in all motion tests.

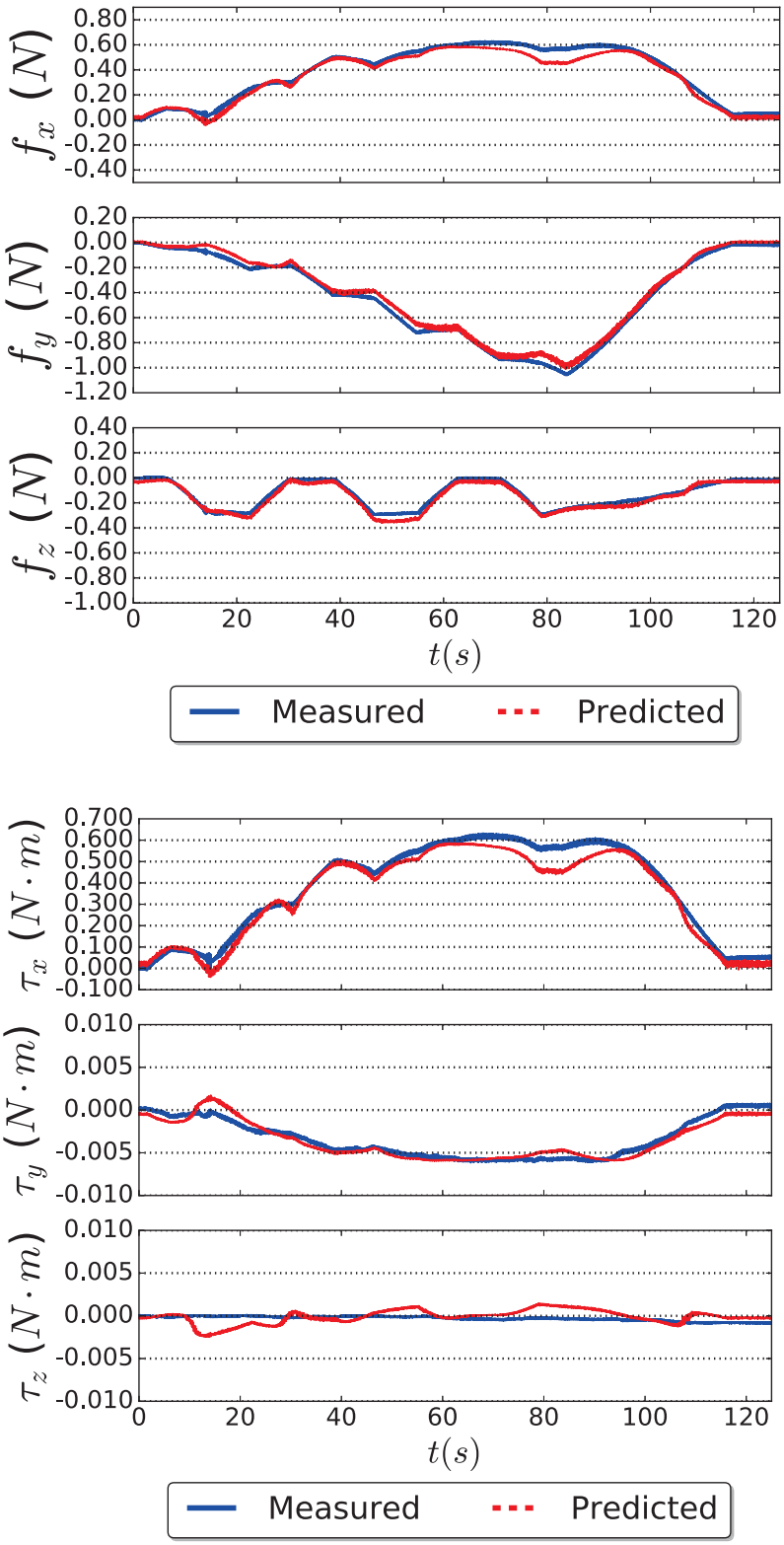

Figure 2.24: Non-contact forces (${}^s\widehat{\boldsymbol{W}}_{nc}$) estimated by the RNNOB for an unseen automatic trajectory with no load attached to the force-torque sensor. The y-axis shows the forces and torques as measured in the force-torque sensor frame

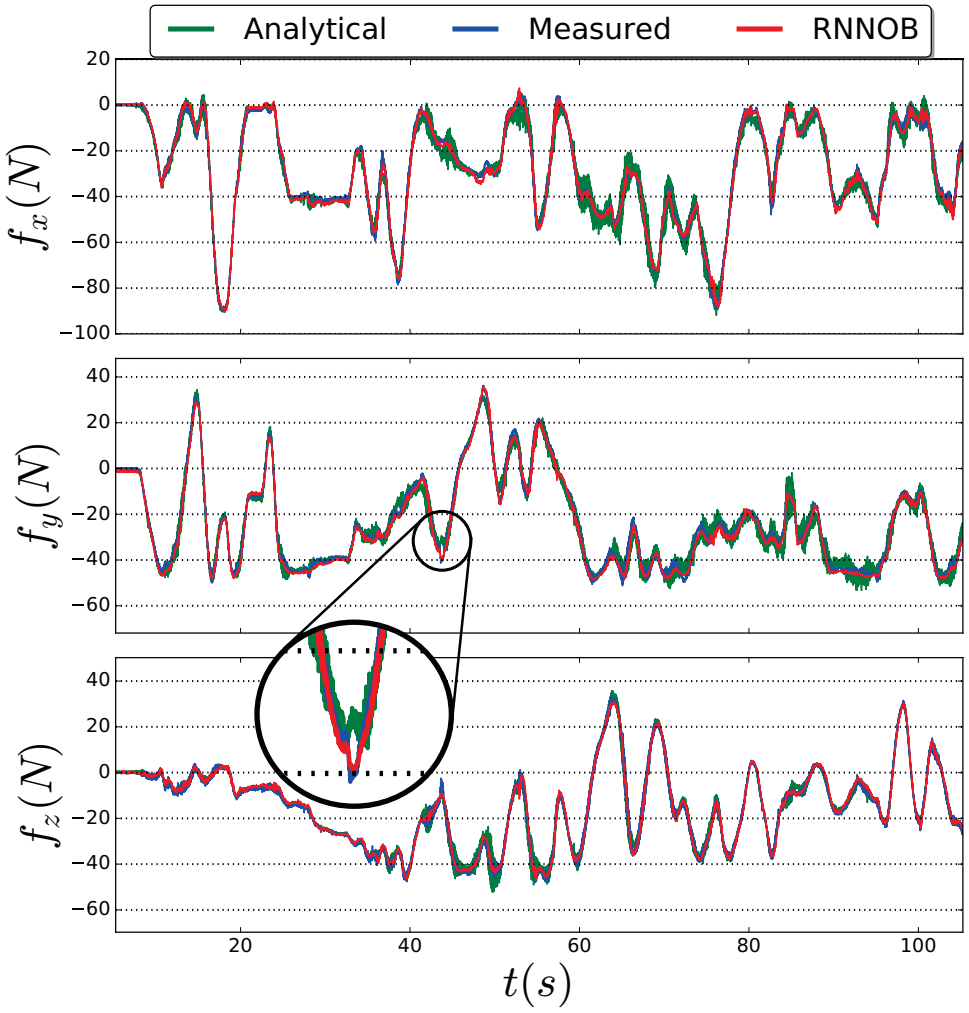

Figure 2.25: Non-contact wrench estimation of the proposed RNNOB compared with an analytical-based approach and as measured by the force-torque sensor for an unseen manual trajectory with an external load. The y-axis shows the forces along x, y and z as measured in the force-torque sensor frame respectively

2.4.3.4 Collision test

The mean error for the ten collisions was of 1.197 ± 0.338 N. One example of the contact tests is shown in Figure 2.26, the contact force is expressed in the reference sensor frame on the table. It can be seen from the figure that the proposed observer can estimate the contacts that are larger than 2 N.

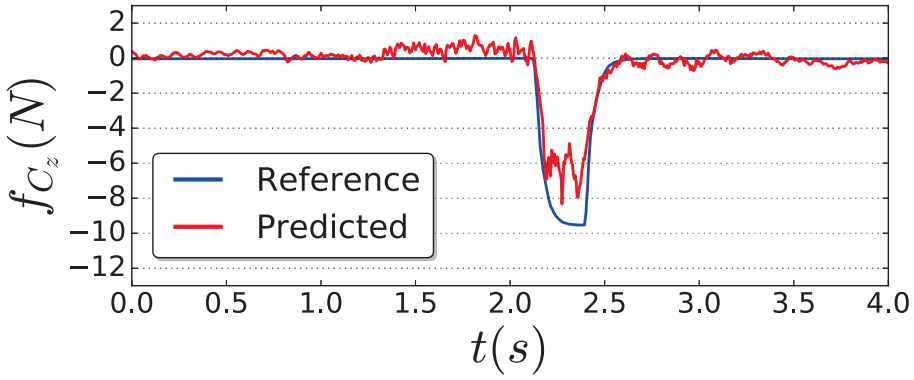

Figure 2.26: Contact force estimation of the proposed approach compared to the reference force measurement

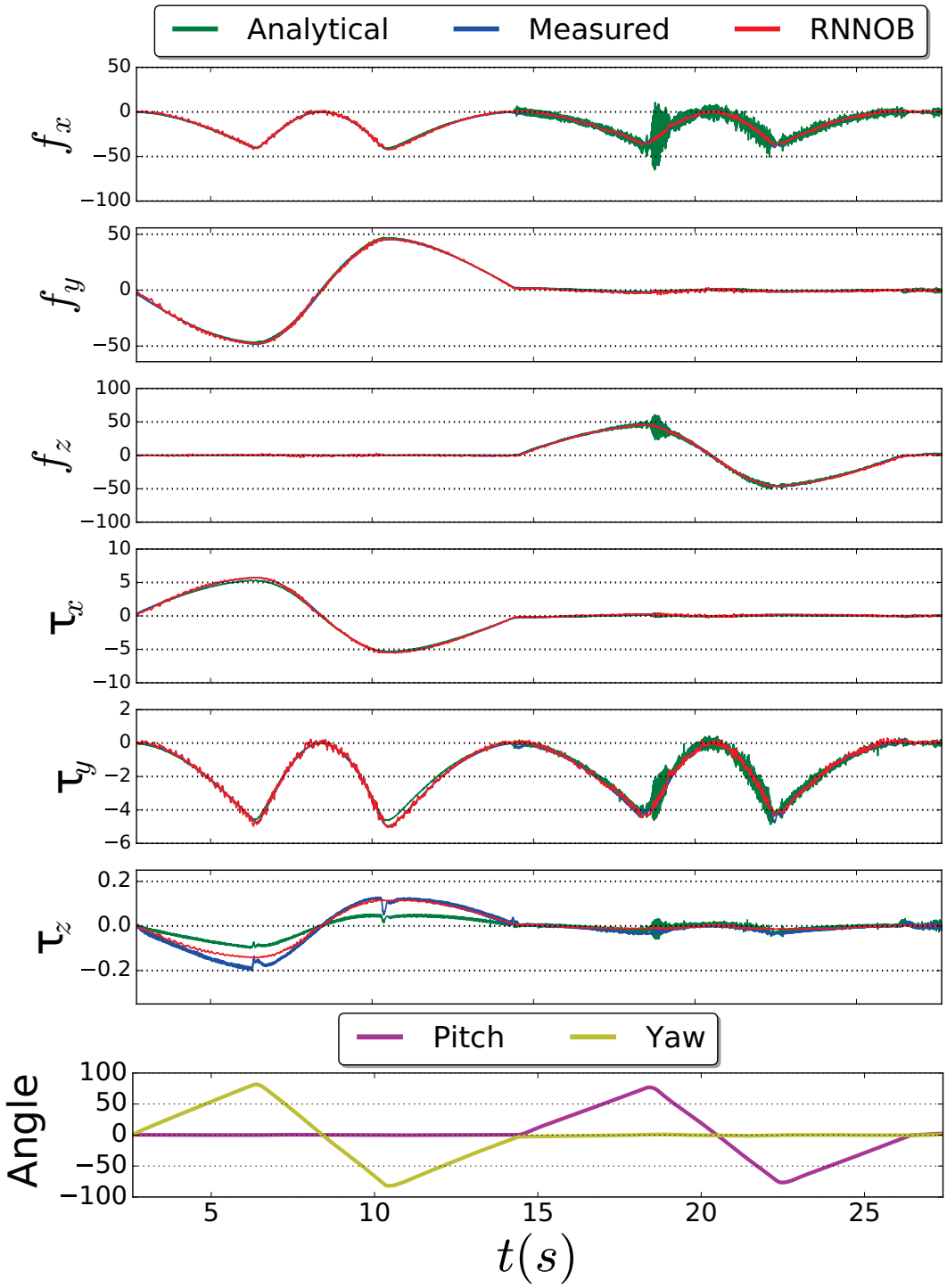

Figure 2.27: Non-contact wrench estimation of the proposed RNNOB compared with an analytical-based approach and as measured by the force-torque sensor. The wrench was generated by rotating the end-effector, with an attached load, around the roll, pitch and yaw axes to experience gravitational forces along the three axis of the sensor. The first three rows show the forces in the x, y and z axes of the force-torque sensor frame and are expressed in N. The next three rows show the torques and are expressed in N·m. The last row shows the rotations around the sensor's y-axis (pitch) and z-axis (yaw) expressed in degrees. The roll angle is not shown since it has no significant effect as the sensor's x-axis is along the gravity vector g

2.5 Conclusion

This chapter presented and explained several disturbance observers that will be used in the controllers in the next chapters. Disturbance observer (DOB) that compensates the internal and external disturbances of the DC motors was detailed. In real applications, the DC motor rotation angle is measured by encoders. However, the DOB requires the angular velocity feedback to estimate the disturbance torque and compensate it. By differentiating the angular position response, angular velocity can be obtained. However, this velocity is noisy and must be filtered which in turn introduces time delay. In order to overcome this problem and synchronize the input torque with the estimated torque calculation, pseudo differentiation with a first order low pass filter was used. The calculation result shows that the disturbance torque can be compensated completely by the DOB. The DOB concept is very useful and can be extended to other applications. The zero-moment-point observer (ZMPOB) is a direct derivation from the DOB, it will be used to compensate errors in zero moment point estimation.

Moreover, a recurrent neural network observer (RNNOB) that estimates the non-contact forces acting on the force-torque sensor was presented, namely: inertial, gravitational, centrifugal and Coriolis forces. The observer is model-free and is able to accurately estimate the non-contact forces when the force-torque sensor is subject to high dynamic motions without the need of an identification process. Additionally, in a variety of highly dynamic motions, the RNNOB outperformed the analytical method based on the identification of the inertial parameters. Furthermore, the input signals used by the proposed observer were unfiltered and thus, no additional delay was introduced. Besides, pure contact forces can be obtained by subtracting the output of the observer from the output of the force-torque sensor such that external contacts can be detected. The observer is limited by its inability to estimate zero forces when the robot is motionless as depicted in Figure 2.26. This is a known issue of RNNs and some work has been proposed to alleviate this problem, as suggested in Erickson et al. [2017]. Another improvement would be to combine the analytical observer with the RNNOB to address the shortcomings of the latter, as well as addressing safety issues by relying on a model-based approach.

Chapter 3

Wall Grinding Based on Active Force Control

In robotic grinding tasks, the robot controller must reactively adapt to changes in the environment and be able to handle uncertainties in texture and disturbances caused by vibrations and friction of the grinding tool operating at high rotational speed. Additionally, the challenge is to achieve a smooth cleaning of the surface while adapting to it. In this chapter, we present a summary of the main works that consider interaction between the robot and the environment as they will be useful for developing our controllers. Additionally, this chapter summarizes and discusses the common works on metallic grinding and polishing since they can be inspiring for developing wall grinding applications. Moreover, the progression in the development of two wall grinding controllers is presented.

Firstly, a smooth hybrid position-force control with compliant wrist is presented; the controller uses the active compliant wrist to maintain the desired force centered on the disc and normal to the surface. The controller switches from force to position based on a smooth transition between free space and contact modes, significantly reducing the impact force and achieving stable interaction with the environment. Hence, it reconsiders the position, force and impedance control strategies together from a practical point of view to achieve the real grinding task.

Secondly, a model based adaptive hybrid velocity-position-force controller for surface (piece of wall in this chapter) grinding is presented. In the proposed controller, the grinding tool is controlled automatically such that its disc adapts to the curvature change of the surface. In addition to that, the controller corrects the desired directions of force and velocity in real-time. These directions are decided based on the contact force and a developed grinding model that estimates the nominal feeding grinding forces. Both controllers are based on active force control. They are tested for a 7-degrees-of-freedom robotic arm equipped with a six-axes force-torque sensor attached to the face of the last joint and, on the other end of the force-torque sensor, the grinding tool is attached. In the next sections, the details of development and evaluation of the controllers is presented, their merits and limitations are discussed and future works are proposed.

3.1 Interaction With the Environment

The development of controllers that can interact with the environment has been the interest of researchers for many years. Hence, many important works have been carried out in the literature. The control strategies proposed can be grouped into two categories as clearly explained in Siciliano and Khatib [2016], namely indirect (e.g. impedance control and its alternatives) and direct force control (e.g. hybrid position-force control). In the former controllers, the motion control is achieved without explicit closure of a force feedback loop, while in the latter controller the force loop is closed on the measured force value. In the next sections a brief review about these types of controllers is presented as they are relevant for grinding and polishing automatic applications.

3.1.1 Impedance control and its alternatives

The impedance controller is explained in Hogan [1985], where the author introduced a method for a robotic arm to interact dynamically with its environment. Moreover, a meaningful set of controllers, that consider constrained manoeuvring, and their respective design specifications to assure compliant motion with stability robustness were described and analyzed in Karerooni et al. [1986]; Kazerooni [1989]. Based on the relationship between interaction forces and manipulator position, one can ensure that the manipulator will be able to manoeuvre in a constrained environment while maintaining appropriate contact forces. A formalism for specifying compliant motion tasks and tracking was explained in De Schutter and Van Brussel [1988] and two kinds of compliance were described, active compliance that reacts to force inputs or the passive compliance in the robot that is changed by the contact forces that generate the trajectory modifications. As the impedance control has no explicit closure of a force feedback loop, the capabilities of impedance control have been enhanced by providing means of force tracking to keep a desired contact force with the environment despite lacking the knowledge of its stiffness and position as described in Seraji and Colbaugh [1997]. The framework proposed for impedance control to be able to track force is based on two simple on-line schemes. The first scheme uses direct adaptive control to generate the reference position on-line as a function of the force-tracking error, the second scheme utilizes an indirect adaptive strategy in which the environmental parameters are estimated on-line. The adaptation allows automatic gain adjustment to provide a uniform performance. Additionally, a force limited impedance and position limited force control were proposed in Almeida et al. [1999] by implementing an impedance controller as an inner loop and integral force controller as an outer loop. This allowed changing the behavior based on the limited external force providing a good position, impedance and force tracking. A more advanced force tracking impedance control based on adaptive methods has been proposed in Jung et al. [2004]. The adaptive technique is based on including the environment position error estimation in the impedance equation and adaptive gain in the damping term. The controller worked well for abrupt changes in the environmental stiffness. Predictive force control that used a fuzzy scaling machine is presented in Baptista et al. [2006], the controller performance was good but it needs the estimation of the environmental stiffness. More recently, learning methods were applied to such kind of controllers. Controllers based on learning to reduce the error and energy to make the robot behave like a human while interacting with unknown environments were presented in Ganesh et al. [2010] and Yang et al. [2011] . It is shown that the robot is resistant to uncertainties after learning but off-line training is essential. Carrying on performance improvement, Ficuciello et al. [2014] includes the redundancy resolution

in the controller by imposing a secondary task in the null space of the end-effector task and try to move the robot towards configurations with maximally decoupled inertia. The interaction problem was solved by allowing the end-effector to comply according to an impedance control law defined in the Cartesian space. More works have been done to ameliorate the performance of the impedance control and to take the external forces into consideration (Morel et al. [1998], Ferretti et al. [2000], Erden and Tomiyama [2010], Prats et al. [2010] and Roveda et al. [2013]). In these works, the researchers combined impedance with extra vision and tactile sensors. Overall, the enhancement of the capabilities of impedance control and providing a means for force tracking is still challenging as the robotic systems suffer from modeling errors, dynamic errors and certain degree of flexibility. Moreover, the behavior of the impedance controller is also dependent on the fact that its parameters may not be fully defined without the knowledge of the environment stiffness.

3.1.2 Hybrid position-force control

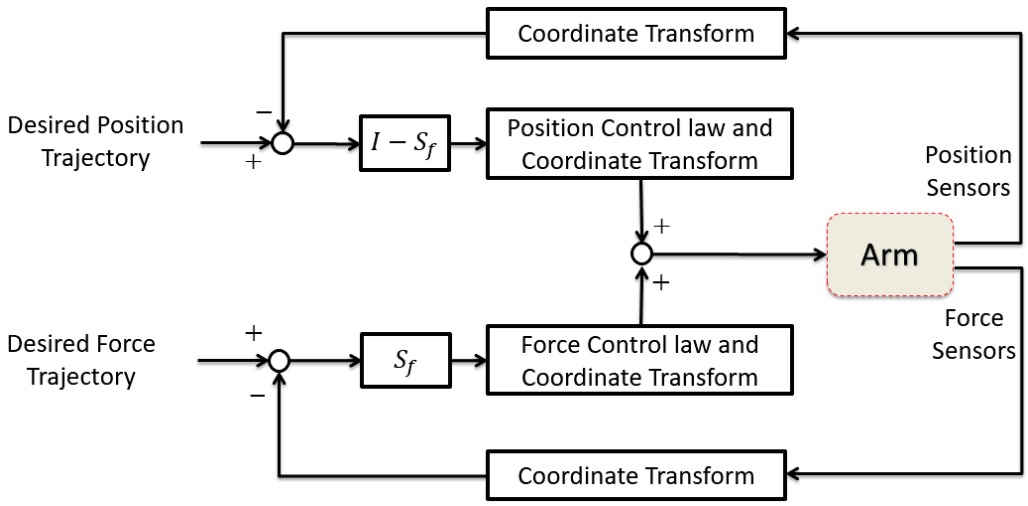

Figure 3.1: Conceptual block diagram of hybrid controller

When the manipulator is in contact with the environment, the end-effector coordinate space can be decomposed into position and force subspaces, then the control in each subspace can be done as presented in Raibert and Craig [1981] and Mason [1981]. Moreover, the force loop is closed on the measured force value in the force controller subspace allowing the force tracking capability. Figure 3.1 depicts the conceptual block diagram of hybrid controller with the decomposed position and force control loops . The explicit model based hybrid control of rigid robot in contact with rigid environments has been studied in Raibert and Craig [1981], Yoshikawa [1987] and in McClamroch and Wang [1988] and with compliant environments in Kankaanranta and Koivo [1988], Siciliano and Villani [1996] and Villani et al. [1999]. A review concerning the approaches used for controlling robots in constrained motions can be found in Yoshikawa [2000]. In Hybrid position-force controllers, the task needs to be perfectly known and the tool frame needs to be well-aligned with the constraint frame. To overcome this problem, a new scheme based on the concept of external control was proposed in Perdereau and Drouin [1993]. The hierarchical juxtaposition of the force control loop on the position control loop in the proposed method provides several advantages: selection matrices and time-dependent geometric transformations are eliminated from the control loop leading to

a controller design independent of the arm configuration. Additionally, since the force control only acts on the reference trajectory, conflicts between force and position controller are avoided. The concept of external control was then used in Mezouar et al. [2007], where the authors combine vision and force to achieve a hybrid force/vision control strategy. In Craig [1989], the problem of manipulator's configuration dynamics was addressed. An additional feedback loop on the normal velocity to the surface was proposed to damp the force oscillations resulting from the varying dynamic behavior of the manipulator. The method was adopted, discussed and validated experimentally on the parallel hybrid force-velocity control architecture in Jatta et al. [2006]. The oscillations in force were damped and the force controller performance was improved.

Additionally, a control strategy to switch between free space and contact modes of the hybrid controllers needs to be implemented. This makes them not robust. Thus, to overcome the robustness and stability issues, researchers put a lot of effort to investigate solutions. Attempts have been made to solve these stability issues, namely switching, impacts and uncertainties using active stiffness and impedance control as presented in Salisbury [1980] and Hogan [1984]. Other solutions reduced environmental stiffness using mechanical means such as soft sensors or compliant covers as in Whitney [1987] and An et al. [1988]. Passive and dynamic damping control was used in Anderson [1989], Anderson [1990] and Chang et al. [1995] as an alternative.

As many studies deduced, using only one sensor limits the tasks the robot can do. Hence to ameliorate the force and position performances in unknown environments, the hybrid control is extended with vision as presented in Castaño and Hutchinson [1994], Nelson et al. [1995] and Hosoda et al. [1996, 1998]. The controllers suffered from disturbance and the closed loop stability was not proven. Then the uncertainties of the robot and the environment were taken into account and more work on the precision of the controllers was presented in Xiao et al. [2000], Chang and Wu [2002], Zhao and Cheah [2004], Olsson et al. [2004], Xie et al. [2005], Leite et al. [2006], Lippiello et al. [2006] and Smits et al. [2006]. Vision is very useful for locating the environment, and determining the relative position and orientation of the robot's end-effector. It has been widely used to improve the human-robot and robot-environment interactions. In Cherubini et al. [2015], the author used vision to detect the different states of the system and continuously switch between controllers and sensor data to ensure safe interaction with the human. Moreover, the work presented in Baeten and De Schutter [2002], Lippiello et al. [2006] and Prats et al. [2010] deploys vision sensors in the applications that require interaction with the environment. Although vision is powerful in canceling unwanted control behaviors and in adding the knowledge about environment, it is usually not sufficient when the environment is rugged and dusty. Moreover, the contact problem (i.e. discontinuity and hight impact forces) has been addressed in the literature, for example in Volpe and Khosla [1991], Nelson et al. [1995] and Zhou et al. [1998]. In Chang and Wu [2002], the force was added just after contact to reduce the impact effect, while in Olsson et al. [2004], the control switches from "position" before contact to "force" control after-wise. The author in Jamisola et al. [2002] used motion control while approaching the environment, followed by impact loading control that dissipates the impact force by setting the force command value negatively proportional to the velocity of the end-effector upon contact. Another example of reducing impact is presented in Alkkiomaki et al. [2006] where the contact velocity is decreased based on vision, addition to that a rubber damper is added to reduce impact.

3.2 Polishing and grinding controllers review

Grinding and polishing processes are time consuming, they are monotonic and strongly rely on skilled human workers. On the other hand, during such operations the tool comes into direct contact with a physical piece or the environment and causes contact forces between them. Hence, the controllers presented in Sections 3.1.1 and 3.1.2 can be deployed to automate grinding and polishing processes as they are direct applications of robot-environment interaction. However, it is challenging to control the interaction forces between the grinding tool and the environment. These forces depend on the depth of the cut, the feed rate, the grinding wheel/disc speed and the material properties. Moreover, the literature is lacking a clear study about modeling and identification of the grinding process of construction materials which is necessary to develop a good grinding controller. To overcome the limitation and shortage of construction grinding controllers in the literature, this section presents a set of relevant controllers that serve for grinding or polishing of metallic and glass materials.

3.2.1 Polishing

Recently, a review of polishing robots was presented in Li et al. [2018], the author presented a great variety of tools that can be carried by the robot for polishing different types of workpieces. As the robots can be controlled flexibly, they can be used to apply stress between the polishing tool and the workpiece while moving with desired feed rate. The contact force has a significant influence on the quality of the polished workpiece surface, whether it is applied by either passive or active compliant control.

3.2.1.1 Passive compliant control robotic polishing

Passive compliant control for polishing systems can be realized by using passive mechanisms, such as springs or elastic materials as illustrated in Figure 3.2. Hence, the contact force between the polishing tool and the workpiece surface can be maintained within a minimum-maximum range. In Furukawa et al. [1996], a passively compliant end-effector polisher was developed and mounted on the wrist of an industrial robot to polish a three-dimensional surface without requiring a prior description of its geometry. The end-effector uses position sensors to measure the misalignment of the robot's wrist from the local surface normal to keep the axis of the polishing tool normal to the local surface. Despite that, the angular error of the contact with the work surface was of 4 to 8 degrees. Similarly, in Huang et al. [2002] a passive compliance tool combined with an adaptive path planning approach is used to overcome the geometry variation problems while polishing a turbine-vane. Moreover, a compliant end-effector is adopted in Han et al. [2017]. The compliance of the manipulator and the tool is modeled and a force control is realized. Interested readers can refer to Li et al. [2018] for more works on passive compliance control for polishing. Most of the works mentioned here and in the survey rely on springs and elastic materials to achieve compliance. Although passive compliance control can achieve the task, it can not control well the contact force in real time especially when the work piece geometry varies significantly. This can damage the workpiece if applied for metallic or construction grinding applications.

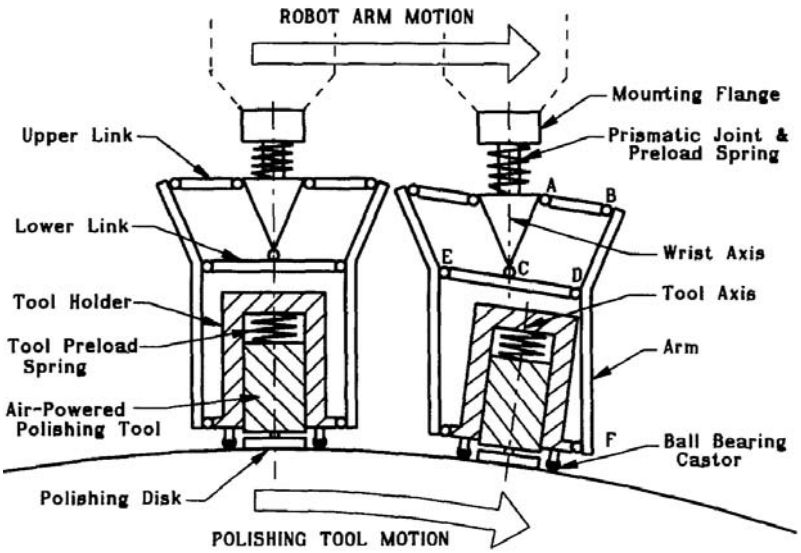

Figure 3.2: End-effector illustrating passive compliant accommodation to the surface using springs (Furukawa et al. [1996])

3.2.1.2 Active compliant control for robotic polishing

In order to get a good polishing quality, the normal force applied on the tool must be controlled accurately. Nevertheless, depending on the feed rate and material properties, sometimes it is troublesome to handle the multi-dimensional force control system in run-time processes. Wang and Wang [1999] presented a surface finishing system with an active single-axis force controller, the tool is fixed on one axis motor fixed on the end effector. Hence, the control of the end effector is separated from the robot. A force observer is used instead of a force-torque sensor and an active proportional-integral-derivative (PID) plus feed-forward force controller applies a desired polishing pressure in the normal direction of the workpiece surface and adjusts the contact angle between the grinder and the workpiece surface. In Jamisola et al. [2002, 2005], a mobile manipulator was deployed for canopy polishing. Operational space formulation is adopted to achieve robust hybrid position-force control, the mobile manipulator end-effector maintains a desired force normal to the canopy surface of an unknown geometry while doing a compliant polishing motion. In order to get an efficient and consistent polishing method, a parallel polishing machine is presented in Li et al. [2014], where a fractional order PID control method is introduced to achieve force-displacement hybrid control. A polishing force control model of the linear motion platform is established. A CAD/CAM-based position-force controller for a mold polishing robot is presented in Nagata et al. [2007], CAD data are used to generate the rough tool path, and the normal and tangential force directions for the tool. Impedance control with force tracking ability is used to apply the polishing force on the piece. The surface state after polishing was evaluated, and consequently a successful surface was observed. In Moura and Erden [2017] and Moura et al. [2018], formulation of a control and path planning approach for a cab front cleaning robot is presented. The local path planning is done by the operational space controller while the cleaning pattern is decided by a high level path planner. The orientation to the surface is controlled based on the minimization of the torque at the contact point. Additionally, a set of polishing robotic methods that use mini robotic systems attached to the main robotic system are presented in Li et al. [2018].

3.2.2 Grinding

Automated grinding is invaluable in the industry, the time and cost savings are substantial. This fact has attracted extensive research to investigate possible methods for achieving the automation of grinding processes. As active force control was usually implemented in polishing applications without feedback from the metal removal process itself, Elbestawi et al. [1991] presented an adaptive predictive force controller for robotic grinding. The task planning and trajectory are defined a priori, while force regulation is established by modifying the position commands on-line. The control laws are designed based on accurate models for the open-loop dynamics of the robot and explicit grinding force model, which are identified from experimental data. The results show a rather good force regulation performance however the controller was sensitive to the arm location in the workspace. Moreover, when grinding with force control, the disc will be deburred and then stop cutting good due to the camber angle, leading to the reduction in the depth of cut, which in turn affects back the cutting force. Ulrich et al. [1992] examined the disc wear and grinding forces where the disc wear is observed to be nonuniform, if the robotic grinding is planned for a subsequent large number of passes, the disc wear is an important aspect which can not be neglected. A simple disc wear and a dynamic force models have been developed taking into account the volume changes of the cut and the disk itself. The system parameters (stiffness and metal removal parameters) are determined experimentally, related to force and then used in the control loop to apply adjustments based on the current changes. Furthermore, robot-assisted grinding is presented in Wang and Jan [2001], where a PID plus feed-forward force controller is used with torque observer to sense the grinding contact force based on the driving current and the output position of the motor. Zigzag and fractal paths on curved surfaces are designed for the grinding processes. The four grinding factors are determined and ordered, based on their effect on surface roughness and their contribution in the grinding process, in descending order as: path pattern, grinding contact pressure, tool diameter, and feed rate. Addition to that, a large scientific analysis and documentation about the industrial grinding process are presented in Rowe [2013] and Hitchiner et al. [2016]. In Liu et al. [2004], a force control technique for hand grinders considering the machine compliance is developed. A corresponding PID controller is designed for grinding force control, it calculates the appropriate CNC spindle displacement according to the measured force from the force sensor. Additionally, active compliant motion control is applied to keep contact between grinding tool and the workpiece in Park et al. [2008]. An auto surface tracking algorithm was developed to automatically track the outline of the workpiece based on the measured force with an acceleration algorithm added to increase the grinding speed to reach 20 mm/sec. In Ziliani et al. [2007], the hybrid force-velocity control strategy was adopted to track and grind the contour of planar workpieces. The controller was combined with a special design of the deburring tool and validated on 2-R planar robot. Recently in Chen et al. [2018], the automation of blisk blade grinding has been presented. An active compliant controller was implemented on a smart two degrees of freedom (dof) end-effector. An approximated grinding model is used to predict the desired force amplitude and direction, which are then controlled by hybrid position-force controller to make sure that the tool adapts to the curvity change of the surface.

In comparison to wall grinding operations in the construction industry, the mentioned industrial grinding operations are different and cannot be directly applied. A major difference is that the industrial grinding robots are stiffer either because of their small size or because there is a mini robotic system attached to their end-effector. Thus,

fixing a construction grinding tool to the end-effector of a relatively long robotic arm and applying active force control will be challenging as the system is less stiff and less precise. Additionally, in industrial grinding operations, cylindrical grinding is usually applied where only one face of the grinding tool operates, i.e. the rotational axis of the tool is parallel to the workpiece surface being ground rather than being normal to the surface as in wall grinding case using a disc. Moreover, although many material removal prediction methods exist in the literature (Li et al. [2018]), neither experimental results nor model can be found concerning the grinding process of construction materials.

3.3 Smooth Position-Force Controller with Compliant Wrist for Wall Grinding

This section presents a decoupled control strategy based on position and orientation. Without loosing generality, this control scheme can be applied to any robotic arm where position and orientation can be decoupled at the joint level. The first three degrees of freedom of the arm are used to ensure a desired force on the wall and trajectory tracking using hybrid position-force control. A conceptual design of the system can be represented as shown in Figure 3.3. The control of wrist joints is based on admittance to ensure the adaptation of the tool to the wall. Additionally, the controller integrates a smooth transition function to ensure the continuity of the system while switching between position (in free space) and force (in contact). The switching function is based on the distance measured between the disc and the wall, it is obtained from radars around the tool. The desired force is then increased linearly to minimize the impact force. Random noise is added in the simulation environment to see the effect of the abrasive disc on the sensory readings, where it is used to validate the controller. Hence, taking the advantage of force measurements and radar information, better fitting to the surface can be achieved while grinding and ensuring a normal contact force on the wall coinciding with the tool center. The control scheme is explained in the following subsections:

3.3.1 Hybrid position-force control in operational space

Expressing the task in operational space requires a precise control of the end-effector motion, which can be achieved by the hybrid control proposed in Siciliano and Khatib [2016]. Based on dynamics, the controller can be expressed as follows:

$$\boldsymbol{W}_{cmd} = \boldsymbol{\Lambda}(\boldsymbol{q})\boldsymbol{S}_v\boldsymbol{\alpha}_m + \boldsymbol{S}_f\boldsymbol{\lambda}_f + \boldsymbol{\mu}(\boldsymbol{q},\dot{\boldsymbol{q}}) \tag{3.1}$$

where $\boldsymbol{W}_{cmd} \in \mathbb{R}^n$ (applied on the first 3 joints and $n = 3$) denotes the output wrench of the end-effector in operational space; $\boldsymbol{q}$ corresponds to joint values, $\boldsymbol{S}_v$ and $\boldsymbol{S}_f$ are the selection matrices of position and force controlled directions respectively; $\boldsymbol{\alpha}_m$ and $\boldsymbol{\lambda}_f$ are the acceleration and force commands respectively, $\boldsymbol{\Lambda}(\boldsymbol{q})$ is the pseudo-inertia matrix defined as,

$$\boldsymbol{\Lambda}(\boldsymbol{q}) = (\boldsymbol{J}\boldsymbol{H}(\boldsymbol{q})^{-1}\boldsymbol{J}^T)^{-1} \tag{3.2}$$

with $\boldsymbol{J}$ denoting the $(n \times n)$ kinematic Jacobian matrix, $\boldsymbol{H}$ is the $(n \times n)$ robot inertia matrix; $\boldsymbol{\mu}$ is the $(n \times 1)$ function to compensate for Coriolis, gravitational and friction forces in the workspace. It is defined as,

$$\boldsymbol{\mu}(\boldsymbol{q},\dot{\boldsymbol{q}}) = \boldsymbol{\Gamma}(\boldsymbol{q},\dot{\boldsymbol{q}})\dot{\boldsymbol{q}} + \boldsymbol{\eta}(\boldsymbol{q}) \tag{3.3}$$

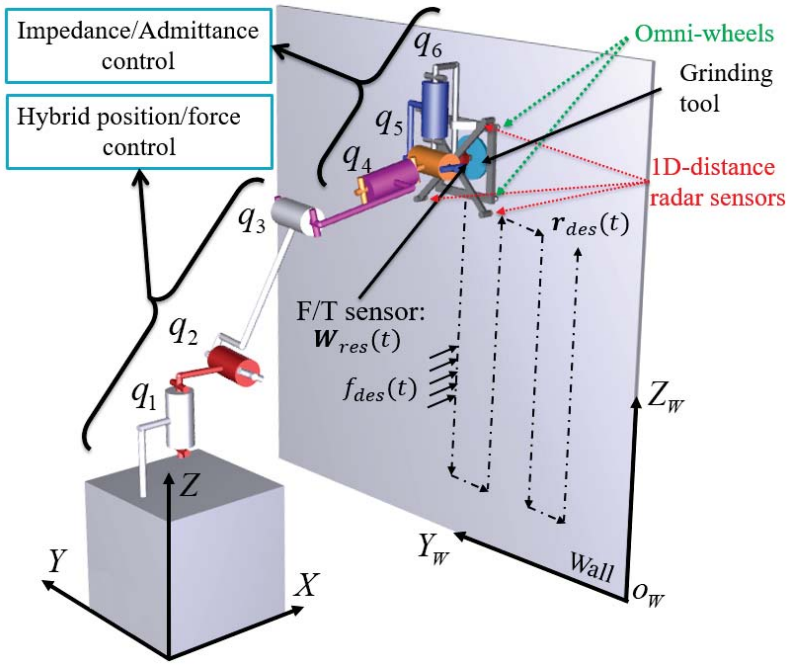

Figure 3.3: Kinematic structure of the robotic system equipped with a grinding tool, several 1D-distance radar sensors around it for attitude measurement, and a force/torque sensor to perform asbestos removal on the wall

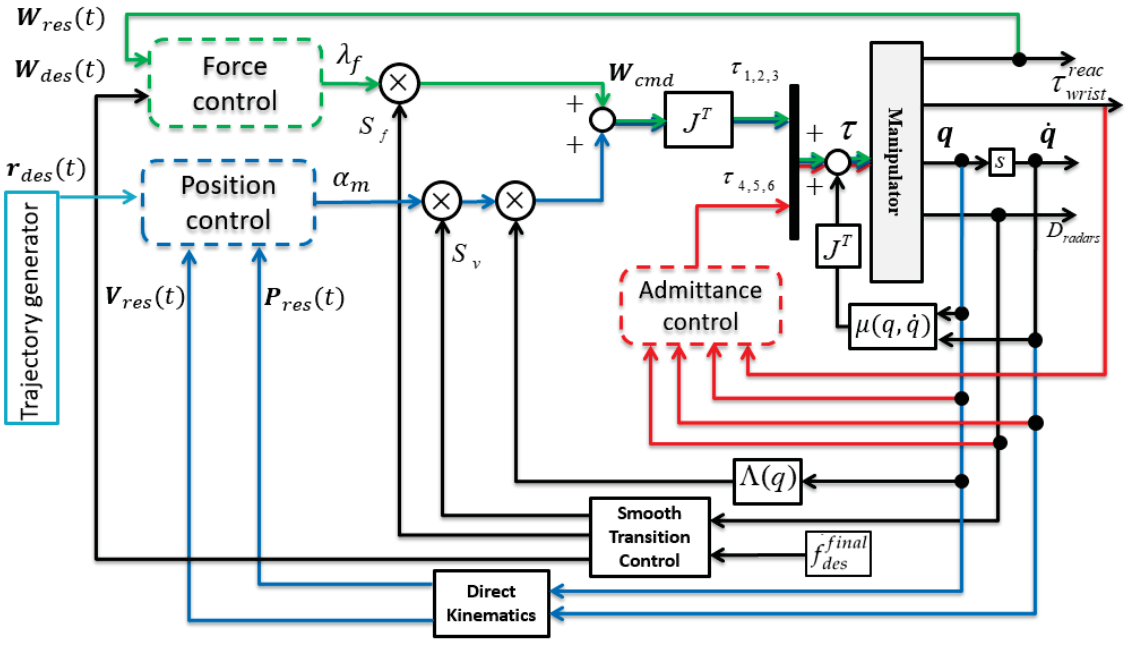

Figure 3.4: Hybrid controller block diagram: force control loop (green), position control loop (blue), admittance control loop (red)

where $\boldsymbol{\Gamma}$ is the wrench mapping the centrifugal, Coriolis and friction effects $\boldsymbol{c}(\boldsymbol{q}, \dot{\boldsymbol{q}})$ from joint space into operational space:

$$\boldsymbol{\Gamma}(\boldsymbol{q}, \dot{\boldsymbol{q}}) = \boldsymbol{J}^{-T}\boldsymbol{c}(\boldsymbol{q}, \dot{\boldsymbol{q}})\boldsymbol{J}^{-1} - \boldsymbol{\Lambda}(\boldsymbol{q})\dot{\boldsymbol{J}}\boldsymbol{J}^{-1} \tag{3.4}$$

and $\boldsymbol{\eta}$ is the wrench mapping the gravitational effects $\boldsymbol{G}(\boldsymbol{q})$ from joint space into the operational space as:

$$\boldsymbol{\eta}(\boldsymbol{q}) = \boldsymbol{J}^{-T}\boldsymbol{G}(\boldsymbol{q}) \tag{3.5}$$

Finally the joint torques $\boldsymbol{\tau}$ can be calculated by:

$$\boldsymbol{\tau} = \boldsymbol{J}^{T}\boldsymbol{W}_{cmd} \tag{3.6}$$

The control loop expressed in equation (3.1) allows full decoupling between the force and velocity controlled subspaces (refer to Figure 3.4).

3.3.2 Force and position control Loops:

The desired wrench $\boldsymbol{W}_{des}$ is the vector of desired forces and torques,

$$\boldsymbol{W}_{des} = \begin{bmatrix} f^x_{des} & f^y_{des} & f^z_{des} & \tau^x_{des} & \tau^y_{des} & \tau^z_{des} \end{bmatrix}^T \tag{3.7}$$

it can be achieved by,

$$\boldsymbol{\lambda}_f = \boldsymbol{W}_{des}(t) + \boldsymbol{K}_{PF}\big(\boldsymbol{W}_{des}(t) - \boldsymbol{W}_{res}(t)\big) \tag{3.8}$$

$\boldsymbol{\lambda}_f$ is the command to the force controller and $\boldsymbol{W}_{res}$ is the reaction wrench value (it can be obtained from ADAMS in simulations and from the force-torque sensor in real experiments). $\boldsymbol{K}_{PF}$ is a suitable positive-definite gain matrix. The proportional feedback is able to reduce the force error due to disturbance forces.

Position control can be achieved by setting:

$$\boldsymbol{\alpha}_m = \ddot{\boldsymbol{r}}_{des}(t) + \boldsymbol{K}_{Dr}\big(\dot{\boldsymbol{r}}_{des}(t) - \boldsymbol{V}_{res}(t)\big) + \boldsymbol{K}_{Pr}\big(\boldsymbol{r}_{des}(t) - \boldsymbol{P}_{res}(t)\big) \tag{3.9}$$

$\boldsymbol{V}_{res}$ and $\boldsymbol{P}_{res}$ are the velocity and position response of the end-effector computed by the direct kinematics; $\boldsymbol{K}_{Dr}$ and $\boldsymbol{K}_{Pr}$ are suitable gain matrices; $\ddot{\boldsymbol{r}}_{des}(t)$, $\dot{\boldsymbol{r}}_{des}(t)$ and $\boldsymbol{r}_{des}(t)$ are the desired acceleration, velocity and position tracking inputs, obtained from the trapezoidal trajectory generator with continuous acceleration as detailed in Khalil and Dombre [2004].

3.3.3 Smooth transition control

As described in Section 3.1.2, the switching problem is of main concern. In order to avoid the discontinuous switching between the controllers, and to reduce the impact force, a new strategy is introduced to change the selection matrix element $\boldsymbol{S}_f(i, j)$ corresponding to the desired direction of force from 0 to 1 smoothly ($i = j$, since $\boldsymbol{S}_f$ is diagonal matrix). This way, the controller inputs are continuous and the control flips smoothly from full position to hybrid control according to the distance from the grinding tool to the wall $D_{wall} = D_{radars} - d$. D_{radars} is obtained from radar readings and d is the offset between the radars and the tool.

$$D_{wall} = min(D_{radar_1}, D_{radar_2}, D_{radar_3}, D_{radar_4}) - d \tag{3.10}$$

Hence, the exponential variation has been chosen as,

$$S_f(i,j) = e^{k_a * D_{wall}} \tag{3.11}$$

$$S_v(i,j) = 1 - S_f(i,j) \tag{3.12}$$

with

$$k_a = -\frac{log(S_{f_{final}})}{D_{final}} + \epsilon \tag{3.13}$$

$$\epsilon = D_{wall}^{final} - D_{wall}^{initial} \tag{3.14}$$

$S_{f_{final}}$ is chosen as a small scalar close to 0, and the impact control is regulated by ϵ according to the distance range defined by $[D_{wall}^{final} - D_{wall}^{initial}]$. When $S_f(i,j)$ reaches 1, f_{des} goes from 0 to the maximum desired value as:

$$f_{des}(t) = \begin{cases} 0 & \text{if } t \leq t_{impact} \\ r_f(t - t_{impact}) + f_0 & \text{if } t_{impact} < t \leq t_{impact} + w \\ f_{des}^{final} & \text{if } t > t_{impact} + w \end{cases} \tag{3.15}$$

where $r_f = \frac{f_{des}^{final}}{w}$ is the force rate, f_0 is the initial value of f_{des} and w is the desired period to reach the maximum force.

3.3.4 Impedance/Admittance based orientation control

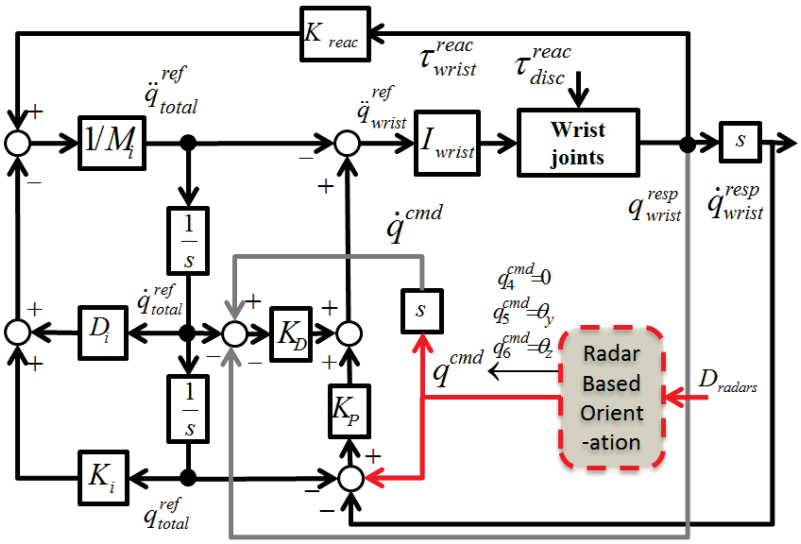

Figure 3.5: Joint based admittance controller block diagram (refer to Sections 3.3.4, 3.3.5)

In order to ensure soft interaction with the environment and stability against impacts, joint based impedance/admittance controller has been utilized for the wrist joints (Mohy El Dine et al. [2016]). It ensures the tool-wall adaption with minimal torques (refer to Figure 3.5). The torque acting on the end-effector when moving along the surface is:

$$\tau_{ext} = K_{reac} \tau_{wrist}^{reac} \tag{3.16}$$

$\boldsymbol{K}_{reac}$ is the gain of reaction forces, $\boldsymbol{\tau}_{wrist}^{reac}$ is the reaction torque on the wrist, obtained from the torque sensor. Hence, the controller can be realized based on accelerations references as:

$$\ddot{\boldsymbol{q}}_{ref}^{total} = \frac{1}{\boldsymbol{M}_i}(\boldsymbol{\tau}_{ext} - \boldsymbol{D}_i\dot{\boldsymbol{q}}_{ref}^{total} - \boldsymbol{K}_i\boldsymbol{q}_{ref}^{total}) \tag{3.17}$$

where $\ddot{\boldsymbol{q}}_{ref}^{total} = [\ddot{q}_{4\ ref}^{total}\ddot{q}_{5\ ref}^{total}, \ddot{q}_{6\ ref}^{total}]^T$ is the reference joint accelerations, the joints reference velocity is $\dot{\boldsymbol{q}}_{ref}^{total} = [\dot{q}_{4\ ref}^{total}, \dot{q}_{5\ ref}^{total}, \dot{q}_{6\ ref}^{total}]^T$ and $\boldsymbol{q}_{ref}^{total} = [q_{4\ ref}^{total}, q_{5\ ref}^{total}, q_{6\ ref}^{total}]^T$ is the joints position reference. $\boldsymbol{M}_i$, $\boldsymbol{D}_i$ and $\boldsymbol{K}_i$ are the impedance gains. They can be tuned for the desired performance by fixing the 2^{nd} order dynamics as:

$$\frac{\boldsymbol{q}_{ref}^{total}}{\boldsymbol{\tau}_{ext}} = \frac{1}{\boldsymbol{M}_i s^2 + \boldsymbol{D}_i + \boldsymbol{K}_i} \tag{3.18}$$

where $\ddot{\boldsymbol{q}}_{wrist}^{ref} = [\ddot{q}_4^{ref}, \ddot{q}_5^{ref}, \ddot{q}_6^{ref}]^T$ is the final acceleration reference to the wrist motors. The natural frequency $\boldsymbol{\omega}_i$ and the damping ratio $\boldsymbol{\zeta}_i$ can be used to define the oscillatory and decaying properties of the sytsem. They are defined as,

$$\boldsymbol{\omega}_i = \sqrt{\frac{\boldsymbol{K}_i}{\boldsymbol{M}_i}} \text{ and } \boldsymbol{\zeta}_i = \frac{\boldsymbol{D}_i}{2\sqrt{\boldsymbol{M}_i\boldsymbol{K}_i}} \tag{3.19}$$

Finally, the motors angular acceleration can be defined as:

$$\ddot{\boldsymbol{q}}_{wrist}^{ref} = -\ddot{\boldsymbol{q}}_{ref}^{total} + \boldsymbol{K}_p(\boldsymbol{q}^{cmd} - \boldsymbol{q}_{ref}^{total} - \boldsymbol{q}_{resp}^{wrist}) + \boldsymbol{K}_d(\dot{\boldsymbol{q}}^{cmd} - \dot{\boldsymbol{q}}_{ref}^{total} - \dot{\boldsymbol{q}}_{resp}^{wrist}) \tag{3.20}$$

where $\boldsymbol{q}_{resp}^{wrist} = [q_{resp}^4, q_{resp}^5, q_{resp}^6]^T$ is the angular response of the wrist joints and $\dot{\boldsymbol{q}}_{resp}^{wrist} = [\dot{q}_{resp}^4, \dot{q}_{resp}^5, \dot{q}_{resp}^6]^T$ is angular velocity response of the wrist joints. They can be obtained from Adams. The reference torque for wrist joints can be defined as,

$$\boldsymbol{\tau}_{wrist}^{ref} = \boldsymbol{I}_{wrist}\ddot{\boldsymbol{q}}_{wrist}^{ref} \tag{3.21}$$

where $\boldsymbol{\tau}_{wrist}^{ref} = [\tau_4^{ref}, \tau_5^{ref}, \tau_6^{ref}]$. $\boldsymbol{K}_p$ and $\boldsymbol{K}_d$ are the PD gain matrices respectively, and $\boldsymbol{I}_{wrist}$ is the wrist inertia matrix.

3.3.5 Radar based orientation

Based on radar measurements (here $D_{radar_i} \equiv r_i$ for clarity), the absolute rotations between the tool and the wall, shown in Figure 3.6 can be calculated as ,

$$\begin{cases} \theta_y &= sign(r_3 - r_2)(\frac{\pi}{2} - \gamma) \\ \theta_z &= sign(r_1 - r_2)(\frac{\pi}{2} - \alpha) \end{cases} \tag{3.22}$$

With

$$\gamma = \begin{cases} tan^{-1}(\frac{d_{r_2r_3}}{r_2 - r_3}) & \text{if } r_3 \leq r_2 \\ tan^{-1}(\frac{d_{r_2r_3}}{r_3 - r_2}) & \text{if } r_3 > r_2 \end{cases}$$

$$\alpha = \begin{cases} tan^{-1}(\frac{d_{r_1r_2}}{r_2 - r_1}) & \text{if } r_1 \leq r_2 \\ tan^{-1}(\frac{d_{r_1r_2}}{r_1 - r_2}) & \text{if } r_1 > r_2 \end{cases}$$

and r_1, r_2 and r_3 are the radar measurements respectively, and $d_{r_ir_j}$ is the distance between radars i and j (refer to Figure 3.6).

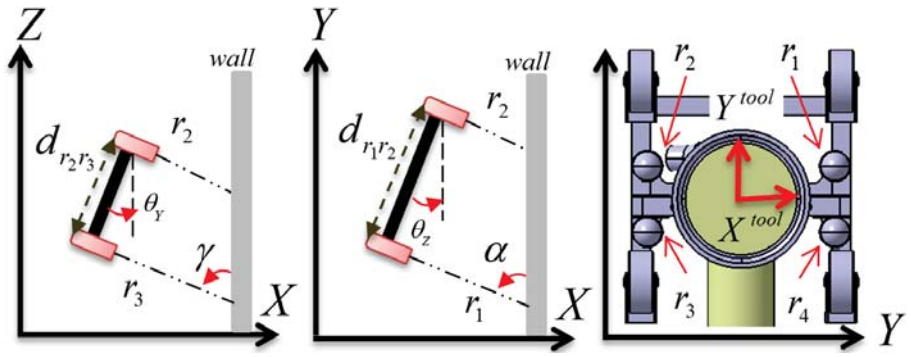

Figure 3.6: Tool absolute orientation

3.3.6 Disturbance grinding torque for simulation

In order to test the control response, and simulate it against noises and impacts of the grinding process, a disturbance torque is added to force readings. In simulation, the disc is assumed lying in the plane of wall. The reaction torque is generated proportional to the feeding velocity of the disc on the wall V_{feed}. Additionally, random impacts δ and limited noise n have been included in the noise function N to represent a real case scenario. Hence the reaction torque generated for grinding process can be simplified as,

$$\tau_{disc}^{reac} \propto \left(|V_{feed}| + N(n, \delta)\right) \tag{3.23}$$

3.3.7 Adams-Matlab/Simulink co-simulation

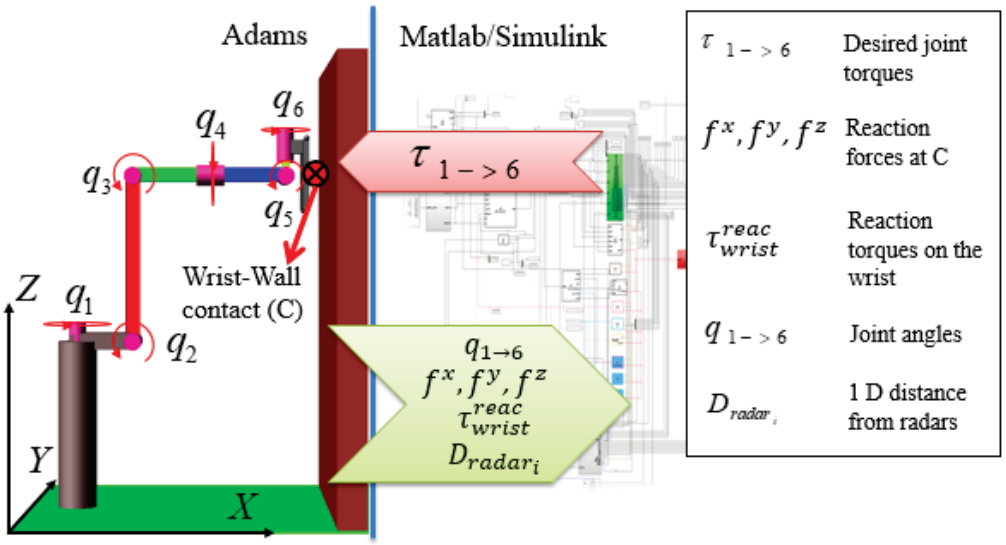

Figure 3.7: Adams-Matlab co-simulation

The control framework in this section is implemented for a 6-R robot using Adams-Matlab co-simulation as Figure 3.7 shows. The system is simulated with a trapezoidal trajectory generator that provides continuous acceleration in the variable velocity phases and constant speed otherwise. The robot is commanded to apply a force of 90 N on the desired path on the wall. It starts from free space and goes into the wall by a smooth transition from position to force control avoiding impact and maintaining the desired force. The admittance controller ensures centering the force and adapting to the wall.

3.3.7.1 Hybrid force-position control behavior

The command-response of trajectory position and velocity are shown in Figures 3.8 and 3.10 respectively. The controller shows good performance in free space and after contact, limiting the position errors to 0 mm before and 5 mm after contact at $t = 1.4$ s as shown in Figure 3.9. This variation in position errors is due to the 0.4 N dynamic friction force between the tool and wall, that is defined in Adams. Consequently the velocity errors are between 0.035 m/s and -0.05 m/s after impact and are shown in Figure 3.11.

Concerning the force control performance, the force desired versus response values are plotted in Figure 3.12. The control with smooth transition in Figure 3.12b shows negligible impact force when touching the wall. Then the desired force reference value is reached in a behavior similar to a step function. The force value is maintained along the path with an error less than 2 N as shown in Figure 3.13b. The smooth transition control shows better values compared to the ones obtained by direct switching in Figure 3.12a, where the impact is clearly high and the force error can exceed 100 N as shown in 3.13a. Thanks to the smooth transition control presented in Section 3.3.3 that flips smoothly from position into force control in a unified manner that avoids switching as Figure 3.14 shows.

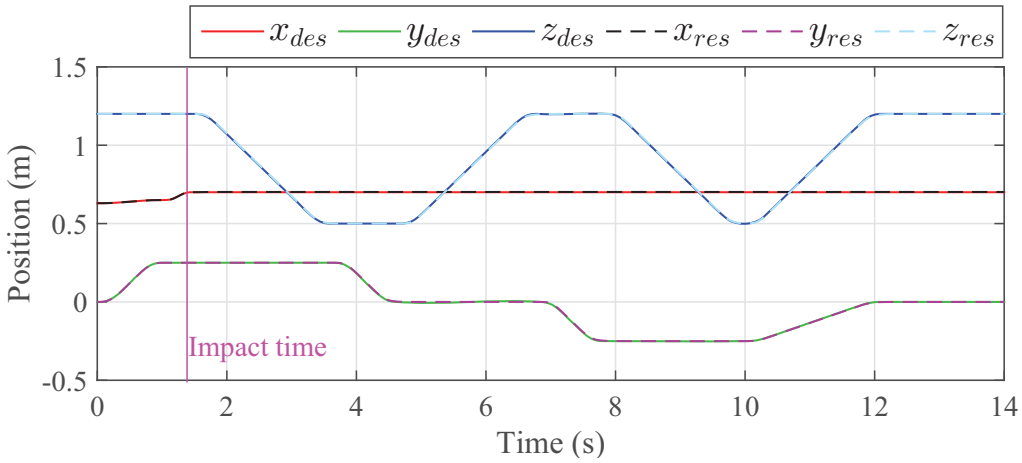

Figure 3.8: Position desired and response values in Adams-Matlab co-simulation

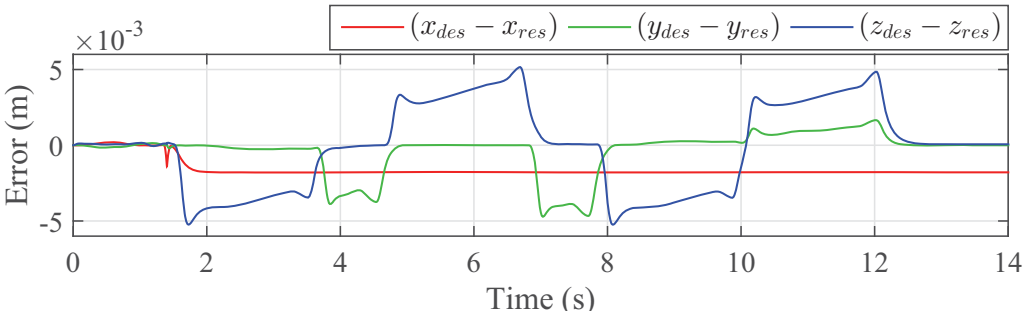

Figure 3.9: Position errors in Adams-Matlab co-simulation

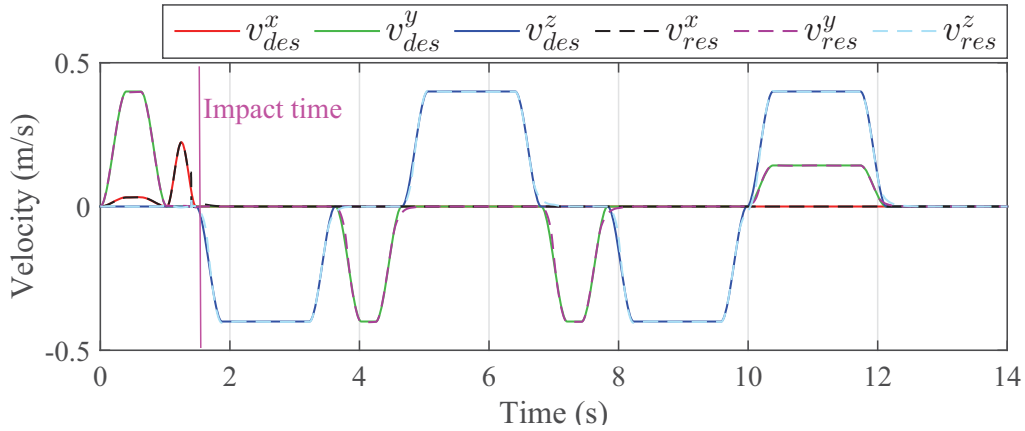

Figure 3.10: Velocity desired and response values in Adams-Matlab co-simulation

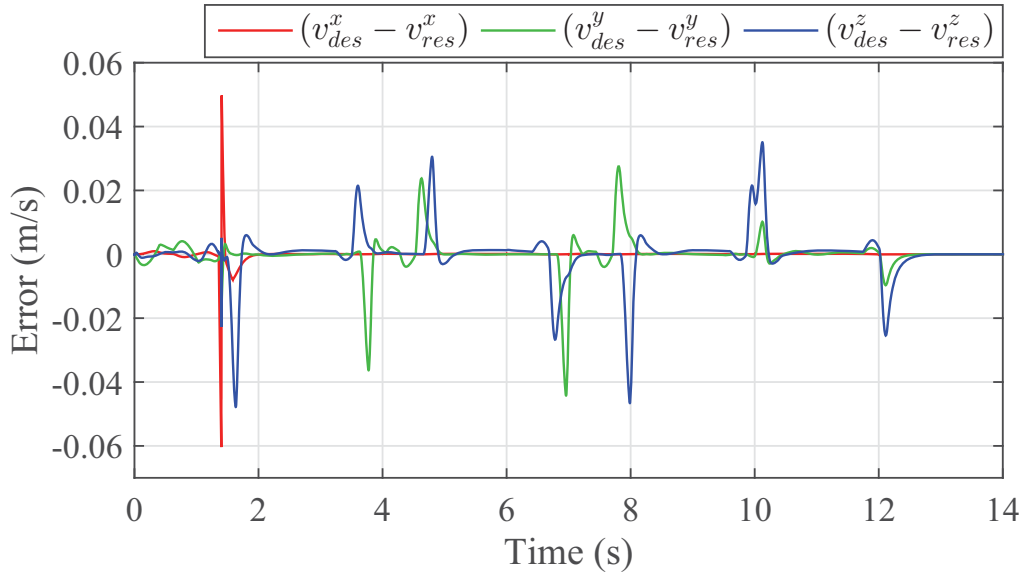

Figure 3.11: Velocity errors in Adams-Matlab co-simulation

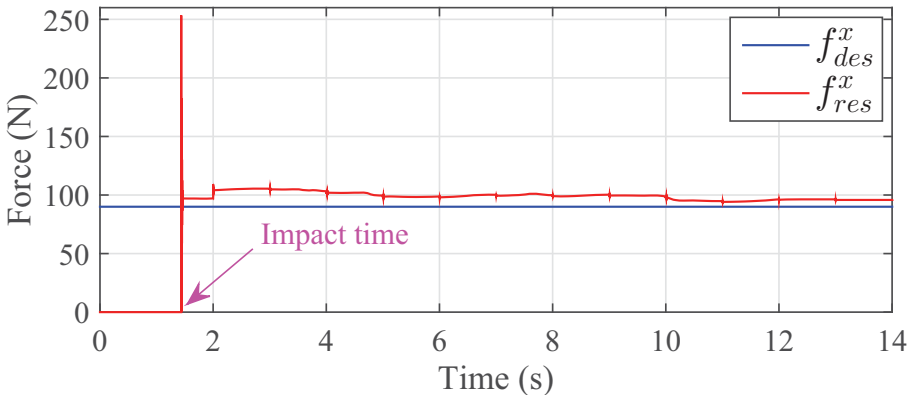

(a) Force desired and response value without smooth transition

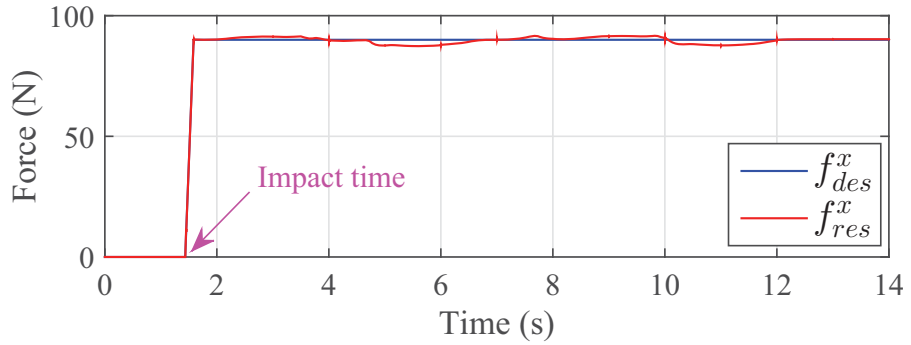

(b) Force desired and response value with smooth transition

Figure 3.12: The desired and response values of normal force on the wall in Adams-Matlab co-simulation

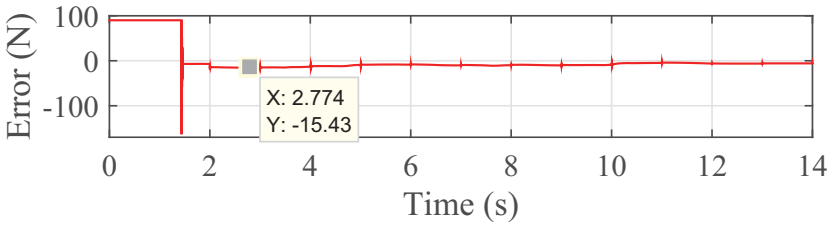

(a) Force command-response error without smooth transition

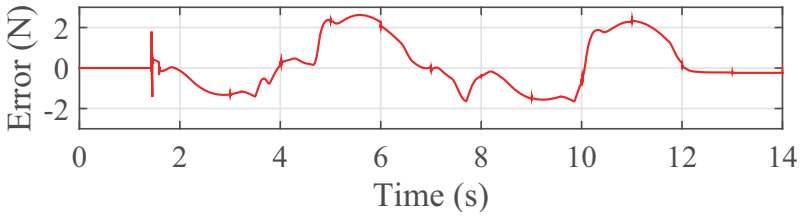

(b) Force desired-response error with smooth transition

Figure 3.13: Normal force desired-response errors in Adams-Matlab co-simulation

3.3.7.2 Admittance control behavior

As described in Section 3.3.4, the wrist motors are based on acceleration control (eq. 3.20) in addition to the torque sensor to measure the reaction torques $\boldsymbol{\tau}_{wrist}^{reac}$. The controller gains $\boldsymbol{M}_i$, $\boldsymbol{D}_i$ and $\boldsymbol{K}_i$ are tuned for 2^{nd} order differential equation to ensure stability and equivalent distribution of contact forces on the end-effector (eqs. 3.18 & 3.19). $\boldsymbol{K}_p$ and $\boldsymbol{K}_d$ are proportional and derivative gains tuned for good tracking of the reference values generated from commands and external torques (eqs. 3.17 & 3.20) as shown in Figure 3.18, where the joint positions are modified based on external torques. The effectiveness of the admittance controller in adapting the tool to the wall, can be deduced from the fact of keeping minimal torques on 5^{th} and 6^{th} joints, that are responsible for the pitch and yaw of the tool as Figure 3.15 shows. Figure 3.16 shows how the controller maintains the force centered as the zero-moment-point of the tool-wall contact gets about the center of the tool (except for the first contact) overcoming the feeding force.

Adding external torque to the disc with some impacts, mainly results on the 4^{th} joint because of the mechanical linkage of the wrist that is similar to a universal joint that couples rotation between two drive-line shafts: the base shaft (axle of the disc) and the follower shaft (joint 4). The results are shown in Figure 3.17 where τ_4 in 3.17a shows the behavior of joint 4 without external torque. However, when the end effector is subjected to external torque as in 3.17b, τ_4 acts as shock absorber and it can suppress noise and impacts of the disc as 3.17c shows, thus avoiding high impacts on the joint.

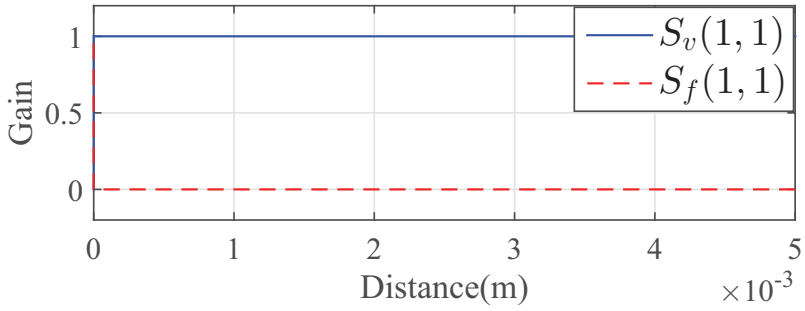

(a) Gains for direct switching from position to force control

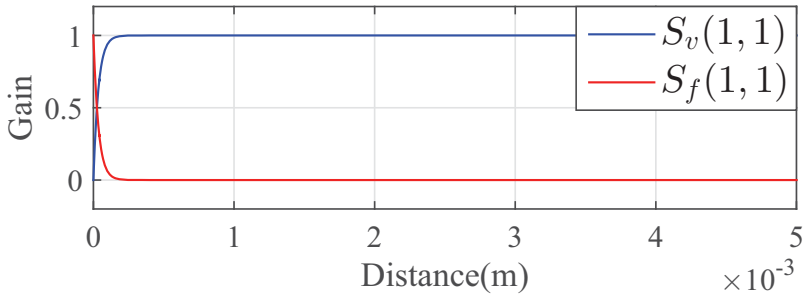

(b) Gains for smooth transition from position to force control

Figure 3.14: Smooth switching from position to force control in Adams-Matlab co-simulation. (1,1) is the index to the first element of the selection matrix

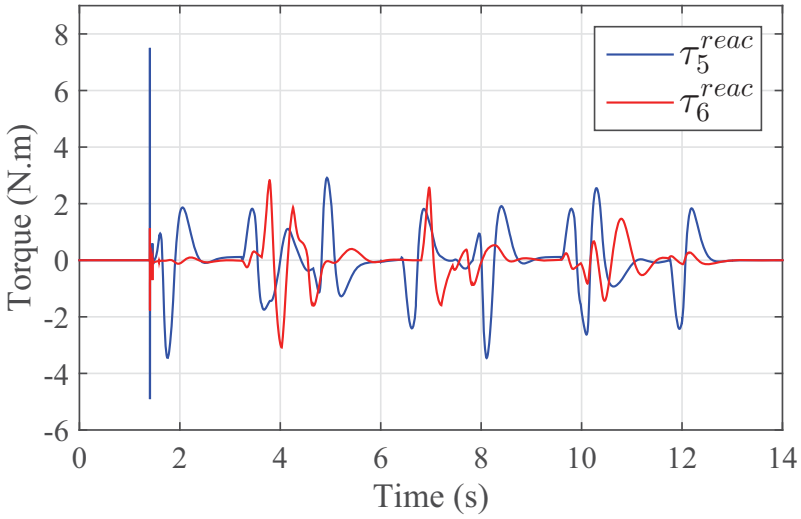

Figure 3.15: The reaction torques on 5th and 6th joints from Adams-Matlab co-simulation

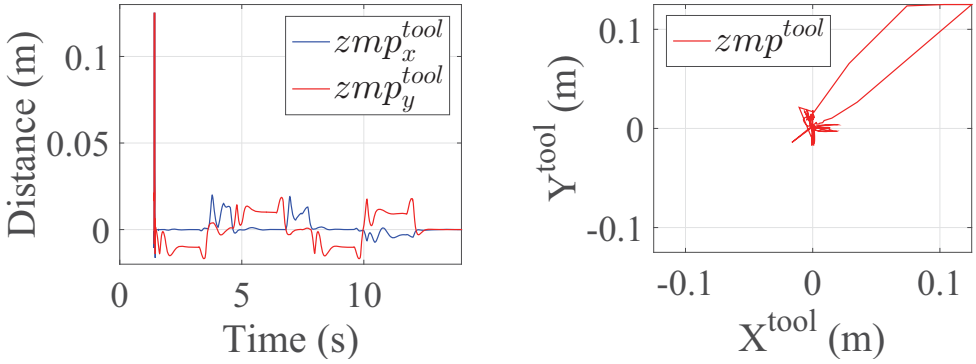

(a) Zmp coordinates

(b) Zmp trajectory

Figure 3.16: Zero-moment-point on the end-effector in Adams-Matlab co-simulation expressed in the tool frame shown in Figure 3.6

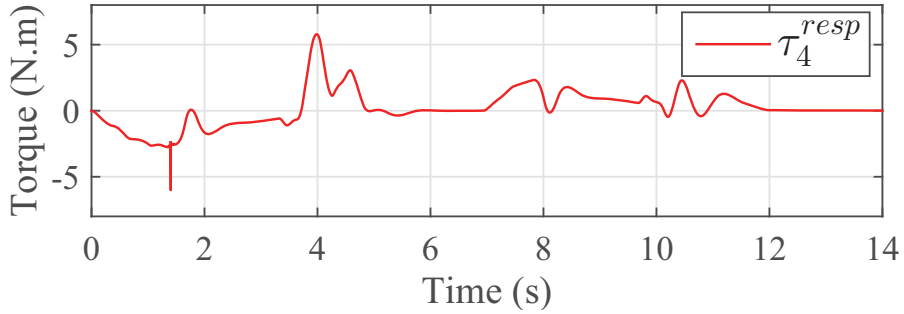

(a) Response of τ_4 without the disc reaction torque

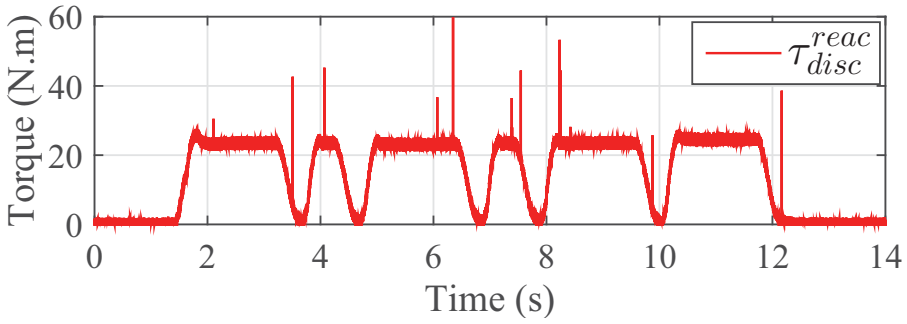

(b) Disc reaction torque plus noise and random impacts

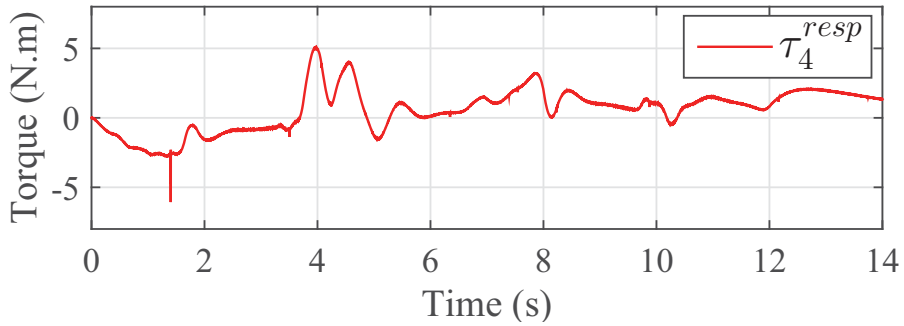

(c) Response of τ_4 with the disc reaction torque added

Figure 3.17: Suppressing the disc noise and random impacts by impedance control in Adams-Matlab co-simulation

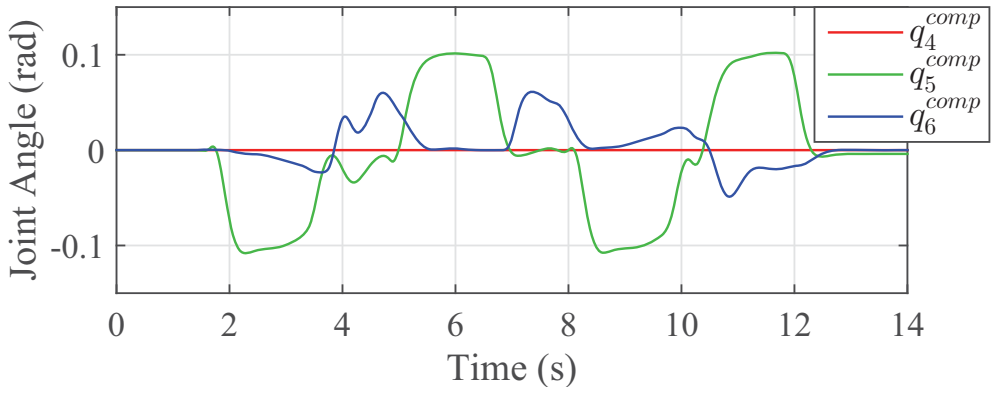

Figure 3.18: Position compensation by admittance control in Adams-Matlab co-simulation

3.3.8 Experiments

The idea is to exert constant normal force on the wall surface while moving along the desired grinding trajectory. The experimental setup consists of a six-axes ATI Gamma[1] force-toque sensor, a KUKA seven-dof light weight robotic arm, a camera, a grinding tool supported with 4 Castor wheels and a piece of wall covered with resurfacing concrete. The experimental setup can be seen in details in Figure 3.19.

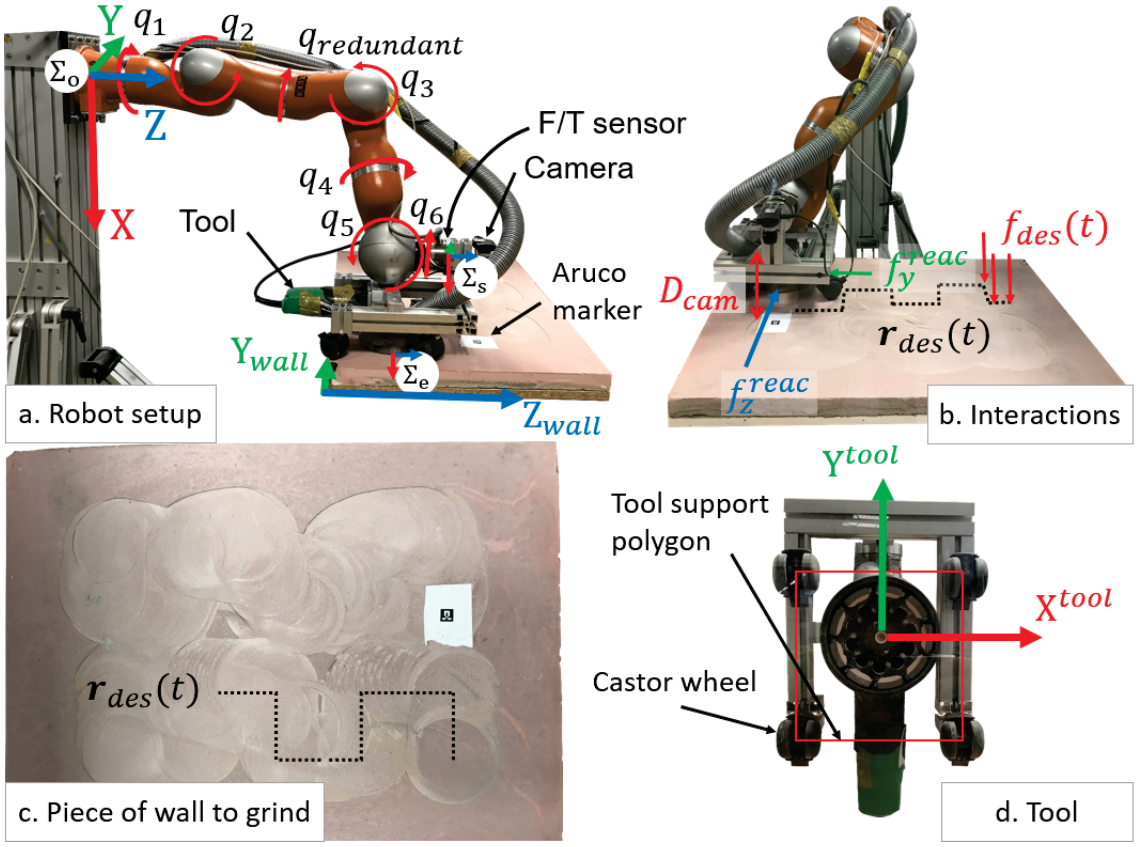

Figure 3.19: The robotic system equipped with a grinding tool, camera for distance measurement, and a force/torque sensor to perform grinding on a piece of wall

To implement the dynamic motion and force control presented in Section 3.3 on the KUKA, its joint impedance controller can be written as,

$$\boldsymbol{\tau}_{cmd} = \boldsymbol{k}_{vs}(\boldsymbol{q}_{FRI} - \boldsymbol{q}_{msr}) + D(\boldsymbol{d}_{vs}) + \boldsymbol{\tau}_{FRI} + \boldsymbol{\tau}_{dynamics} + \boldsymbol{\tau}_{dis} \tag{3.24}$$

where $\boldsymbol{\tau}_{cmd}$ is the final commanded torque to the robot joints, $\boldsymbol{\tau}_{dis}$ is disturbance torque at each joint, it is compensated using the disturbance observer explained in Section 2.2. $\boldsymbol{k}_{vs}$ is the proportional gain of the joint level virtual spring, $\boldsymbol{q}_{FRI}$ is the desired joint value to be sent to the Fast Research Interface (FRI) that manages the communication between KUKA controller and the ordinary PC sending the desired commands, $\boldsymbol{q}_{msr}$ is the joint angular response measured by the encoder, $\boldsymbol{d}_{vs}$ is the joint damping gain and $\boldsymbol{\tau}_{dynamics}$ is the torque vector compensating the gravity, friction and Coriolis forces. $\boldsymbol{\tau}_{FRI}$ is the FRI torque input to each joint. Hence, in order to use KUKA joint impedance controller in torque mode, the gains $\boldsymbol{k}_{vs}$ and $\boldsymbol{d}_{vs}$ are set to 0 for joints: 1, 2 and 3. For the impedance

[1] http://www.ati-ia.com/products/ft/ft_models.aspx?id=Gamma

control of joints: 4, 5 and 6, $\tau_{FRI}^{4,5,6}$ is set to 0. The redundant joint $q_{redundant}$ of KUKA is fixed at the same position in this experiment. The wrench ${}^{s}\boldsymbol{W}_{res}$ measured at the sensor frame is transformed to the end-effector frame shown in Figure 3.19 as,

$$ {}^{e}\boldsymbol{W}_{res} = \begin{bmatrix} {}^{e}\boldsymbol{F}_{res} \\ {}^{e}\boldsymbol{\Gamma}_{res} \end{bmatrix} = {}^{e}\boldsymbol{Ad}_{s}\ {}^{s}\boldsymbol{W}_{res} \tag{3.25} $$

with ${}^{e}\boldsymbol{F}_{res}$ and ${}^{e}\boldsymbol{\Gamma}_{res}$ are the force and torque vectors in the end-effector frame respectively. ${}^{e}\boldsymbol{Ad}_{s}$ is the adjoint transformation matrix that rotates the force and torque vectors from the force-torque sensor frame $\{s\}$ into the end-effector frame $\{e\}$ as,

$$ {}^{e}\boldsymbol{Ad}_{s} = \begin{bmatrix} {}^{e}\boldsymbol{R}_{s} & \boldsymbol{0} \\ -{}^{e}\boldsymbol{R}_{s}\hat{\boldsymbol{p}}_{se} & {}^{e}\boldsymbol{R}_{s} \end{bmatrix} \tag{3.26} $$

It includes an additional torque of the form $-\boldsymbol{p}_{se} \times {}^{s}\boldsymbol{F}$, which is the torque generated by applying a force ${}^{s}\boldsymbol{F}$ at a distance $-\boldsymbol{p}_{se}$. ${}^{e}\boldsymbol{R}_{s}$ is the rotation matrix between the frames $\{s\}$ and $\{e\}$. Similarly, in order to have the end-effector forces expressed in the world frame, the wrench ${}^{e}\boldsymbol{W}_{res}$ is projected to the operational space frame as,

$$ {}^{o}\boldsymbol{W}_{res} = \begin{bmatrix} \boldsymbol{F}_{res} \\ \boldsymbol{\Gamma}_{res} \end{bmatrix} = {}^{o}\boldsymbol{Ad}_{e}\ {}^{e}\boldsymbol{W}_{res} \tag{3.27} $$

with,

$$ {}^{o}\boldsymbol{Ad}_{e} = \begin{bmatrix} {}^{o}\boldsymbol{R}_{e} & \boldsymbol{0} \\ \boldsymbol{0} & {}^{o}\boldsymbol{R}_{e} \end{bmatrix} \tag{3.28} $$

The control block diagram adapted for KUKA is shown in Figure 3.20. The control framework is implemented using Robot Operating System (ROS) that communicates

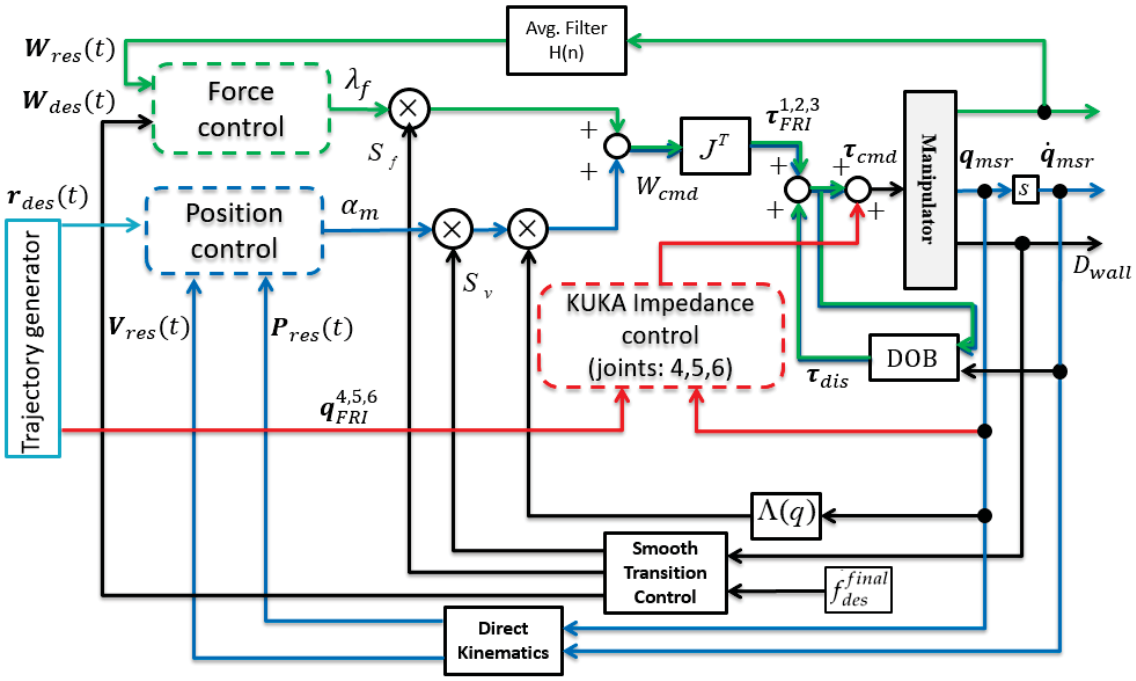

Figure 3.20: Hybrid controller block diagram in Figure 3.4 adapted for KUKA LWR tests: force control loop (green), position control loop (blue), KUKA impedance control loop (red)

with the KUKA FRI, the force sensor publishes data at a rate of 1000 Hz, the ROS control update loop and the trajectory node are updated at 500 Hz. The desired robot path is generated by a trapezoidal trajectory generator that provides continuous acceleration in the variable velocity phases and constant speed otherwise. The spindle runs with 11000 rpm, it rotates a disc with abrasive grains of 125 mm diameter. The robot is commanded to apply a force of 80 N on the desired path on the wall. The max velocity for the path was set to 0.015 m/s and the max acceleration was 0.1 m/s^2. The robot starts from free space and goes into the wall by a smooth transition from position to force control using the distance $D_{wall} = D_{cam} - d$ between the tool and the wall. d is the offset between the camera and the tool. D_{cam} is obtained using a camera that detects a special pattern marker (Aruco marker) fixed on the wall with a precision of 1 mm, thus avoiding impact and maintaining the desired force. The impedance based orientation controller tries centering the force on the tool and adapting its orientation to the wall. The controller gains used in the experiment are shown in Table 3.1.

Table 3.1: Controller gains used in the experiments

Gain	$\boldsymbol{K}_{PF}(i,i)$ $i=1$	$\boldsymbol{K}_{Pr}(i,i)$ $i=2,3$	$\boldsymbol{K}_{Dr}(i,i)$ $i=2,3$	k_{vsi} (N.m/rad) $i=4,5,6$	d_{vsi} (N.m/rad) $i=4,5,6$
Value	1.2	1000	60	10	1

The desired and response values of tool trajectory position and velocity are shown in Figure 3.21 and Figure 3.22 respectively. The controller shows good performance in free space and after contact, the position error along the X direction is around 2 mm at maximum, and relatively small compared to Y and Z directions where the errors reach 7.2 mm and 9.1 mm respectively as shown in Figure 3.23, this is due to the insufficient force capacity of the arm. This variation in position errors is due to the reaction forces on the tool (Figure 3.19b and Figure 3.24). For the force control, since the sensor data needed for the feedback is very noisy because of the vibrations (Figure 3.24), a moving average filter $H(n) = \sum_1^n f(n)/n$ with $n = 200$ samples is used for smoothing; hence, $f_{res}^x = H(n)$. The force desired versus response values are plotted in Figure 3.25. The control with smooth transition shows negligible impact force when touching the wall, this is due to the transition control presented in Section 3.3.3 that flips smoothly from position into force control in a unified manner that avoids switching as Figure 3.27 shows. The desired force reference value is reached in a behavior similar to a step function. The force value is maintained along the path with an error less than 10 N as shown in Figure 3.26.

The efficiency of the impedance controller in adapting the tool to the wall can be deduced from the fact of keeping the pressure centered inside the tool support polygon shown in Figure 3.19d. Figure 3.28 shows how the controller tries to maintain the force inside the tool frame as the zero-moment-point of the tool-wall contact is inside the frame of the tool. There are some exceptions where the zero-moment-point goes out of the support polygon, the first exception corresponds to the first contact, then the others are along where the controller tries to overcome the relatively high feeding force (around t = 80 and 100 seconds in Figure 3.28a).

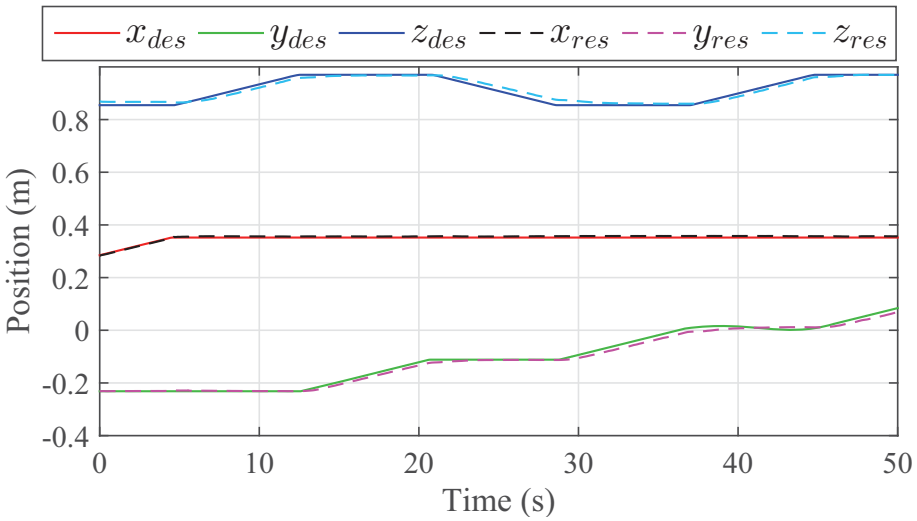

Figure 3.21: Position desired versus response values

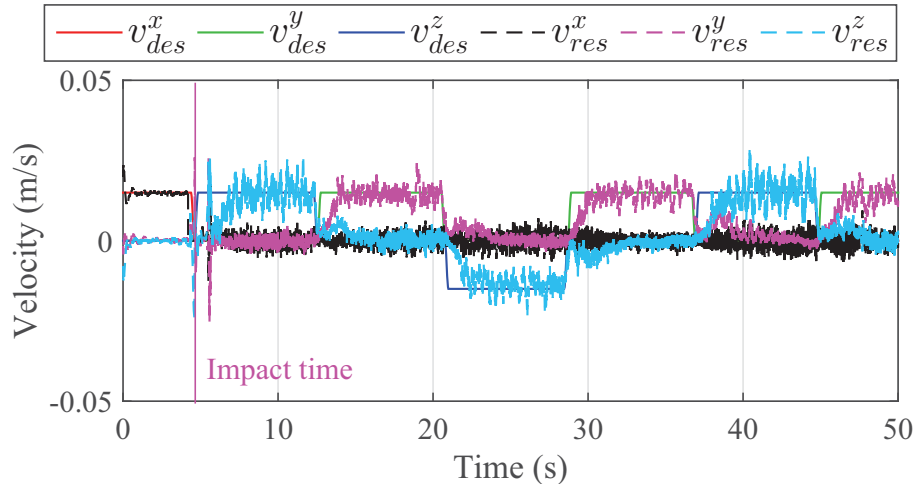

Figure 3.22: Velocity desired versus response values

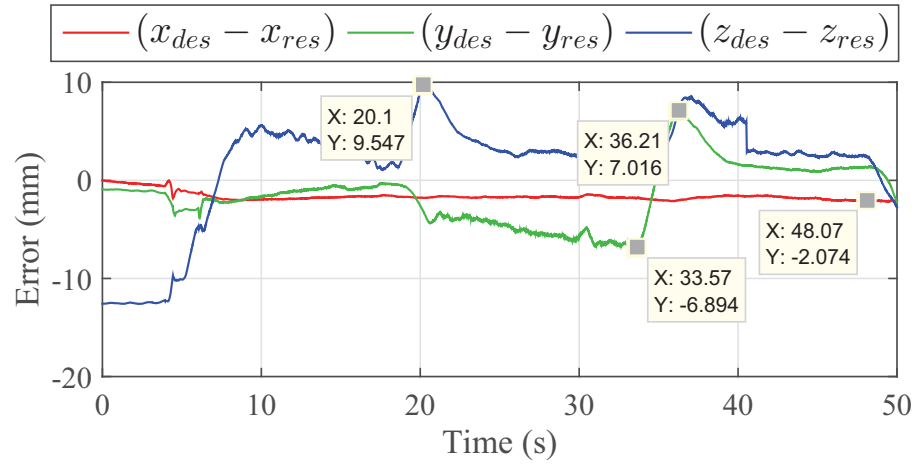

Figure 3.23: Position desired-response errors

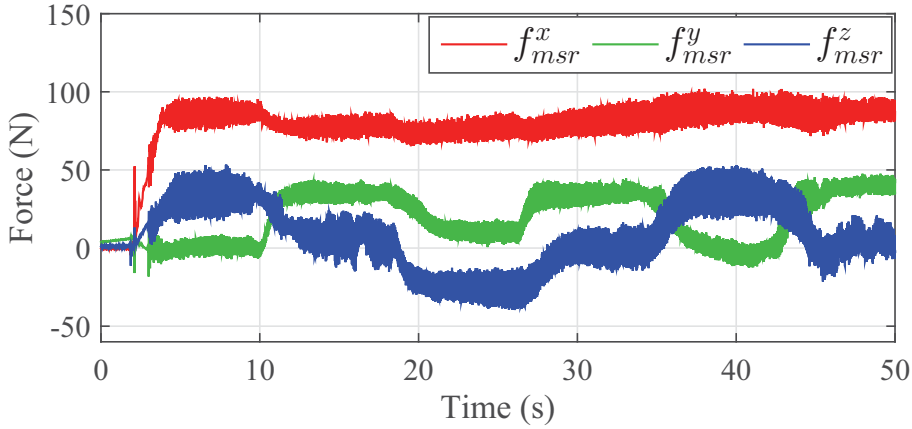

Figure 3.24: Raw reaction forces on the tool while grinding

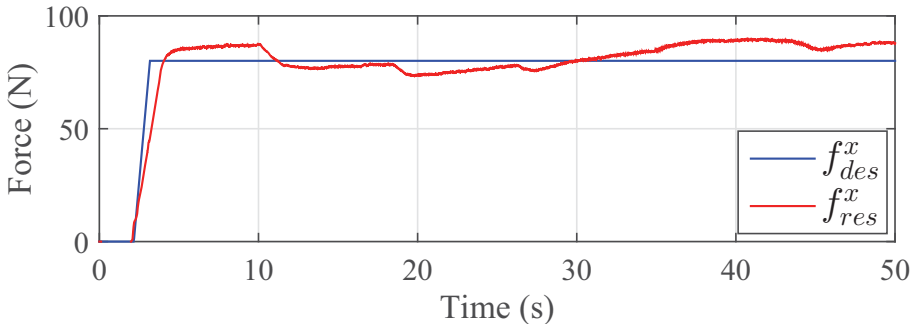

Figure 3.25: The desired and response value of normal force on the wall

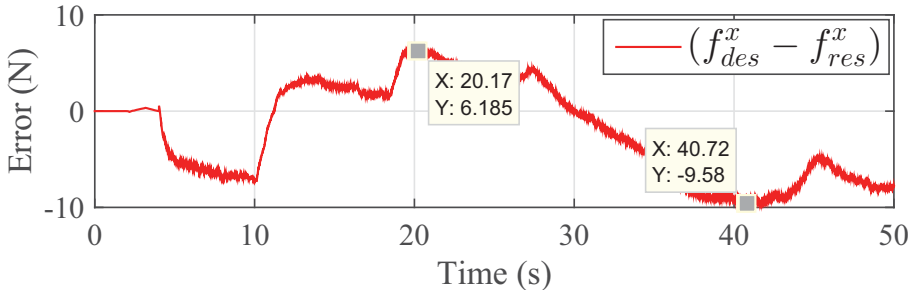

Figure 3.26: Normal force error

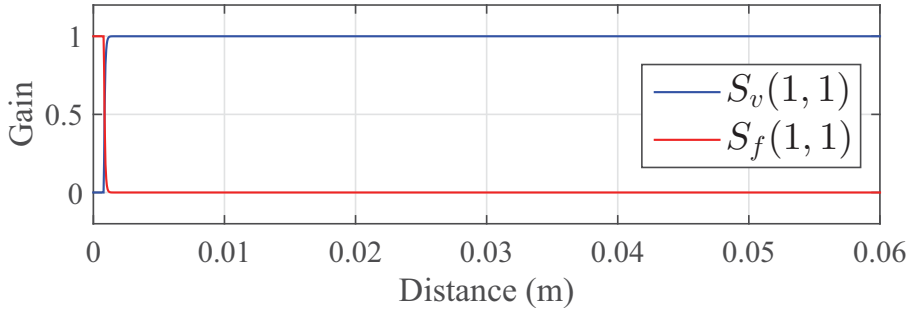

Figure 3.27: Smooth switching from position to force control. $(1,1)$ is the index to the first element of the selection matrix

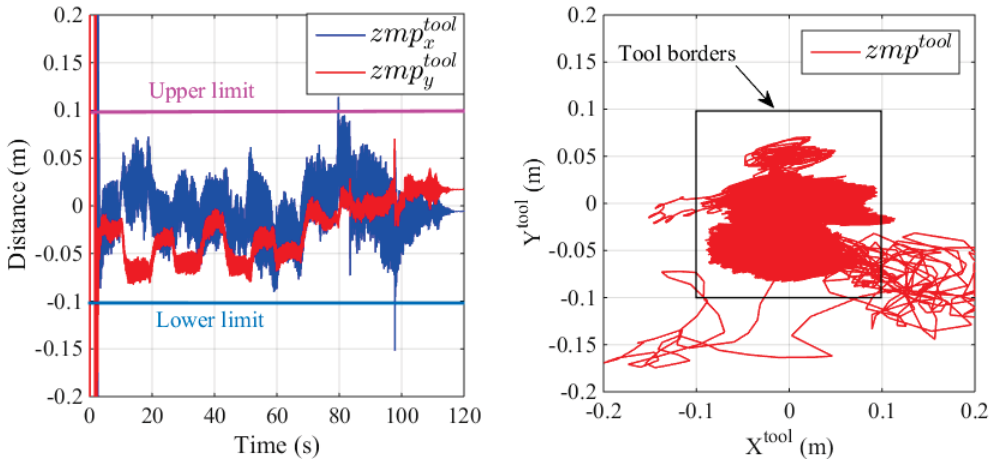

(a) Zmp coordinates (b) Zmp trajectory

Figure 3.28: Zero-moment-point on the end-effector expressed in the tool frame shown in Figure 3.19d

3.3.9 Conclusion

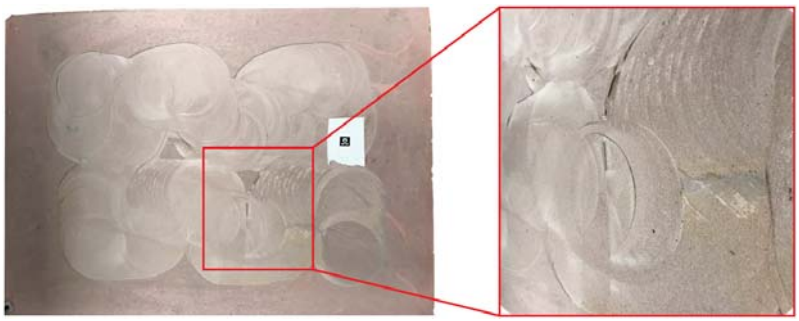

Figure 3.29: Grinding quality obtained from the position-force controller with compliant wrist

Section 3.3 presented a smooth position-force hybrid controller for grinding. The control is validated by simulations on a 6-dof anthropomorphic arm based on 1D-distance measurement radars and admittance control for tracking the surface, it maintains a desired force centered on the disc and normal to the surface. The switching problem is overcome by proposing a smooth transition control. The controller changes smoothly between free space and contact modes, thus reducing impact force. The simulation results showed good position and force tracking performances and impact force close to zero. Moreover, the concept of the controller is tested on KUKA LWR using camera and force-torque sensor. The results of position and force tracking performances are acceptable and the impact force was small. Nevertheless, the feeding force has an important effect on the controller as there is large offset between the disc center and the wrist center which generates large tilting wrenches. Additionally, as Figure 3.19d shows, the controller is dependent on the wheels around the tool, in case of irregular surface some of them will not touch it. Also, the cutting parameters (feeding velocity, grinding force) was not estimated accurately, hence leading to inaccurate results. The grinding quality of this controller is satisfactory as Figure 3.29 shows. These shortcomings will be the focus of the new controller presented in the next section, where the grinding model

will be identified and included in the controller, and the wheels around the tool will be removed. In addition to that, the controller will be unified, i.e. the arm and the wrist are commanded as one unit.

3.4 Model Based Adaptive Hybrid Velocity-Position-Force Controller for Wall Grinding

As discussed in the previous section, the grinding task requires the robot to apply a specific normal force on the wall surface while simultaneously performing a compliant motion keeping the disc of the grinding tool tangentially in contact with the wall. This section presents the development and implementation of a unified control strategy that overcomes the shortcomings of the previous controller and achieves better grinding quality. The controller employs the hybrid velocity-force control strategy expressed in a desired frame in the end-effector. Addition to that, the proposed controller makes the disc of the grinding tool adapt to the curvity change of the wall surface and corrects the desired directions of force and velocity in real-time. The desired force and velocity directions are decided based on the contact force and a developed grinding model that estimates the nominal feeding grinding forces. Moreover, the controller includes compensation module that eliminates the non-contact forces (force due to gravity, inertia and Coriolis effects) from the force-torque sensor. The tool path is generated on-line so that it passes through previously decided way-points, i.e. the robot will move in a desired velocity toward the next way-point until it reaches its position in the plane parallel to the motion one (ex: if x and y are the velocity controlled directions, then only the x and y positions of the way-point are used). The controller is tested on the KUKA LWR 7-dof robotic arm programmed to grind different planar and curved walls with unknown geometry. The KUKA arm is equipped with a six-axes ATI Gamma[2] force-torque sensor and a grinding tool to perform on a piece of wall covered with resurfacing concrete. The setup is similar to the one used in Section 3.3, however there is no wheels supporting the tool, the setup is shown in Figure 3.30. The control scheme is explained in the following subsections:

3.4.1 Hybrid velocity-force control in the compliant frame

Recalling the operational space formulation in equation 3.1, the robot dynamics as seen at the end-effector can be rewritten as,

$$\boldsymbol{W}_{cmd} = \boldsymbol{\Lambda}(\boldsymbol{q})\boldsymbol{\alpha}_m + \boldsymbol{\lambda}_f + \boldsymbol{\mu}(\boldsymbol{q}, \dot{\boldsymbol{q}}) \tag{3.29}$$

Here $\boldsymbol{W}_{cmd} \in \mathbb{R}^n$ $(n = 6)$ denotes the output wrench of the end-effector in operational space; $\boldsymbol{\alpha}_m$ and $\boldsymbol{\lambda}_f$ are the acceleration and force commands respectively, they are calculated based on velocity and force errors in the compliant frames $\{\text{cv}\}$ and $\{\text{cf}\}$ respectively. Then the joint torques $\boldsymbol{\tau}$ can be calculated by:

$$\boldsymbol{\tau} = \boldsymbol{J}^T \boldsymbol{W}_{cmd} + \boldsymbol{\tau}_{dis} \tag{3.30}$$

$\boldsymbol{\tau}_{dis}$ is the disturbance torque, it can be compensated using the DOB presented in chapter 2.

Choice of the compliant frames:

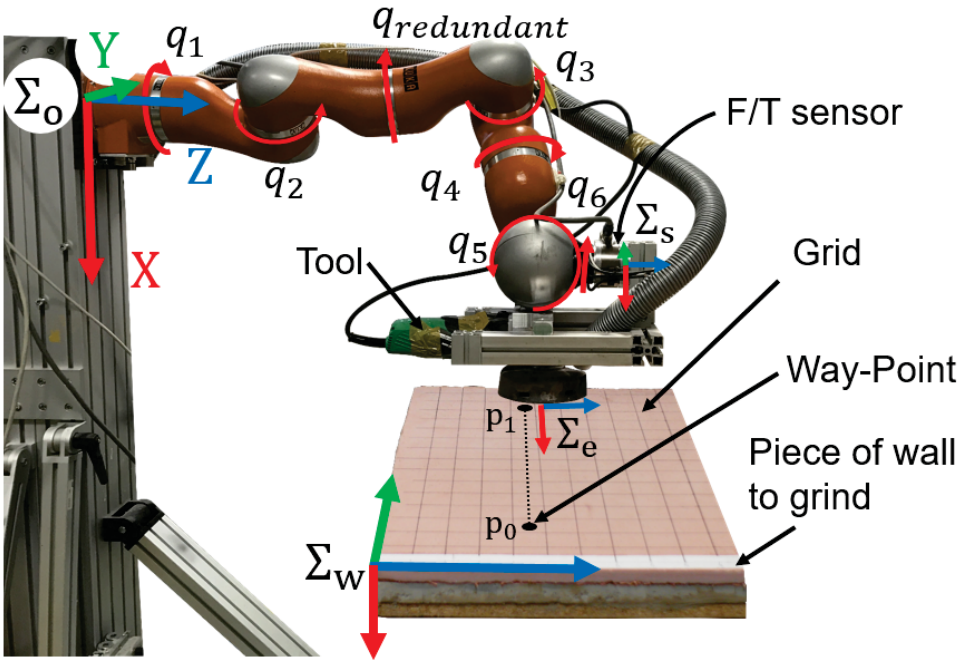

Figure 3.30: The robotic system equipped with grinding tool and force/torque sensor to perform grinding on a piece of wall. The grid is to evaluate the wall before and after grinding

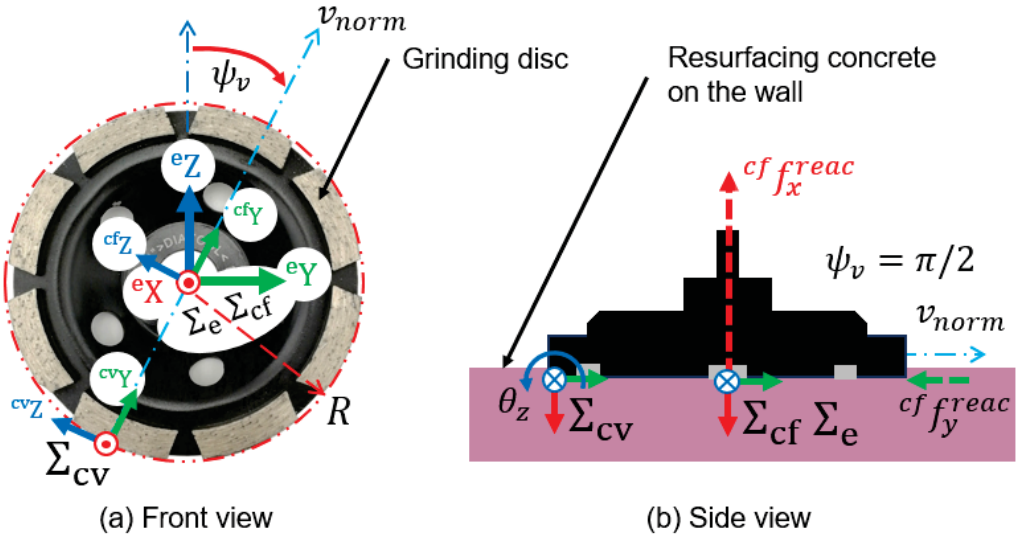

Figure 3.31: The choice of the frames for simultaneous force and motion control

The choice of the velocity and force control frames in the grinding controller implemented here is crucial. The chosen frame for force control is {cf} on the center of the disc, it coincides with the end-effector frame origin {e} and it is rotated by $\frac{\pi}{2} - \phi_v$ around ${}^{e}X$, while the control frame for velocity and motion control is {cv} fixed at an offset $-R$ along the z direction of {cf}. The frames are depicted on the disc in Figure 3.31. ϕ_v can be calculated from the z and y components of the velocity normal to the disc ${}^{e}v_{norm}$ as,

$$\phi_v = \frac{\pi}{2} - tan^{-1}\left(\frac{{}^{e}_{z}v_{norm}}{{}^{e}_{y}v_{norm}}\right) \tag{3.31}$$

There are several reasons why these frames are chosen like this. The force control frame must be fixed to the center of the grinding disc to have good measurements of the feeding force acting on the disc, and good force control of the normal force at the wall along the direction ${}^{cf}\vec{x}$, hence there is no velocity control along this direction while the disc is in contact with the wall. This released direction allows the robot to move along the surface of the wall while maintaining the axis of force control normal to the surface. Hence, a desired force can be controlled between the disc and the wall along this direction.

Velocity control is applied in the frame {cv} along the remaining linear directions, namely ${}^{cv}\vec{y}$ and ${}^{cv}\vec{z}$. Hence, position control is applied in the same frame to the remaining axes which are not controlled in force or velocity: the three orientations around ${}^{cv}\vec{x}$, ${}^{cv}\vec{y}$ and ${}^{cv}\vec{z}$. The reason why {cv} is chosen as in Figure 3.31, is that the proposed controller needs to adapt automatically to the surface based on a special orientation controller that will be explained in the next sections. Hence, if the disc is moving along the wall with velocity v_{norm} along ${}^{cv}\vec{y}$ and it needs to orient, applying rotation θ_z around ${}^{cv}\vec{z}$ will generate no reaction force along ${}^{cv}\vec{x}$ which is natural and important for the grinding quality. However, if {cv} was chosen to coincide with {cf}, applying the rotation θ_z around ${}^{cv}\vec{z}$ will generate reaction force along ${}^{cv}\vec{x}$ and the wall can be damaged.

3.4.2 Modeling of the feeding grinding force

The key idea of this controller is to adapt the orientation of the disc to the wall surface based on keeping the feeding reaction force ${}^{cf}f^{feed}$ around a desired value that should be appropriate for grinding. However, for the case of wall grinding in the construction industry, there have been no published models that identify the nominal grinding feeding force f^{feed}_{nom}. Moreover, the desired normal grinding force ${}^{cf}f^{reac}$ and the translational velocity of the disc on the wall ${}^{cv}v_{norm}$ are not known as well.

Hence, in order to explore the relation between ${}^{cf}f^{reac}_{x}$, ${}^{cv}v_{norm}$ and the nominal grinding feeding force f^{feed}_{nom} , it is necessary to firstly have an idea about the values of ${}^{cf}f^{reac}$ and ${}^{cv}v_{norm}$ that should be used as input desired values for the controller. Thus, assisted manual grinding tests are carried out with the experimental setup shown in Figure 3.32. These tests were done by setting the robot controller to Cartesian impedance mode, this mode allows to constraint the motion in some directions and release it for others. The wall used for the data collection is assumed planar and its frame {w} is set parallel to the frame {o}. To this end, the robot is set to move freely by hand along the ${}^{o}\vec{x}$ and ${}^{o}\vec{y}$ directions while the direction along ${}^{o}\vec{z}$ is locked. The three orientations around ${}^{e}\vec{x}$, ${}^{e}\vec{y}$ and ${}^{e}\vec{z}$ are fixed such that the frame {e} is parallel to {w} in order to keep the disc parallel to the wall. Then, the operator performed three grinding tests by moving the wrist

[2] http://www.ati-ia.com/products/ft/ft_models.aspx?id=Gamma

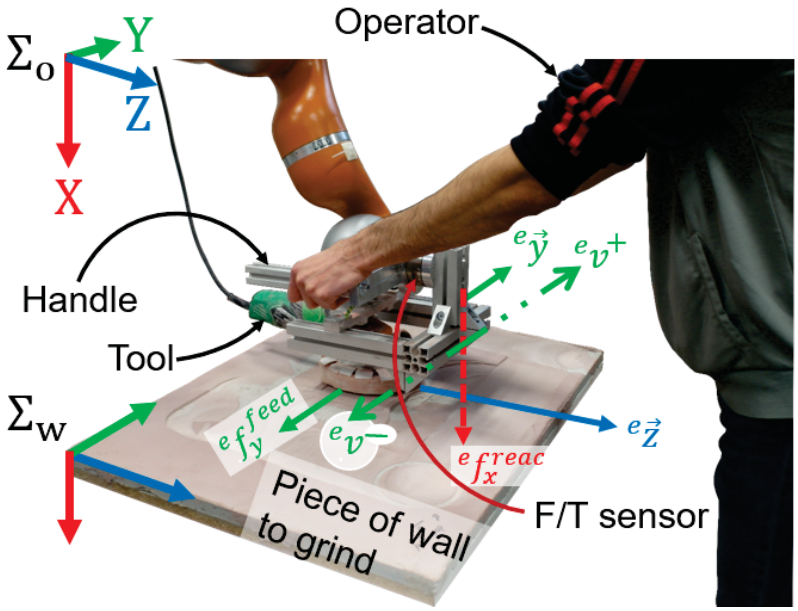

Figure 3.32: The manual grinding setup used to determine the normal grinding force f^{reac} and the translational velocity of the disc on the wall v_{norm}. The system equipped with grinding tool, force/torque sensor and a handle to perform grinding on the wall

manually along ${}^{e}\vec{y}$ and pressing along ${}^{e}\vec{x}$ to grind the piece of wall. Therefore, the values of the normal force are recorded from the force sensor with the proper transformations, they are shown in Figure 3.33 . The average value of the normal forces in the three tests is 26.21 N. Concerning the feeding velocities, they are obtained from the robot kinematics and they can be seen in Figure 3.34, their mean square average is 0.0243 m/s. This speed is considerably high for the KUKA LWR to execute the grinding task on the wall. For this issue, the feeding velocity is scaled down to 0.015 m/s and consequently the force to 15 N by respecting the approximate proportional value ($f^{reac}/v_{norm} \approx 1000$). It is assumed here that the normal force is proportional to the translational velocity because of the collision between the disc and the wall.

The grinding tool used in the experiment (Figure 3.32) is made of an electric spindle rotating in a high speed with the abrasive disc attached to its end (Figure 3.35). From the literature, in industrial cylindrical grinding, only one face of the disc operates and the grinding force f^{feed} is expressed as,

$$f_{nom}^{feed} = \mu_e \frac{v_{norm} db}{v_{tan}} \tag{3.32}$$

with,

$$\mu_e \propto \frac{1}{t} \tag{3.33}$$

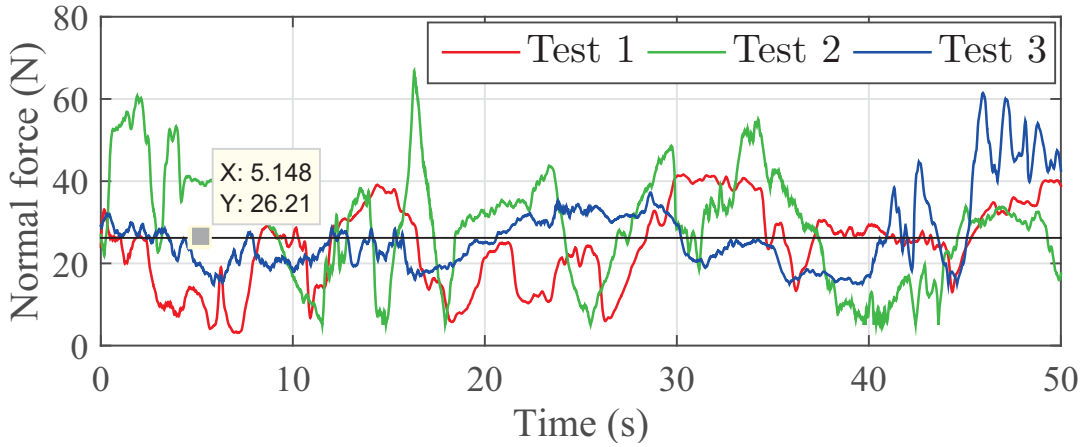

Figure 3.33: Normal grinding forces collected from 3 manual tests

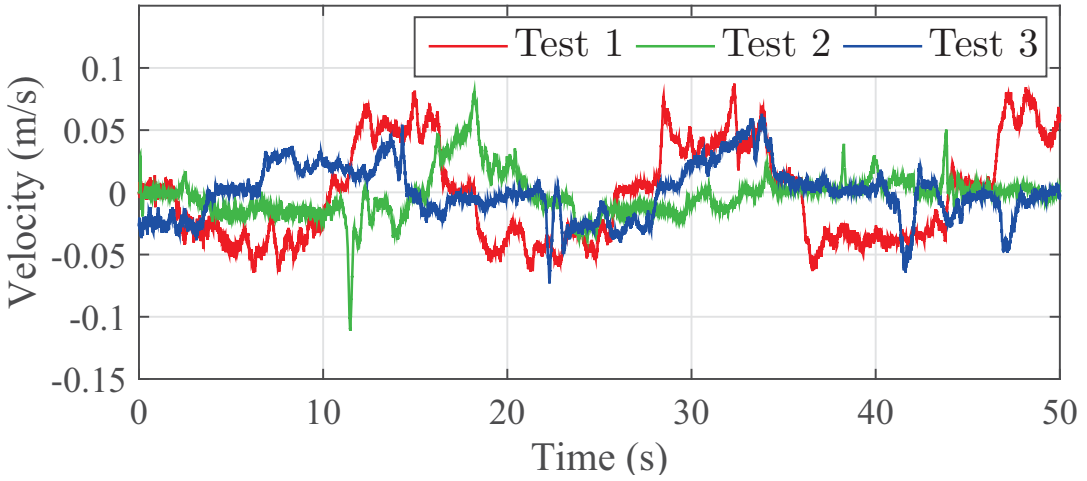

Figure 3.34: Translational velocities of the disc on the wall collected from 3 manual tests

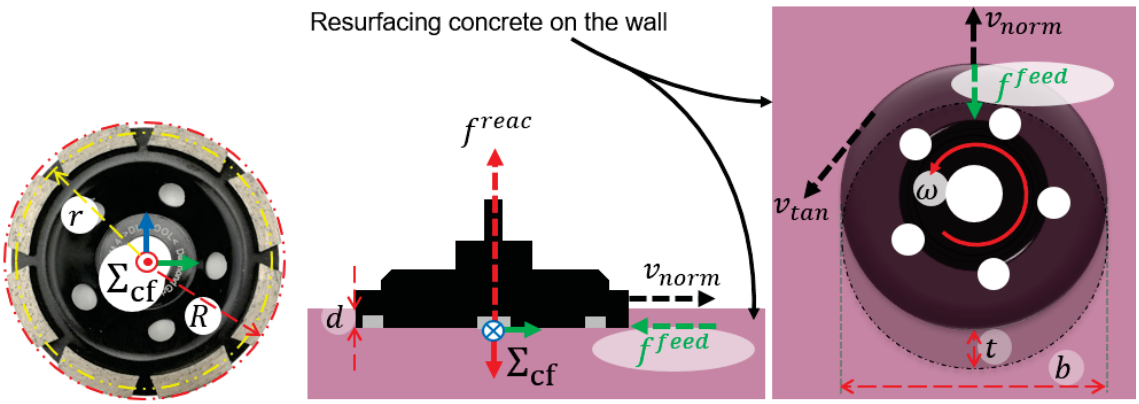

Figure 3.35: Grinding parameters

Table 3.2: Parameters of the grinding model

Variable	Unit	Explanation
μ_e	$\frac{W/s}{m^3}$	Energy gain
ω	rad/s	Rotational speed of the disc
f^{reac}	N	Applied force
t	m	Thickness of the cut ahead
R, r	m	Contact radii on the disc
d	m	Depth of the cut
b	m	Width of the cut
v_{norm}	m/s	Translational velocity of the disc on the wall
v_{tan}	m/s	Tangential velocity of the disc
μ_f		Friction constant

and,

$$v_{tan} = \omega R \tag{3.34}$$

The description of the grinding parameters is detailed in Table 3.2. However, in the wall grinding operations, the two faces of disc operate as can be seen in Figure 3.35. Hence, equation 3.32 can be modified by adding the effect of the applied force as,

$$f_{nom}^{feed} = \mu_e \frac{v_{norm} db}{v_{tan}} + \mu_f \frac{-f^{reac}}{2\pi r} \tag{3.35}$$

The disc used in the tests has the outer radius $R = 0.0625$ m and the inner radius $r = 0.0575$ m. The spindle rotates 11000 revolutions per min (rpm), this is equivalent to $\omega = 1.1519 \times 10^3$ rad/s. F^{reac} and v_{norm} can be obtained from the force-torque sensor and the robot kinematics respectively. Thus, the remaining missing variables in equation 3.35 are: μ_e, μ_f and d. In order to determine them, two automatic grinding tests were performed using the setup in Figure 3.30. Similar to the manual setup, the wall used is planar and its frame {w} is set parallel to the frame {o}. Also, the orientation of the end-effector is fixed such that the disc is parallel to the wall. Then, the robot is commanded using hybrid control in the operational frame {o} to execute normal grinding force f^{reac} along ${}^o\vec{x}$ and translational velocity v_{norm} on the wall along ${}^o\vec{y}$. The values of f^{reac} and v_{norm} are the ones deduced previously from the manual grinding tests as 15 N and 0.015 m/s respectively. As mentioned before, the feeding and normal forces (f_{msr}^{reac} and f_{msr}^{feed}) are recorded from the force-torque sensor measurements, the value of v_{norm} is obtained from the robot kinematics and the depth of the cut d is measured using a coordinate measurement machine and found to be 0.002 m. The surface's profile of the automatic grinding tests is evaluated using the profilometer in Figure 3.36, their average roughness is 16.7 μm and they were smooth enough by tactile sensing as well. Accordingly, the values of μ_e, μ_f are optimized using the linear least square method of the form,

$$\min_{\mu_e,\, \mu_f} \frac{1}{2} \left\| \left(\begin{bmatrix} \frac{v_{norm} db}{v_{tan}} & \frac{-f_{msr}^{reac}}{2\pi r} \end{bmatrix} \begin{bmatrix} \mu_e \\ \mu_f \end{bmatrix} - f_{msr}^{feed} \right) \right\|_2^2 \tag{3.36}$$

The estimation of the nominal feeding $\hat{f}_{nom}^{feed}$ is plotted against the real value measured from the force-torque sensor in Figure 3.37. The root mean square error (RMSE) of the feeding force estimation in the automatic grinding test in Figure 3.37a is 1.3 N. However, the RMSE of the feeding force estimation from manual grinding test data in Figure 3.37b

is 10.4 N. The error is higher in the manual grinding test because the depth of the cut is not constant.

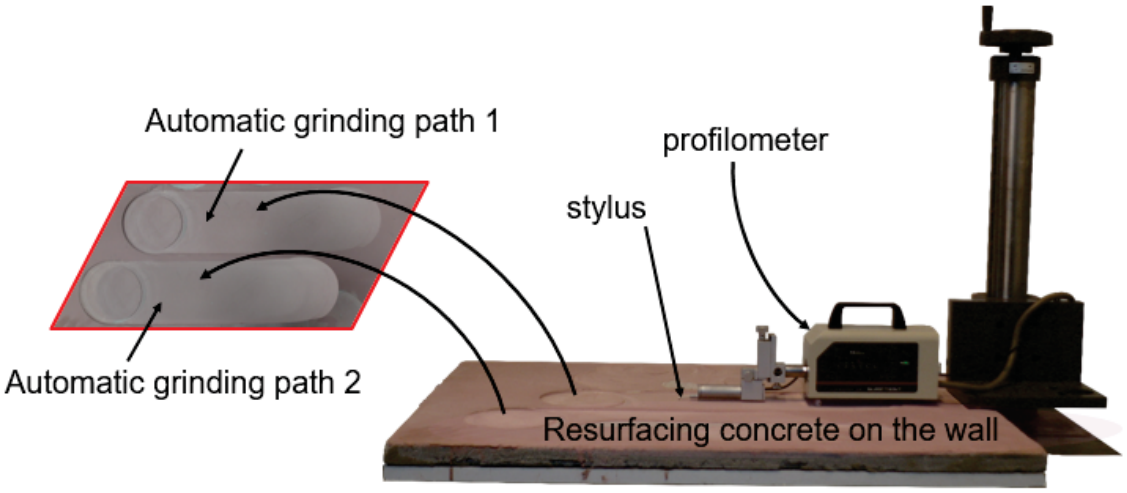

Figure 3.36: Surface roughness measurement setup

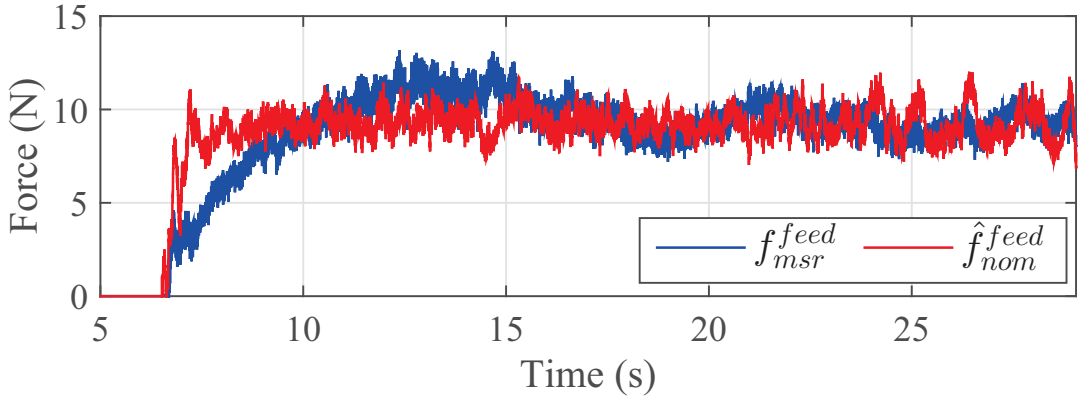

(a) Feeding force estimation of automatic grinding test ($d = 0.002$ m).

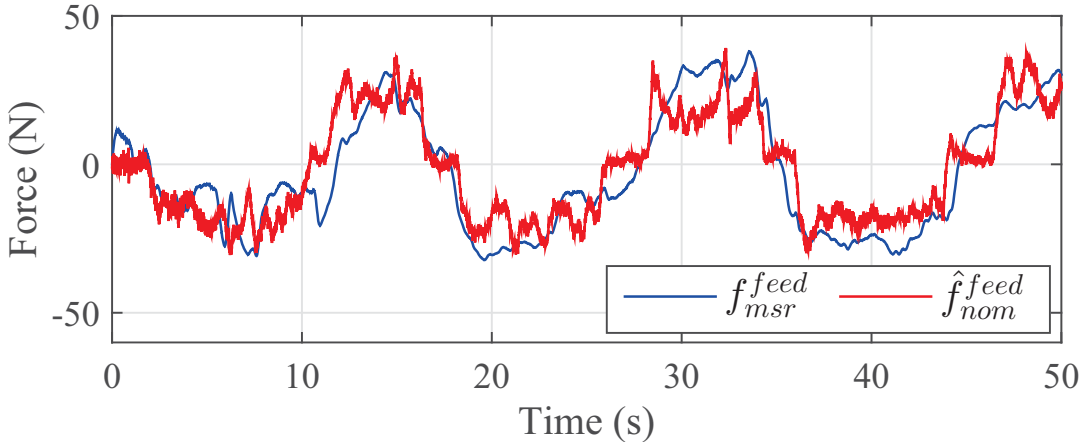

(b) Feeding force estimation of manual grinding test (d is random between 0 and 0.003 m).

Figure 3.37: Feeding force estimation ($\mu_e = 3.469 \times 10^8$ and $\mu_f = 0.00126$)

3.4.3 Non-contact forces elimination from the force-torque sensor readings

Non-contact forces compensation in force-torque sensor readings is important in the grinding task. It is necessary to decouple the forces caused by the weight, inertia, Coriolis and centrifugal effects of the grinding tool from the pure contact forces with the environment. The force-torque sensor provides the readings of wrench $\boldsymbol{W}$ acting on the sensor frame $\{\mathrm{s}\}$ with respect to the frame itself as,

$$ {}^{s}\boldsymbol{W}_{msr} = {}^{s}\boldsymbol{W}_{c} + {}^{s}\boldsymbol{W}_{nc} + {}^{s}\boldsymbol{W}_{offset} \tag{3.37} $$

where

$$ {}^{s}\boldsymbol{W}_{nc} = {}^{s}\boldsymbol{W}_{gravity} + {}^{s}\boldsymbol{W}_{inertia} + {}^{s}\boldsymbol{W}_{coriolis+centrifugal} \tag{3.38} $$

is the disturbance wrench affecting the sensor due to the non-contact forces and torques. ${}^{s}\boldsymbol{W}_{offset}$ is the force-torque sensor offset used to automatically zero out the sensor readings upon activation/reseting. The sensor is activated when the robot is not moving and the disc is facing down, that is, the sensor frame $\{\mathrm{s}\}$ is parallel to the operational frame $\{\mathrm{o}\}$. $\boldsymbol{W}_{c}$ is the pure contact wrench due to contact forces and torques. Thus, it is necessary to first estimate the non-contact forces and then subtract them from the force-torque sensor output in order to obtain the pure contact forces as,

$$ {}^{s}\boldsymbol{W}_{c} = {}^{s}\boldsymbol{W}_{msr} - {}^{s}\hat{\boldsymbol{W}}_{nc} \tag{3.39} $$

In order to estimate these non-contact forces (${}^{s}\hat{\boldsymbol{W}}_{nc}$), the Recurrent Neural Network observer (RNNOB) proposed in Section 2.4 is used as it was shown to outperform analytically based methods. However, unlike the observer in Section 2.4, the inertial measurement unit (IMU) measurements are not used here. Instead, the recurrent neural network model is trained using the force-torque sensor pose (${}^{s}\boldsymbol{p}_{o}$,${}^{s}\,\boldsymbol{o}_{o}$), twist (${}^{s}\boldsymbol{v}_{o}$,${}^{s}\,\boldsymbol{\omega}_{o}$), and its accelerations (${}^{s}\dot{\boldsymbol{v}}_{o}$,${}^{s}\,\dot{\boldsymbol{\omega}}_{o}$), obtained from direct kinematics, to estimate ${}^{s}\boldsymbol{W}_{nc}$. Figure 3.38 depicts the block diagram of the RNNOB used here to estimate the contact forces.

The data was collected by *manual*, *automatic* and *rotational* trajectories with the grinding tool attached to the force-torque sensor as Figure 3.30 shows. The manual data was collected by setting the robot controller to gravity compensation mode and then moving the wrist manually to various poses in the workspace with random velocities and accelerations. The automatic data was generated by turning the grinder on and moving the robot between random points in its workspace using various trapezoidal velocity profiles. The *rotational* trajectory was generated by rotating the sensor frame $\{\mathrm{s}\}$ and the compliant frame $\{\mathrm{cv}\}$ around each of their axis sequentially. The manual data was collected in 2 trials, each about three minutes long; similarly the automatic data was collected in 3 trials with an average time of 1.5 minutes each as well, and the rotational data was collected in two trials (in the frames $\{\mathrm{s}\}$ and $\{\mathrm{cv}\}$) about 2 minutes long each. These datasets were then combined into one training dataset, where one trial of the automatic data and the rotational data around $\{\mathrm{cv}\}$ were separated to create a test dataset. The manual data was used entirely for training. The RNN model is trained for 20 epochs using an architecture with two hidden layers, with 15 and 10 Long Short-Term Memory (LSTM) units respectively, and a sequence length for the input layer of 15 time steps. Stochastic Gradient Descent was applied in the output layer with 0.01 learning rate to minimize the mean square error of the regression problem. A hyperbolic tangent sigmoid function was used as the activation function between the hidden layers and a linear activation function was used for the output layer. The efficiency of the RNNOB in estimating gravitational forces was evaluated by the rotational test around $\{\mathrm{cv}\}$. The

results can be seen in Figures 3.39 and 3.40, and their corresponding RMSE are shown in Table 3.3. The RNNOB with its new inputs shown in Figure 3.38 outperforms the one proposed in Section 2.4.

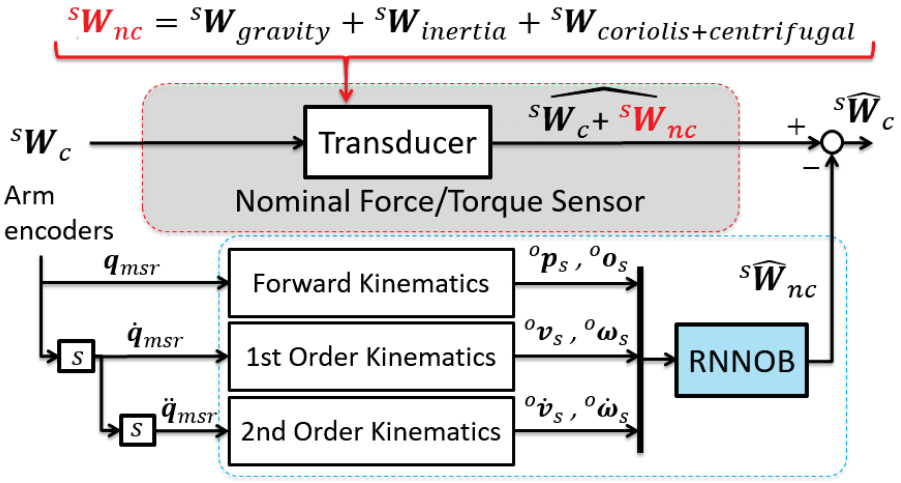

Figure 3.38: Recurrent neural network observer to estimate non-contact forces. {o} is the robot operational frame and {s} is the force-torque sensor frame

Table 3.3: The RNNOB root mean square errors on the rotational test dataset with the grinder attached.

	f_{nc}^x	f_{nc}^y	f_{nc}^z	τ_{nc}^x	τ_{nc}^y	τ_{nc}^z
RMSE	0.232	0.211	0.757	0.057	0.094	0.048

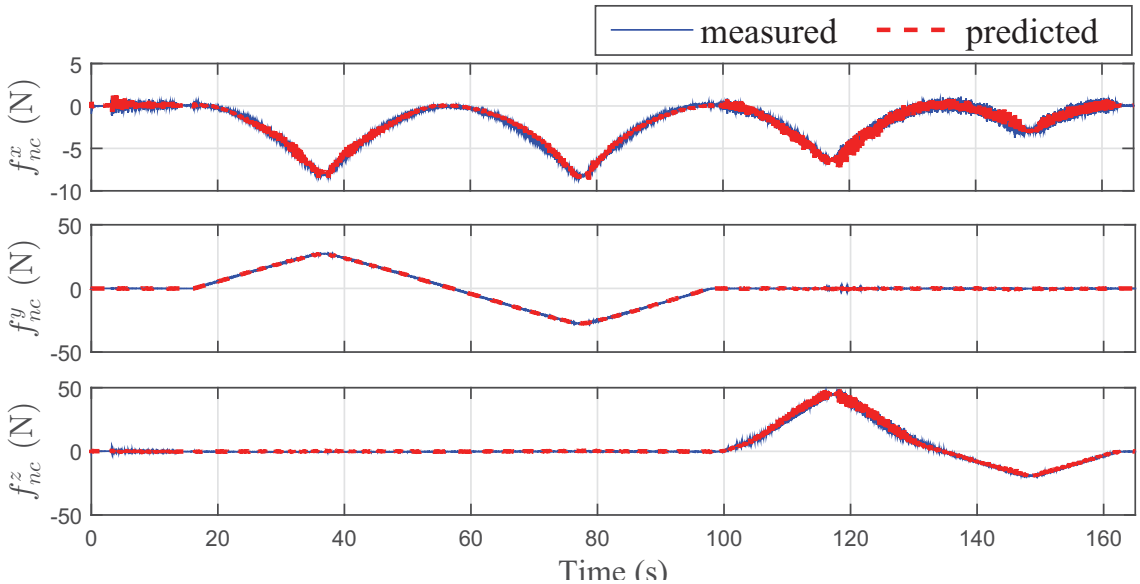

Figure 3.39: Non-contact forces estimated by the RNNOB against the ones measured by the force torque sensor

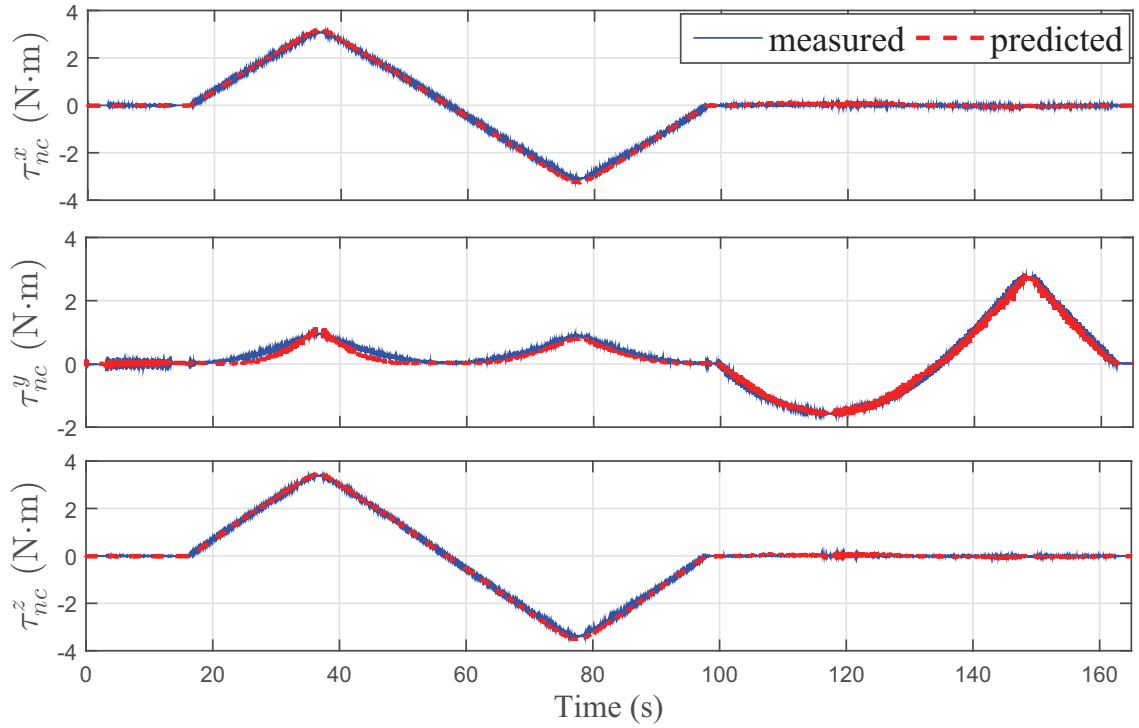

Figure 3.40: Non-contact torques estimated by the RNNOB against the ones measured by the force torque sensor

3.4.4 Force and motion control Loops

As mentioned in Section 3.4.1, the hybrid control is expressed in the compliant frames {cv} and {cf}. The force is controlled along ${}^{cf}\vec{x}$ direction, ${}^{cv}\vec{y}$ and ${}^{cv}\vec{z}$ directions are controlled in velocity, and the three remaining orientations around ${}^{cv}\vec{x}$, ${}^{cv}\vec{y}$ and ${}^{cv}\vec{z}$ are controlled in position. Thus, when in contact, the selection matrices ${}^{cv}\boldsymbol{S}_m$ and ${}^{cf}\boldsymbol{S}_f$ of motion and force controlled directions in the compliant frames {cv} and {cf} respectively are,

$$ {}^{cv}\boldsymbol{S}_m = \begin{bmatrix} {}^{cv}\boldsymbol{S}_v & \boldsymbol{0} \\ \boldsymbol{0} & {}^{cv}\boldsymbol{S}_p \end{bmatrix} = \begin{bmatrix} 0 & 0 & 0 & 0 & 0 & 0 \\ 0 & 1 & 0 & 0 & 0 & 0 \\ 0 & 0 & 1 & 0 & 0 & 0 \\ 0 & 0 & 0 & 1 & 0 & 0 \\ 0 & 0 & 0 & 0 & 1 & 0 \\ 0 & 0 & 0 & 0 & 0 & 1 \end{bmatrix} \tag{3.40} $$

and for the force controlled direction is,

$$ {}^{cf}\boldsymbol{S}_f = \boldsymbol{I} - {}^{cv}\boldsymbol{S}_m = \begin{bmatrix} 1 & 0 & 0 & 0 & 0 & 0 \\ 0 & 0 & 0 & 0 & 0 & 0 \\ 0 & 0 & 0 & 0 & 0 & 0 \\ 0 & 0 & 0 & 0 & 0 & 0 \\ 0 & 0 & 0 & 0 & 0 & 0 \\ 0 & 0 & 0 & 0 & 0 & 0 \end{bmatrix} \tag{3.41} $$

The three control laws are detailed in the next sections.

3.4.4.1 Force control in the compliant frame {cf}

The desired wrench $\boldsymbol{W}_{des}$ in the compliant frame {cf} is the vector of desired forces and torques,

$$ {}^{cf}\boldsymbol{W}_{des} = \begin{bmatrix} f^x_{des} & f^y_{des} & f^z_{des} & \tau^x_{des} & \tau^y_{des} & \tau^z_{des} \end{bmatrix}^T \tag{3.42} $$

It can be achieved by setting $\boldsymbol{\lambda}_f$ in equation 3.29 as,

$$ \boldsymbol{\lambda}_f = {}^{o}\boldsymbol{R}_{cf}\ {}^{cf}\boldsymbol{S}_f\ \boldsymbol{K}_{PF}\Big({}^{cf}\boldsymbol{W}_{des}(t) - {}^{cf}\boldsymbol{W}_c(t)\Big) \tag{3.43} $$

${}^{o}\boldsymbol{R}_{cf}$ is the rotation matrix between the operational frame {o} and the compliant frame {cf}. $\boldsymbol{\lambda}_f$ is the force controller command and $\boldsymbol{K}_{PF}$ is a suitable 6×6 positive-definite gain matrix. ${}^{cf}\boldsymbol{W}_c$ is the pure contact wrench measured at the compliant frame {cf}, it can be obtained by transforming the pure contact wrench ${}^{s}\boldsymbol{W}_c$ obtained from the RNNOB at the sensor frame as,

$$ {}^{cf}\boldsymbol{W}_c = {}^{cf}\boldsymbol{Ad}_s\ {}^{s}\boldsymbol{W}_c \tag{3.44} $$

with ${}^{cf}\boldsymbol{Ad}_s$ is the adjoint transformation matrix that transforms the force and torque vectors from the force-torque sensor frame $\{s\}$ into the force control frame $\{cf\}$. It can be expressed as,

$$ {}^{cf}\boldsymbol{Ad}_s = \begin{bmatrix} {}^{cf}\boldsymbol{R}_s & \boldsymbol{0} \\ -\,{}^{cf}\boldsymbol{R}_s\hat{\boldsymbol{p}}_{s\ cf} & {}^{cf}\boldsymbol{R}_s \end{bmatrix} \tag{3.45} $$

${}^{cf}\boldsymbol{R}_s$ and $\hat{\boldsymbol{p}}_{s\ cf}$ are the rotation matrix and the position vector respectively between the frames $\{s\}$ and $\{cf\}$.

3.4.4.2 Velocity and position control in the compliant frame {cv}

The acceleration command, $\boldsymbol{\alpha}_m$ in equation 3.29, can be expressed as,

$$\boldsymbol{\alpha}_m = \begin{bmatrix} \boldsymbol{\alpha}_{lin} \\ \boldsymbol{\alpha}_{ang} \end{bmatrix} \tag{3.46}$$

with $\boldsymbol{\alpha}_{lin}$ and $\boldsymbol{\alpha}_{ang}$ are respectively, the linear and angular acceleration commands for the motion controller. The desired linear velocities vector in the compliant frame {cv} is,

$${}^{cv}\boldsymbol{V}_{des} = \begin{bmatrix} v^x_{des} & v^y_{des} & v^z_{des} \end{bmatrix}^T \tag{3.47}$$

It can be achieved by setting $\boldsymbol{\alpha}_{lin}$ in equation 3.46 as,

$$\boldsymbol{\alpha}_{lin} = {}^{o}\boldsymbol{R}_{cv}\, {}^{cv}\boldsymbol{\alpha}_{lin} \tag{3.48}$$

${}^{o}\boldsymbol{R}_{cv}$ is the rotation matrix between the operational frame {o} and the compliant frame {cv}. ${}^{cv}\boldsymbol{\alpha}_{lin}$ is the acceleration command generated at the compliant frame level as,

$${}^{cv}\boldsymbol{\alpha}_{lin} = {}^{cv}\boldsymbol{S}_v \dot{\boldsymbol{V}}_{des}(t) + {}^{cv}\boldsymbol{S}_v \Big(\boldsymbol{K}_{DV} \big({}^{cv}\boldsymbol{V}_{des}(t) - {}^{cv}\boldsymbol{V}_{res}(t) \big) \Big) \tag{3.49}$$

$\boldsymbol{K}_{DV}$ is a suitable 3×3 positive-definite gain matrix. ${}^{cv}\boldsymbol{V}_{res}$ is the velocity of the end-effector in {cv} frame, it can be obtained by transforming the end-effector velocity in the operational frame as,

$${}^{cv}\boldsymbol{V}_{res} = {}^{o}\boldsymbol{R}^T_{cv}\, {}^{o}\boldsymbol{V}_{res} \tag{3.50}$$

${}^{o}\boldsymbol{V}_{res}$ can be obtained from the second order kinematics of the robot using $\boldsymbol{q}_{msr}$, the vector of joints angular response measured by the encoders.

The desired orientation of the disc is expressed in the compliant frame {cv} with respect to the operation frame {o} as,

$${}^{o}\boldsymbol{\theta}^{cv}_{des} = \begin{bmatrix} \theta^x_{des} & \theta^y_{des} & \theta^z_{des} \end{bmatrix}^T \tag{3.51}$$

It can be achieved by setting $\boldsymbol{\alpha}_{ang}$ in equation 3.46 as,

$$\boldsymbol{\alpha}_{ang} = {}^{o}\ddot{\boldsymbol{\theta}}^{cv}_{des}(t) + \boldsymbol{K}_{DO} \big({}^{o}\dot{\boldsymbol{\theta}}^{cv}_{des}(t) - {}^{o}\dot{\boldsymbol{\theta}}^{cv}_{res}(t) \big) + \boldsymbol{K}_{PO} \big({}^{o}\boldsymbol{\theta}^{cv}_{des}(t) - {}^{o}\boldsymbol{\theta}^{cv}_{res}(t) \big) \tag{3.52}$$

$\boldsymbol{K}_{PO}$ and $\boldsymbol{K}_{DO}$ are suitable 3×3 positive-definite gain matrices. The rotation θ^x_{des} around ${}^{cv}\vec{x}$ is not convenient for grinding, it is fixed at 0. The rotation θ^y_{des} around ${}^{cv}\vec{y}$ is fixed such that ${}^{cv}\vec{z}$ is parallel to ${}^{w}\vec{z}$ (i.e. the problem addressed here is grinding 2D curved surfaces). However, θ^z_{des} around ${}^{cv}\vec{z}$ is controlled based on the adaptive function shown in Figure 3.41 as,

$$\theta^z_{des} = \theta^z_{res} + \delta\theta^z \tag{3.53}$$

$$\dot{\theta}^z_{des} = \frac{\delta\theta^z}{T} \tag{3.54}$$

$$\ddot{\theta}^z_{des} = \frac{\dot{\theta}^z_{des}}{T} \tag{3.55}$$

T is the update period of the controller. The adaptive function can be expressed as,

$$\delta\theta^z = \delta\theta_{max} \frac{1}{1 + e^{-a e^{feed}_f + \iota}} + \delta\theta_{max} \frac{1}{1 + e^{-a e^{feed}_f - \iota}} + \delta\theta_{min} \tag{3.56}$$

$\delta\theta_{max}$ is the maximum safe increment of θ^z that can be achieved in a single update period T of the controller. a is the slope of the adaptive function; ι is a parameter used to tune Ω, the threshold error magnitude that must be exceeded for the adaptive function to be reactive. ϵ_f^{feed} is the feeding force error, it can be obtained as,

$$\epsilon_f^{feed} = \hat{f}_{nom}^{feed} - f_{msr}^{feed} \tag{3.57}$$

The proposed function in equation 3.56 uses the feeding force error along ${}^{cv}\vec{y}$ to incre-

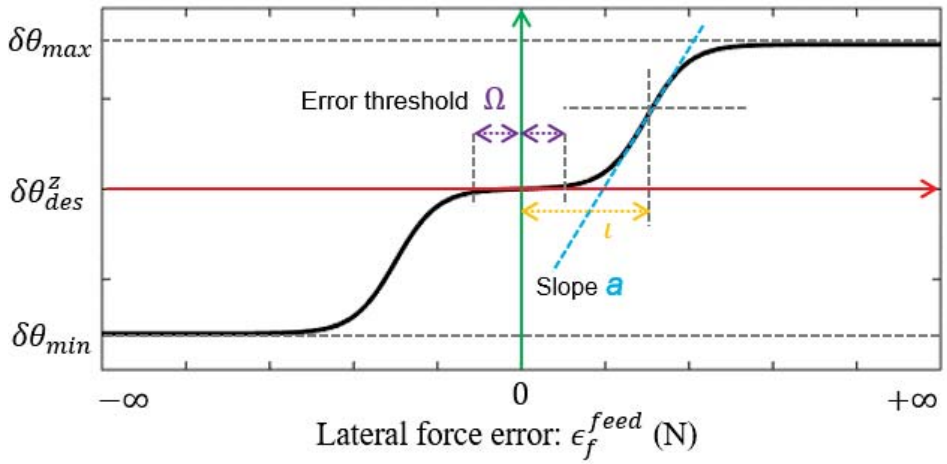

Figure 3.41: Orientation adaptive function

ment/decrement θ^z so the disc can follow the surface. This is specifically used when the disc plunges in the resurfacing material more/less than the desired depth of cut (2 mm measured in the automatic grinding tests for identification of feeding force) and would need to orient.

3.4.5 Experimental evaluation

In order to validate the effectiveness of the proposed hybrid controller, wall grinding experiments are carried out on three different cases: (1) on flat surface; (2) on convex surface; (3) on concave surface. The curvature radius in the cases (2) and (3) is chosen such that the full contact between the disc and the surface is on its limits (e.g. if the radius of curvature is too big, the contact between the disc and the surface will be a disc, else the contact will be small segments at the contact points). The wall samples can be seen in Figures 3.42a, 3.42b and 3.42c respectively. In order to later evaluate the grinding quality, the initial state of the surface of each of the wall samples is evaluated using the coordinate-measuring machine (CMM) (ex: Figure 3.42a). The CMM measures the surface geometry of the walls by sensing the discrete points of the mesh projected on their surface using the probe shown in Figure 3.42a. Thus, the initial surface geometry of the walls is shown in Figures 3.42d, 3.42e and 3.42f.

The experimental grinding setup is shown in Figure 3.30. The KUKA lightweight arm is controlled by an external computer. The control framework is implemented on the computer using Robot Operating System (ROS) that communicates with the KUKA Fast Research interface (FRI) at a rate of 500 Hz. The six-axes ATI force-torque sensor is attached to the face of the six joint (q_6). Then, on the other end of the force-torque sensor, the grinding tool with a speed of 11000 rpm is attached. The tool rotates a disc with abrasive grains of 125 mm diameter. The overall end-effector (tool+disc+tool-frame)

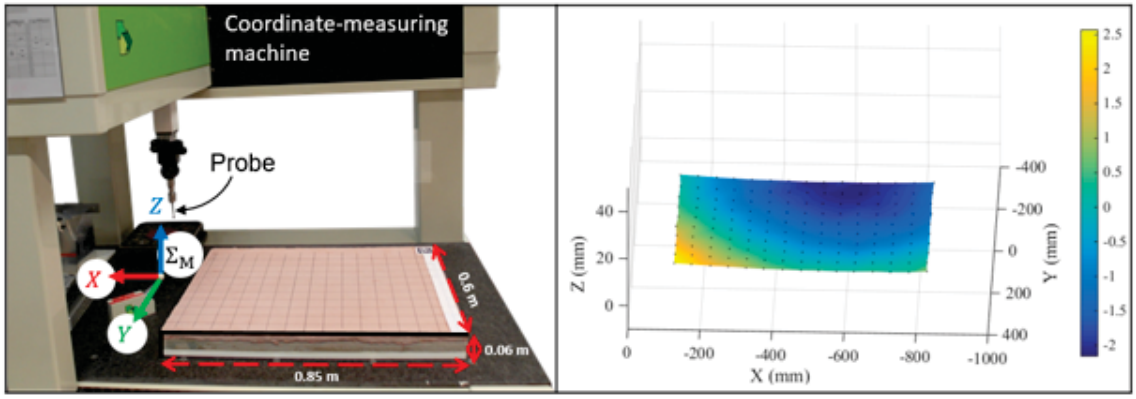

(a) Flat surface

(d) Flat surface mesh from the coordinate-measurement machine

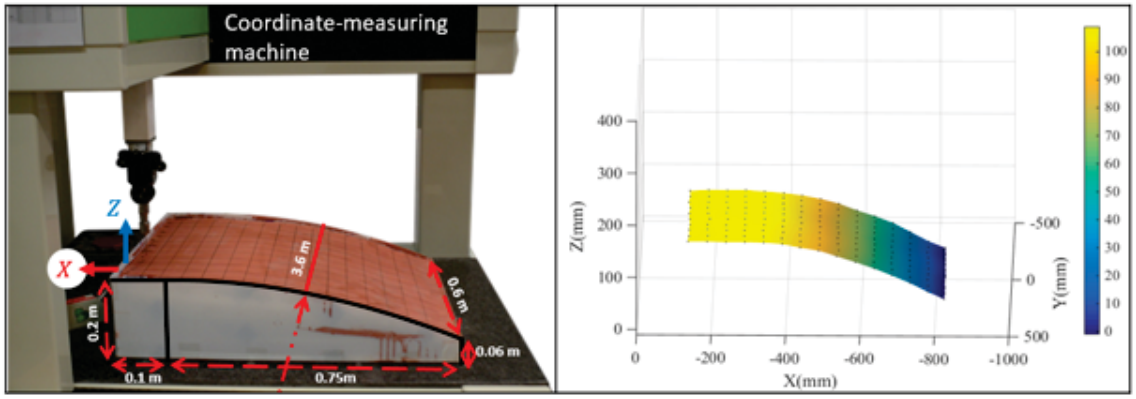

(b) Convex surface

(e) Convex surface mesh from the coordinate-measurement machine

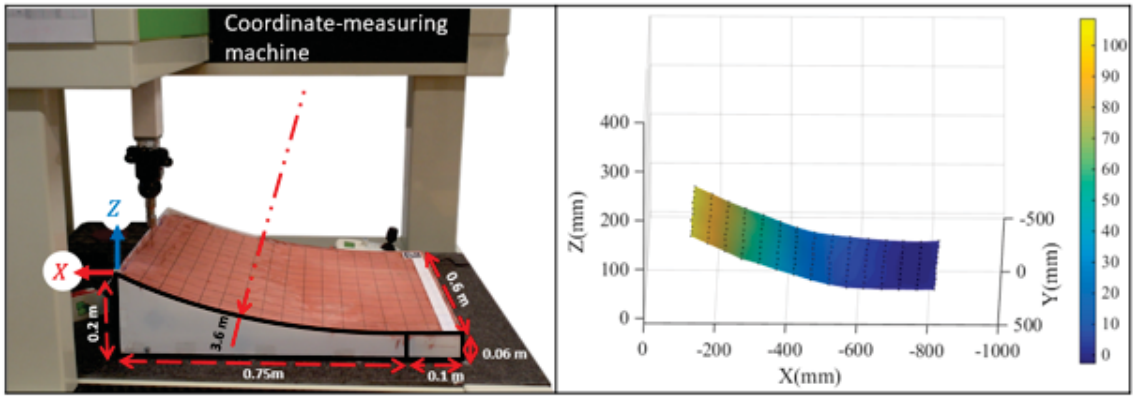

(c) Concave surface

(f) Concave surface mesh from the coordinate-measurement machine

Figure 3.42: Different wall geometries to grind. On the left side of the figure, the walls are placed on coordinate-measuring machine (CMM) to evaluate their surface before grinding. On the left side is the mesh obtained for each wall, it is measured in the machine frame {M} shown in the figure a.1. The color map corresponds to the depth along ${}^{M}\vec{z}$

is around 7.3 kg; its weight, inertia, Coriolis and centrifugal effects on the force-torque sensor readings are accurately estimated and compensated using the RNNOB presented in Section 3.4.3. The force sensor publishes data at a rate of 1000 Hz and the RNNOB runs at 500 Hz. The force sensor output is filtered using moving average window of 25 samples. To simplify the complexity of the experiments, the distance sensor (camera) to detect the contact between the disc and the wall was not used here. However, in all tests, the robot starts very close to the surface then continuous switching from velocity to force control is achieved using a Graphical User Interface (GUI) with interactive slider as shown in Figure 3.43. When the controller switches from velocity to force control along ${}^{cf}\vec{x}$, the robot exerts on the wall the instantaneous normal force required for grinding, it is obtained in Section 3.4.2 and equals to 15 N. Along with exerting normal force on the wall, the disc moves on the wall with the identified desired velocity $v_{norm} = 0.015$ m/s along ${}^{cv}\vec{y}$ while it adapts automatically the surface based on the adaptive orientation controller. The controller gains used in the experiments are shown in Table 3.4.

Table 3.4: Controller gains used in the experiments

	Gain	Value
Force control	$\boldsymbol{K}_{PF}(i,i)\ i = 1 \rightarrow 6$	0.5
Velocity control	$\boldsymbol{K}_{DV}(i,i)\ i = 1 \rightarrow 3$	25.0
Orientation control	$\boldsymbol{K}_{PO}(i,i)\ i = 1 \rightarrow 3$	700.0
	$\boldsymbol{K}_{DO}(i,i)\ i = 1 \rightarrow 3$	10.0
Adaptive orientation function	δ_{min} (rad)	-0.0016
	δ_{max} (rad)	0.0016
	a (rad/N)	0.015
	ι (N)	6.0
DOB	Cut-off frequency g	20.0

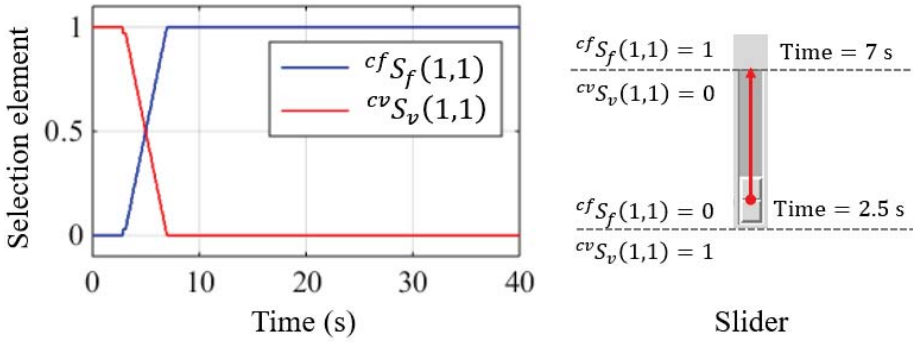

Figure 3.43: Switching from velocity to force control using interactive slider

In the next paragraphs, graphs are shown for the velocity control responses, the force control responses and the orientation control responses as function of feeding force variation. In addition to that, the surface geometry of each wall is measured by the CMM after grinding in order to evaluate the grinding quality.

Case 1: flat surface

The robot is commanded to grind one way of 0.55 meters length with velocity v_{norm} between the way-points p_0 and p_1 on the flat wall shown in Figures 3.42a and 3.48. The disc starts parallel to the surface with ${}^{o}\theta^{z} = 0.03$ radians. When the slider in Figure 3.43

goes from 0 to 1, ${}^{cf}\boldsymbol{S}_f(1,1)$ goes from 0 to 1 and the robot starts executing the task. The desired and response values of force and velocity controllers are shown in Figures 3.44a and 3.45a respectively. The controller shows good performance in force and velocity tracking, the tracking errors are shown in Figures 3.44b and 3.45b, the RMSE of the force along the path is 0.409 N and the RMSE of the velocity is 0.0016 m/s. Figure 3.46a shows a small variation in ${}^{o}\theta^{z}$ since the wall is not perfectly flat as the depth map in Figure 3.42d shows. Hence, ${}^{o}\theta^{z}$ varies as function of the pure contact feeding force f_c^{feed} acting on the disc (Figure 3.47a). When f_c^{feed} is less than the estimated one ($\hat{f}_{nom}^{feed}$) the disc try to plunge into the resurfacing material (From time = 7.5 s to 17.5 s) and vice-versa from time = 17.5 s to 28 s. The orientation controller is accurate, the error is bounded as Figure 3.46b shows, it tracks the ${}^{o}\theta^{z}_{des}$ along the path with RMSE equals to 0.001 radians.

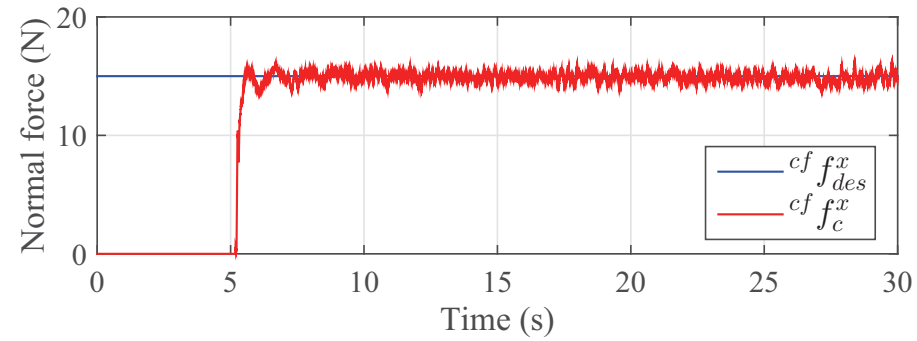

(a) Force tracking

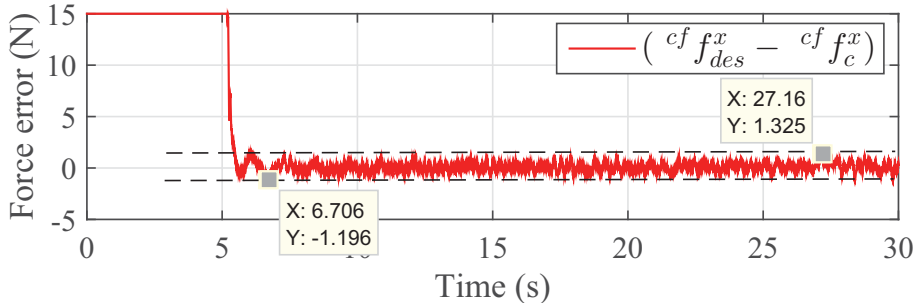

(b) Force tracking error

Figure 3.44: Force control performance in tracking the desired force value

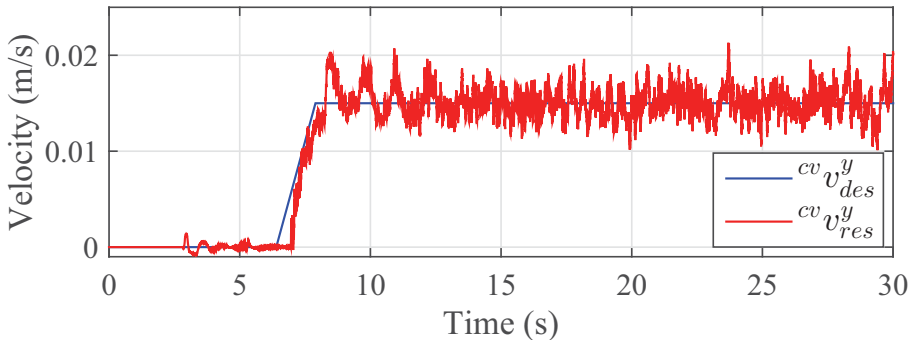

(a) Velocity tracking

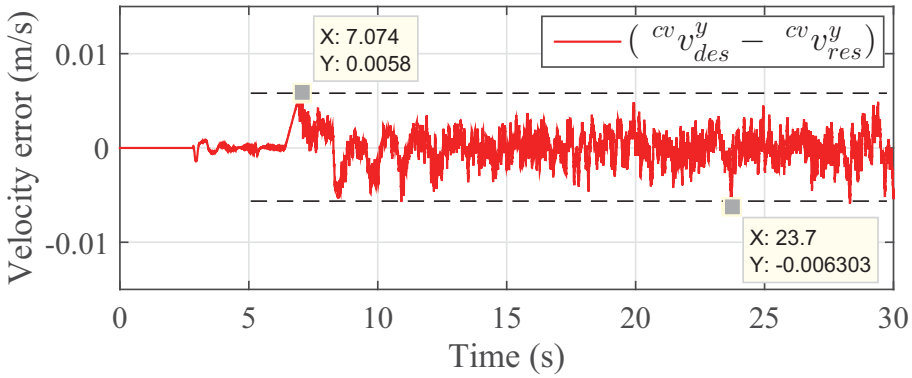

(b) Velocity tracking error

Figure 3.45: Velocity control performance in tracking the desired velocity value

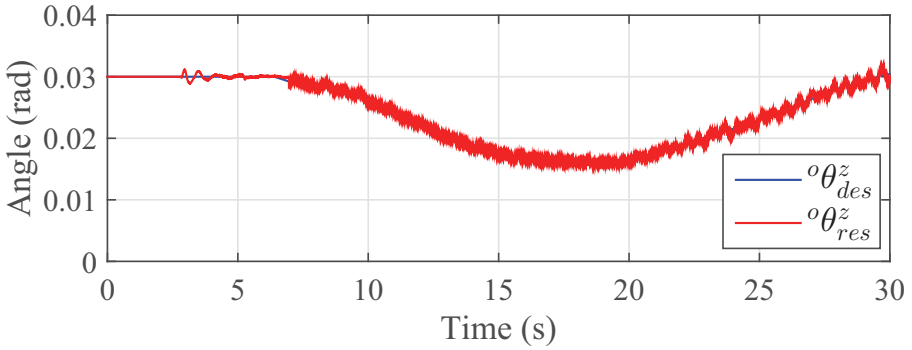

(a) Orientation tracking

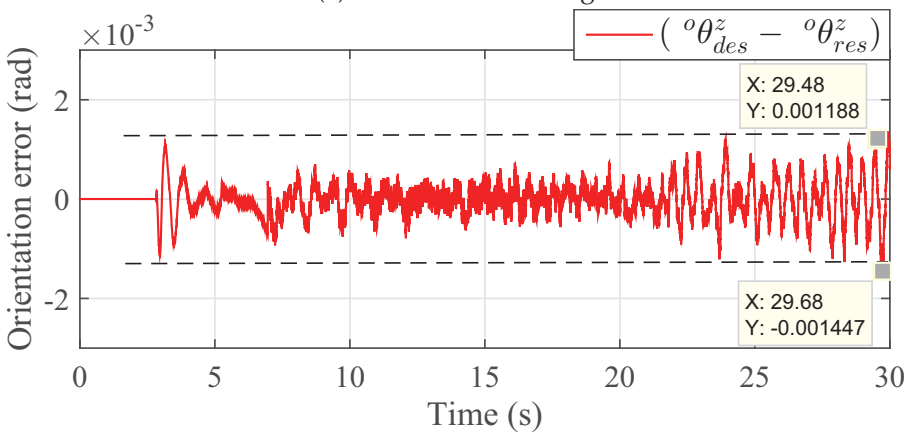

(b) Orientation tracking error

Figure 3.46: Orientation control performance in tracking the desired angle value

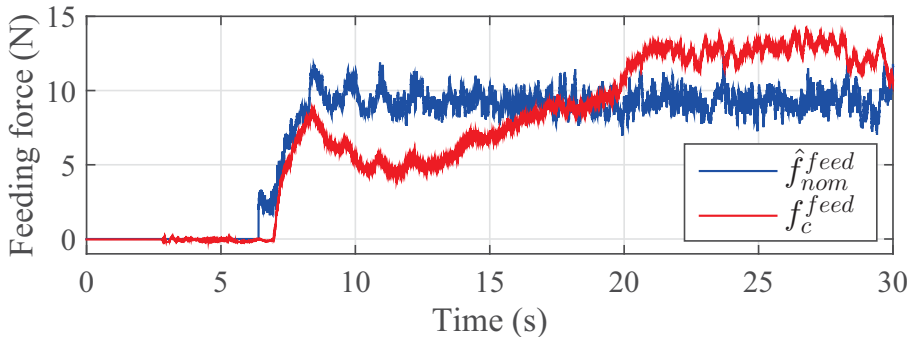

(a) Nominal estimated feeding force vs. the measured one

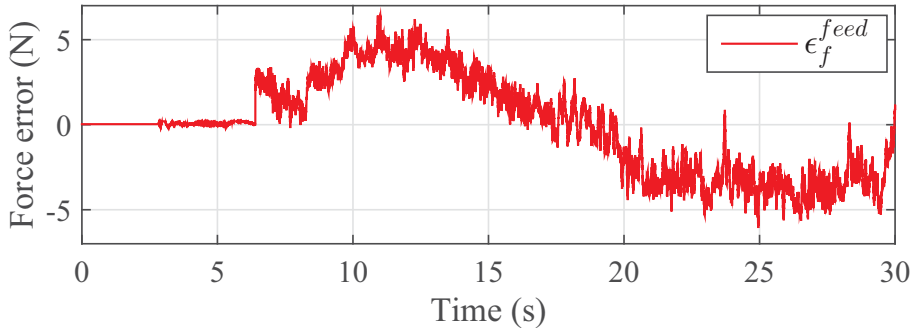

(b) Feeding force difference

Figure 3.47: Feeding force variation

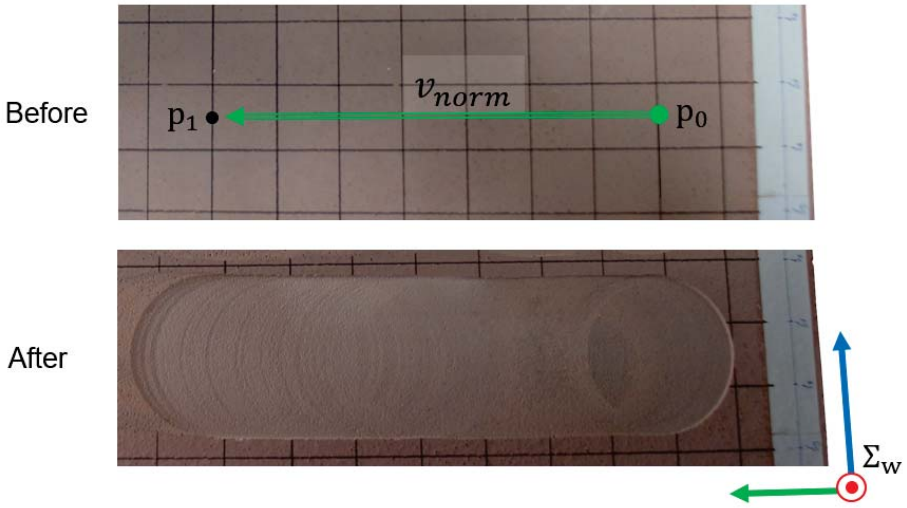

Figure 3.48: Flat wall top view before and after grinding straightly between p_0 and p_1

In order to evaluate the grinding quality, the ground surface of the flat wall is evaluated in Figures 3.49 and 3.50. Figure 3.49a shows the superposition of the meshes measured before and after grinding. The two meshes are subtracted and the depth of the cut along the lines L_1 and L_2 shown in Figure 3.49b is plotted in Figure 3.50. The Figure shows that the grinding depth varies between 1 and 2.67 mm along the ground path. The average depth of the cut under L_1 and L_2 is 1.79 and 1.86 mm respectively.

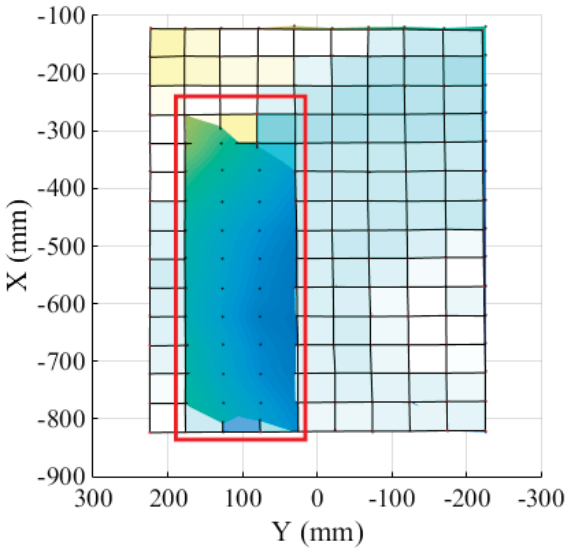

(a) Top view of the superposed meshes describing the flat wall surface geometry before and after grinding. The meshes are measured in the coordinate-measurement machine frame {M} shown in figure 3.42a

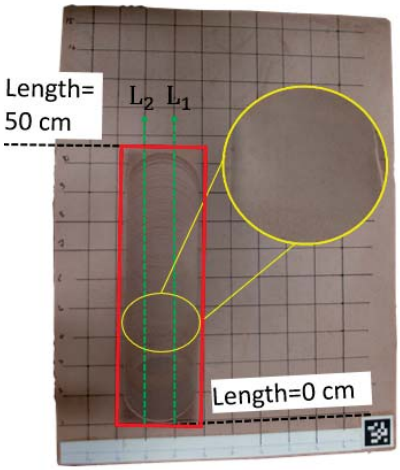

(b) Flat wall after grinding. The depth of the cut is evaluated for 50 cm under the two lines L_1 and L_2

Figure 3.49: The surface state of the flat wall evaluated before and after grinding. Inside the red boxes, where the mesh disappears, is the ground area

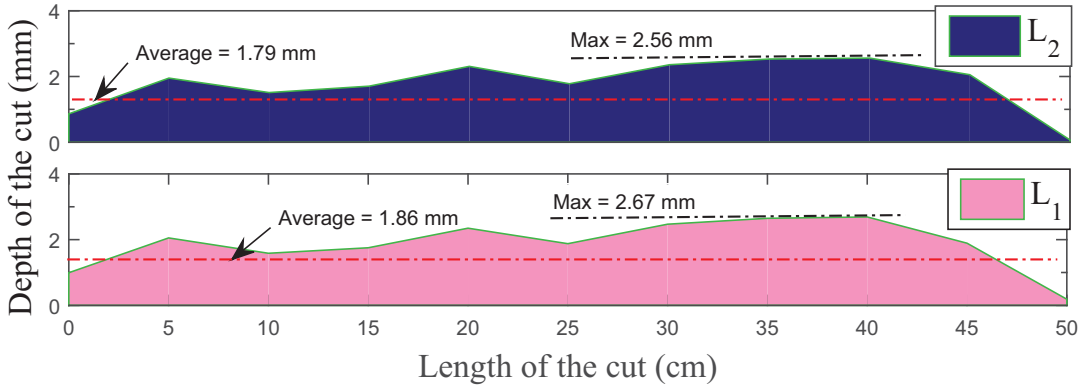

Figure 3.50: Grinding path depth evaluated under the lines L_1 and L_2 shown in Figure 3.49b

Case 2: convex surface

Similar to the test on the flat wall, the robot is commanded to grind the path determined by the way-points (p_0 to p_{11}) in Figure 3.55 with desired velocity v_{norm} on the convex

wall shown in Figures 3.42b and 3.55. The disc starts in contact with the surface with ${}^{o}\theta^{z} = 0.01$ radians. The desired and response values of force and velocity controllers are shown in Figures 3.51a and 3.52a respectively. The controller performance still good in force and velocity tracking, the tracking errors are shown in Figures 3.51b and 3.52b, the RMSE of the force along the path is 0.85 N and the RMSE of the velocity is 0.0019 m/s. Figure 3.53a shows how ${}^{o}\theta^{z}$ varies to track the convex shape of the wall shown in Figures 3.42b and 3.42e. In order to maintain the disc tangent to the wall surface, ${}^{o}\theta^{z}$ varies as function of the pure contact feeding force f_c^{feed} acting on the disc (Figure 3.54a). The robot orients the tool to minimize the difference between the feeding force f_c^{feed} and the estimated one ($\hat{f}_{nom}^{feed}$). Hence, the disc tries to adjust its plunge in the resurfacing material. The orientation controller is accurate, the error is bounded as Figure 3.53b shows, it tracks the ${}^{o}\theta^{z}_{des}$ along the path with RMSE equals to 0.001 radians.

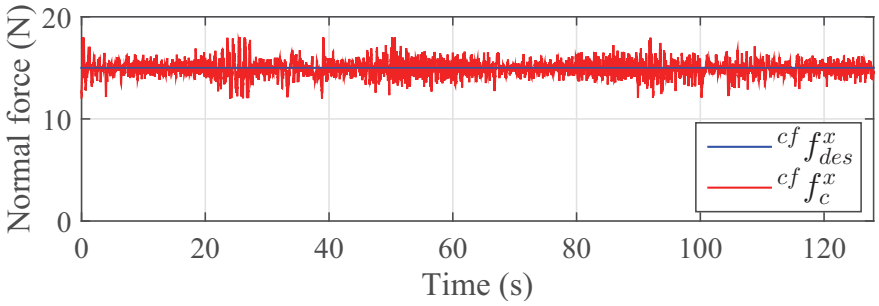

(a) Force tracking

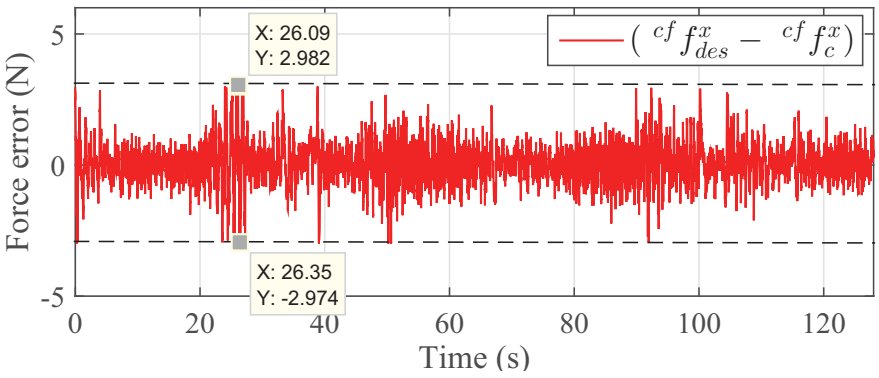

(b) Force tracking error

Figure 3.51: Force control performance in tracking the desired force value

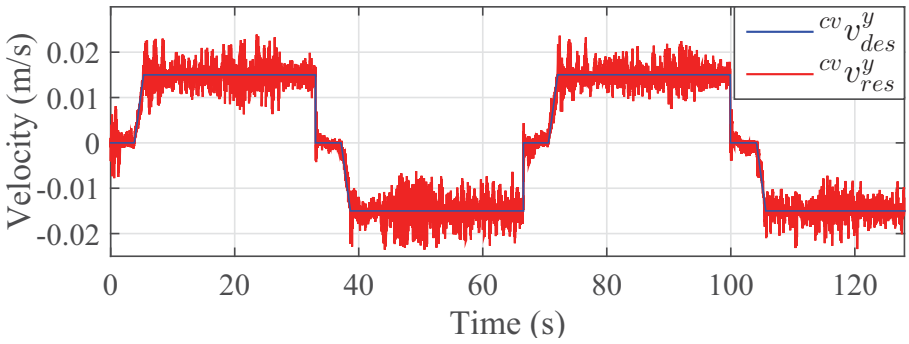

(a) Velocity tracking

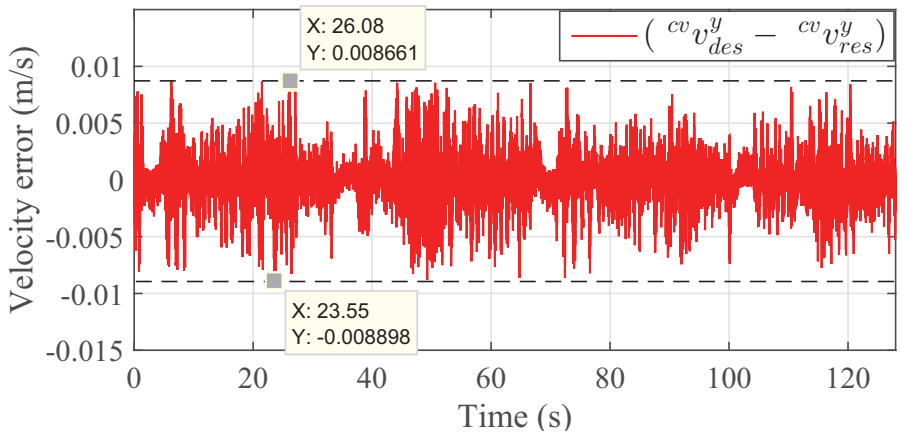

(b) Velocity tracking error

Figure 3.52: Velocity control performance in tracking the desired velocity value

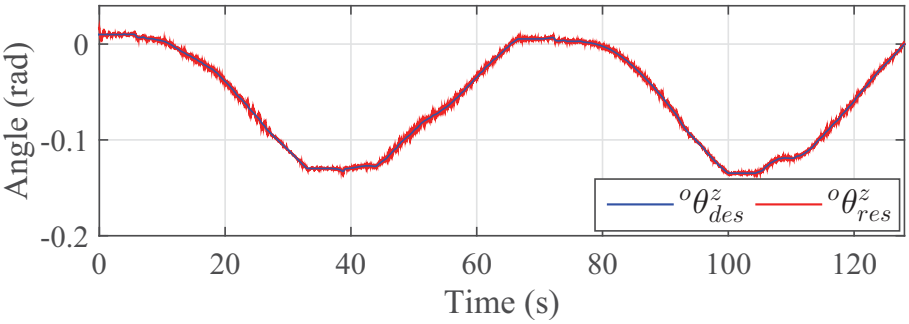

(a) Orientation tracking

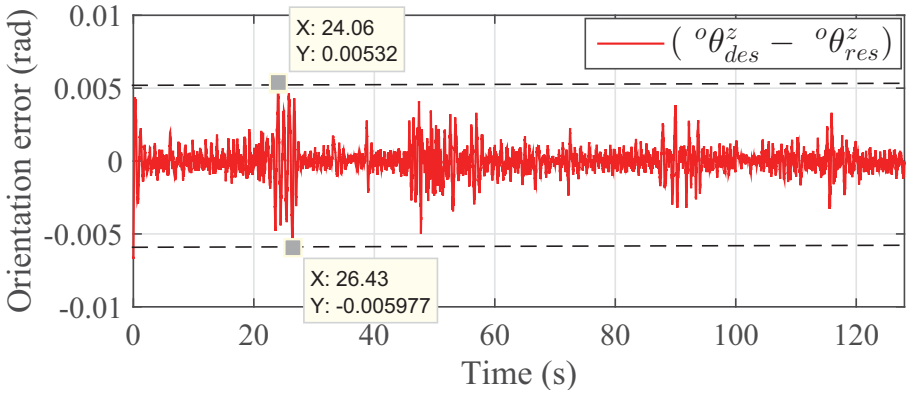

(b) Orientation tracking error

Figure 3.53: Orientation control performance in tracking the desired angle value

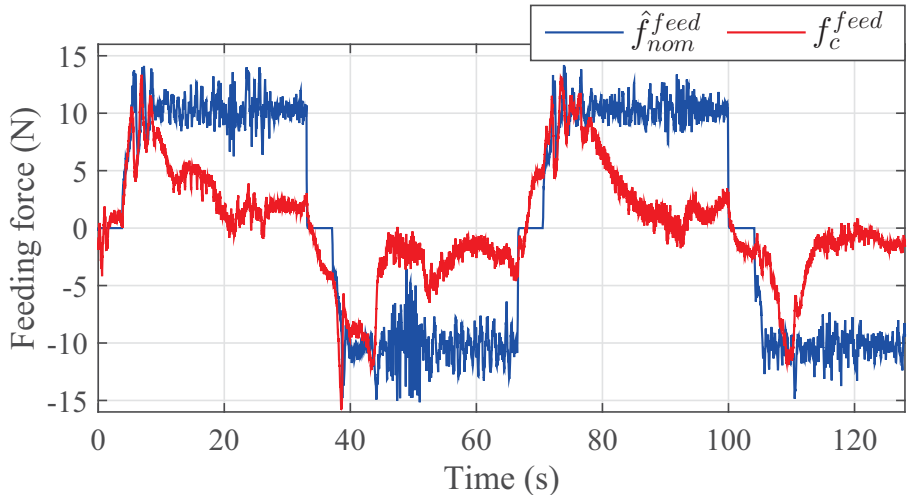

(a) Nominal estimated feeding force vs. the measured one

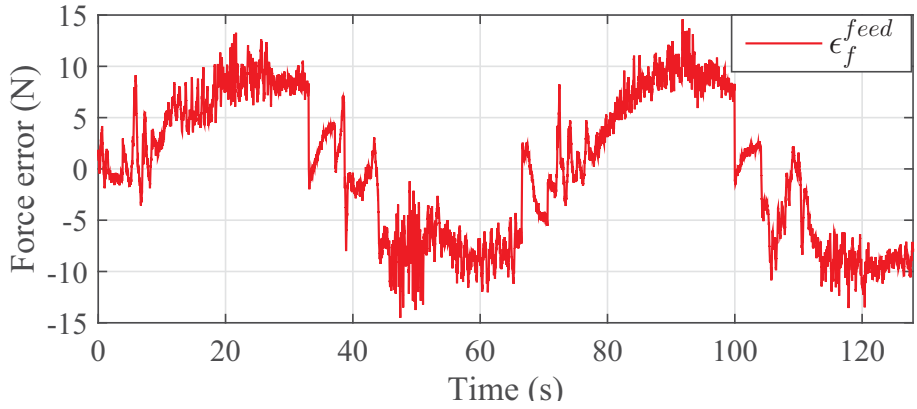

(b) Feeding force difference

Figure 3.54: Feeding force variation

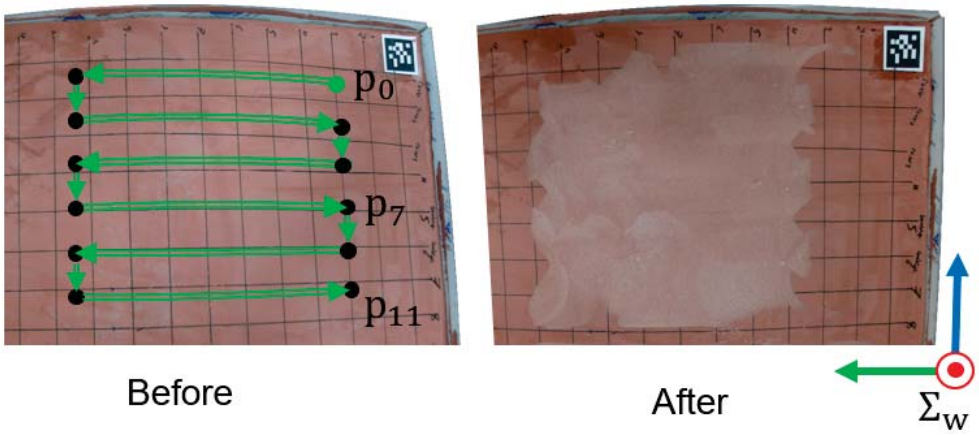

Figure 3.55: Convex wall top view before and after grinding straightly between the way-points p_0 to p_{11}

The grinding quality on the convex surface is evaluated as well. The ground surface of the wall is described in Figures 3.56, 3.57 and 3.58. Figure 3.56a shows the superposition of the meshes measured before and after grinding. The depth of the cut can be obtained by calculating the Euclidean distances between the points of the meshes measured before and after grinding. A top view of the map describing the depth of the cut is shown in Figure 3.57. Addition to that Figure 3.58 shows the depth of the cut evaluated under the curves C_1 to C_7 shown in Figure 3.56b. The Figure shows that the grinding depth varies between 0 and 3.5 mm in the ground area. The average depth of the cut under each Curve C_i is shown in the Figure 3.58 and the overall average depth of the cut in the ground area is 1.64 mm.

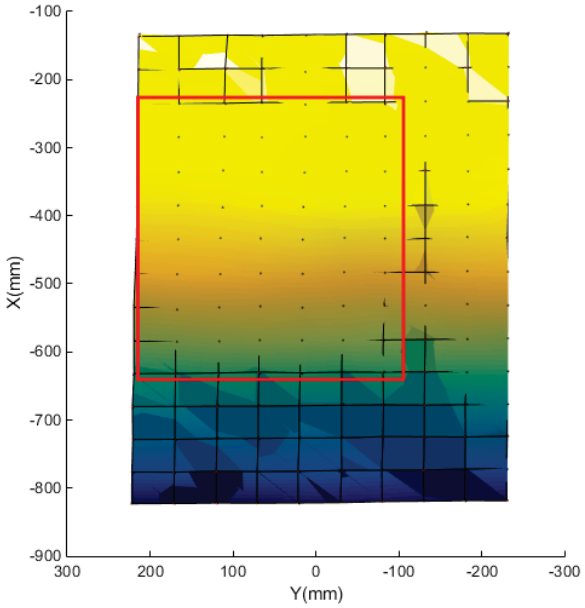

(a) Top view of the superposed meshes describing the convex wall surface geometry before and after grinding. The meshes are measured in the coordinate-measurement machine frame {M} shown in figure 3.42a

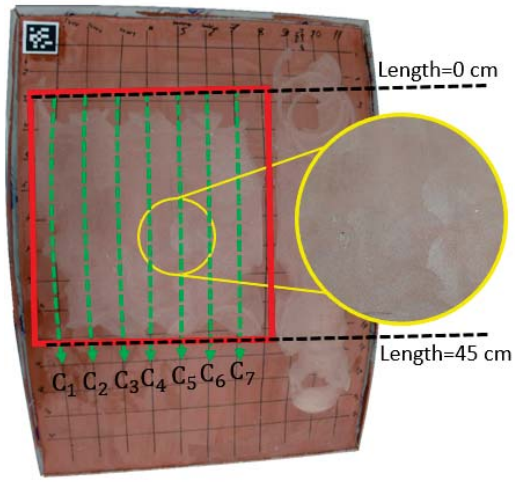

(b) Convex wall top view after grinding. The length of the ground area is 45 cm, its depth is evaluated under the curves C_1 to C_7

Figure 3.56: The surface state of the convex wall evaluated before and after grinding. Inside the red boxes, where the mesh disappears, is the ground area

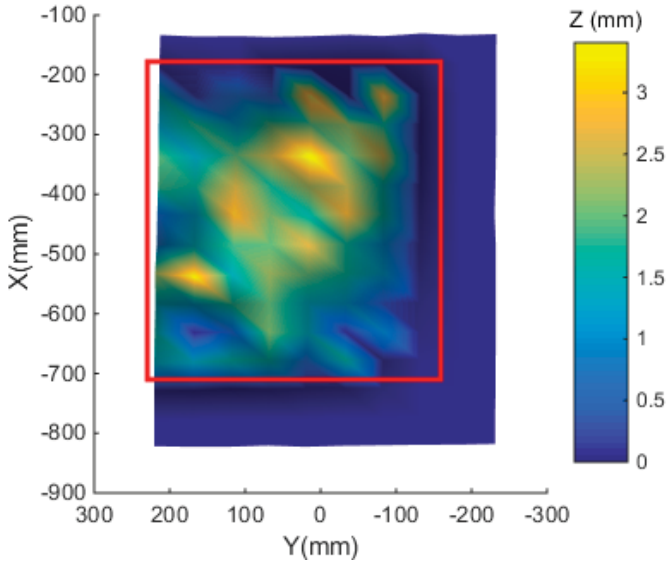

Figure 3.57: Depth map describing the shortest distance (depth of the cut) between the meshes before and after grinding shown in Figure 3.56a

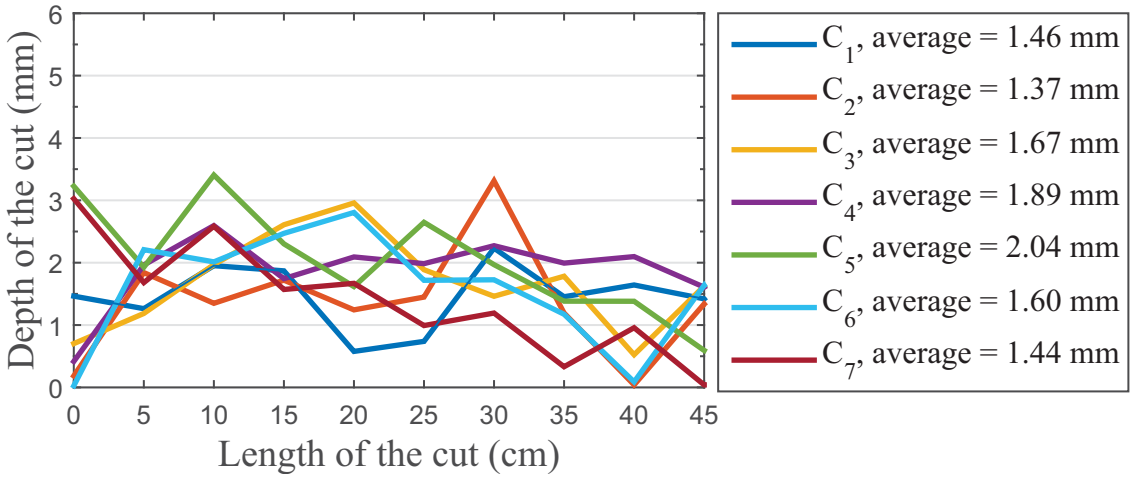

Figure 3.58: Grinding path depth evaluated under the curves C_1 to C_7 shown in Figure 3.56b

Case 3: concave surface

Similar to the test on the convex wall, the robot is commanded to grind the path determined by the way-points (p_0 to p_{10}) in Figure 3.63 with desired velocity v_{norm} on the concave wall shown in Figures 3.42c and 3.63. The disc starts very near to the surface with ${}^{o}\theta^{z} = 0.03$ radians. When the control switches completely to force along ${}^{cf}\vec{x}$ the robot executes the trajectory. The desired and response values of force and velocity controllers are shown in Figures 3.59a and 3.60a respectively. The controller performance is good in force and velocity tracking, the tracking errors are shown in Figures 3.59b and 3.60b, the RMSE of the force along the path is 1.16 N and the RMSE of the velocity is 0.0027 m/s. Figure 3.61a shows how ${}^{o}\theta^{z}$ varies and tries to track the concave shape of the wall shown in Figures 3.42c and 3.42e. Similar to previous tests, ${}^{cf}\vec{x}$ ${}^{o}\theta^{z}$ varies as function of the pure contact feeding force f_c^{feed} acting on the disc (Figure 3.62a). The robot orients the tool to minimize the difference between the feeding force f_c^{feed} and the estimated one ($\hat{f}_{nom}^{feed}$). The orientation controller is accurate, the error is bounded as Figure 3.61b shows, it tracks the ${}^{o}\theta^{z}_{des}$ along the path with RMSE equals to 0.001 radians. Although the controller performances are good here, the grinding quality is not as good as the previous tests. The reason for this is that the controller is getting fooled when performing on such kind of surface. Looking at Figure 3.61a, the zones A, B and C correspond to the disc velocity v_{norm} along ${}^{w}\vec{y}$. In these zones, the ${}^{o}\theta^{z}_{des}$ varies with small values. This happened because the radius of the curvature is small. Thus, the disc couldn't be in full contact with the wall. Therefore the nominal feeding force is not so correct leading the disc to keep its orientation in order to maintain the nominal feeding force.

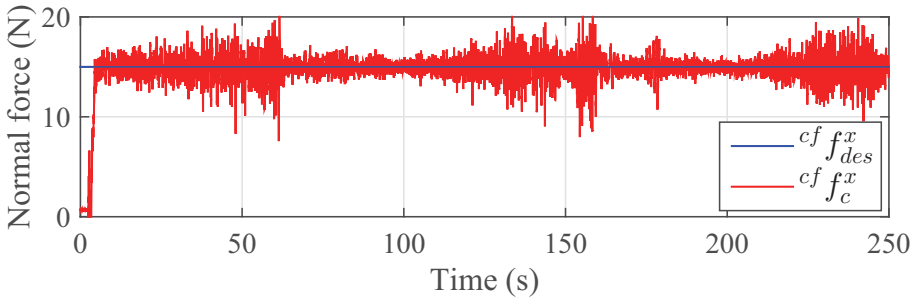

(a) Force tracking

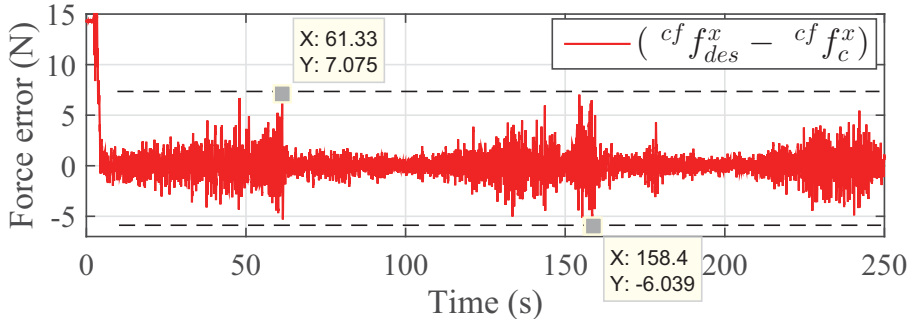

(b) Force tracking error

Figure 3.59: Force control performance in tracking the desired force value

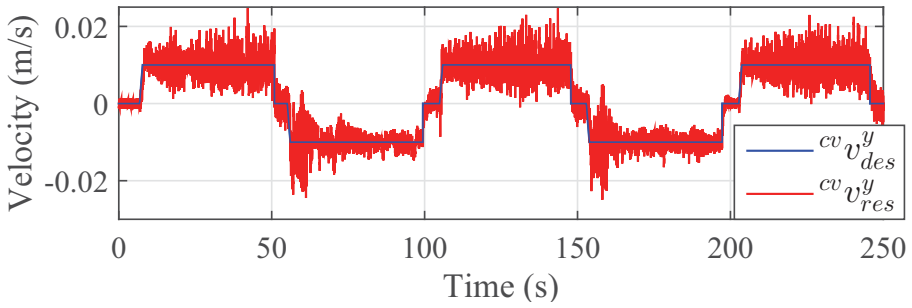

(a) Velocity tracking

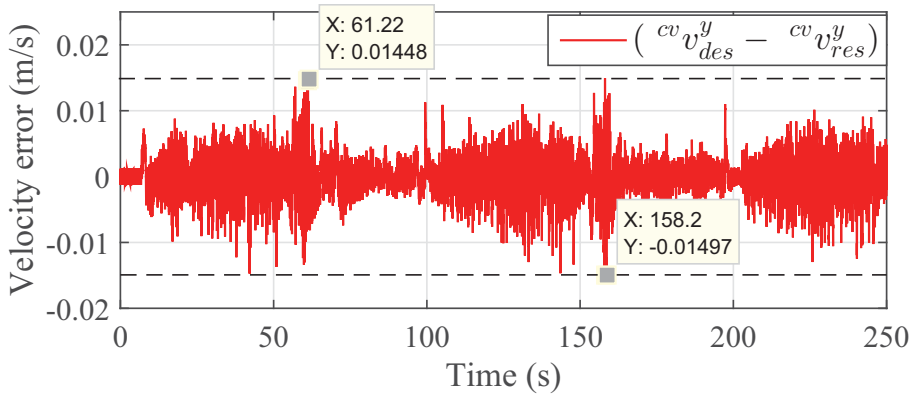

(b) Velocity tracking error

Figure 3.60: Velocity control performance in tracking the desired velocity value

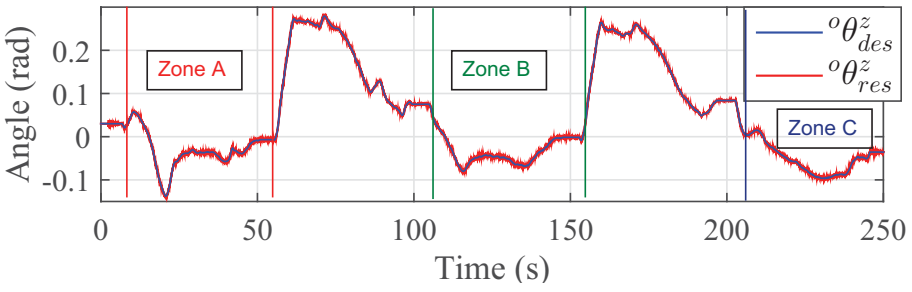

(a) Orientation tracking

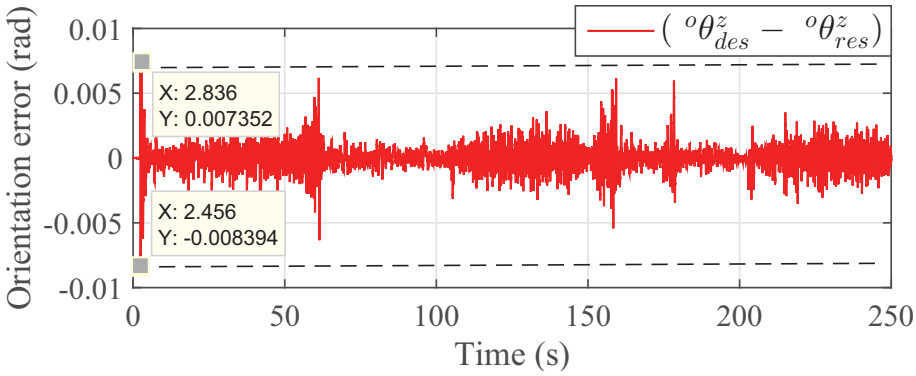

(b) Orientation tracking error

Figure 3.61: Orientation control performance in tracking the desired angle value

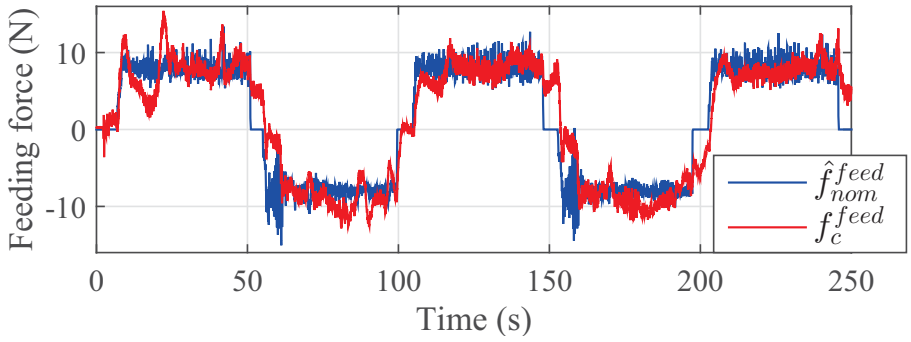

(a) Nominal estimated feeding force vs. the measured one

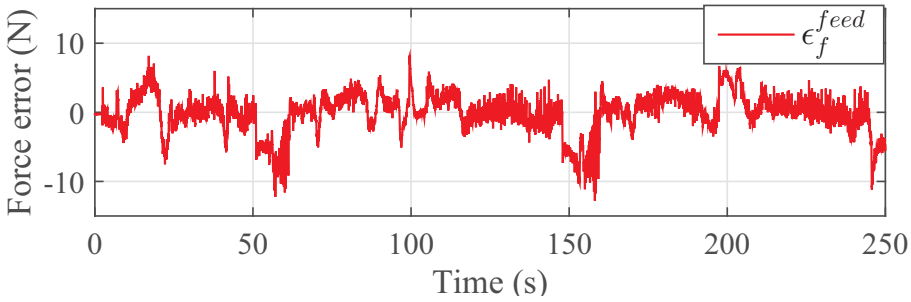

(b) Feeding force difference

Figure 3.62: Feeding force variation

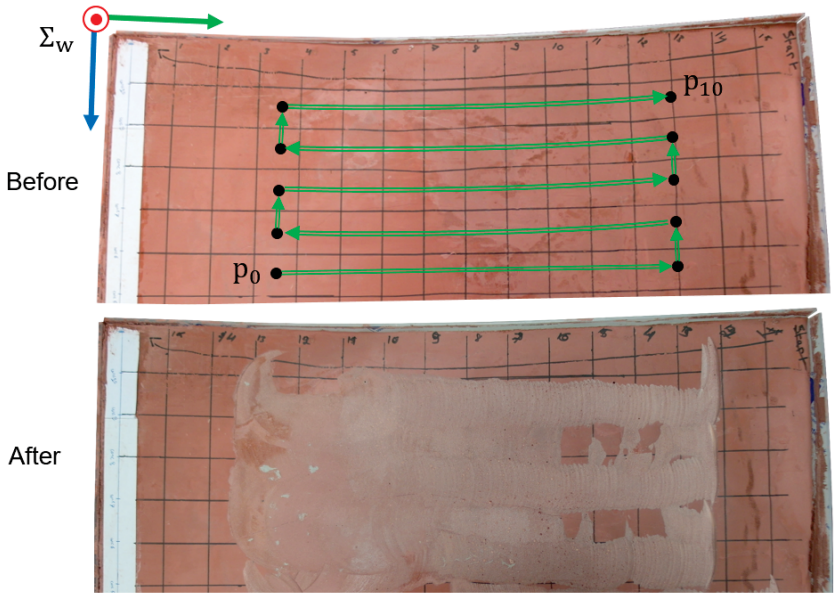

Figure 3.63: Concave wall top view before and after grinding straightly between the way-points p_0 to p_{10}

The grinding quality on the concave surface is evaluated additionally. The ground surface of the wall is described in Figures 3.64, 3.65 and 3.66. The superposition of the meshes before and after grinding is shown in Figure 3.64a. Similar to the previous case, the depth of the cut is obtained by calculating the Euclidean distances between the points of the meshes measured before and after grinding. A top view of the map describing the depth of the cut is shown in Figure 3.65. Addition to that Figure 3.66 shows the depth of the cut evaluated under the curves C_2 to C_5 shown in Figure 3.64b. The Figure shows that the grinding depth varies between 0 and 2.5 mm in the ground area. The average depth of the cut under each Curve C_i is shown in the Figure 3.58 and the overall average depth of the cut in the ground area is 1.43 mm.

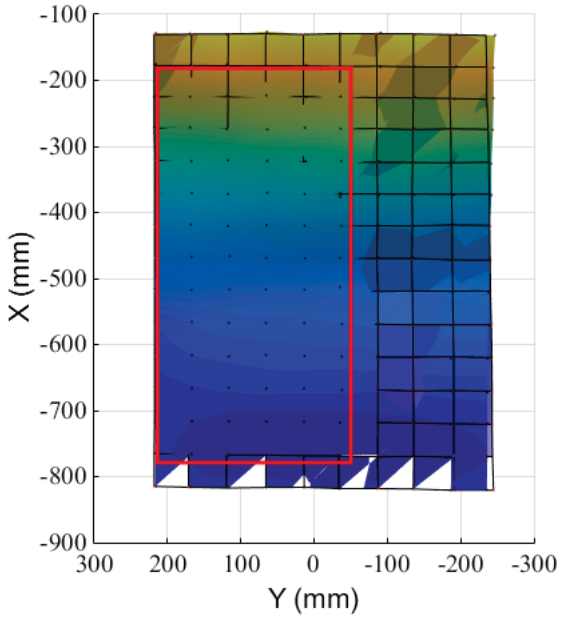

(a) Top view of the superposed meshes describing the concave wall surface geometry before and after grinding. The meshes are measured in the coordinate-measurement machine frame {M} shown in figure 3.42a

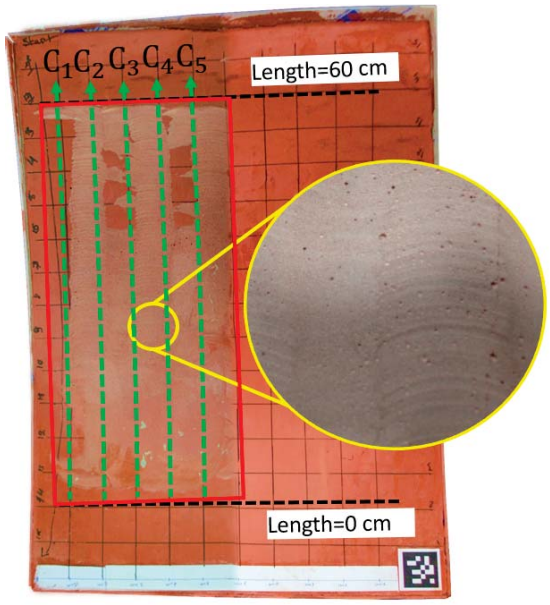

(b) Concave wall top view after grinding. The length of the ground area is 60 cm, its depth is evaluated under the curves C_1 to C_5

Figure 3.64: The surface state of the concave wall evaluated before and after grinding. Inside the red boxes, where the mesh disappears, is the ground area

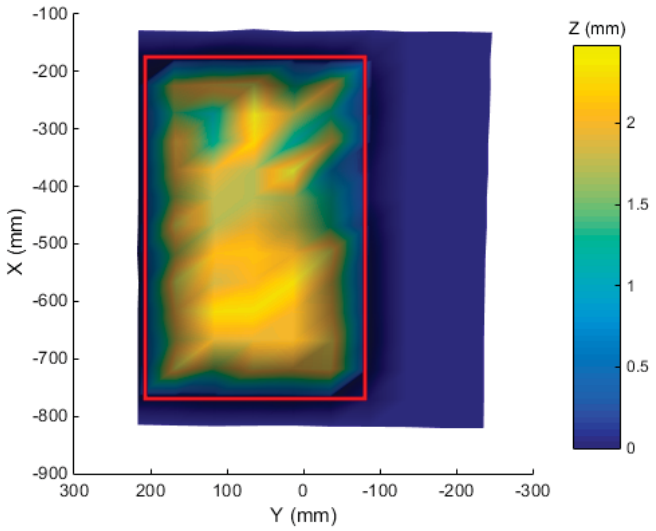

Figure 3.65: Depth map describing the shortest distance (depth of the cut) between the meshes before and after grinding shown in Figure 3.64a

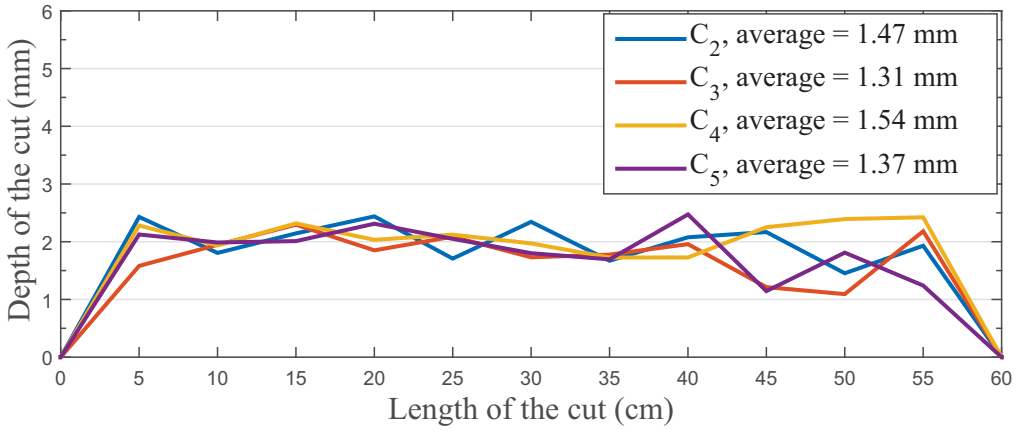

Figure 3.66: Grinding path depth evaluated under the curves C_2 to C_5 shown in Figure 3.64b

3.4.6 Discussions

As described in section 3.4.4.2, the surface tracking is established by modifying the orientation commands on-line based on a feeding grinding force model that was developed. Hence, it is important to mention here that the proposed controller does not aim for precise feeding grinding force tracking, but surface tracking based on the feeding force. Thus, the feeding force errors in Figures 3.47b, 3.54b and 3.62b are not critical. In general, the less the feeding force variations are, the smoother the grinding is. Nevertheless, the feeding grinding force is sensible and can be variable as the resurfacing material itself is not uniform and the wall surface can not be perfect before grinding (ex: Figure 3.42d).

Concerning the grinding quality, it was evaluated for the three test cases and good grinding was shown. The grinding quality can be seen visually in Figures 3.49b, 3.56b and 3.64b. The depth of the grinding cut in the flat wall case is around 1.8 mm (refer to Figure 3.50). For the convex wall case, the depth of the cut varies between 0 and 3.5 mm (refer to Figure 3.58). And for the concave wall case the depth of the cut is around 2 mm (refer to Figure 3.66). The main reason why the depth of the cut in the tests is not constant is that it is not controlled directly, i.e., the depth of the cut should be around 2 mm (the depth of the automatic grinding tests used for identifying the nominal grinding feeding force in section 3.4.2) if the robot executes the identified normal force and the feeding velocity on the wall. In addition to that, the walls surface was not smooth before grinding (it had some bumps). Moreover, the feeding grinding force model used is valid when the disc is in full contact with the wall (see Figure 3.35). In case the radius of curvature of the surface to be ground is small, the disc will not be in full contact with the wall, and then the feeding force model will have some error which in turn will lead to some variations in the depth of the cut.

3.4.7 Conclusions

In section 3.4, a model based adaptive hybrid position-velocity-force controller for wall grinding is presented. Its is developed to overcome the shortcomings of the controller presented in section 3.3. Hence, the nominal grinding feeding force is predicted using a model obtained through identification tests. Moreover, the orientation of the disc on the wall is controlled by an adaptive position controller, the orientation controller is based on an adaptive function that minimizes the error in feeding grinding force. The desired normal contact force and the velocity tracking on the wall are achieved by the velocity-force controller. The unified controller has been tested on KUKA LWR equipped with a grinding tool and a force-torque sensor. As the force-torque sensor reads both contact and non-contact forces, the latter are estimated and eliminated from the sensor readings by the recurrent neural network disturbance observer. Grinding tests were done on 3 different surface geometries: flat, convex and concave. Although the geometries of the surfaces were not known before hand, the grinding task was achieved with the disc exerting a normal force of 15 N on the wall surface while tracking its curvature. The experimental results showed good velocity, force and orientation tracking performances. In addition to that, the grinding quality is evaluated and the controller is promising. The shortcomings of the controller are discussed, and further work would be focused on collecting a bigger amount of grinding data with more variations in forces and velocities to have more accurate feeding force model. Additional improvement to the orientation controller can be achieved by adding zero moment control to the adaptive one in order to adjust the rotation θ_z around ${}^{cv}\vec{z}$.

3.5 Summary

This chapter introduced the research field of robot-environment interaction. It also reviewed the recent technical advances in metallic polishing and grinding operations. The presented studies showed that a variety of polishing and grinding systems can be realized by passive compliance or active compliance that combines position and force control. Based on the existing studies, two wall grinding controllers were proposed in this chapter. The principles of these controllers were explained and a proper evaluation method was presented.

It has been challenging to replace the humans in such wall grinding activities that require contact with unstructured environments. However, adaptive hybrid position-velocity-force controllers may provide a solution to this problem. The proposed control techniques have the potential to trigger industrial innovations in the construction industry. Thus, using these controllers, it is possible to automate the wall grinding operation and let the robots take over the hazardous human activities in the construction industry (ex: asbestos removal). The proposed controllers were verified experimentally by using a 7-DOF manipulator equipped with a grinder and six dimensional force torque sensor. Although the model-based adaptive hybrid position-velocity-force method had better performance compared to hybrid position-force control with compliant wrist, yet there is a wide scope of development of new control techniques that can serve in perfectly automating such dangerous and tiring tasks.

Chapter 4

Mobile Manipulator Control for On-line Tip-over Avoidance

Due to their significant maneuverability and large workspace, mobile manipulators have attracted the interest of researchers in last years. The system generally consists of a mobile base with a robotic arm fixed on its top. Such systems are being widely deployed in industry and service, for example, risky tasks such as fire fighting and transportation of toxic materials like asbestos and nuclear wastes (Bots2ReC [2015] and Shneier and Bostelman [2015]). Besides, the stability of mobile manipulators can be affected if the center of mass (COM) is relatively high and the support polygon is small. Additionally, the stability of mobile manipulators is affected by the high dynamic motions and the forces applied by their end-effector on the environment. Thus, stability constraints limit the efficiency and productivity of mobile manipulators as they might tip over. For the various applications of mobile manipulators, several stability strategies have been considered and they can be classified in three categories, namely: (1) stability monitoring and evaluation through static and dynamic indices, (2) off-line planning based on stability constraints and (3) on-line stability control.

In the first category, a vast research has been done. The shortest horizontal distance between the COM and the support pattern boundary projected onto a horizontal plane was used as static stability index in Orin et al. [1976], McGhee and Frank [1968] and McGhee and Iswandhi [1979]. Other static approaches like the gradient based method and the potential energy criterion were proposed to evaluate stability in Hirose [1978] and Messuri and Klein [1985], then the use of projection plane was eliminated using a net force vector in Sreenivasan and Wilcox [1994]. However, static approaches were not efficient for top-heavy systems with high dynamics and the zero moment point was introduced for the first time in the context of mobile manipulators in Sugano et al. [1993]. The authors of Ghasempoor and Sepehri [1995], Papadopoulos and Rey [1996] and Yoneda and Hirose [1996] have considered forces and system dynamics. They introduced them to the criteria proposed in Messuri and Klein [1985], Hirose [1978] and McGhee and Frank [1968] respectively. Evaluation of the previous approaches was presented in Moosavian and Alipour [2007] and a new tip-over stability measure based on moments was derived. Although it is true that the indices in category (1) were able to detect falling, regardless of their accuracy, they are not sufficient to recover or avoid tumbling when the system dynamics are significant. To deal with this issue, researchers have been studying motion planning for mobile manipulators considering stability (category (2)). A plan that permits a mobile manipulator to execute quick tasks considering

the dynamic limits of the vehicle is presented in Dubowsky and Vance [1989]. Redundancy was used for optimal task planning and stability in Carriker et al. [1991]. In Huang et al. [1994], Huang and Sugano [1995] and Huang et al. [2000], ZMP was used to plan motions based on gradient methods and inertias, but the kinematic and force restraints on the end-effectors were not considered. Conventional methods developed in category (1) were used to plan stable motions in Yoneda and Hirose [1996], then stability was evaluated using the forces and moments acting on the line connecting two contact points. More research that studied the stability of mobile manipulators during the planning stage is presented in Nunez et al. [2006] and Wang et al. [2009]. Yet, off-line motion planning and optimization processes are time consuming, they can not handle general situations and overcome disturbances. When the end-effector motion is subject to disturbances or is driven based on a sensor, some reactions need to be done in real time to compensate instability. Finally, in category (3), many works benefit from the base/arm motions to compensate the stability on-line. In Orin et al. [1976] and Fukuda et al. [1992] the center of gravity is used to optimize and control stability, but the dynamics were ignored. In Huang et al. [1998], Furuno et al. [2003] and Kim and Chung [2006] the vehicle-arm motion coordination is based on potential functions and the valid stable regions are based on (ZMP) criterion. However, these methods are weak in treating dynamic environments and have less efficiency in moving the robot as one synchronized unit. The arm motions were used for stability compensation in Choi et al. [2012] and Lee et al. [2012]. They showed good performance but there was no restriction on the behaviors of the end-effector. Works that deal with on-line stability control using fuzzy logic, neural networks and quadratic programming were presented in Li and Liu [2006], Ghaffari et al. [2008] and Yu et al. [2010]. On-line stability control challenges come from the dynamic coupling between the mobile base and the arm on one hand, and the nonholonomic constraints of the base on the other. These two issues have been taken into consideration in the literature of mobile manipulators control. Decentralized control for base and arm have been developed in Liu and Lewis [1990], Yamamoto and Yun [1992], Khatib et al. [1996b] and Chung and Velinsky [1999]. Although the interaction between the two controllers is considered, it still difficult to tune as mentioned in Yamamoto and Yun [1994] and Yamamoto and Yun [1996]. On the contrary, centralized controllers that deal with the robot as one system are presented in Miksch and Schroeder [1992], Seraji [1998], Umeda et al. [1999] and Tan and Xi [2001].

In this chapter, a unified dynamic scheme that actively controls the stability of the whole system on a desired point is presented. Additionally, unlike previous methods that use ZMP and ignore the errors in COM positions of the links and their inertia, the ZMP reference used in the proposed controller is based on disturbance observer presented in Section 2.3 that estimates the effect of the mentioned errors. The proposed method does not need planning and it is based on real time adaptive control to damp the oscillatory motions. Feed-forward terms are used to track the desired stable point on the ground to prevent the robot from tipping over. The end-effector constraints to follow a desired spatial trajectory are retained at the same time.

4.1 Control Framework

4.1.1 Operational space dynamics

To develop a unified kinematic and dynamic models for the whole system, the mobile base is considered as a set of virtual joints and modeled along with the manipulator

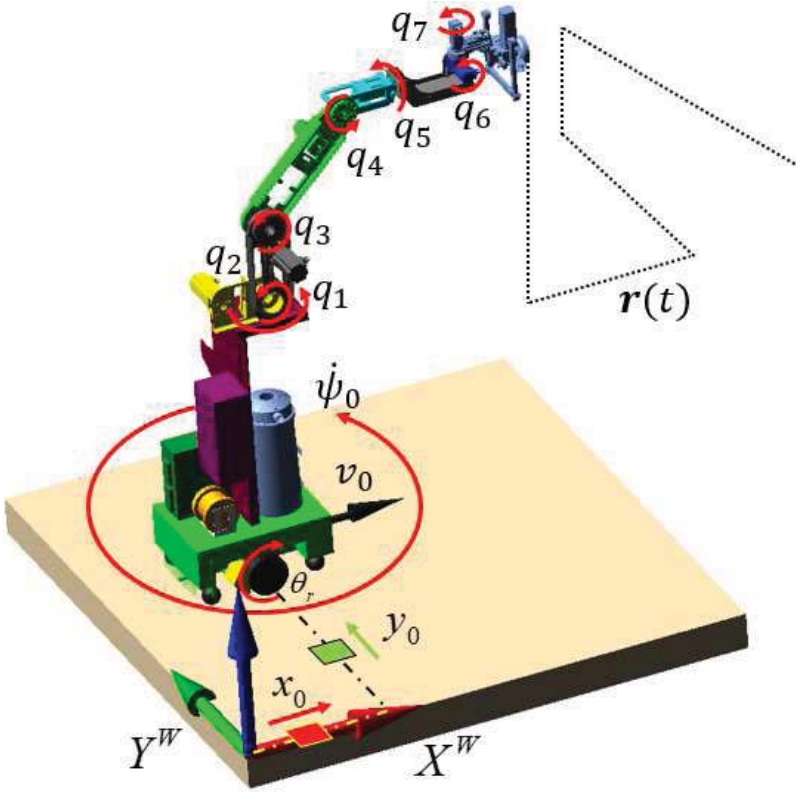

Figure 4.1: A top heavy mobile manipulator following a spatial trajectory $\boldsymbol{r}(t)$ is critically unstable and might tip over. The kinematics of the robot are depicted in the figure above

(Figure 4.1). The operational space dynamics of a robot with m-dof executing a general task of n-dof can be expressed as,

$$\boldsymbol{W}_{cmd} = \boldsymbol{\Lambda}(\boldsymbol{q})\boldsymbol{\alpha}_m + \boldsymbol{\mu}(\boldsymbol{q}, \dot{\boldsymbol{q}}) \tag{4.1}$$

$\boldsymbol{q} = [\boldsymbol{q}_b, \boldsymbol{q}_a]^T$ is the m joint positions. $\boldsymbol{q}_b$ is the base virtual joints $[x_0, y_0, \psi_0]^T$, and $\boldsymbol{q}_a$ is the arm joint positions $[q_1 ... q_{m-3}]^T$. $\boldsymbol{W}_{cmd} \in R^n$ is the generalized end-effector wrench (Khatib et al. [1996a]), $\boldsymbol{\alpha}_m$ is the motion acceleration command. $\boldsymbol{\mu}(\boldsymbol{q}, \dot{\boldsymbol{q}})$ is the $(n \times 1)$ function to compensate for Coriolis, gravitational and friction forces in the workspace. $\boldsymbol{\Lambda}(\boldsymbol{q})$ is the pseudo-inertia matrix defined by:

$$\boldsymbol{\Lambda}(\boldsymbol{q}) = (\boldsymbol{J}(\boldsymbol{q})\boldsymbol{A}(\boldsymbol{q})^{-1}\boldsymbol{J}^T(\boldsymbol{q}))^{-1} \tag{4.2}$$

with $\boldsymbol{J}(\boldsymbol{q})$ denoting the $(n \times m)$ kinematic Jacobian matrix, $\boldsymbol{A}(\boldsymbol{q})$ is the full rank $(m \times m)$ robot inertia matrix. Finally, for a redundant system with $m > n$ the joint forces $\boldsymbol{\tau}_{cmd} = [\boldsymbol{\tau}_b, \boldsymbol{\tau}_a]^T$ corresponding to $\boldsymbol{W}_{cmd}$ are:

$$\boldsymbol{\tau}_{cmd} = \boldsymbol{J}^T(\boldsymbol{q})\boldsymbol{W}_{cmd} + (\boldsymbol{I} - \boldsymbol{J}^T(\boldsymbol{q})\tilde{\boldsymbol{J}}^T(\boldsymbol{q}))\boldsymbol{\tau}_{null} + \boldsymbol{\tau}_{dis} \tag{4.3}$$

$\tilde{\boldsymbol{J}}(\boldsymbol{q})$ is the dynamically consistent generalized inverse:

$$\tilde{\boldsymbol{J}}(\boldsymbol{q}) = \boldsymbol{A}^{-1}(\boldsymbol{q})\boldsymbol{J}^T(\boldsymbol{q})\boldsymbol{\Lambda}(\boldsymbol{q}) \tag{4.4}$$

$\boldsymbol{\tau}_{null}$ are joint forces that can be applied in the null space without affecting the end-effector's dynamic behavior. In case $n >= m$, the system is not redundant and the

second term in eq.(4.3) will be canceled. $\boldsymbol{\tau}_{dis}$ is the disturbance torque on the joints:

$$\boldsymbol{\tau}_{dis} = \boldsymbol{\tau}_{int} + \boldsymbol{\tau}_{ext} + \boldsymbol{\tau}_{fri} + \boldsymbol{\tau}_{unc} \tag{4.5}$$

The disturbance torques $\boldsymbol{\tau}_{int}, \boldsymbol{\tau}_{ext}, \boldsymbol{\tau}_{fri}$ and $\boldsymbol{\tau}_{unc}$ are the internal, external, friction and uncertain motor dynamics respectively, they can be compensated using the DOB presented in Section 2.2. If the base is subject to nonholonomic constraints, its corresponding virtual joint forces, $\boldsymbol{\tau}_b = [f_{x0}, f_{y0}, \tau_{z0}]^T$ needs to be transposed into the differential wheels torque $\boldsymbol{\tau}_w$ as:

$$\boldsymbol{\tau}_w = \boldsymbol{J}_d^+ \boldsymbol{\tau}_b \tag{4.6}$$

$\boldsymbol{J}_d$ is a dynamic Jacobian that takes into account the nonholonomic constraints and $\boldsymbol{J}_d^+$ is its pseudo inverse, they are dependent on the mobile base type. For differential drive robots (ex: Figure 4.1) they can be expressed as:

$$\boldsymbol{J}_d = \begin{bmatrix} \frac{1}{R}\cos\psi_0 & \frac{1}{R}\cos\psi_0 \\ \frac{1}{R}\sin\psi_0 & \frac{1}{R}\sin\psi_0 \\ \frac{W}{2R} & \frac{-W}{2R} \end{bmatrix} \tag{4.7}$$

$$\boldsymbol{J}_d^+ = \begin{bmatrix} \frac{R\cos\psi_0}{2} & \frac{R\sin\psi_0}{2} & \frac{R}{W} \\ \frac{R\cos\psi_0}{2} & \frac{R\sin\psi_0}{2} & -\frac{R}{W} \end{bmatrix} \tag{4.8}$$

W, R and ψ_0 are the mobile base parameters defined in Table 4.1.

4.1.2 Operational space position control of the end-effector

Position control can be achieved by setting the acceleration command $\boldsymbol{\alpha}_m$ in equation 4.1 as,

$$\boldsymbol{\alpha}_m = \ddot{\boldsymbol{r}}_{des}(t) + \boldsymbol{K}_{Dr}[\dot{\boldsymbol{r}}_{des}(t) - \boldsymbol{v}_{res}(t)] + \boldsymbol{K}_{Pr}[\boldsymbol{r}_{des}(t) - \boldsymbol{p}_{res}(t)] \tag{4.9}$$

$\boldsymbol{v}_{res}$ and $\boldsymbol{p}_{res}$ are the velocity and position response of the end-effector computed by the direct kinematics; $\boldsymbol{K}_{Dr}$ and $\boldsymbol{K}_{Pr}$ are suitable gain matrices; $\boldsymbol{r}_{des}(t)$, $\dot{\boldsymbol{r}}_{des}(t)$ and $\ddot{\boldsymbol{r}}_{des}$ are the desired pose, twist and acceleration tracking inputs as,

$$\boldsymbol{r}_{des} = [x_{des} \;\; y_{des} \;\; z_{des} \;\; \theta^x_{des} \;\; \theta^y_{des} \;\; \theta^z_{des}]^T \tag{4.10}$$

$$\dot{\boldsymbol{r}}_{des} = [v^x_{des} \;\; v^y_{des} \;\; v^z_{des} \;\; \omega^x_{des} \;\; \omega^y_{des} \;\; \omega^z_{des}]^T \tag{4.11}$$

$$\ddot{\boldsymbol{r}}_{des} = [\dot{v}^x_{des} \;\; \dot{v}^y_{des} \;\; \dot{v}^z_{des} \;\; \dot{\omega}^x_{des} \;\; \dot{\omega}^y_{des} \;\; \dot{\omega}^z_{des}]^T \tag{4.12}$$

They are smooth enough for the operational space control in section 4.1.1. Here, they are obtained from the trapezoidal trajectory generator with continuous acceleration as detailed in Khalil and Dombre [2004].

4.1.3 Stability controller

4.1.3.1 Mobile base velocity controller

The modeling parameters of the mobile base are defined in Table 4.1 and depicted in Figure 4.2. The linear and angular velocities of the base can be calculated as a function of the wheels angular speed as,

$$\begin{bmatrix} v_0 \\ \dot{\psi}_0 \end{bmatrix} = \boldsymbol{J}_k \begin{bmatrix} \dot{\theta}_r \\ \dot{\theta}_l \end{bmatrix} \tag{4.13}$$

Table 4.1: Mobile base parameters.

Variable	Unit	Explanation
W	m	Gauge of fixed wheels
R	m	Radius of fixed wheels
x_0, y_0	m	Base center position in the world frame
ψ_0	rad	Base orientation
θ_r, θ_l	rad	Rotation angle of the wheels
m	kg	Total mass of mobile manipulator
I_W	kgm^2	Inertia of the wheels
I_ψ	kgm^2	Inertia around the center of the cart
$\mathbf{B}_n$		Nominal inertia matrix
$\boldsymbol{K}_v$		Diagonal velocity gain matrix

$\boldsymbol{J}_k$ is the kinematic Jacobian defined as:

$$\boldsymbol{J}_k = \begin{bmatrix} \frac{R}{2} & \frac{R}{2} \\ \frac{R}{W} & -\frac{R}{W} \end{bmatrix} \tag{4.14}$$

Changing the input velocity to the wheels rotational speed gives:

$$\begin{bmatrix} \dot{\theta}_r \\ \dot{\theta}_l \end{bmatrix} = \boldsymbol{J}_k^{-1} \begin{bmatrix} v_0 \\ \dot{\psi}_0 \end{bmatrix} \tag{4.15}$$

Consequently, the 2^{nd} order kinematics can be expressed as:

$$\begin{bmatrix} \ddot{\theta}_r \\ \ddot{\theta}_l \end{bmatrix} = \boldsymbol{J}_k^{-1} \begin{bmatrix} \dot{v}_0 \\ \ddot{\psi}_0 \end{bmatrix} \tag{4.16}$$

Considering the mass of the whole system, nominal dynamics on the wheels can be written as,

$$\boldsymbol{\tau}_w = \boldsymbol{B}_n \ddot{\boldsymbol{\theta}}_{ref} \tag{4.17}$$

$\boldsymbol{\tau}_w = [\tau_r, \tau_l]^T$ is the torque applied on the wheels and $\ddot{\boldsymbol{\theta}}_{ref} = [\ddot{\theta}_r^{ref}, \ddot{\theta}_l^{ref}]^T$ is the wheels acceleration reference. By applying the Lagrange-Euler formulation to equation 4.17, the nominal inertia matrix $\boldsymbol{B}_n$ can be expressed as,

$$\boldsymbol{B}_n = \begin{bmatrix} \frac{mR^2}{4} + I_W + \frac{R^2}{W^2} I_\psi & 0 \\ 0 & \frac{mR^2}{4} + I_W + \frac{R^2}{W^2} I_\psi \end{bmatrix} \tag{4.18}$$

The velocity controller of the mobile base can be derived as:

$$\boldsymbol{\tau}_w = \boldsymbol{B}_n \ddot{\boldsymbol{\theta}}_{ref} = \boldsymbol{B}_n \big(\boldsymbol{K}_v (\dot{\boldsymbol{\theta}}_{des} - \dot{\boldsymbol{\theta}}_{res}) + \ddot{\boldsymbol{\theta}}_{des} \big) \tag{4.19}$$

4.1.3.2 Zero moment point control in the null space

In the proposed approach, the $\widehat{ZMP}$ is obtained from the zero-moment-point observer presented in Section 2.3, it is expressed in the mobile base frame as shown in Figure 4.2. The desired point ZMP_{des} lies on the x-axis of the mobile base x_m as it is proven to be the stablest place (Sugano et al. [1993]). For a general arm, with $n \geq 6$ the mobile base can be controlled in the null space and the motions generated by $\boldsymbol{\tau}_w$ will fall in $\boldsymbol{\tau}_{null}$ in

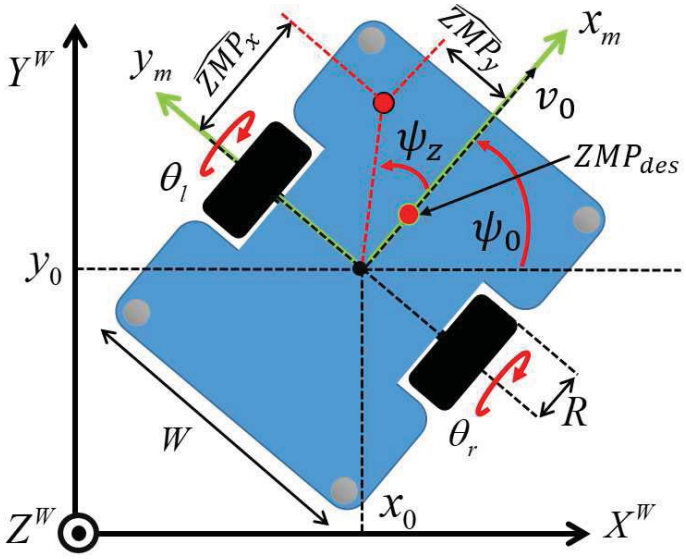

Figure 4.2: Mobile base modeling

equation 4.3 by using eq.(4.6). Hence, the stability controller can be designed using the velocity controller presented in Section 4.1.3.1 to maintain the $\widehat{ZMP}$ on ZMP_{des} as,

$$\begin{aligned} v_0^{cmd} &= K_{ps}(\widehat{ZMP}_x - ZMP_{des}) + K_{ds}(COM_x - \widehat{ZMP}_x) \\ &\quad + \dot{r}_{des}^x(t)\cos(\psi_0) + \dot{r}_{des}^y(t)\sin(\psi_0) \end{aligned} \tag{4.20}$$

$$\dot{\psi}_0^{cmd} = K_{p\psi}\psi_z + K_{d\psi}(\psi_z - \psi_c) \tag{4.21}$$

$$\dot{v}_0^{cmd} = \ddot{r}_{des}^x(t)\cos(\psi_0) + \ddot{r}_{des}^y(t)\sin(\psi_0) \tag{4.22}$$

with the angles ψ_z and ψ_c measured from x_m to $\widehat{ZMP}$ and the COM positions in the base frame respectively:

$$\begin{cases} \psi_z = \arctan 2(\widehat{ZMP}_y, \widehat{ZMP}_x) \\ \psi_c = \arctan 2(\widehat{COM}_y, \widehat{COM}_x) \end{cases} \tag{4.23}$$

$$COM_x = \frac{\Sigma_{i=1}^m m_i x_i}{\Sigma_{i=1}^m m_i}, COM_y = \frac{\Sigma_{i=1}^m m_i y_i}{\Sigma_{i=1}^m m_i} \tag{4.24}$$

The adaptive terms $(COM_x - \widehat{ZMP}_x)$ and $(\psi_z - \psi_c)$ are used to damp the high dynamic motions of the ZMP. It is acknowledged that the COM is static with low dynamics compared to ZMP. The velocity and acceleration commands of the base in equations 4.20 to 4.22 can be applied to the wheels torques $\boldsymbol{\tau}_w$ using equations 4.15, 4.16 and 4.19. The latter is then changed to the corresponding virtual joint forces of the base as:

$$\boldsymbol{\tau}_b = \boldsymbol{J}_d \boldsymbol{\tau}_w \tag{4.25}$$

4.1.4 Maximum manipulability in the null space

When the manipulability of manipulator goes low in the direction of motion, the mobile manipulator can be easily affected by disturbance and its motion becomes unstable. For the redundant arm in Figure 4.1, maximum manipulability is used to solve the

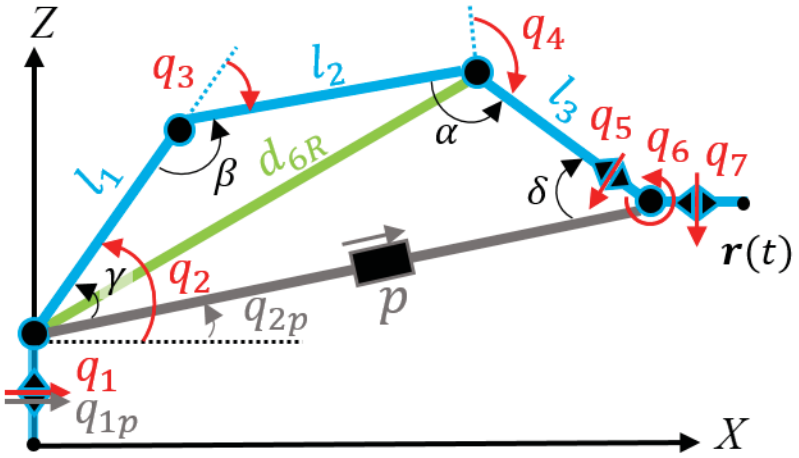

Figure 4.3: 7-dof robotic arm kinematics for maximum manipulability.

redundancy. For desired position $\boldsymbol{r}_{des}(t)$, the inverse geometric model (IGM) of the prismatic robot (q_{1p}, q_{2p}, p) gives $q_{1p}^{max}, q_{2p}^{max}$ and p_{max}. For the maximum manipulability $w_{max} = max(\sqrt{det(\boldsymbol{J}(\boldsymbol{q})\boldsymbol{J}^T(\boldsymbol{q}))})$ with respect to the desired position, the quadrilateral formed by connecting (q_2, q_3, q_4, q_6) needs to be with maximum possible area, this can be deduced from Yoshikawa [1985]. Its inner angles in Figure 4.3 will be,

$$\begin{cases} \alpha = acos\left(\frac{l_2^2+l_3^2-l_1^2-p_{max}^2}{2(l_2 l_3+l_1 p_{max})}\right) \\ \delta = acos\left(\frac{l_3^2 p_{max}^2-l_2^2-l_1^2}{2(l_3 p_{max}+l_2 l_1)}\right) \\ \beta = \pi - \delta \\ \gamma = \pi - \alpha \end{cases} \tag{4.26}$$

Then,

$$q_2^{max} = q_{2p}^{max} + \gamma - \frac{\pi}{2} \tag{4.27}$$

$$q_3^{max} = \beta - \pi \tag{4.28}$$

$$q_4^{max} = \alpha - \frac{3\pi}{2} \tag{4.29}$$

To maintain the desired orientation, the IGM of the 6R robot $(q_1, q_2, q_4, q_5, q_6, q_7)$ gives the desired joint values q_5^{max}, q_6^{max} and q_7^{max}. d_{6R}^{max} can be calculated as:

$$d_{6R}^{max} = l_3^2 + p_{max}^2 - 2 l_3 p_{max} \cos\delta \tag{4.30}$$

The explicit IGM derivations can be found in Khalil and Dombre [2004] and the desired joint values for maximum manipulability are:

$$\boldsymbol{q}^{MaxManip} = [q_1^{max}, q_2^{max}, q_3^{max}, q_4^{max}, q_5^{max}, q_6^{max}, q_7^{max}]^T \tag{4.31}$$

Hence, the arm redundancy can be controlled by means of maximum manipulability as,

$$\boldsymbol{\tau}_{null}^{arm} = \boldsymbol{P}(\boldsymbol{q}^{MaxManip} - \boldsymbol{q}_a) + \boldsymbol{D}\frac{d}{dt}(\boldsymbol{q}^{MaxManip} - \boldsymbol{q}_a) \tag{4.32}$$

$\boldsymbol{P}$ and $\boldsymbol{D}$ are proportional and derivative gain matrices respectively.

4.2 Adams-Matlab/Simulink Dynamic Simulation

To test the efficiency of the proposed control, the mobile manipulator is built as shown in Figure 4.1. The platform consists of a 7-dof arm fixed on a nonholonomic mobile base. The system is simulated using Adams, a simulator with powerful physics engine that allows to study the dynamics of moving parts, and the distribution of forces throughout the mechanical system. The robot dimensions and masses are well respected in comparison to the real platform, friction forces are added to the joints as 0.5 N·m for static friction and 0.3 N·m for the dynamic one. The rolling resistance coefficient between the driving wheels and the ground is set to 0.01. The control strategies discussed above have been successfully implemented in Matlab-Simulink. The Simulink/Adams interface allows bilateral communication. Simulink can send the joint torques to Adams which returns the status of the system (joint positions). The end-effector of the robot is commanded to follow the spatial trajectory $\boldsymbol{r}(t)$ shown in Figure 4.1 while maintaining its stability. The Cartesian desired and response values of the trajectory's position and velocity are shown in Figures 4.4 and 4.5 respectively. The controller shows good performance, the errors in position are around 0 mm in constant velocity phases and less than 1 mm during acceleration (Figures 4.6 and 4.8), consequently the velocity errors are around zero in the constant phases and maximum of 0.01 m/s in the variable phases. No wonder the errors are small as we apply the disturbance observer (DOB) to each joint. In order to ensure the stability of the mobile manipulator while executing the trajectory, the desired zero moment point ZMP_{des} is set at 0.2 m on the mobile base axis x_m from the base origin (Figure 4.2). The stability controller presented in Section 4.1.3 is able to control the zero moment point around the desired value all along the trajectory, with errors along x_m fluctuating around 0 mm in the constant velocity phases, and less than 5 mm when the accelerations of the trajectory are on their peak (1m/s^2) (Figure 4.8), the ZMP behavior and its errors are shown in Figure 4.9. Similarly for the orientation, the deviation of the ZMP from x_m axis is relatively small, around 0.01 rad as can be seen in Figure 4.10. The mobile base velocity controller is able to execute the desired velocities v_0^{cmd} needed to maintain the ZMP on its desired position, the command and response of the base are plotted in Figure 4.11a, their corresponding errors are shown in Figure 4.11b. The base velocity is feasible and the execution errors are less than 0.051 m/s, they are small enough as the ZMP tracking errors are small (Figure 4.9b). Finally, a top view of the ZMP projection on the base is shown in Figure 4.12. In this Figure it can be seen that the initial value is driven to the desired one shortly then it stays around $x_m = 0.2$ m all along the path. Hence, on-line stability control of the mobile manipulator is adequately achieved.

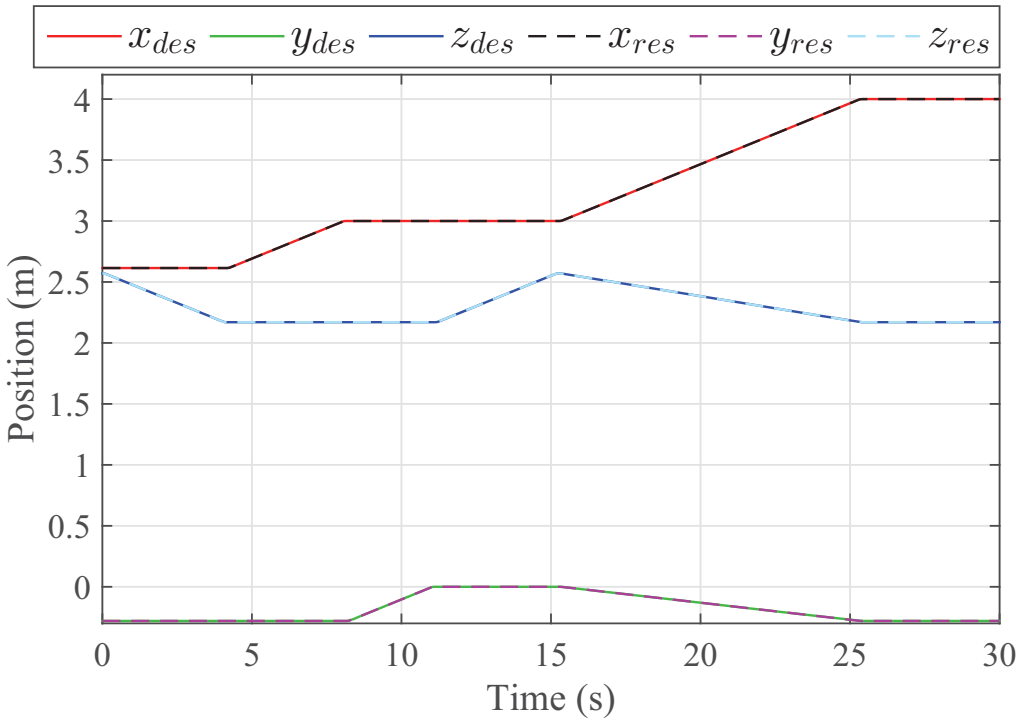

Figure 4.4: Position desired vs. response values

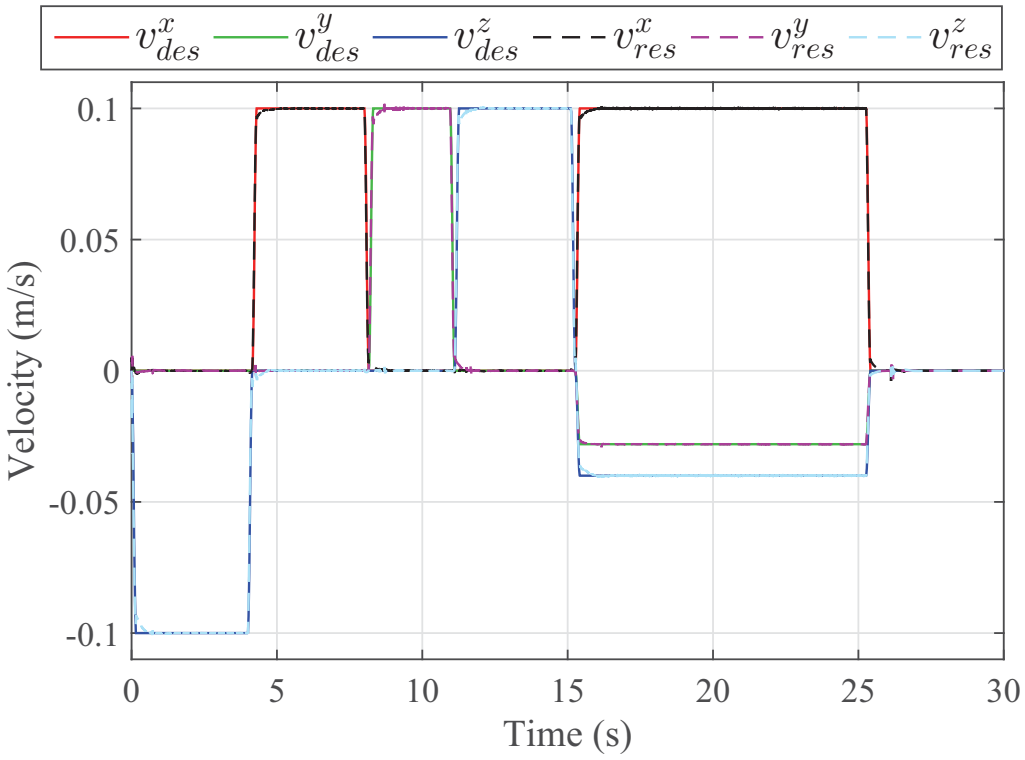

Figure 4.5: Velocity desired vs. response values

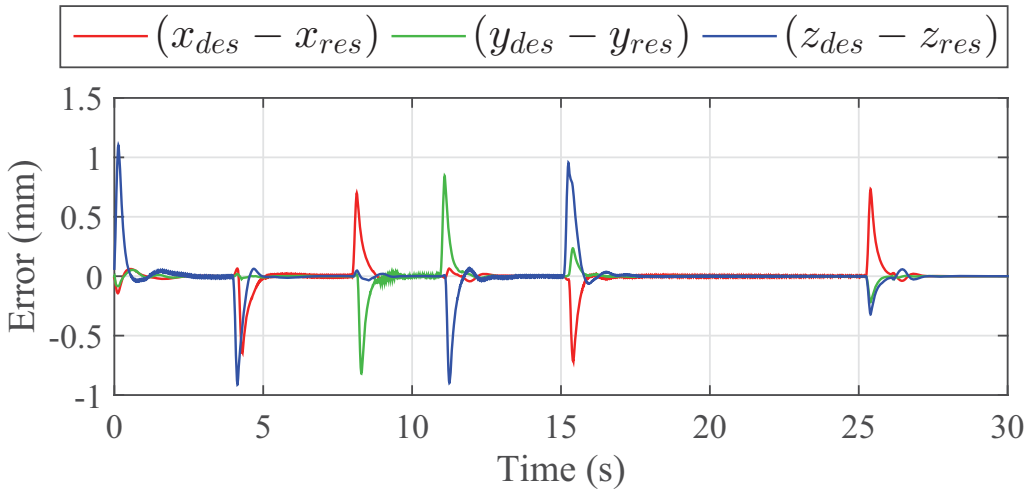

Figure 4.6: End-effector position errors

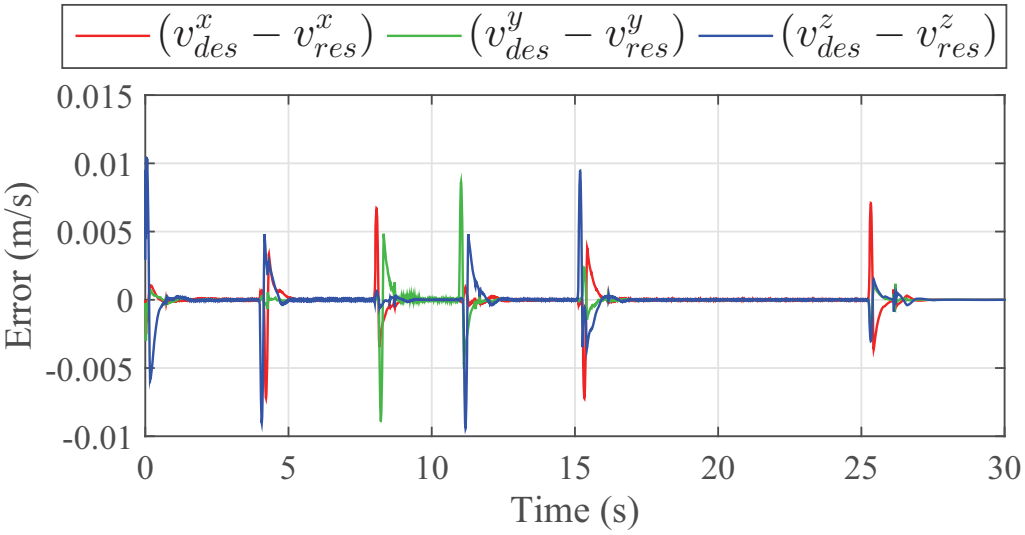

Figure 4.7: End-effector velocity errors

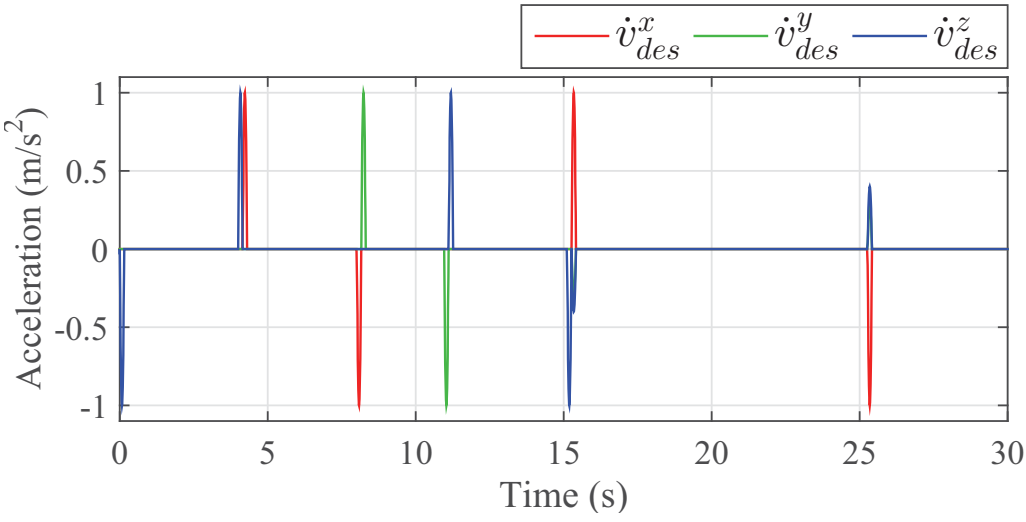

Figure 4.8: Desired accelerations.

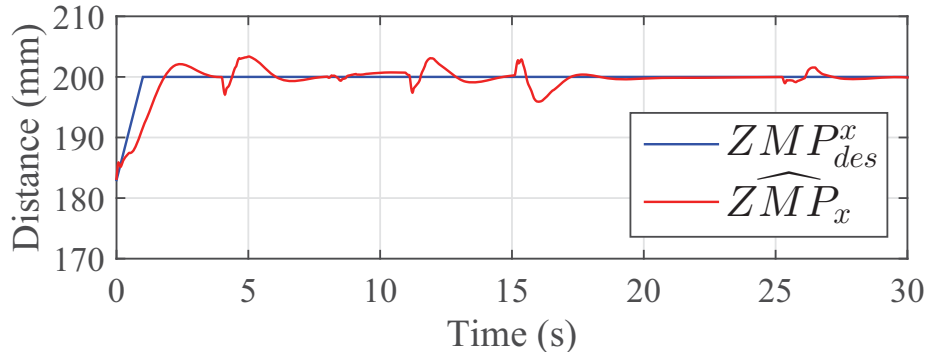

(a) Estimated value $\widehat{ZMP_x}$ vs. the desired one ZMP^x_{des}

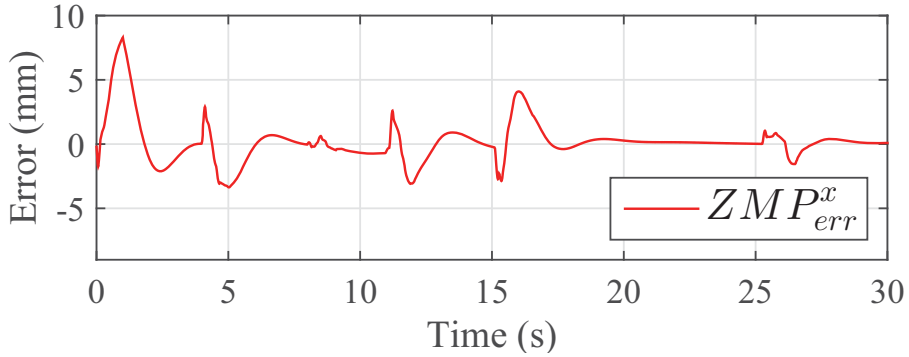

(b) Errors of the ZMP around the desired stable point

Figure 4.9: Zero moment point control on a desired point during the trajectory execution

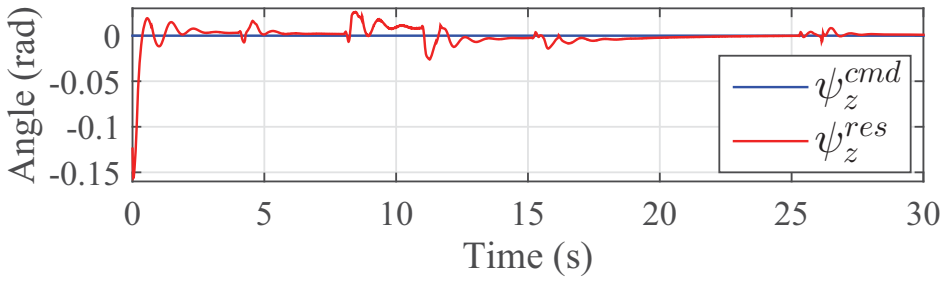

(a) The command vs. response of the ZMP angle from axis x_m

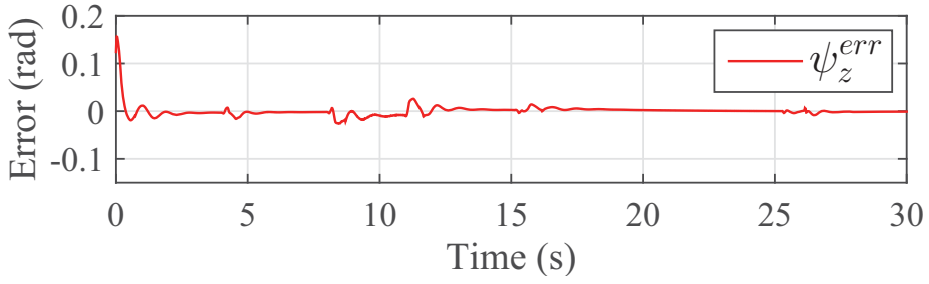

(b) ZMP deviation error from axis x_m

Figure 4.10: Orientation control of the ZMP deviation from the axis x_m (Figure 4.2)

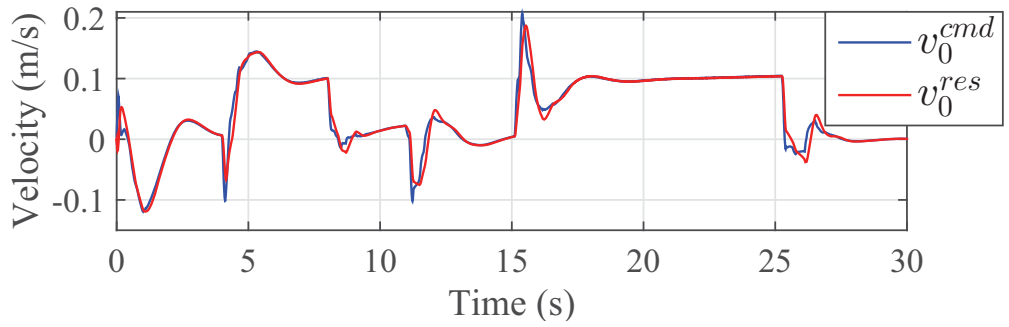

(a) The command vs. response of the mobile base velocity v_0

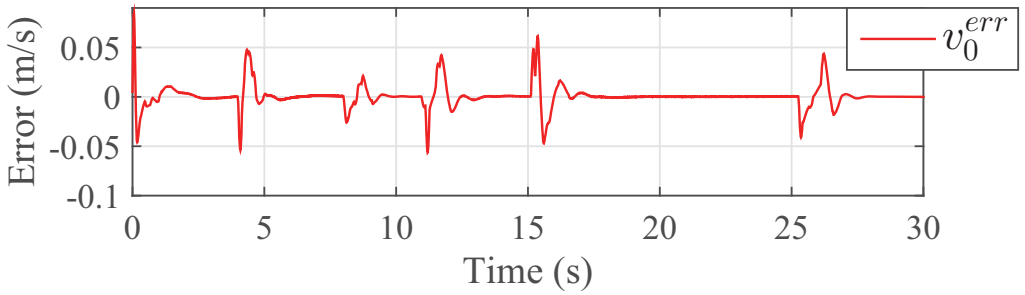

(b) Mobile base velocity errors

Figure 4.11: Velocity control behavior of the mobile base

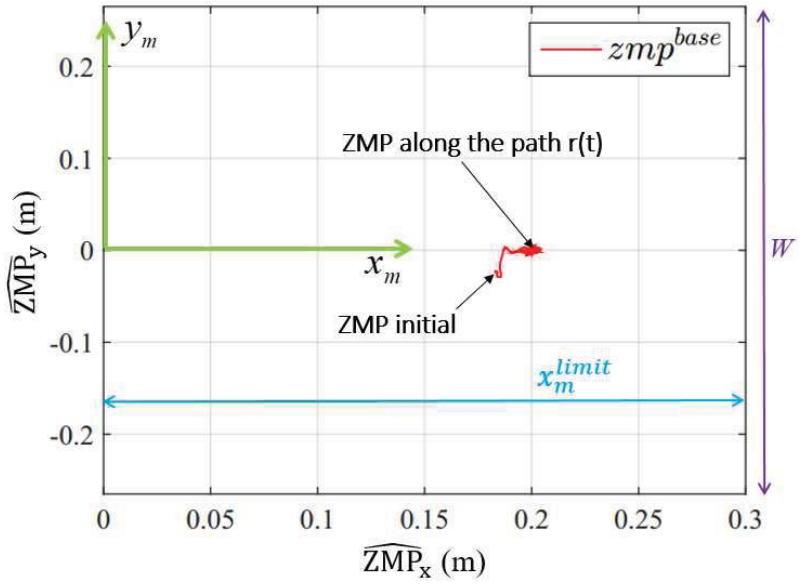

Figure 4.12: ZMP projection in the base support plane.

4.3 Summary

This chapter reviewed several tip-over stability strategies presented in the literature. Additionally it presented a new approach for controlling the stability of mobile manipulators in real time. In the proposed controller, the base is controlled using task redundancy in the null configuration space of the robot, to keep the zero moment point on a desired stable point without affecting the end-effector performance. Moreover, the zero moment point observer proposed in Chapter 2 was used. The observer estimates the effect of errors in center of mass positions and inertias of the links, and includes it in the zero moment point position estimation. The controller was validated through dynamic simulations. Not only stability was ensured, but good spatial velocity and position tracking were achieved with very small errors as well (errors in millimeters are considered small compared to the base dimensions of the robot and they have no big effect on stability). In the near future, the controller will be extended to meet the kinematic limits of the arm then it will be implemented on the real mobile manipulator.

General conclusion and perspectives

The dissertation was composed of four chapters with three major proposals.

- Methods to compensate the modeling and sensors uncertainties.
- Achieving a grinding task based on adaptive active force control.
- Active on-line maintenance of tip-over stability of the mobile manipulator while moving.

In chapter 2 of this dissertation, fundamental technologies of disturbance compensation in motion control were explained and the disturbance observer (DOB) derivation was discussed in details. In addition to that, a zero-moment-point disturbance observer (ZMPOB) was introduced to compensate errors in zero-moment-point estimation. Moreover, a model-free observer based recurrent neural network (RNNOB), was developed to estimate non-contact forces when the force-torque sensor is subject to high dynamic motions. The observer proved to accurately estimate the effects of inertia, gravity, centrifugal and Coriolis forces on the force-torque sensor without the need of an identification process. Then, the estimated non-contact forces can be subtracted from the raw sensor feedback ensuring a pure contact force reading. The mentioned observers (DOB, ZMPOB and RNNOB) are well integrated in the controllers presented in the next chapters for accurate and precise control.

Chapter 3 is mainly about achieving a surface grinding task using robots for the civil engineering sector. This application is new in the robotics domain and never done before in the literature. Hence, Chapter 3 introduced the research field of robot-environment interaction and reviewed the recent technical advances in metallic polishing and grinding operations. Thus, based on the existing studies, two wall grinding controllers were proposed in this chapter. The first controller was based on smooth position-force hybrid controller with compliant wrist for grinding. It was validated by both simulations and experiments using a 7-degrees-of-freedom robotic arm equipped with camera and force-torque sensor. The switching problem was overcome by proposed transition control were the controller changes smoothly between free space and contact modes, thus reducing impact force. The controller showed good position and force tracking performances and impact force close to zero in simulations. Addition to that, the desired force was maintained centered on the disc and normal to the surface. However, in real experiments, although the results of position and force tracking performances are acceptable and the impact force was small, nevertheless the reaction forces have an important effect on the controller as there is large offset between the center of disc and the one of the wrist which generates large tilting wrenches. This controller was also dependent on the wheels around the tool that might not touch the surface in case of irregularities, and it used estimated grinding parameters that lead to inaccurate results and satisfactory grinding quality.

The shortcomings of this controller are then studied and a model based adaptive hybrid velocity-position-force controller for wall grinding was proposed next. Hence, the nominal grinding feeding force was predicted using a developed model. This force is then used in an adaptive controller that keeps the disc parallel to the wall. The desired normal contact force and the velocity tracking on the wall were achieved by hybrid velocity-force controller. The controller was tested on 7-degrees-of-freedom robotic arm equipped with a grinding tool and a force-torque sensor as well. Grinding tests were done on different unknown surface geometries and the task was achieved with the disc exerting a normal force on the wall surface while tracking its curvature. The experimental results showed good velocity, force and orientation tracking performances. Addition to that, the grinding quality was evaluated and the controller is promising.

Addition to that, chapter 4 presents a new approach for controlling the stability of mobile manipulators in real time based on the ZMPOB. The base is controlled using task redundancy in the null configuration space of the robot to keep the zero moment point on a desired stable point without affecting the end-effector performance. The controller is validated through dynamic simulations using ADAMS. The stability of the mobile manipulator was ensured and good spatial velocity and position tracking was achieved with minimal errors.

Many different tests and experiments have been left for the future due to lack of time (the experiments with real grinding are usually very time consuming, requiring special setup and walls for testing). Future work concerns deeper analysis of the grinding process and collecting a bigger amount of grinding data with more variations in forces and velocities to have more accurate feeding force model. Moreover, it will be interesting to test experimentally the proposed tip-over stability controller and extend it to consider the interaction with the environment by combining it with the adaptive controller for wall grinding. Additionally, there are some ideas that I would have liked to try during the thesis like introducing haptic control for wall grinding. The haptic controller will define how the user can supervise, interact and share the control with the system to modify some tasks while having haptic feedback. For instance, the operator will have a force feedback while moving the end effector on the wall in case of collision and a vibration feedback in case of extensive pushing into the wall.

Finally, the construction industry is still lagged behind other industries in the implementation of robots. This is because of the challenges, abilities and limitations of the robots in such industry. “Construction sites are very different from the majority of workplaces in that most of the work takes place outside, in highly unstructured environments,” said ABI Research director of robotics research Dan Kara in an interview with CBC last year. Additionally, “The robotic technologies that have been available either haven’t presented a true end-to-end automated solution, or they take an inordinate amount of time to set up, or have limitations in terms of materials or their ability to implement different designs,” says Mark Pivac, chief technology officer at Fastbrick Robotics, a Perth-based robotics company that is developing a robotic bricklaying system dubbed Hadrian X.

Hence, the gap in automating the construction industry is wide and there is enough space for the researchers to contribute to the development and control of the state of art construction robotics.

List of publications

During Masters:

1. **Kamal Mohy El Dine**, Chuan Yang, Takahiro Nozaki and Toshiyuki Murakami. "Novel walking assist device based on generic human motion tracking criteria". In 2016 IEEE 14th International Workshop on Advanced Motion Control (AMC), April 2016.

During Ph.D.:

1. **Kamal Mohy El Dine**, Juan-Antonio Corrales-Ramon, Youcef Mezouar and Jean-Christophe Fauroux. "A smooth position-force controller for asbestos removal manipulator". In 2017 IEEE International Conference on Robotics and Biomimetics (ROBIO), December 2017.

2. **Kamal Mohy El Dine**, Juan-Antonio Corrales-Ramon, Laurent Lequievre, Youcef Mezouar and Jean-Christophe Fauroux. "Hybrid position/force control with compliant Wrist for grinding". In MUGV 2018 (Machines et Usinage à Grande Vitesse) & Manufacturing'21, June 2018.

3. **Kamal Mohy El Dine**[1], Jose Sanchez[1], Juan Corrales, Youcef Mezouar and Jean-Christophe Fauroux. "Force-torque sensor disturbance observer using deep learning". In 2018 International Symposium on Experimental Robotics (ISER), November 2018.

4. **Kamal Mohy El Dine**, Juan-Antonio Corrales-Ramon, Youcef Mezouar and Jean-Christophe Fauroux. "A Unified Mobile Manipulator Control for On-line Tip-over Avoidance Based on ZMP Disturbance Observer". In 2018 IEEE International Conference on Robotics and Biomimetics (ROBIO), December 2018.

5. **Kamal Mohy El Dine**, Juan-Antonio Corrales-Ramon, Youcef Mezouar and Jean-Christophe Fauroux. "Model-based adaptive hybrid velocity-position-force Controller for Wall Grinding". **Under preparation to be submitted to the Journal of Robotics and Computer-Integrated Manufacturing**.

[1] Authors contributed equally to the work

Bibliography

O. Alkkiomaki, V. Kyrki, H. Kalviainen, Y. Liu, and H. Handroos. Smooth transition from motion to force control in robotic manipulation using vision. In *2006 9th International Conference on Control, Automation, Robotics and Vision*, pages 1–6. IEEE, 2006.

J. E. Alleman and B. T. Mossman. Asbestos revisited. *Scientific American*, 277(1):70–75, 1997.

F. Almeida, A. Lopes, and P. Abreu. Force-impedance control: a new control strategy of robotic manipulators. *Recent advances in Mechatronics*, pages 126–137, 1999.

C. H. An, C. G. Atkeson, and J. M. Hollerbach. *Model-based control of a robot manipulator*. MIT press, 1988.

R. J. Anderson. Passive computed torque algorithms for robots. In *Decision and Control, 1989., Proceedings of the 28th IEEE Conference on*, pages 1638–1644. IEEE, 1989.

R. J. Anderson. Dynamic damping control: Implementation issues and simulation results. In *Robotics and Automation, 1990. Proceedings., 1990 IEEE International Conference on*, pages 68–77. IEEE, 1990.

Asbestos Trade Association, France.

Association Nationale de Défense des Victimes de l'Amiante. Amiante et economie: Importations, couts. http://www.andeva.fr/?Amiante-et-Economie-Importations, 2011. [Online; accessed 1-april-2019].

J. Baeten and J. De Schutter. Hybrid vision/force control at corners in planar robotic-contour following. *IEEE/ASME Transactions on mechatronics*, 7(2):143–151, 2002.

L. Baptista, J. Sousa, and J. S. da Costa. Predictive force control of robot manipulators in nonrigid environments. *from Industrial Robotics: Theory, Modeling and Control*, pages 841–874, 2006.

Bots2ReC. Robots to Re-Construction. http://bots2rec.eu, 2015. [Online; accessed 26-february-2019].

Bouygues Construction. Apparent asbestos consumption in europe in the last century, 2015.

Bouygues Construction and Audencia Junior Conseil. Étude du marché du désamiantage en europe, 2015. [Study commissioned by Bouygues Construction].

W. F. Carriker, P. K. Khosla, and B. H. Krogh. Path planning for mobile manipulators for multiple task execution. *IEEE Transactions on Robotics and Automation*, 7(3):403–408, 1991.

A. Castaño and S. Hutchinson. Visual compliance: Task-directed visual servo control. *IEEE transactions on Robotics and Automation*, 10(3):334–342, 1994.

P. Chang, D. Kim, and K. Park. Robust force/position control of a robot manipulator using time-delay control. *Control Engineering Practice*, 3(9):1255–1264, 1995.

W.-C. Chang and C.-C. Wu. Integrated vision and force control of a 3-dof planar robot. In *Control Applications, 2002. Proceedings of the 2002 International Conference on*, volume 2, pages 748–753. IEEE, 2002.

F. Chaventré and C. Cochet. Centre Scientifique et Technique du Bâtiment : L'amiante dans le parc de bâtiments français. http://docplayer.fr/1923126-L-amiante-dans-le-parc-de-batiments-francais.html, 2005. [Online; accessed 30-march-2019].

F. Chen, H. Zhao, D. Li, L. Chen, C. Tan, and H. Ding. Robotic grinding of a blisk with two degrees of freedom contact force control. *The International Journal of Advanced Manufacturing Technology*, pages 1–14, 2018.

A. Cherubini, R. Passama, P. Fraisse, and A. Crosnier. A unified multimodal control framework for human–robot interaction. *Robotics and Autonomous Systems*, pages 106 – 115, 2015.

D. Choi, M. Kim, and J.-H. Oh. Development of a rapid mobile robot with a multi-degree-of-freedom inverted pendulum using the model-based zero-moment point stabilization method. *Advanced Robotics*, 26(5-6):515–535, 2012.

J. H. Chung and S. A. Velinsky. Robust interaction control of a mobile manipulator–dynamic model based coordination. *Journal of Intelligent & Robotic Systems*, 26(1):47–63, 1999.

J. J. Craig. Introduction to robotics: Mechanics and control, 2nd edn. addisson-wesley. *Reading, MA*, 1989.

J. De Schutter and H. Van Brussel. Compliant robot motion i. a formalism for specifying compliant motion tasks. *The International Journal of Robotics Research*, 7(4):3–17, 1988.

T. Detert, S. Charaf Eddine, J.-C. Fauroux, T. Haschke, F. Becchi, B. Corves, R. Guzman, F. Herb, B. Linéatte, and D. Martin. Bots2rec: introducing mobile robotic units on construction sites for asbestos rehabilitation. *Construction Robotics*, 1(1):29–37, Dec 2017.

S. Dubowsky and E. Vance. Planning mobile manipulator motions considering vehicle dynamic stability constraints. In *Robotics and Automation, 1989. Proceedings., 1989 IEEE International Conference on*, pages 1271–1276. IEEE, 1989.

M. Elbestawi, K. Yuen, A. Srivastava, and H. Dai. Adaptive force control for robotic disk grinding. *CIRP Annals-Manufacturing Technology*, 40(1):391–394, 1991.

G. Ellis. *Observers in control systems: a practical guide*. Elsevier, 2002.

M. S. Erden and T. Tomiyama. Human-intent detection and physically interactive control of a robot without force sensors. *IEEE Transactions on Robotics*, 26(2):370–382, 2010.

Z. Erickson, A. Clegg, W. Yu, G. Turk, C. K. Liu, and C. C. Kemp. What does the person feel? Learning to infer applied forces during robot-assisted dressing. In *IEEE International Conference on Robotics and Automation*, pages 6058–6065, Singapore, 2017.

G. Ferretti, G. Magnani, P. Rocco, F. Cecconello, and G. Rossetti. Impedance control for industrial robots. In *Robotics and Automation, 2000. Proceedings. ICRA'00. IEEE International Conference on*, volume 4, pages 4027–4032. IEEE, 2000.

F. Ficuciello, A. Romano, L. Villani, and B. Siciliano. Cartesian impedance control of redundant manipulators for human-robot co-manipulation. In *2014 IEEE/RSJ International Conference on Intelligent Robots and Systems*, pages 2120–2125. IEEE, 2014.

French Agency for Food, Environmental and Occupational Health and Safety. Asbestos: Presentation, health effects, exposure and regulatory framework. https://www.anses.fr/en/content/asbestos, 2019. [Online; accessed 30-march-2019].

French government. Décret no 96-1133 du 24 décembre 1996 relatif à l'interdiction de l'amiante, pris en application du code du travail et du code de la consommation. https://www.legifrance.gouv.fr/affichTexte.do?cidTexte=JORFTEXT000000734637, 1996. [Online; accessed 30-march-2019].

French Ministry of Health. Le repérage de l'amiante dans les bâtiments. https://solidarites-sante.gouv.fr/sante-et-environnement/batiments/article/le-reperage-de-l-amiante-dans-les-batiments, 2016. [Online; accessed 30-march-2019].

French Ministry of Labor. Article r.4412-100 of the french labour code, as set out in ministerial order 2012-639. https://www.legifrance.gouv.fr/affichCodeArticle.do?cidTexte=LEGITEXT000006072050&idArticle=LEGIARTI000018490587&dateTexte=&categorieLien=cid, 2012. [Online; accessed 30-march-2019].

T. Fukuda, Y. Fujisawa, K. Kosuge, F. Arai, E. Muro, H. Hoshino, T. Miyazaki, K. Utubo, and K. Uehara. Manipulator/vehicle system for man-robot cooperation. In *Robotics and Automation, 1992. Proceedings., 1992 IEEE International Conference on*, pages 74–79. IEEE, 1992.

T. Furukawa, D. Rye, M. Dissanayake, and A. Barratt. Automated polishing of an unknown three-dimensional surface. *Robotics and computer-integrated manufacturing*, 12 (3):261–270, 1996.

S. Furuno, M. Yamamoto, and A. Mohri. Trajectory planning of mobile manipulator with stability considerations. In *Robotics and Automation, 2003. Proceedings. ICRA'03. IEEE International Conference on*, volume 3, pages 3403–3408. IEEE, 2003.

Future Timeline. Asbestos production is ending globally. https://www.futuretimeline.net/21stcentury/2070-2079.htm#asbestos, 2018. [Online; accessed 30-march-2019].

G. Ganesh, A. Albu-Schäffer, M. Haruno, M. Kawato, and E. Burdet. Biomimetic motor behavior for simultaneous adaptation of force, impedance and trajectory in interaction tasks. In *Robotics and Automation (ICRA), 2010 IEEE International Conference on*, pages 2705–2711. IEEE, 2010.

J. G. García, A. Robertsson, J. G. Ortega, and R. Johansson. Force and Acceleration Sensor Fusion for Compliant Robot Motion Control. In *IEEE International Conference on Robotics and Automation*, pages 2709–2714, Barcelona, Spain, 2005.

A. Ghaffari, A. Meghdari, D. Naderi, and S. Eslami. Tipover stability enhancement of wheeled mobile manipulators using an adaptive neurofuzzy inference controller system. In *Proceedings of World Academy of Science, Engineering and Technology*, volume 35, 2008.

A. Ghasempoor and N. Sepehri. A measure of machine stability for moving base manipulators. In *Robotics and Automation, 1995. Proceedings., 1995 IEEE International Conference on*, volume 3, pages 2249–2254. IEEE, 1995.

A. Graves, A.-r. Mohamed, and G. Hinton. Speech recognition with deep recurrent neural networks. In *IEEE International Conference on Acoustics, Speech and Signal Processing*, pages 6645–6649, Vancouver, Canada, 2013.

J.-Y. Guérin and A. Jouan. Amiante et hlm : le plan a minima du gouvernement. http://www.lefigaro.fr/actualite-france/2014/09/23/01016-20140923ARTFIG00241-amiante-et-hlm-le-plan-a-minima-du-gouvernement.php, 2014. [Online; accessed 1-april-2019].

N. Hadji and A. Rahmani. Observer for an omnidirectional mobile robot. In *Proceedings of the 2010 Spring Simulation Multiconference*, page 216. Society for Computer Simulation International, 2010.

D. Han, X. Duan, M. Li, T. Cui, A. Ma, and X. Ma. Interaction control for manipulator with compliant end-effector based on hybrid position-force control. In *Mechatronics and Automation (ICMA), 2017 IEEE International Conference on*, pages 863–868. IEEE, 2017.

I. Hirose. Umetani: Static stability criterion for walking vehicles. In *21st SICE Symposium*, pages 253–254, 1978.

M. P. Hitchiner, I. D. Marinescu, E. Uhlmann, W. B. Rowe, and I. Inasaki. *Handbook of machining with grinding wheels*. CRC Press, 2016.

N. Hogan. Impedance control of industrial robots. *Robotics and Computer-Integrated Manufacturing*, 1(1):97–113, 1984.

N. Hogan. Impedance control: An approach to manipulation: Part ii—implementation. *Journal of dynamic systems, measurement, and control*, 107(1):8–16, 1985.

K. Hosoda, K. Igarashi, and M. Asada. Adaptive hybrid visual servoing/force control in unknown environment. In *Intelligent Robots and Systems' 96, IROS 96, Proceedings of the 1996 IEEE/RSJ International Conference on*, volume 3, pages 1097–1103. IEEE, 1996.

K. Hosoda, K. Igarashi, and M. Asada. Adaptive hybrid control for visual and force servoing in an unknown environment. *IEEE Robotics & Automation Magazine*, 5(4): 39–43, 1998.

H. Huang, Z. Gong, X. Chen, and L. Zhou. Robotic grinding and polishing for turbine-vane overhaul. *Journal of materials processing technology*, 127(2):140–145, 2002.

Q. Huang and S. Sugano. Manipulator motion planning for stabilizing a mobile-manipulator. In *Intelligent Robots and Systems 95.'Human Robot Interaction and Cooperative Robots', Proceedings. 1995 IEEE/RSJ International Conference on*, volume 3, pages 467–472. IEEE, 1995.

Q. Huang, S. Sugano, and I. Kato. Stability control for a mobile manipulator using a potential method. In *Intelligent Robots and Systems' 94.'Advanced Robotic Systems and the Real World', IROS'94. Proceedings of the IEEE/RSJ/GI International Conference on*, volume 2, pages 839–846. IEEE, 1994.

Q. Huang, K. Tanie, and S. Sugano. Stability compensation of a mobile manipulator by manipulatorpaper motion: feasibility and planning. *Advanced Robotics*, 13(1):25–40, 1998.

Q. Huang, K. Tanie, and S. Sugano. Coordinated motion planning for a mobile manipulator considering stability and manipulation. *The International Journal of Robotics Research*, 19(8):732–742, 2000.

IFR. Executive summary world robotics 2018 service robots. https://ifr.org/downloads/press2018/WR_Presentation_Industry_and_Service_Robots_rev_5_12_18.pdf, 2018. [Online; accessed 07-june-2017].

R. Jamisola, M. H. Ang, D. Oetomo, O. Khatib, T. M. Lim, and S. Y. Lim. The operational space formulation implementation to aircraft canopy polishing using a mobile manipulator. In *Robotics and Automation, 2002. Proceedings. ICRA'02. IEEE International Conference on*, volume 1, pages 400–405. IEEE, 2002.

R. S. Jamisola, D. N. Oetomo, M. H. Ang, O. Khatib, T. M. Lim, and S. Y. Lim. Compliant motion using a mobile manipulator: an operational space formulation approach to aircraft canopy polishing. *Advanced Robotics*, 19(5):613–634, 2005.

F. Jatta, G. Legnani, A. Visioli, and G. Ziliani. On the use of velocity feedback in hybrid force/velocity control of industrial manipulators. *Control Engineering Practice*, 14(9): 1045–1055, 2006.

S. Jung, T. C. Hsia, and R. G. Bonitz. Force tracking impedance control of robot manipulators under unknown environment. *IEEE Transactions on Control Systems Technology*, 12(3):474–483, 2004.

R. K. Kankaanranta and H. N. Koivo. Dynamics and simulation of compliant motion of a manipulator. *IEEE Journal on Robotics and automation*, 4(2):163–173, 1988.

H. Karerooni, T. Sheridan, and P. Houpt. Robust compliant motion for manipulators, part i: The fundamental concepts of compliant motion, part ii: Design method. *IEEE J. Robotics Automat*, 2(2):83–105, 1986.

M. Karlsson, A. Robertsson, and R. Johansson. Detection and Control of Contact Force Transients in Robotic Manipulation without a Force Sensor. In *IEEE International Conference on Robotics and Automation*, pages 21–25, Brisbane, Australia, 2018.

H. Kazerooni. On the robot compliant motion control. *Journal of dynamic systems, measurement, and control*, 111(3):416–425, 1989.

W. Khalil and E. Dombre. *Modeling, identification and control of robots*. Butterworth-Heinemann, 2004.

O. Khatib, K. Yokoi, K. Chang, D. Ruspini, R. Holmberg, and A. Casal. Coordination and decentralized cooperation of multiple mobile manipulators. *Journal of Field Robotics*, 13(11):755–764, 1996a.

O. Khatib, K. Yokoi, K. Chang, D. Ruspini, R. Holmberg, and A. Casal. Vehicle/arm coordination and multiple mobile manipulator decentralized cooperation. In *Intelligent Robots and Systems' 96, IROS 96, Proceedings of the 1996 IEEE/RSJ International Conference on*, volume 2, pages 546–553. IEEE, 1996b.

J. Kim and W. K. Chung. Real-time zero moment point compensation method using null motion for mobile manipulators. *Advanced Robotics*, 20(5):581–593, 2006.

A. King. Asbestos, explained. https://www.chemistryworld.com/news/why-asbestos-is-still-used-around-the-world/3007504.article, 2017. [Online; accessed 30-march-2019].

M. Kollmitz, D. Büscher, T. Schubert, and W. Burgard. Whole-Body Sensory Concept for Compliant Mobile Robots. In *(To appear in) IEEE International Conference on Robotics and Automation*, Brisbane, Australia, 2018. ISBN 9781538630808.

T. Kröger, D. Kubus, and F. Wahl. 6D Force and Acceleration Sensor Fusion for Compliant Manipulation Control. In *IEEE/RSJ International Conference on Intelligent Robots and Systems*, pages 2626–2631, Beijing, China, 2006.

D. Kubus and F. M. Wahl. Scaling and eliminating non-contact forces and torques to improve bilateral teleoperation. In *IEEE/RSJ International Conference on Intelligent Robots and Systems*, pages 5133–5139, St. Louis, USA, 2009.

S. Lee, M. Leibold, M. Buss, and F. C. Park. Online stability compensation of mobile manipulators using recursive calculation of zmp gradients. In *Robotics and Automation (ICRA), 2012 IEEE International Conference on*, pages 850–855. IEEE, 2012.

A. C. Leite, F. Lizarralde, and L. Hsu. Hybrid vision-force robot control for tasks on unknown smooth surfaces. In *Proceedings 2006 IEEE International Conference on Robotics and Automation, 2006. ICRA 2006.*, pages 2244–2249. IEEE, 2006.

B. Li, G. Li, W. Lin, and P. Xu. Design and constant force control of a parallel polishing machine. In *2014 4th IEEE International Conference on Information Science and Technology*, pages 324–328. IEEE, 2014.

J. Li, T. Zhang, X. Liu, Y. Guan, and D. Wang. A survey of robotic polishing. In *2018 IEEE International Conference on Robotics and Biomimetics (ROBIO)*, pages 2125–2132. IEEE, 2018.

Y. Li and Y. Liu. Real-time tip-over prevention and path following control for redundant nonholonomic mobile modular manipulators via fuzzy and neural-fuzzy approaches. *Journal of dynamic systems, measurement, and control*, 128(4):753–764, 2006.

V. Lippiello, B. Siciliano, and L. Villani. Robot interaction control using force and vision. In *2006 IEEE/RSJ International Conference on Intelligent Robots and Systems*, pages 1470–1475. IEEE, 2006.

C. Liu, A. Chen, Y.-T. Wang, and C.-C. Chen. Modelling and simulation of an automatic grinding system using a hand grinder. *The International Journal of Advanced Manufacturing Technology*, 23(11-12):874–881, 2004.

K. Liu and F. L. Lewis. Decentralized continuous robust controller for mobile robots. In *Robotics and Automation, 1990. Proceedings., 1990 IEEE International Conference on*, pages 1822–1827. IEEE, 1990.

J. M. S. Loza, C. Mateo, J. Corrales, B.-C. Bouzgarrou, and Y. Mezouar. Online shape estimation based on tactile sensing and deformation modeling for robot manipulation. In *IEEE/RSJ International Conference on Intelligent Robots and Systems*, 2018.

L'Union sociale pour l'habitat. Amiante. https://www.union-habitat.org/centre-de-ressources/patrimoine-maitrise-d-ouvrage/amiante-fiches-de-communication-de-crise, 2014. [Online; accessed 30-march-2019].

M. T. Mason. Compliance and force control for computer controlled manipulators. *IEEE Transactions on Systems, Man, and Cybernetics*, 11(6):418–432, 1981.

N. H. McClamroch and D. Wang. Feedback stabilization and tracking of constrained robots. *IEEE Transactions on Automatic Control*, 33(5):419–426, 1988.

R. B. McGhee and A. A. Frank. On the stability properties of quadruped creeping gaits. *Mathematical Biosciences*, 3:331–351, 1968.

R. B. McGhee and G. I. Iswandhi. Adaptive locomotion of a multilegged robot over rough terrain. *IEEE transactions on systems, man, and cybernetics*, 9(4):176–182, 1979.

Mesothelioma and Asbestos Awareness Center. Asbestos. https://www.maacenter.org/asbestos/, 2019. [Online; accessed 30-march-2019].

D. Messuri and C. Klein. Automatic body regulation for maintaining stability of a legged vehicle during rough-terrain locomotion. *IEEE Journal on Robotics and Automation*, 1 (3):132–141, 1985.

Y. Mezouar, M. Prats, and P. Martinet. External hybrid vision/force control. In *Intl. Conference on Advanced Robotics (ICAR'07)*, 2007.

W. Miksch and D. Schroeder. Performance-functional based controller design for a mobile manipulator. In *Robotics and Automation, 1992. Proceedings., 1992 IEEE International Conference on*, pages 227–232. IEEE, 1992.

K. Mohy El Dine, C. Yang, T. Nozaki, and T. Murakami. Novel walking assist device based on generic human motion tracking criteria. In *Advanced Motion Control (AMC), 2016 IEEE 14th International Workshop on*, pages 38–43. IEEE, 2016.

S. A. A. Moosavian and K. Alipour. On the dynamic tip-over stability of wheeled mobile manipulators. *International Journal of Robotics & Automation*, 22(4):322, 2007.

G. Morel, E. Malis, and S. Boudet. Impedance based combination of visual and force control. In *Robotics and Automation, 1998. Proceedings. 1998 IEEE International Conference on*, volume 2, pages 1743–1748. IEEE, 1998.

J. Moura and M. S. Erden. Formulation of a control and path planning approach for a cab front cleaning robot. *Procedia CIRP*, 59:67–71, 2017.

J. Moura, W. Mccoll, G. Taykaldiranian, T. Tomiyama, and M. S. Erden. Automation of train cab front cleaning with a robot manipulator. *IEEE Robotics and Automation Letters*, 3(4):3058–3065, 2018.

T. Murakami, F. Yu, and K. Ohnishi. Torque sensorless control in multidegree-of-freedom manipulator. *IEEE Transactions on Industrial Electronics*, 40(2):259–265, 1993.

F. Nagata, T. Hase, Z. Haga, M. Omoto, and K. Watanabe. Cad/cam-based position/force controller for a mold polishing robot. *Mechatronics*, 17(4-5):207–216, 2007.

B. J. Nelson, J. D. Morrow, and P. K. Khosla. Improved force control through visual servoing. In *American Control Conference, Proceedings of the 1995*, volume 1, pages 380–386. IEEE, 1995.

V. Nunez, N. Nadjar-Gauthier, K. Yokoi, P. Blazevic, and O. Stasse. Whole body posture controller based on inertial forces. In *Humanoid Robots, 2006 6th IEEE-RAS International Conference on*, pages 188–193. IEEE, 2006.

K. Ohnishi. Robust motion control using disturbance observer. *IEEE/ASME Trans. Mechatron.*, 11(4):486–493, 1993a.

K. Ohnishi. Robust motion control by disturbance observer. *Journal of the Robotics Society of Japan*, 11(4):486–493, 1993b.

K. Ohnishi, M. Shibata, and T. Murakami. Motion control for advanced mechatronics. *IEEE/ASME Trans. Mechatron.*, 1(1):56–67, Mar. 1996.

T. Olsson, R. Johansson, and A. Robertsson. Flexible force-vision control for surface following using multiple cameras. In *Intelligent Robots and Systems, 2004.(IROS 2004). Proceedings. 2004 IEEE/RSJ International Conference on*, volume 1, pages 789–803. IEEE, 2004.

D. E. Orin, R. B. McGhee, and V. Jaswa. Interactive compute-control of a six-legged robot vehicle with optimization of stability, terrain adaptibility and energy. In *Decision and Control including the 15th Symposium on Adaptive Processes, 1976 IEEE Conference on*, volume 15, pages 382–391. IEEE, 1976.

E. Papadopoulos and D. A. Rey. A new measure of tipover stability margin for mobile manipulators. In *Robotics and Automation, 1996. Proceedings., 1996 IEEE International Conference on*, volume 4, pages 3111–3116. IEEE, 1996.

J. Park, S. H. Kim, and S. Kim. Active compliant motion control for grinding robot. *IFAC Proceedings Volumes*, 41(2):4285–4289, 2008.

V. Perdereau and M. Drouin. A new scheme for hybrid force-position control. *Robotica*, 11(5):453–464, 1993.

M. Prats, P. J. Sanz, and A. P. Del Pobil. Reliable non-prehensile door opening through the combination of vision, tactile and force feedback. *Autonomous Robots*, 29(2):201–218, 2010.

M. H. Raibert and J. J. Craig. Hybrid position/force control of manipulators. *Journal of Dynamic Systems, Measurement, and Control*, 103(2):126–133, 1981.

L. Roveda, F. Vicentini, and L. M. Tosatti. Deformation-tracking impedance control in interaction with uncertain environments. In *2013 IEEE/RSJ International Conference on Intelligent Robots and Systems*, pages 1992–1997. IEEE, 2013.

W. B. Rowe. *Principles of modern grinding technology*. William Andrew, 2013.

J. K. Salisbury. Active stiffness control of a manipulator in cartesian coordinates. In *Decision and Control including the Symposium on Adaptive Processes, 1980 19th IEEE Conference on*, pages 95–100. IEEE, 1980.

H. Seraji. A unified approach to motion control of mobile manipulators. *The International Journal of Robotics Research*, 17(2):107–118, 1998.

H. Seraji and R. Colbaugh. Force tracking in impedance control. *The International Journal of Robotics Research*, 16(1):97–117, 1997.

M. Shneier and R. Bostelman. Literature review of mobile robots for manufacturing. *National Institute of Standards and Technology, US Department of Commerce*, 2015.

B. Siciliano and O. Khatib. *Springer handbook of robotics*. Springer, 2016.

B. Siciliano and L. Villani. A passivity-based approach to force regulation and motion control of robot manipulators. *Automatica*, 32(3):443–447, 1996.

L. Simoni, E. Villagrossi, M. Beschi, A. Marini, N. Pedrocchi, L. M. Tosatti, G. Legnani, and A. Visioli. On the use of a temperature based friction model for a virtual force sensor in industrial robot manipulators. In *2017 22nd IEEE International Conference on Emerging Technologies and Factory Automation (ETFA)*, pages 1–6. IEEE, 2017.

A. C. Smith, F. Mobasser, and K. Hashtrudi-Zaad. Neural-network-based contact force observers for haptic applications. *IEEE Transactions on Robotics*, 22(6):1163–1175, 2006. doi: 10.1109/TRO.2006.882923.

R. Smits, H. Bruyninckx, W. Meeussen, J. Baeten, P. Slaets, and J. Schutter. Model based position-force-vision sensor fusion for robot compliant motion control. In *Proc. IEEE Int. Conf. on Multisensor Fusion and Integration for Intelligent Systems*, pages 501–506, 2006.

S. Sreenivasan and B. Wilcox. Stability and traction control of an actively actuated micro-rover. *Journal of Field Robotics*, 11(6):487–502, 1994.

K. Straif, L. Benbrahim-Tallaa, R. Baan, Y. Grosse, B. Secretan, F. El Ghissassi, V. Bouvard, N. Guha, C. Freeman, L. Galichet, et al. A review of human carcinogens—part c: metals, arsenic, dusts, and fibres. *The lancet oncology*, 10(5):453–454, 2009.

S. Sugano, Q. Huang, and I. Kato. Stability criteria in controlling mobile robotic systems. In *Intelligent Robots and Systems' 93, IROS'93. Proceedings of the 1993 IEEE/RSJ International Conference on*, volume 2, pages 832–838. IEEE, 1993.

O. Tahri, D. Boutat, and Y. Mezouar. Brunovsky's linear form of incremental structure from motion. *IEEE Transactions on Robotics*, 33(6):1491–1499, 2017.

J. Tan and N. Xi. Unified model approach for planning and control of mobile manipulators. In *Robotics and Automation, 2001. Proceedings 2001 ICRA. IEEE International Conference on*, volume 3, pages 3145–3152. IEEE, 2001.

B. Ulrich, A. Srivastava, and M. Elbestawi. Analysis of the robotic disc grinding process. *The International Journal of Advanced Manufacturing Technology*, 7(2):82–92, 1992.

Y. Umeda, D. Nakamura, T. Murakami, and K. Ohnishi. Hybrid position/force control of a mobile manipulator based on cooperative task sharing. In *Industrial Electronics, 1999. ISIE'99. Proceedings of the IEEE International Symposium on*, volume 1, pages 139–144. IEEE, 1999.

UNRV. Asbestos in the roman empire. https://www.unrv.com/economy/asbestos.php, 2019. [Online; accessed 30-march-2019].

L. Villani, C. C. De Wit, and B. Brogliato. An exponentially stable adaptive control for force and position tracking of robot manipulators. *IEEE Transactions on Automatic Control*, 44(4):798–802, 1999.

R. Volpe and P. Khosla. Experimental verification of a strategy for impact control. In *Robotics and Automation, 1991. Proceedings., 1991 IEEE International Conference on*, pages 1854–1860. IEEE, 1991.

J. Wang, Y. Li, and C. Qiu. Analysis of dynamic stability constraints for a mobile humanoid robot. In *Robotics and Biomimetics, 2008. ROBIO 2008. IEEE International Conference on*, pages 377–382. IEEE, 2009.

Y. Wang and Y. Jan. Path planning for robot-assisted grinding processes. In *Robotics and Automation, 2001. Proceedings 2001 ICRA. IEEE International Conference on*, volume 1, pages 331–336. IEEE, 2001.

Y. Wang and C. Wang. Development of a polishing robot system. In *Emerging Technologies and Factory Automation, 1999. Proceedings. ETFA'99. 1999 7th IEEE International Conference on*, volume 2, pages 1161–1166. IEEE, 1999.

D. E. Whitney. Historical perspective and state of the art in robot force control. *The International Journal of Robotics Research*, 6(1):3–14, 1987.

World Health Organization et al. Asbestos: elimination of asbestos-related diseases: World health organization media centre; 2017, 2017.

D. Xiao, B. K. Ghosh, N. Xi, and T. J. Tarn. Sensor-based hybrid position/force control of a robot manipulator in an uncalibrated environment. *IEEE Transactions on Control Systems Technology*, 8(4):635–645, 2000.

H. Xie, L. Chen, L. Sun, and W. Rong. Hybrid vision-force control for automatic assembly of miniaturized gear system. In *Proceedings of the 2005 IEEE International Conference on Robotics and Automation*, pages 1368–1373. IEEE, 2005.

Y. Yamamoto and X. Yun. Coordinating locomotion and manipulation of a mobile manipulator. In *Decision and Control, 1992., Proceedings of the 31st IEEE Conference on*, pages 2643–2648. IEEE, 1992.

Y. Yamamoto and X. Yun. Modeling and compensation of the dynamic interaction of a mobile manipulator. In *Robotics and Automation, 1994. Proceedings., 1994 IEEE International Conference on*, pages 2187–2192. IEEE, 1994.

Y. Yamamoto and X. Yun. Effect of the dynamic interaction on coordinated control of mobile manipulators. *IEEE Transactions on Robotics and Automation*, 12(5):816–824, 1996.

C. Yang, G. Ganesh, S. Haddadin, S. Parusel, A. Albu-Schaeffer, and E. Burdet. Human-like adaptation of force and impedance in stable and unstable interactions. *IEEE transactions on robotics*, 27(5):918–930, 2011.

K. Yoneda and S. Hirose. Tumble stability criterion of integrated locomotion and manipulation. In *Intelligent Robots and Systems' 96, IROS 96, Proceedings of the 1996 IEEE/RSJ International Conference on*, volume 2, pages 870–876. IEEE, 1996.

T. Yoshikawa. Manipulability of robotic mechanisms. *The international journal of Robotics Research*, 4(2):3–9, 1985.

T. Yoshikawa. Dynamic hybrid position/force control of robot manipulators–description of hand constraints and calculation of joint driving force. *IEEE Journal on Robotics and Automation*, 3(5):386–392, 1987.

T. Yoshikawa. Force control of robot manipulators. In *Robotics and Automation, 2000. Proceedings. ICRA'00. IEEE International Conference on*, volume 1, pages 220–226. IEEE, 2000.

L. Yu, Q. Cao, C. Li, and C. Qiu. On-line planning of nonholonomic mobile manipulators based on stability twist constraint. *Journal of the Brazilian Society of Mechanical Sciences and Engineering*, 32(2):165–170, 2010.

Y. Zhao and C.-C. Cheah. Hybrid vision-force control for robot with uncertainties. In *Robotics and Automation, 2004. Proceedings. ICRA'04. 2004 IEEE International Conference on*, volume 1, pages 261–266. IEEE, 2004.

Y. Zhou, B. J. Nelson, and B. Vikramaditya. Fusing force and vision feedback for micromanipulation. In *Robotics and Automation, 1998. Proceedings. 1998 IEEE International Conference on*, volume 2, pages 1220–1225. IEEE, 1998.

G. Ziliani, A. Visioli, and G. Legnani. A mechatronic approach for robotic deburring. *Mechatronics*, 17(8):431–441, 2007.